Titre: Title:	Development of Solid-Stabilized High Internal Phase Emulsions for Sound Absorbing Porous Materials
Auteur: Author:	Mina Saghaei
Date:	2025
Type:	Mémoire ou thèse / Dissertation or Thesis
Référence: Citation:	Saghaei, M. (2025). Development of Solid-Stabilized High Internal Phase Emulsions for Sound Absorbing Porous Materials [Thèse de doctorat, Polytechnique Montréal]. PolyPublie. https://publications.polymtl.ca/65773/

URL de PolyPublie: PolyPublie URL:	https://publications.polymtl.ca/65773/
Directeurs de recherche: Advisors:	Louis Fradette, & Annie Ross
Programme: Program:	Génie chimique

POLYTECHNIQUE MONTRÉAL

affiliée à l'Université de Montréal

Development of Solid-Stabilized High Internal Phase Emulsions for Sound Absorbing Porous Materials

MINA SAGHAEI

Département de génie chimique

Thèse présentée en vue de l'obtention du diplôme de *Philosophiæ Doctor*

Génie chimique

Avril 2025

POLYTECHNIQUE MONTRÉAL

affiliée à l'Université de Montréal

Cette thèse intitulée :

Development of Solid-Stabilized High Internal Phase Emulsions for Sound Absorbing Porous Materials

présentée par **Mina SAGHAEI**

en vue de l'obtention du diplôme de *Philosophiæ Doctor*

a été dûment acceptée par le jury d'examen constitué de :

Nick VIRGILIO, président
Louis FRADETTE, membre et directeur de recherche
Annie ROSS, membre et codirectrice de recherche
Sampada BODKHE, membre
Farhad EIN-MOZAFFARI, membre externe

DEDICATION

To my husband, my best friend and greatest support.

To my mother, for her endless kindness and love.

To my sisters for our memorable moments.

To my father, whose spirit guides me every moment.

ACKNOWLEDGEMENTS

I would like to sincerely thank my supervisors, Prof. Louis Fradette and Prof. Annie Ross. Their unwavering support, guidance, and patience over the years were essential to the completion of this research. I encountered several challenges and obstacles, and at times, I felt as though I was lost in an ocean of darkness. During those moments, you both were like guiding stars, illuminating the best path forward and inspiring me to find better solutions. Your encouragement kept me motivated and excited about the journey.

I would also like to express my deep gratitude to Edith Roland Fotsing. I have learned so much from you about acoustics—each meeting felt like an informative course. Your suggestions for correlating different sections of my project were truly enlightening and sparked new ideas that greatly benefited my work.

Special thanks to my teammates in Prof. Louis Fradette's group: Bing Wan, Tiffany Bellanger, Sophia Roy, and Mohammed Zriki. Your support and kindness were invaluable throughout every step of my project. I would also like to thank Matthieu Gauthier and Claire Cerclé, who trained me to conduct chemical experiments, as well as Gino Robin and Martine Lamarche, who helped provide materials and lab equipment.

I would like to express my gratitude to Prof. Tavares, whose kindness and guidance were always helpful throughout my PhD journey. I am also thankful to the members of his lab, who were my office mates and provided constant support by listening to the challenges I faced during my PhD: William Simon, Darius Klassen, Andres Sanchez, Wendell Rafael, and David Brassard.

My gratitude also goes to all the members of LAVA who assisted me with the acoustic aspects of my project: Prof. David Vidal, for helping me simulate acoustic results with GeoDict; Mohamad Amin Ben Lassoued (Postdoctoral Researcher), Manuel Flores (Postdoctoral Researcher), Imen Rzig, Davide de Cicco, Elissa El Hajj (PhD student), Niloofar Rastegar Dehkordi (PhD student), and Mernoosh Abedi (PhD student). Your support and insights were invaluable.

I would also like to thank all the professors and technicians in the Chemical Engineering Department who assisted me with the setup and preparation for the mixing experiments. In particular, I am grateful to Prof. Bruno Blais, Sébastien Chénard, and Alejandro Velez Garcia for their guidance and help. Also, I would like to thank Jacopo de Tommaso from Professor Patience's laboratory for providing me with the large oven for curing the large samples.

Last but not least, I would like to thank my husband, Emad Alavi, who has been my greatest companion throughout the entire process of my PhD. In addition to his emotional support, he was also my scientific collaborator at every stage of this project. His understanding of the challenges of a PhD—being a PhD student himself—was an invaluable source of comfort and strength.

RÉSUMÉ

De nos jours, la pollution sonore est un problème majeur, notamment en milieu urbain. Plusieurs types d'absorbeurs acoustiques, tels que les mousses à base de polyuréthane, sont actuellement utilisés pour réduire le bruit des véhicules. Cependant, ces matériaux présentent des inconvénients notables. Ils contiennent des ingrédients nocifs et complexes, et leur structure inflammable les rend impropres à l'industrie aéronautique.

Cette recherche explore une nouvelle approche de production de matériaux acoustiques poreux grâce à une formulation respectueuse de l'environnement et un procédé simple. La méthode consiste à créer une émulsion solide-stabilisée, contenant deux liquides non miscibles (une phase aqueuse et une phase huileuse) et des particules solides qui stabilisent les gouttelettes de la phase dispersée (ici, la phase huileuse). Le post-traitement comprend l'évaporation des liquides et le frittage des particules. Ces émulsions solides-stabilisées sont également appelées émulsions de Pickering, du nom de leur découvreur.

Pour obtenir la structure souhaitée, le pourcentage volumique de phase dispersée (phase interne) doit dépasser 74 % vol., ce qui correspond à la fraction d'entassement maximale de la phase dispersée. Au-delà de ce point, les gouttes de la phase dispersée sont déformées par la présence de leurs voisines et la viscosité de l'émulsion augmente significativement, donnant naissance à un matériau à l'apparence d'une pâte. L'émulsion de Pickering à phase interne élevée, abrégée en HIPPE, est utilisée dans cette thèse pour produire un matériau poreux en vue d'évaluer son potentiel pour l'absorption du son.

En relevant les défis liés à la production de grosses gouttelettes dans les HIPPE et en augmentant leur production à grande échelle, ces travaux font progresser la compréhension fondamentale et les applications pratiques des HIPPE en régime d'écoulement laminaire. L'étude s'articule autour de trois objectifs principaux:

Production de larges gouttelettes mono dispersées dans les HIPPEs: Un nombre capillaire modifié a été utilisé pour prédire précisément la taille des gouttelettes en intégrant la viscosité effective de la phase continue, influencée par l'agrégation des particules et les conditions de traitement. À l'aide de mesures in-situ de couple, l'impact des paramètres de traitement tels que le taux de cisaillement, le temps d'émulsification et la concentration en PVA sur la taille des

gouttelettes a été analysé. Les résultats soulignent le rôle essentiel des propriétés des particules telles que la taille, la forme et la structure fractale sur formation des gouttelettes monodisperses de grande taille, indispensables pour les applications impliquant les matériaux poreux.

Mise à l'échelle des HIPPEs dans un régime laminaire : L'étude a établi qu'un exposant de mise à l'échelle de $\alpha = 0$ (vitesse de rotation constante à toutes les échelles) garantit une taille de gouttelettes cohérente, à condition que la géométrie et la formulation restent constantes. Ce travail a également démontré que le maintien d'une puissance par volume constante (*P/V*) est essentielle pour assurer la cohérence de la taille des gouttelettes, ce qui peut être réalisé soit en maintenant une vitesse de rotation constante, soit en ajustant la viscosité de la phase continue pour compenser les limitations des équipements. La relation entre la taille des gouttelettes, l'énergie spécifique (*e/V*) et la puissance (*P/V*) fournit un outil prédictif pour la mise à l'échelle de la production des HIPPEs, du laboratoire à l'industrie.

Performance acoustique des structures poreuses produites par HIPPEs : En ajustant les conditions de traitement, des structures poreuses avec des tailles de pores, des niveaux de porosité, de connectivité et de tortuosité variés, ont été obtenues. Les structures résultantes ont montré un niveau d'absorption acoustique modulable: les plus grandes tailles de pores et de porosité ont permis une absorption maximale à des fréquences élevées, tandis qu'une tortuosité plus importante a amélioré l'absorption à de plus basses fréquences. En utilisant la modélisation des réseaux de pores ouverts (OpenPNM), la microstructure 3D des matériaux poreux a été analysée afin de déterminer la relation entre la morphologie des pores, les paramètres non acoustiques et les performances acoustiques. Le comportement sous-longueur d'onde de la mousse HIPPE en fait le meilleur choix pour les applications où le poids et l'espace sont limités.

Ce travail démontre la flexibilité et la robustesse de l'approche de production de matériaux poreux par la génération de HIPPEs comme gabarit. Cette méthode permet la constance et la prévisibilité de l'émulsion à toutes les échelles. Pour la production de matériaux acoustiques, cette prévisibilité est un atout majeur pour la qualité du produit fini.

ABSTRACT

Nowadays, people suffer from the noise pollution, especially in urban areas. Several type of sound absorbers, such as polyurethane-based foams, are currently used to reduce vehicle noise; however, these materials have notable drawbacks. They contain harmful and complex ingredients and possess a flammable structure, making them unsuitable for use in aviation industry.

This research explores a novel approach for producing acoustic porous materials through an environmentally friendly formulation and straightforward process. The method involves creating a solid-stabilized emulsion, which contains two immiscible liquids (an aqueous phase and oil phase) and solid particles that stabilize the droplet of the dispersed phase (the oil phase, in in this case), and post processing, includes the evaporation of liquids and sintering particles. These solid-stabilized emulsions also called Pickering emulsions, named in honor of their original discoverer.

To achieve the desired structure, the volume percentage of dispersed phase (internal phase) must exceed 74 vol.%, which is the maximum packing fraction of dispersed phase. Beyond this point, the viscosity of emulsion increase significantly, resulting in a paste-like material. The high internal phase Pickering emulsion, which abbreviated as HIPPE are used in this thesis to produce sound absorbing porous material.

By addressing the challenges associated with producing large droplets in HIPPEs and scaling up their production, this work advances both the fundamental understanding and practical applications of HIPPEs in the laminar flow regime. The study is divided into three key objectives:

Production of Monodisperse Large Droplets in HIPPEs: A modified capillary number was developed to accurately predict droplet size by incorporating the effective viscosity of the continuous phase, which is influenced by particle aggregation and processing conditions. Using in-situ torque monitoring, the impact of process parameters such as shear rate, emulsification time, and PVA concentration on droplet size was quantified. The findings highlight the critical role of particle properties (size, shape, and fractal structure) in modified capillary number and ultimately, achieving monodisperse large droplets, which are essential for porous material applications.

Scale-Up of HIPPEs in the Laminar Regime: The study established that a scale-up exponent of $\alpha = 0$ (constant rotational speed across scales) ensures consistent droplet size, provided the geometry and formulation remain constant. This work further demonstrated that maintaining

constant power per volume (*P/V*) is key to droplet size consistency, which can be achieved by either maintaining constant rotational speed or adjusting the continuous phase viscosity to account for equipment limitations. The relationship between droplet size, energy input (*e/V*), and power (*P/V*) provides a predictive tool for scaling up HIPPE production from laboratory to industrial scales.

Acoustic Performance of Porous Structures Derived from HIPPEs: By adjusting processing conditions, porous structures with varying pore size, porosity, connectivity, and tortuosity were obtained. The resulting structures demonstrated tunable sound absorption performance, with larger pore sizes and higher porosity achieving maximum sound absorption at higher frequencies, while higher tortuosity enhanced absorption at lower frequencies. Using open pore network modeling (OpenPNM), the 3D microstructure of porous materials was analyzed, validating the relationship between pore morphology, non-acoustical parameters, and acoustic performance. The subwavelength behavior of HIPPE foam suggests it has significant potential for applications where the weight and space are constrained.

This work demonstrates the scalability and versatility of HIPPEs as a template for functional porous materials, particularly in acoustic applications. By bridging the gap between formulation, processing conditions, and scale-up strategies, this research offers a practical framework for industrial production while paving the way for future studies on numerical simulation, alternative formulations, and advanced impeller designs.

TABLE OF CONTENTS

LIST OF TABLES

LIST OF FIGURES

LISTE OF SYMBOLS AND ABBREVIATIONS

The list of acronyms and abbreviations presents, in alphabetical order, the acronyms and abbreviations used in the thesis and their meaning.

Abbreviations

DHR	Double helical Ribbon
DSD	Droplet size distribution
JCA	Johnson-Champoux-Allard
JCAL	Johnson-Champoux-Allard-Lafarge
JCAPL	Johnson-Champoux-Allard-Pride-Lafarge
MF/GO	Melamine foam/Graphen oxide
micro-CT	Microscope using X-ray computerized tomography
NCC	Nano crystalline cellulose
O/W	Oil in water emulsion
OpenPNM	Open pore network modelling
PBT	Pitched blade turbine
PBTD	Down-pumping pitched blade turbine
PBTU	Up-pumping pitched blade turbine
PI	Polyimide
PolyHIPPE	Polymeric high internal phase Pickering emulsion
PSD	Particle size distribution
PU/CNT	Polyurethane/Carbon nano tube
PVA	Polyvinyl alcohol
ROI	Region of interest
RPM	Rotation per minute

RT	Rushton turbine
SEF	Simple extension flow
SEM	Scanning Electron Microscopy
SHR	Single helical ribbon
SSE	Solid stabilized emulsion
SSF	Simple shear flow

Roman Letters

A_{cov} (m^2)	Total surface area of droplets that covered with particle
Am (Pa)	Amplitude of a reflective wave with a porous material
Ar (Pa)	Amplitude of a reflective wave with a perfectly rigid surface
C_0 (m/s)	Sound speed in the air
Ca (-)	Capillary number $Ca = \frac{\mu\dot{\gamma}}{2\sigma/D_{43}}$
D (m)	Impeller diameter
D_{10} (μm)	Droplet/particle size at which 10% of all droplets/particles are smaller than this size
D_{32} (μm)	Surface area weighted average, Sauter mean
D_{43} (μm)	Volume weighted average
D_{50} (μm)	Droplet/particle size at which 50% of all droplets/particles are smaller than this size
D_{90} (μm)	Droplet/particle size at which 90% of all droplets/particles are smaller than this size
D_f (-)	Fractal dimensions
Di (μm)	Diameter of individual droplet/particle
E (J)	Attachment energy of particle at the droplet surface
Ei (J)	Incident sound energy
Ea (J)	Absorbed sound energy

Et (J)	Transmitted sound energy
Er (J)	Refracted sound energy
e/V (J/m^3)	Energy consumed per unit volume of emulsion
f (Hz)	Frequency
Fc (N)	Collision force of particle-droplet
G'(Pa)	Elastic modulus
G''(Pa)	Viscose modulus
H (cm)	Height of material in the tank
h (μm)	Thickness of particle around the droplets
I (s^{-1})	Scatter intensity
K (S/m)	Specific conductivity
k (Pa·s^n)	consistency index of fluid
$\tilde{k}$ (-)	Wave number
$\tilde{K}_e$ (N/m^2)	Bulk modules of equivalent fluid
K_g(-)	Structure prefactor, compactness of particle
k_p (-)	Power constant $k_{p=}N_P * Re$
k_s (-)	Metzner and Otto constant
KT (J)	Energy Boltzmann unit
l (m)	Thickness of porous material
N (s^{-1})	Rotational speed of impeller
n (-)	Power law index
ni (-)	Number of droplet/particle at size class i in the Mastersizer report
Njs (s^{-1})	Just suspended rotational speed
N_P (-)	Power number $N_P = \frac{P}{\rho N^3 D^5}$

np (-)	Number of primary particle in the aggregated particle
$N_{p\ total}$ (-)	Total number of particle in the emulsion
Nr (-)	Revolution number
N_{ref} (s^{-1})	Reference rotational speed
P (W)	Consumed power during mixing $P = 2\pi N\Gamma$
P_r (-)	Prandtl number
p (-)	Viscosity ratio $p = \frac{\mu_d}{\mu_c}$
Pjs (W)	Just suspended power
P/V (W/m^3)	Power consumed per unit volume of emulsion
q (radian)	Scattering angle
q_0 (m^2)	Static viscous permeability
$q_{0'}$ (m^2)	Static thermal permeability
r (-)	reflection coefficient
r_0 (m)	Minimum primary particle radius
Rd (m)	Radius of pure droplet without particle surrounded
Re(-)	Reynolds number: $Re = \frac{\rho N D^2}{\mu}$
R_{eff} (m)	Effective radius of droplets
Rg (m)	Gyration radius
R_P (m)	Particle radius
T (m)	Tank diameter/Thickness of sample
V (m^3)	Total volume of emulsion/pore volume
V_{tip} (m/s)	Tip speed at the edge of impeller= πND
We (-)	Weber number: $we = \frac{\rho N^2 D^3}{\sigma}$

$\tilde{Z}$ (Pa/m^3) Surface impedance

Z_0(Pa/m^3) Air impedance

$\widetilde{Z_c}$ (Pa/m^3) Characteristic impedance

Greek letters

α (-) Scale-up exponent/ sound absorption coefficient

α_∞ (-) Tortuosity

γ (-) Adiabatic constant

γ_{ow} (N/m) Interfacial tension between oil and water

$\dot{\gamma}$ (s^{-1}) Shear rate $\dot{\gamma} = k_s N$

Γ (N.m) Torque

ε (J/s) Energy dissipation rate

ζ (mV) Zeta potential

ς (-) Frequency of particle-droplet collision

$[\eta]$ (Pa.s) intrinsic viscosity

η_r (-) Relative viscosity

θ (degree) Contant angle of particle at the droplet surface/Contant angle between source and receiver of signal in the tortuosity test

ω (Hz) Frequency

Λ(m) Viscous characteristic length

Λ'(m) Thermal characteristic length

λ (m) Kolmogorov length scale

μ (Pa.s) Viscosity of medium

μ_c (Pa.s) Continuous phase viscosity

μ_d (Pa.s) Dispersed phase viscosity

υ (Pa.s)	Dynamic viscosity
ξ (F/m)	Absolute permittivity in electromagnetic
ρ (kg/m^3)	Density of medium
ρ_b(kg/m^3)	Bulk density
$\tilde{\rho}_e$ (kg/m^3)	Density of equivalent fluid
ρ_m (kg/m^3)	Density of porous material
σ (Pa/m^2)	Air flow resistivity
Φ (-)	Open porosity
ϕ (-)	Volume fraction of dispersed phase
ϕ_s (-)	Effective volume fraction in diluted emulsion
ϕ_{eff} (-)	Effective volume fraction in concentrated emulsion
ϕ_g (-)	Glass transmission of volume fraction of dispersed phase (jammed emulsion)
ϕ_m (-)	Maximum packing factor of particle in suspension

LIST OF APPENDICES

CHAPTER 1 INTRODUCTION

1.1. Global Challenges

In recent decades, health problems induced by noise pollution have become a serious concern, particularly due to the rapid development of the transportation industry. For instance, jet engines emit the noise ranging from 200 Hz to 2kHz [1]. It has been also reported that during takeoff, significant low-frequency (100-500 Hz) noise is generated, which can propagate over long distance and significantly impact communities, since this noise is within the range of human hearing sensitivity (20-20 kHz)[2][3]. The aviation industry has been trying to control aircraft engine noise by means of many improvements and acoustic liners represent one of them [4]. These liners have evolved from honeycomb structures to complex metamaterial structures which includes designing internal microchannel [4].Figure 1.1 illustrates the different types of these metamaterials and their complex design.

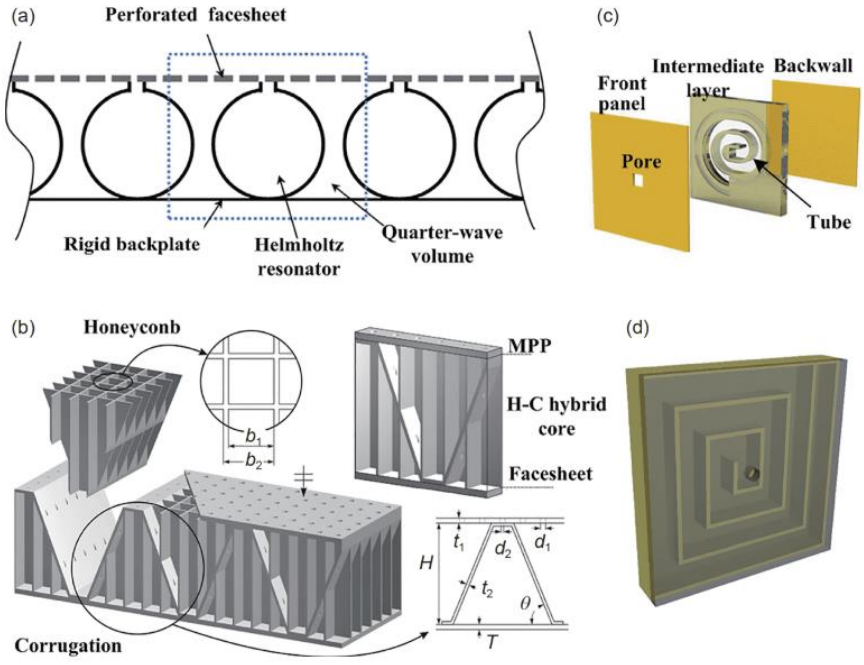

Figure 1.1. Different metamaterial designs for low frequency sound absorption.[4] (a) dual resonate metamaterial [5]; (b) perforated honey-comb-corrugation hybrid metamaterial [6]; (c) and (d) two different space coiling designs [7][8].

Recent developments in the controlled production of polymer foams and their applications in sound dissipation have captured researchers' attention [9]. This polymeric foams requires less installation space and simplifies the challenges of designing metamaterial structures. It accomplishes this by providing an internal structure with highly interconnected cavities that efficiently dissipates noise. It is reported that the pore size has a significant effect on the sound absorption coefficient [10]; smaller pores increase the number of cavities to trap the sound waves, making porous structure appropriate for dissipating low-frequency noise (for instance a 200-micron pore size in Figure 1.2). However, a further decrease in pore size increase the sound reflection, leading to a low sound absorption coefficient (100-micron pore size in Figure 1.2(a))[10].

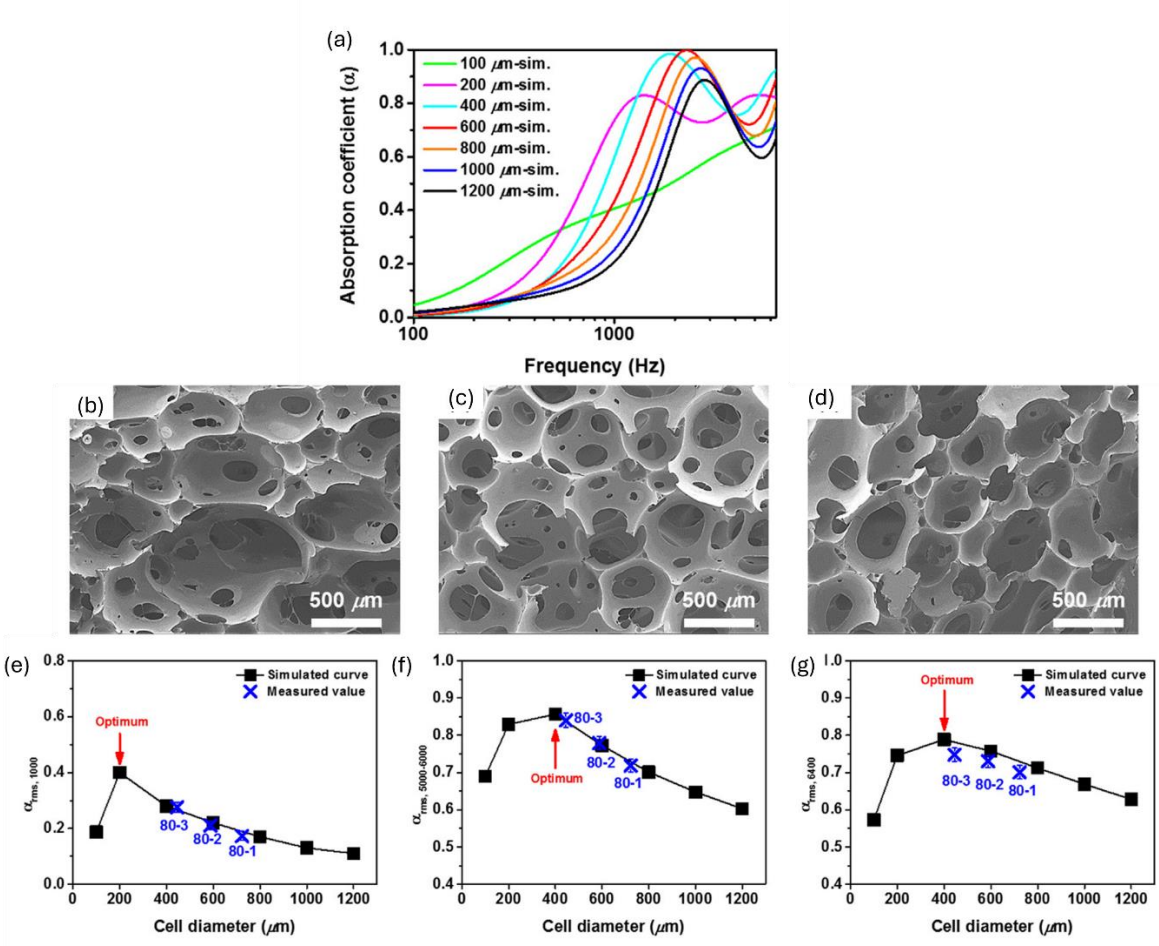

Figure 1.2. (a) simulated sound absorption at different pore size, (b-d) SEM image of sample 80-1, 80-2,80-3, (e)-(g) root mean square value of sound absorption curve from 0-2000 Hz ($\alpha_{rms,1000}$), 5000-6000 ($\alpha_{rms,5000\text{-}6000}$), and ($\alpha_{rms,6400}$) [10]

Achieving such a precise structure relies on complex formulations, which are extremely difficult to perfect due to the unpredictability of chemical reactions during the foaming process [11] ; for instance, Figure 1.3 (c) cannot be achieved due to complexity of ingredients. Moreover, the use of harmful ingredients, like isocyanates, and catalysts in their formulation poses an additional cost for implementing safety measures for operators' health.

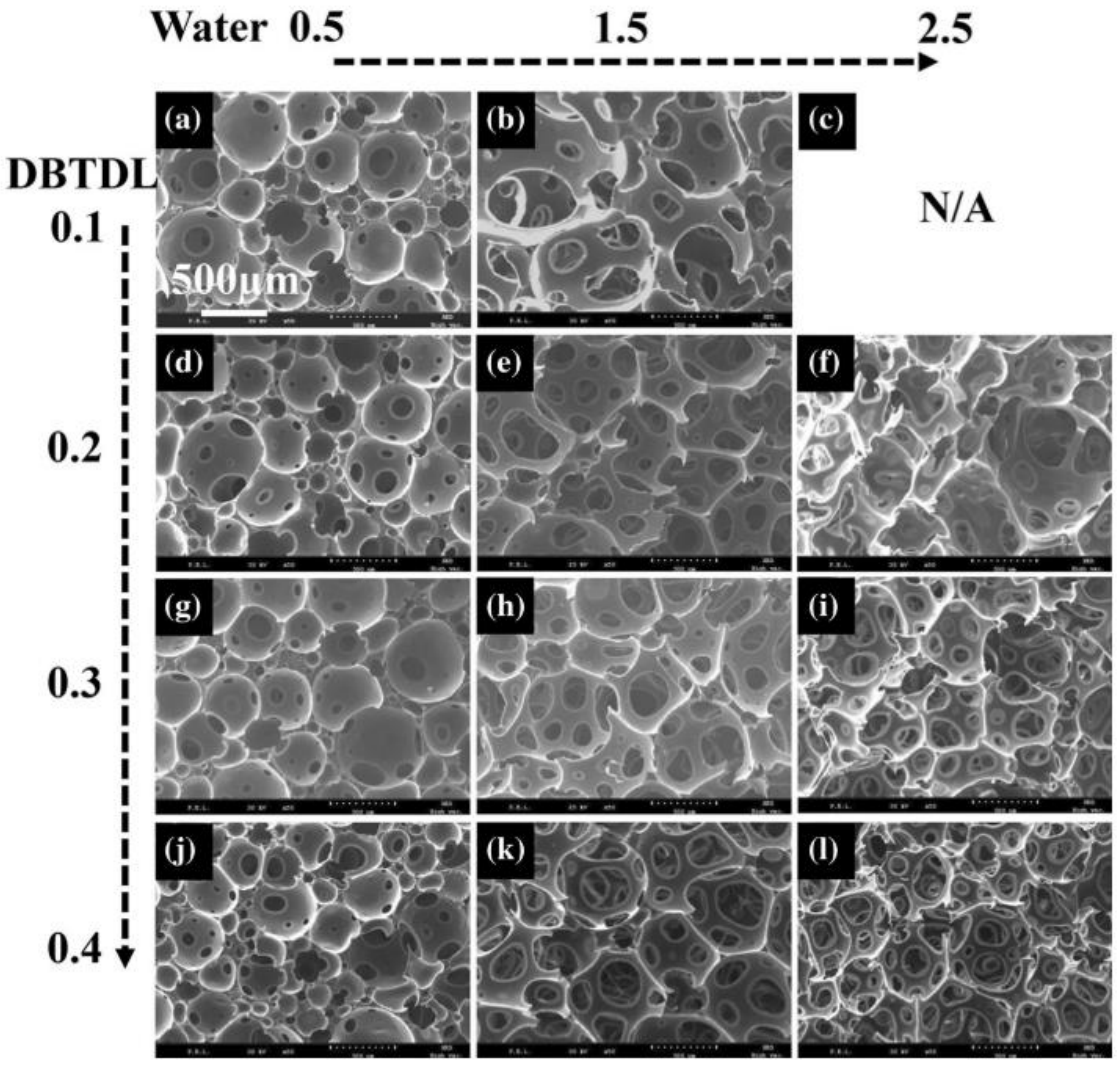

Figure 1.3. SEM images of polyurethane samples, at different water and catalyst (DBTDL)content. Magnification for all samples is the same. The sample at condition c cannot be obtained[12].

1.2. A Novel Solution

This thesis introduces a novel approach for fabricating porous structures from solid-stabilized emulsions. These emulsions consist of a continuous aqueous phase containing solid particles and a dispersed oil phase. During the mixing process, the immiscible oil phase is broken into droplets, which are subsequently stabilized by the adsorption of solid particles at the oil-water interface. A schematic of droplet stabilization by particles is illustrated in Figure 1.4 (A) [13]. The emulsions can have varying concentrations of dispersed phase. A concentration of 74 vol% represents the maximum amount at which the emulsion forms spherical droplets (Figure 1.4 (C)). Below this concentration, the droplets remain stabilized but spaced farther apart (Figure 1.4 (B). Above this concentration, the droplets adopt a polygonal shape resulting from the close proximity of their neighbours and result in a structure of deformed drops separated by a thin film of the continuous phase between the drops, everywhere in the produced emulsion. The result is an extremely high viscosity, increasing with smaller drops, which makes these emulsions particularly suitable as templates for structured materials.

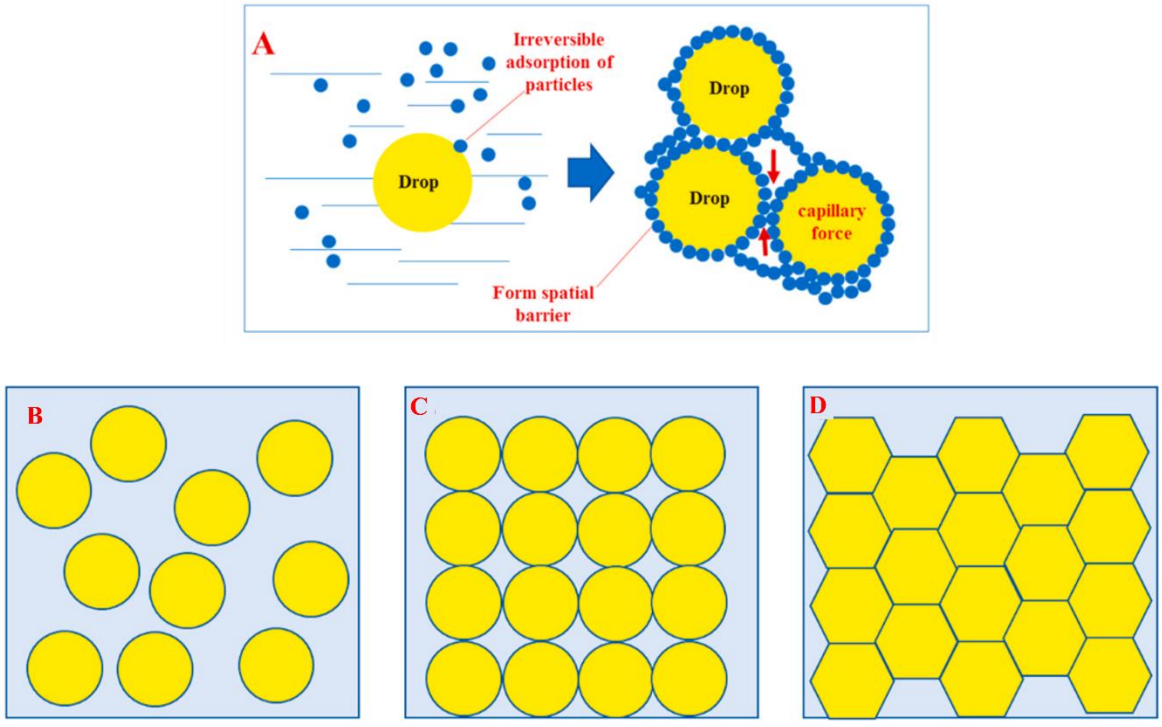

Figure 1.4. (A) Schematic of Pickering emulsion, (B)-(D) Schematic morphology of emulsion at <74 vol%, =74 vol.%, >74 vol.%, respectively[13].

The size of these stabilized droplets is controlled through process conditions and formulation parameters, directly affecting the porous structure morphology. These emulsions, also known as Pickering emulsions – named after their first introducers, Walter Ramsden and Spencer Umfreville Pickering, in the 19th century [14] . Recently, Pickering emulsions have found applications of porous materials for biomaterials [15], catalysis [16], membranes [17], and more. However, their acoustic performance remains unexplored.

In the field of sound absorption, an efficient material must have 1- maximum porosity, 2- the largest number of interconnected pores, and 3- precise control of pore size to achieve the maximum sound absorption performances [18]. During this project we aim to show that our novel approach, producing acoustic porous structure from Pickering emulsion, can answer all of this requirements:

1- Extremely high porosity can be achieved using concentrated Pickering emulsions. This is achieved by evaporation of all liquids (continuous and dispersed phases) and by keeping the particles as the remaining solid structure. The result is a high porosity structure. The dispersed phase must reach concentrations exceeding 74 vol % to obtain these structures. It is preferable to work at higher concentrations, and, in some case, the dispersed phase concentration can surpass 85%. At these extreme conditions, the emulsions are called high internal phase Pickering emulsion, or HIPPE.
2- The interconnectivity between pores can be achieved by creating small open holes in the walls of the pores. These holes are formed through process such as particle sintering and the evaporation of oil and water.
3- Finally, precise control of pores sizes can be achieved by adjusting the process condition during the mixing of HIPPEs. HIPPE naturally tends to produce very uniform drop size distributions, a very useful feature in applications with strict performance requirements from the porous structure. The challenge is that HIPPE naturally tend to produce very small droplets once equilibrium is reached. This is due to the autogenous milling effect of the closely packed drops forced in motion by the agitator in the tank. Obviously, higher concentrations of dispersed phase will tend to create conditions favorable to smaller sizes. This phenomenon is similar to pushing a pile of rocks with a bulldozer; rocks will be crushed naturally in result of the forces motion of the pile. In our case, controlling the size reduction of the drops is the main challenge and the conditions to achieve this control are not known.

HIPPE offers all three requirements for producing porous materials for sound-proofing applications. Hence, the production of porous materials using high internal phase Pickering emulsion as templates represents a novel and promising approach for acoustic porous materials.

1.3. Addressing key challenges in the project

Controlling the large droplet size in HIPPE production is a significant challenge. The high percentage of dispersed phase and the particles concentration both increase the viscosity of emulsions [19] and the motion of the fluid in the viscous conditions favors the breakage of the drops, hence reducing their droplet sizes below the desired value. Furthermore, high-pressure, or rotor-stator mixers, commonly used to disperse particles and break droplets in these emulsions, amplify the breakage capacity and damage the particles' structure [20]. This excessive breakage leads to small droplets and ultimately small pore size in the final porous structure (less than 20 microns), which is unsuitable for sound absorption applications.

To achieve the required droplet sizes when processing HIPPEs, an appropriate mixing process operating in the laminar regime is required. Among various impellers, the double helical ribbon (DHR) is the most efficient, as it minimizes the energy consumption of high-viscosity emulsion mixing within the laminar regime. Factors impacting droplet size, such as particle concentration, viscosities of the dispersed and continuous phase, rotational speed, oil injection speed, and emulsification time, should be systematically studied to achieve optimal control.

Maintaining similar droplet sizes across scales is essential for consistent control over the final porous structure. While scale-up rules for mixing emulsions in the turbulent regime have been well-documented showing that constant specific power or energy consumption can be considered for scale-up criteria [21] – a knowledge gap persists in determining the scale-up rules for HIPPE in the laminar regime.

Producing acoustic porous materials from HIPPE is a novel alternative approach for the acoustic industry. Thus, there is no knowledge about the correlation between the emulsification processing parameter, pore size, interconnectivity, and final sound absorption performance, and all of them should be investigated.

While various solid particles can be used in HIPPE, selecting the appropriate particle for the final porous material applicable to the aviation industry is challenging. Since the porous acoustic

material can be employed in harsh conditions, such as those found in aircraft engines, the particle should have high thermal resistance. On the other hand, the particle should have an appropriate affinity with the oil-water interface to provide maximum stability of droplets in the HIPPE.

1.4. Originality of this thesis

The general objective of the thesis is to develop a scalable process to prepare HIPPE as templates for producing porous foams with controlled pore size distribution after post-processing of the concentrated emulsion.

- This study introduces a straightforward and controllable method for producing porous materials without the need for complex chemical components. Unlike existing approaches, our method enables precise control over the material's morphology through systematic adjustments of the formulation and the processing parameters.
- We present the first investigation into the effects of formulation and processing conditions on the stability of high internal phase Pickering emulsions (HIPPEs) to achieve monodisperse large droplet sizes—an aspect that has not been previously explored in the literature.
- Furthermore, we establish, for the first time, a scaleup framework for HIPPEs, addressing a critical gap in the understanding of their large-scale production.
- We validate the applicability of the foams resulting from the HIPPE templates to sound absorption. The foam structure is analyzed and characterized in order to determine the relationship between the pore structure and the soundproofing characteristics.

1.5. Structure of the thesis

This paper-based thesis consists of three articles that have been published or submitted to scientific journals. Chapters are organized as follows:

- Chapter 1: Introduction: this chapter highlights the novelty of the thesis and its contribution to addressing the global challenge, providing a comprehensive overview of the research context and objectives.
- Chapter 2: Literature review: This chapter provides a thorough review of the relevant literature, discussing the current state of knowledge in the field and identifying the research gaps that this thesis aims to address.

- Chapter 3: First Article: “Production of Monodisperse Large Drop Emulsions by Means of High Internal Phase Pickering Emulsions-Processing and Formulation”. This chapter presents focuses on the production of monodisperse large drop emulsions using High Internal Phase Pickering Emulsions (HIPPEs), exploring the processing and formulation aspects of this technique.
- Chapter 4: Second Article: “Scale-up in High Internal Phase Pickering Emulsions”. This chapter investigates the scale-up of HIPPEs, examining the challenges and opportunities associated with large-scale production of these emulsions
- Chapter 5: Third Article: “High Internal Phase Pickering Emulsion for Enhanced Sound Absorbing Materials”. This chapter explores the application of High-Internal-Phase Emulsions (HIPPEs) in the development of enhanced sound absorbing materials.
- Chapter 6 discusses the broader implications of the research.
- Chapter 7 concludes the thesis and provides recommendations for future research.

CHAPTER 2 LITRATURE REVIEW

2.1 Solid-stabilized emulsion

Solid stabilized emulsions utilize particles as stabilizers which adsorb onto the interface of two immiscible liquids spontaneously. These emulsions are called Pickering to honor of the first introducer of this technique “Pickering” [14]. Current research aims to substitute stabilizer with particles due to the numerous advantages of solid stabilization. Compared to surfactants, particles provide more stability, which is around 8 years for Pickering emulsion with starch granule [22]. for the emulsion since they reduce coalescence through steric barrier repulsion [23]. These emulsions have recently gained significant attention in the academic community with more than one thousand papers published annually over the past three years (Figure 2.1).

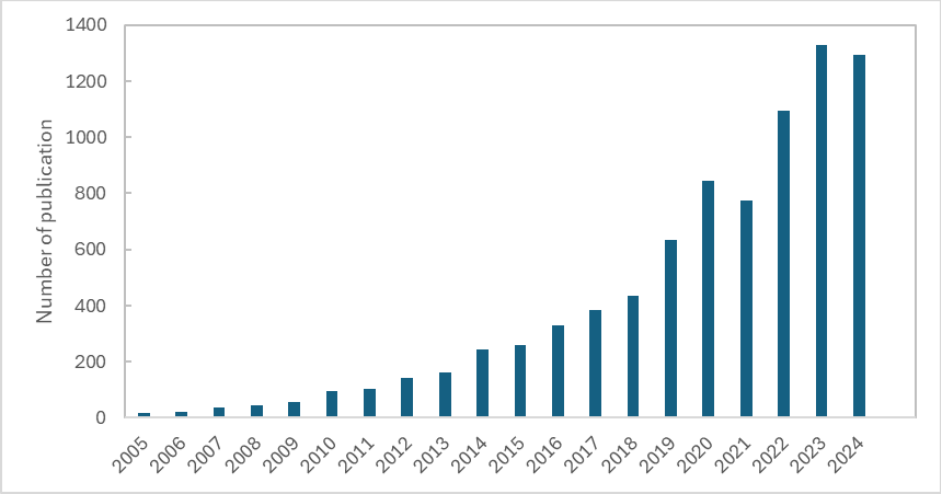

Figure 2.1. Number of publications related to the “Pickering emulsion” in recent years, adapted from Compendex.

Many different particle types can be employed for Pickering emulsions. They have lower toxicity, which make them applicable to drug delivery applications [24]. Particles can have special properties like conductivity, and environmental sensitivity, enabling application such as environment-responsive material [25]. These emulsions are also used in food [26], catalysis [16], filtration membranes [17], and cosmetics [27].

Figure 2.2 categorizes the topics covered in Pickering emulsion research, focusing on nano materials and their industrial applications.

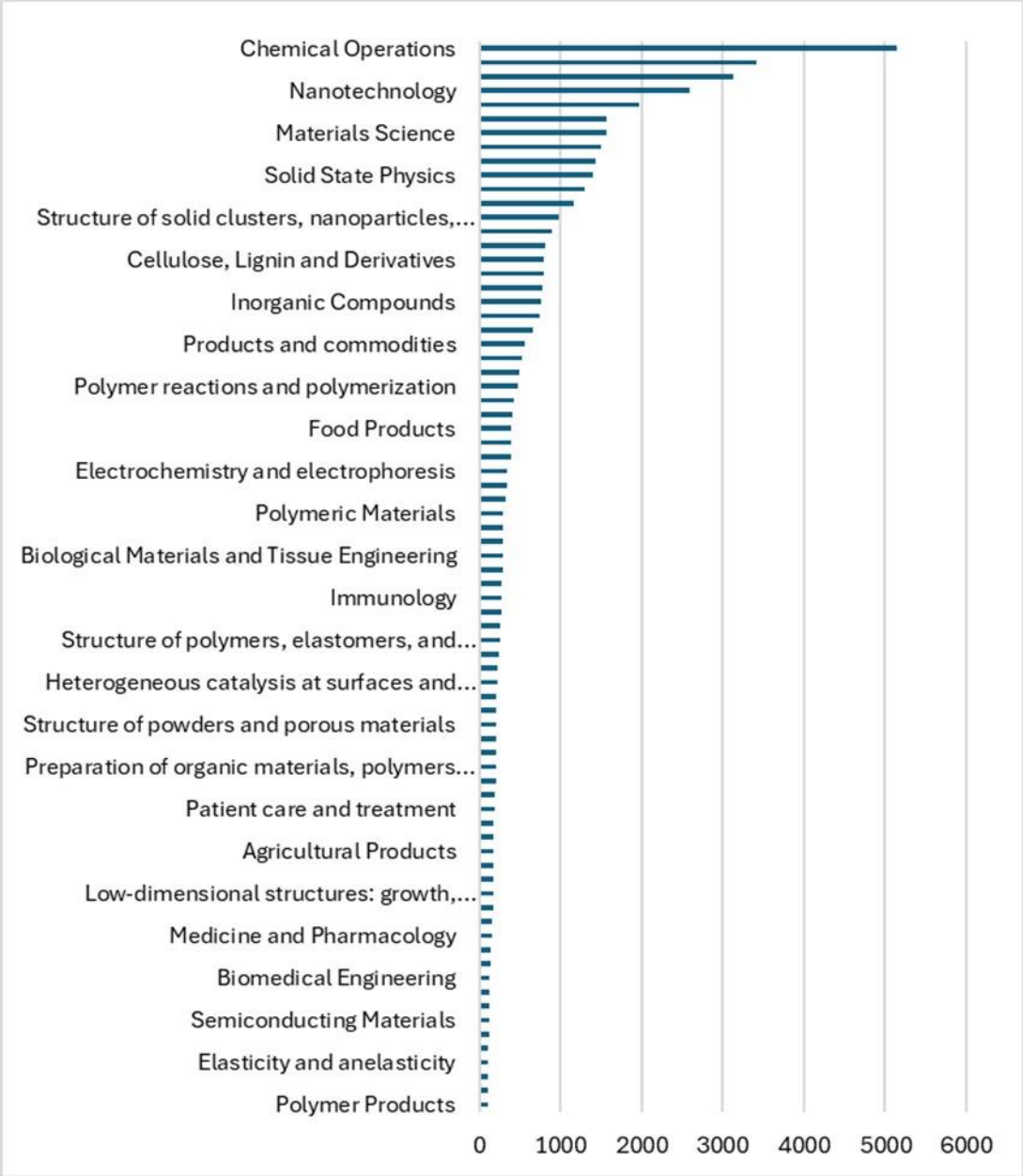

Figure 2.2. Summary of the classification codes applied to Pickering emulsions research papers, adapted from Compendex

2.2 Definitions

2.2.1 Solid-stabilized emulsion

Solid-stabilized emulsions are type of emulsions that contain two immiscible liquids and solid particles that can disperse in one of the two phases. The wettability of particles, which are quantified by the three-phase contact angle (θ), dictated the type of emulsion [28]:

If θ<90 : oil phase is the dispersed phase and aqueous phase will be the continuous phase (oil-in-water emulsion); and if θ>90: aqueous phase is the dispersed phase and the oil phase will be the continuous phase (water-in-oil emulsion),see Figure 2.3. When θ=90, particle adsorb with maximum adsorption energy, and provide optimal stability [29].

Applying shear force during mixing, breaks the dispersed phase into droplets, and solid particles adsorb at the newly generated interfaces, which prevent coalescence and enhance stability of emulsion.

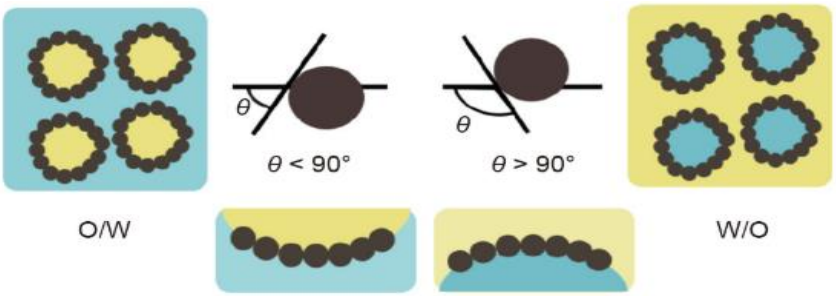

Figure 2.3. Schematic of particle adsorption around droplets, black spheres: particles, blue medium: water, and yellow medium: oil[28]

2.2.2 Droplet size and size distribution

In the literature, different terminologies have been used to describe the drop size. The most important one is the Sauter mean diameter (surface area weighted mean), D_{32}, which is determined as follows:

$$D_{32} = \frac{\sum n_i d_i^3}{\sum n_i d_i^2} \tag{2.1}$$

n_i is the number of drops, and d_i is the diameter of individual droplet within size class i. Volume-weighted average (D_{43}) is another average that is used in the literature. It is given by:

$$D_{43} = \frac{\sum n_i d_i^4}{\sum n_i d_i^3} \tag{2.2}$$

D_{10}, D_{50}, and D_{90} are also obtained in the cumulative volume droplet size distribution (DSD) plots, which represent the droplet sizes at which 10%, 50%, and 90% of all drops are smaller than those sizes.

Uniformity is another critical number that indicates the range of the size distribution:

$$uniformity = \frac{\sum v_i(d_{50} - d_i)}{d_{50} \sum v_i} \tag{2.3}$$

where vi is the volume frequency in each size class.

2.2.3 Concentration of dispersed phase

The concentration of dispersed phase (ϕ) plays a critical role in determining the coalescence frequency and the rheology of the emulsion. In the dilute systems, (ϕ < 0.01) only hydrodynamics affects the droplet size, since the collision frequency is extremely low, and coalescence can be ignored [21]. In the moderately concentrated emulsions (0.01 < ϕ < 0.2), the coalescence may occur, except for non-coalescing emulsions. The droplet size distribution is predictable based on the single-phase flow concept, due to the small amount of dispersed phase which does not significantly affect the rheology of continuous phase [21].

More concentrated emulsions (0.2 < ϕ < 0.50) are widely used in industry. In these emulsions, the droplet size depends on its position in the vessel, due to the rapid coalescence. By employing suspending agents, the theories for predicting droplet size for dilute systems can also be applied to these emulsions [21].

Highly concentrated dispersed phase (ϕ > 0.75) emulsions reach their maximum packing state. For monodisperse spherical droplets, the maximum packing value is around 74% (hexagonal close packing). When the emulsion reaches this packing state, the viscosity increases sharply and remains high thereafter [30]. As a results, the mechanism of droplet breakage is completely different in this type of emulsion. The drop size reduction results from the sole motion of the fluid mass. In this state, the viscosity is orders of magnitude higher than any of the phase present in the emulsion. The size reduction mechanism is similar to autogenous milling in the mineral industry.

2.2.4 Flow regime in emulsion preparations

Droplet size in the emulsion is determined by three different flow regimes [21] defined by the Reynolds number:

Re which is calculated using the following equation:

$$Re = \frac{D^2 N \bar{\rho}}{\bar{\mu}} \tag{2.4}$$

where D is impeller diameter and N is rotational speed; $\bar{\mu}$ and $\bar{\rho}$ represent the bulk viscosity and density of the emulsion, respectively [21].

The flow regimes are defined as follows:

- $0 < Re < 10$: Laminar flow, characterized by smooth, continuous, and orderly fluid motion.

- $10 < Re < 10^4$: Transition flow, where the flow starts to become unstable and turbulent, but still exhibits some laminar characteristics.

- $Re > 10^4$: Fully turbulent flow, marked by chaotic, irregular, and three-dimensional fluid motion

The dilute emulsion is always controlled by turbulent flow, while in highly concentrated emulsions the turbulent eddies are damped out and the bulk viscosity increases significantly. As a result, laminar flow controls droplet dispersion in these emulsions. Droplet size prediction theories in turbulent flow are not applicable in these emulsions, and models based on capillary number may be applied.

2.3 Stabilization mechanism

A solid-stabilized emulsion can be much more stable than emulsions stabilized by surfactants, due to steric particle barrier around the droplets, which prevents coalescence [29][23]. Capillary force and particle interactions at the interface also play a vital role in stabilizing the emulsion when a close-packed network of particles is formed [31][32].

2.3.1 Particle wettability

Particle wettability is determined by a three-phase contact angle at the interface of particles within the oil-water interface. This contact angle is correlated with balance of free surface energy in the particle-oil-water interface. Binks et al. conducted an extensive investigation regarding the stability of Pickering emulsion, and they found that the stability of particles at the oil-water interface dictates the type of emulsion and the stability emulsions. Based on the universal energy equation (2.5), they found that the emulsion is most stable when the particle attachment energy reaches the maximum at a contact angle of 90º [29][33] (Figure 2.4):

$$E = \pi R_p^2 \gamma_{ow} (1 + cos\theta_{ow})^2 \tag{2.5}$$

where γ_{ow} is the interfacial tension between the oil and water phases, R_p is particle radius, and $\theta_{ow}$is the contact angle of the particle at the interface of two phases. It is concluded that the

emulsion type is determined solely by particle wettability when oil and water are present in equal proportions. The more hydrophobic particles, $\theta > 90^{\circ}$, stabilize a water in oil (W/O) emulsion, while more hydrophilic particles, $\theta < 90^{\circ}$ tend to produce an oil in water (O/W) emulsion [29][34]. The required energy to remove the particle from the interface of the two phases is several times *KT*, which resulting in irreversible stabilization [35].

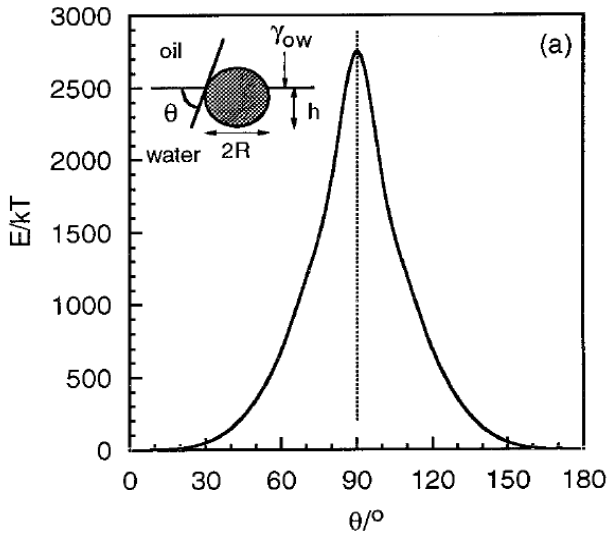

Figure 2.4. The energy of particle attachment at the interface of two phases [29]

2.3.2 Particle size and shape

It is known that by increasing the particle size, the average droplet size increases gradually until the emulsions become unstable and prone to coalescence [36]. Reducing particle size to a hundred nanometers lowers the required particle concentrations to stabilize the emulsion, resulting in a highly stable emulsion that remains intact even after 90 days of storage. For example, Tan et al., prepared a highly stable emulsion with only 0.5 wt% of 200 nm-particles [37].

The shape of the particle can vary including irregular [38], rod-like [39], globular [40], disk-like [41], and spherical shapes. Creighton et al. also revealed that the maximum free energy of adsorption occurs at a contact angle of 90˚, and for disc-shaped particles, it is considerably higher at the same surface area (Figure 2.5) [41].

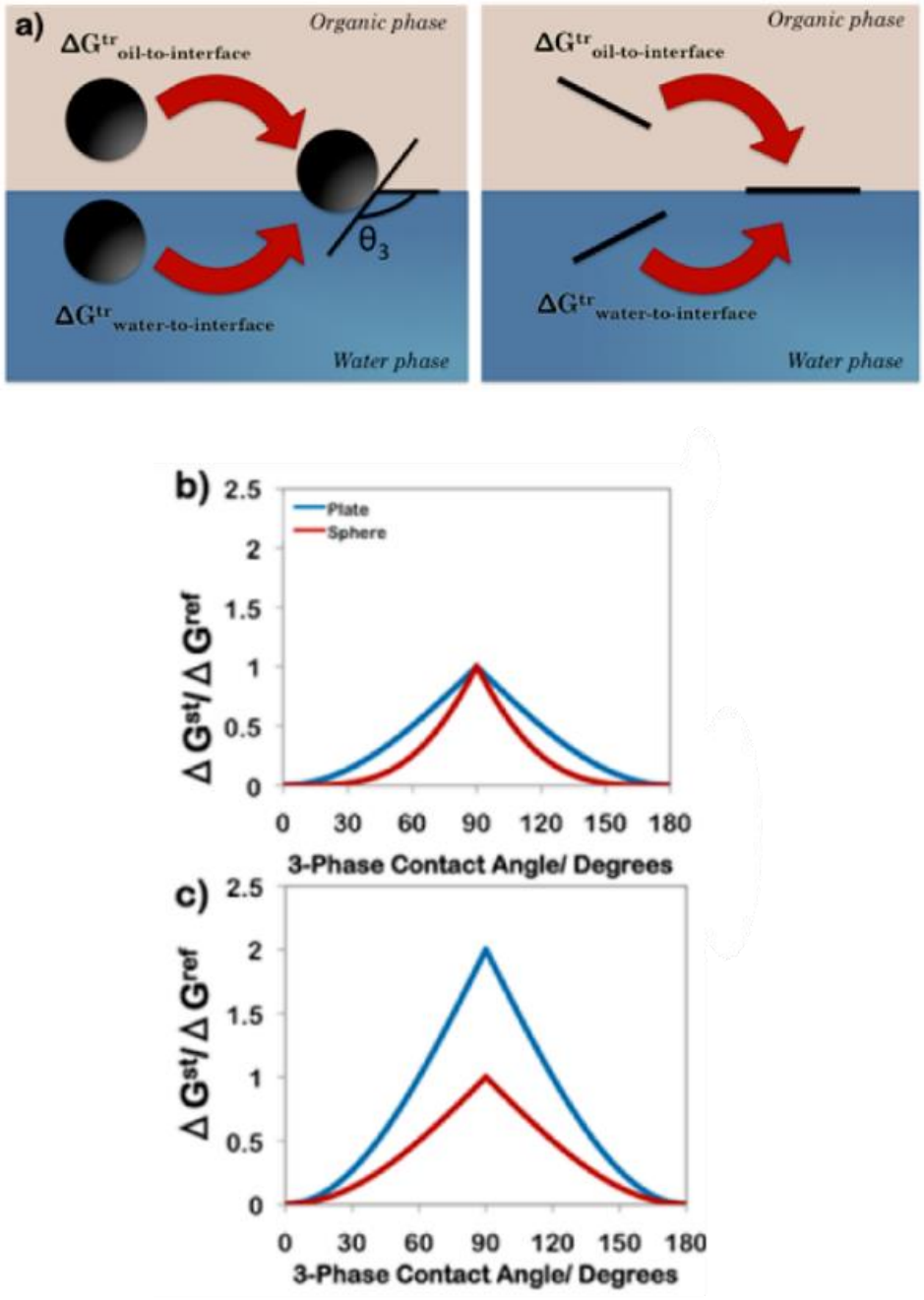

Figure 2.5. (a) Definition of transfer free energies for spherical and ultrathin disk-like particles; free energy of stabilization (b) in an equal radius of a disk-shaped and spherical particle; (c) in a similar surface area of a disk-shaped and spherical particle [41].

2.3.3 Electrolyte and particle surface charge

The particle surface charge has a strong impact on the stability of Pickering emulsions, and it correlates with the pH and ionic strength [42]. The pH of the aqueous phase controls the electrostatic and steric interactions between particles. The optimum level of interactions is essential

for stable dispersion, preventing droplet coalescence, and ultimately ensuring the stability of the emulsion [43].

It is reported that increasing the salt concentration to the oil/water-silica particle emulsion weakens the repulsive forces between particles. Two phenomena can occur: firstly, it leads to the excess particle aggregation in the aqueous phase and the resulting silica particle network increases the emulsion's viscosity once the electrolyte concentration exceeds a certain threshold (Figure 2.6) [44][45]. Secondly, it reduces the electrostatic and steric repulsion and leads to emulsion coalescence [21].

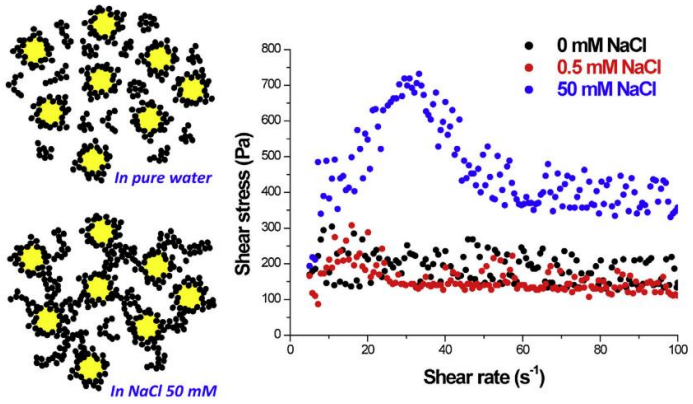

Figure 2.6. Flow curve of o/w emulsion containing 10% silicone oil droplets stabilized by 5% H30 and various NaCl[45].

2.3.4 Particle concentrations

The particle concentration significantly impacts the droplet size and final stability of the emulsion. To stabilize the droplets, the total surface area of droplets should be covered by a monolayer of particles[35]. Wan showed that if the ratio of the number of particles to the surface generated is smaller than the critical value, phase inversion from stable O/W emulsion to unstable W/O emulsion occurs under constant mixing process conditions[46]. By considering the geometry of the droplet and solid particle adsorbed as a dense layer, the total particle mass for the desired droplet size in the o/w emulsion was estimated using the following equation[47].

$$D_{mean} = \frac{6}{\rho_{oil} a_{solid}} \frac{M_{oil}}{M_{solid}} \tag{2.6}$$

Where M_{oil} is the oil mass, D_{mean} is the average droplet size, and a_{solid} is the interfacial area covered per mass of particles (M_{solid})[47].

Tsabet et al. demonstrated that to estimate the effectively covered interface, the particle size, contact angle at the interface, and the coverage rate must be considered (Figure 2.7)[48].

$$A_{cov/drop} = p\%4\pi\left(\frac{D_{mean} - \left(2R_p - h\right)}{2}\right)^2 \tag{2.7}$$

where $p\%$ represents packing fraction for a hexagonal close-packed particle configuration on the surface, calculated as $\frac{\pi}{2\sqrt{3}} = 0.9069$. R_p is particle radius and h is given by [48] :

$$h = R_p(1 - cos\theta_{ow}) \tag{2.8}$$

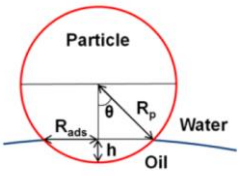

Figure 2.7. The contact angle between particle, oil, and water, and estimated the surface of droplet which covered by particle [48].

Tsabet et al. also developed a semiempirical approach for estimating the final covered interface. They defined two key concepts: The first one named the coverage potential, is a function of particle properties such as particle size, concentration, or number ($N_{p_{total}}$), and wettability. The second concept, called the interface generation, is a function of processing parameters[48]. The balance between these two definitions dictates the final covered interface. If the coverage potential is lower than the generated interface, the final covered interface is a function of wettability, particle size, and total number of particles $N_{p_{total}}$:

$$A_{cov} = \pi(R_p sin\theta_{ow})^2(N_{p_{total}}) \tag{2.9}$$

If the coverage potential is higher than the interface generated, the processing parameters dictate the final covered interface and several efficiency parameters can be adjusted to modify it [48].

Wan et al. [49] emulsified 5-10 vol% Pickering emulsions using pitched blade turbine (PBT) at 700 and 350 RPM, and investigated the effect of particles on the droplet breakage and coalescence. They found that by decreasing rotational speed the droplet size increased noticeably when emulsions stabilized with insufficient particles. In contrast, when the droplet size of emulsions stabilized with sufficient particles remained constant.

2.4 Low-to-moderately concentrated Pickering Emulsions

2.4.1 Preparation techniques

Mostly low-to-moderately concentrated emulsions are prepared with high-intensity mixers. Rotor-stator homogenization is one of the techniques commonly used for preparing Pickering emulsification [20][50]. In this technique, the rotation speed of the rotor and the homogenization time control the droplet size. The rotational speed of the rotor ranges from 5000 to 30,000 RPM and the homogenization time ranges from 30 seconds to a few minutes, which leads to droplet sizes ranging from a few microns to hundreds of microns [20][50].

High-pressure homogenization is a continuous emulsification process that has been used for Pickering emulsification [20][51][52]. A pre-emulsification process with a rotor-stator is typically required before using the high-pressure homogenizer. In this technique, a high-pressure pump and a homogenizing nozzle apply pressure to break the droplets, and the emulsion passes through between 1 to 10 times to repeat the process (Figure 2.8). The pressure valve and the number of circulation control the droplet size. The pressure ranges from tens to hundreds of MPa and the droplet size ranges from hundreds of nanometers to hundreds of microns [20].

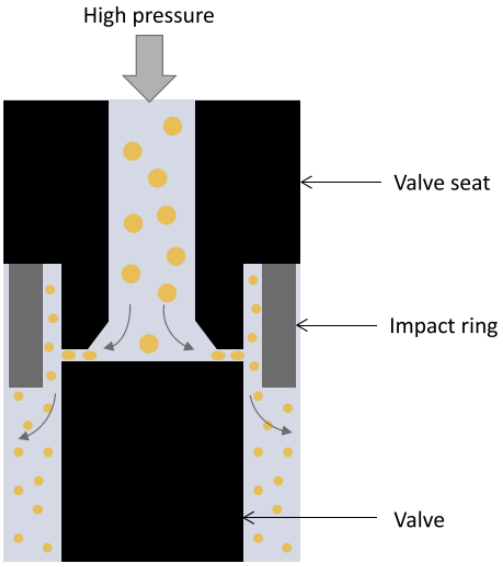

Figure 2.8. Schematic of high-pressure homogenizer with standard homogenizing nozzle[20].

A few studies used the ultrasonic probe technique for Pickering emulsion preparations[39][20]. In this technique, the probe vibrates at a frequency of 16kHz to 100kHz providing sufficient energy for emulsification. Frequencies and amplitude of the probe and the emulsification time control the

droplet size. The frequency of 20-40 kHz, the power intensity amplitude of tens to hundreds of W/m^2, and an emulsification time of a few minutes leads to droplets ranging from hundreds of nanometers to hundreds of microns [20].

The membrane technique is another approach for Pickering emulsification which is typically combined with an agitation system to facilitate droplet detachment from the membrane [20][53]. The pore size, injection rate, and the agitation speed control the droplet size in this emulsification process. The pore size ranges from tens of nanometers to tens of microns and the final droplet size is usually 3 to 9 times the pore size (Figure 2.9-a, b and c). Decreasing the injection speed decreases the droplet size and improve uniformity, leading to a monodisperse size distribution. The increase in agitation speed also decreases the size of the droplets by facilitating droplet detachment from the membrane (Figure 2.9-d and e). In this process, a low viscous liquid should be used and the particle adsorption rate at the oil-water interface must be considered to control the droplet size [20].

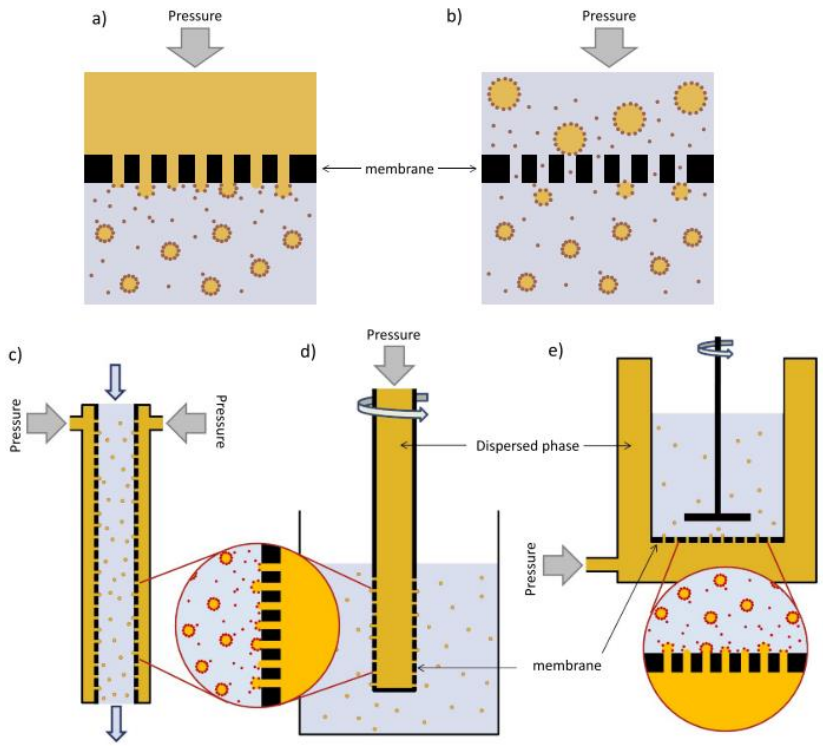

Figure 2.9. Schematic of membrane emulsification, a) Direct membrane emulsification, b) premix membrane emulsification, c) crossflow membrane (XME), d) rotational membrane (RME), e) stirred-cell membrane (SCME)[20].

Microfluidic devices are used for preparing Pickering emulsions [54][20]. In this technique, droplets in the laminar flow are broken by simple shear flow or elongational flow, and the

continuous phase, containing the particles, stabilizes the droplets. The microchannel geometry and flow rate precisely control the droplet size and enable to produce a monodisperse emulsion [54][20].

Stirred vessel techniques, which are widely used in conventional industrial emulsification, have recently been used for Pickering emulsifications [49][55][56][57][58][59]. Several types of impellers have been used in these studies: pitched-blade turbine (PBT) [49][55][56][57][59], Rushton turbine (RT) [56][57][58], and they produce droplet sizes that are two orders of magnitude larger than the droplets produced by rotor stator homogenizers, high-pressure homogenizers, membranes, and microchannels. Table 2.1summarizes all the production techniques for Pickering emulsions. From this table, we can conclude that the smallest droplet sizes are obtained with high pressure homogenizer, ultrasonication, and membrane techniques, while the largest droplet size obtained with PBT and RT impellers. The shortest emulsification time, approximately 30 sec, is achieved using rotor stator mixers. Except for the microchannel approach, all of these techniques operate in the turbulent regime. all of these techniques, except the PBT and RT, are not suitable for the scale-up production of Pickering emulsions.

Table 2.1. Summary of the production technique for Pickering emulsions

Technique	**Droplet size**	**Emulsification time**	**Process conditions**	**Disadvantages**	**Size**	**Ref.**
Rotor stator	1μm-hundreds μm	30s-minutes	Rotational speed: 5000-30,000 RPM	-Non-Uniform emulsions -Particle destruction	mL-hundreds mL	[20][50]
High-pressure homogenizer	hundreds nm-hundreds μm	A few minutes/ cycle- several cycles	Pressure: 10-hundreds MPa	-High energy consumption -Risk of damaging equipment with abrasive material -Particle destruction -Difficult cleaning	10 mL-hundreds mL	[20][51][52]
Ultrasonic	hundreds nm-hundreds μm	A few minutes	Amplitude: 10s-100s watt Frequency: 20-40Hz	-Broad distributions -Particle destruction -Inappropriate for scale-up -Heat build-up	Hundreds μL-hundreds mL	[39][20]
Membrane	hundreds nm-hundreds μm	A few hr to tens hrs	Flow rate: 0.1 $m^3.hr^{-1}$	-Only low viscous liquids -Longer emulsification -Inappropriate for scale-up	mL-hundreds mL	[20][53]48]
Microchannels	1μm-hundreds μm	Less than 1 minute (depending on the total volume and flow rate)	Flow rate: 2-17mL.hr^{-1}	-Low throughput production -Interaction of channel with material -Inappropriate for scale-up	mL	[54][20]
Mixing PBT Mixing RT	200-800μm 100-800 μm	1-1000 minute 24 hrs.	Rotational speed: 350-700 RPM Weber number=100-320	-Limited to turbulent regime -Medium concentration of internal phase	1L	[49][55] [55]

2.4.2 Effect of process conditions

For dispersed phase concentrations below 0.2 (ϕ<0.2), Chen and Middleman developed a model for estimating the droplet size in the stirred tank based on the Weber number (We), defined as:

$$We = \frac{D^3 N^2 \rho}{\sigma} \tag{2.10}$$

where *D* is impeller diameter, *N* is rotational speed, ρ is emulsion's density, and σ is interfacial tension. Based on Kolmogorov theory the droplet size is a function of *We* and impeller diameter [60]:

$$D_{32}/_D = AWe^{-0.6} \tag{2.11}$$

where A is an adjustable constant which is a function of formulation. This model is only valid for turbulent regimes where droplets are broken by turbulent eddies.

For concentrated emulsions, where the dispersed phase concentration is 0.2<ϕ<0.74, the droplet coalescence increases due to the higher probability of collisions. In the turbulent stirred tank, the frequency of particle droplet collisions and collision force dissipation are related to the energy dissipation rate [55]:

$$\varsigma(D_{p,}D_d) \approx \varepsilon^{\frac{1}{3}} \tag{2.12}$$

for $\frac{D_d D_P}{D_d + D_P} > \lambda$

$$F_c \approx \frac{\pi}{2} * \rho_c \varepsilon^{\frac{2}{3}} (\frac{D_d D_p}{D_d + D_p})^{\frac{8}{3}} \tag{2.13}$$

for $\frac{D_d D_P}{D_d + D_P} \leq \lambda$

$$F_c \approx \frac{\pi}{4} * \rho_c^2 \frac{\left(\frac{D_d D_P}{D_d + D_P}\right)^4}{\mu} \tag{2.14}$$

where D_d and D_P are the diameter of droplets and particles, ς is the collision frequency of droplet and particle, ε is the turbulent energy dissipation rate,

$$\varepsilon = \frac{P}{m_t} = \frac{N_p \rho_c N^3 D^5}{m_t} \tag{2.15}$$

where ρ_c is continuous phase density λ is the Kolmogorov length scale:

$$\lambda = \left(\frac{\upsilon^3}{\varepsilon}\right)^{\frac{1}{4}} \tag{2.16}$$

and υ is the dynamic viscosity of emulsion.

Tsabet used the Calabrese model [61] to estimate the droplet size of a 53 vol% dispersed phase emulsion [55]. This equation accounts for the impact of dispersed phase viscosity on the final droplet size [55].

$$\frac{d_{32}}{D} = 0.053We^{-0.6}(1 + 0.97 * Vi^{0.79})^{0.6} \tag{2.17}$$

$$Vi = \frac{\mu_d ND}{\sigma}\left(\frac{\rho_c}{\rho_d}\right)^{0.5} \tag{2.18}$$

where σ is interfacial tension between the two phases, ρ_c and ρ_d are densities of continuous and dispersed phases, respectively.

Utomo et al. [59] compared the droplet size of emulsions stabilized with an emulsifier and nano clay, using a PBT operated at 250 RPM to emulsify systems with 10-50 vol.% of the dispersed phase. They found that D_{32} decreased with energy density per unit mass (E_m), and derived the following equation:

$$D_{32} = C{E_m}^x \tag{2.19}$$

where *C* and *x* are constants that depend on the type of stabilizer. Utomo et al. concluded that the droplet size of emulsion stabilized with nano clay has a stronger dependence on the energy dissipation rate (C=1000-1700, and *x* ranges from -1 to -1.5), while the dependency of droplet size of emulsion stabilized with an emulsifier showed a weaker dependence on the energy dissipation rate (C=0.7-1.5, and *x* ranges from -0.26 to -0.4)[59].

Donmez et al.[57] emulsified a 43 vol % O/W Pickering emulsion using PBT and RT impellers at 800-1800 RPM. They found that energy dissipation rate and tip speed ($V_{tip} = \pi ND$) has a

significant effect on the final droplet size. At constant tip speed, RT, which produces more power, resulted in a smaller D_{32} compared to PBT. For the same energy dissipation rate, PBT resulted in the smallest droplet size since RT has a lower rotational speed at this constant energy dissipation rate.

Donmez et al. [57] also investigated the effect of impeller size and the feeding time for the dispersed phase on the final droplet size. They concluded that increasing impeller diameter increases the tip speed at constant power per unit mass of emulsion, thus decreasing the droplet size. However, increasing the feeding time of the dispersed phase diminishes the effect of impeller diameter and results in a constant droplet size for impellers with T/2 and T/3, where T is the tank diameter.

2.4.3 Rheology of Pickering Emulsion

Pickering emulsions exhibit complex rheological behavior. While dilute emulsions show Newtonian behavior, as the dispersed phase concentration increases, the viscosity increases, and non-Newtonian behavior observed. Moderately concentrated Pickering emulsions exhibit shear thickening followed by shear thinning. Wolf et al. compared the rheological behavior of conventional emulsions with Pickering emulsions, and observed that increasing the dispersed phase volume fraction made both shear thickening and shear thinning behaviors more pronounced [62] (Figure 2.10).

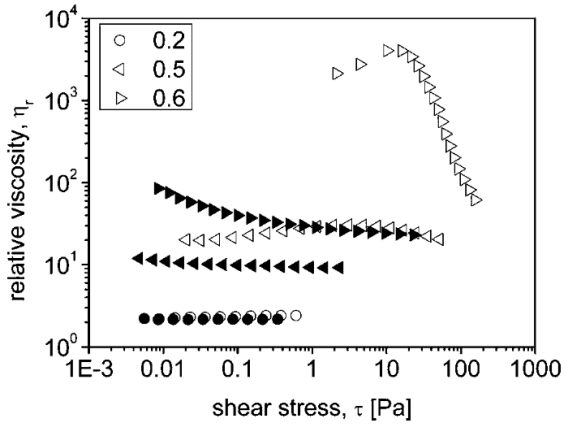

Figure 2.10. Relative viscosity versus shear stress, open symbols: Pickering emulsions, Filled symbols: surfactant emulsions[62]

Kinra and Pal [19] also investigated the shear thinning behavior of Pickering emulsions stabilized by nanocrystalline cellulose (NCC). They used homogenizers to prepare emulsions of 12-74 vol.%

dispersed phase at different particle concentrations. They found that increasing the dispersed phase volume fraction significantly increases the viscosity, which in turn increase the consistency index (k), and decreases the power-law index (n) ($\mu = k\dot{\gamma}^{n-1}$) . This effect is amplified at higher particle concentrations and a sharp increase in k was observed at 50 vol% of the dispersed phase (Figure 2.11). They attributed the shear thinning behavior of Pickering emulsion to two mechanisms. First, by increasing the shear rate, the aggregates of droplets breaks up, and secondly, the droplets align under higher shear[19].

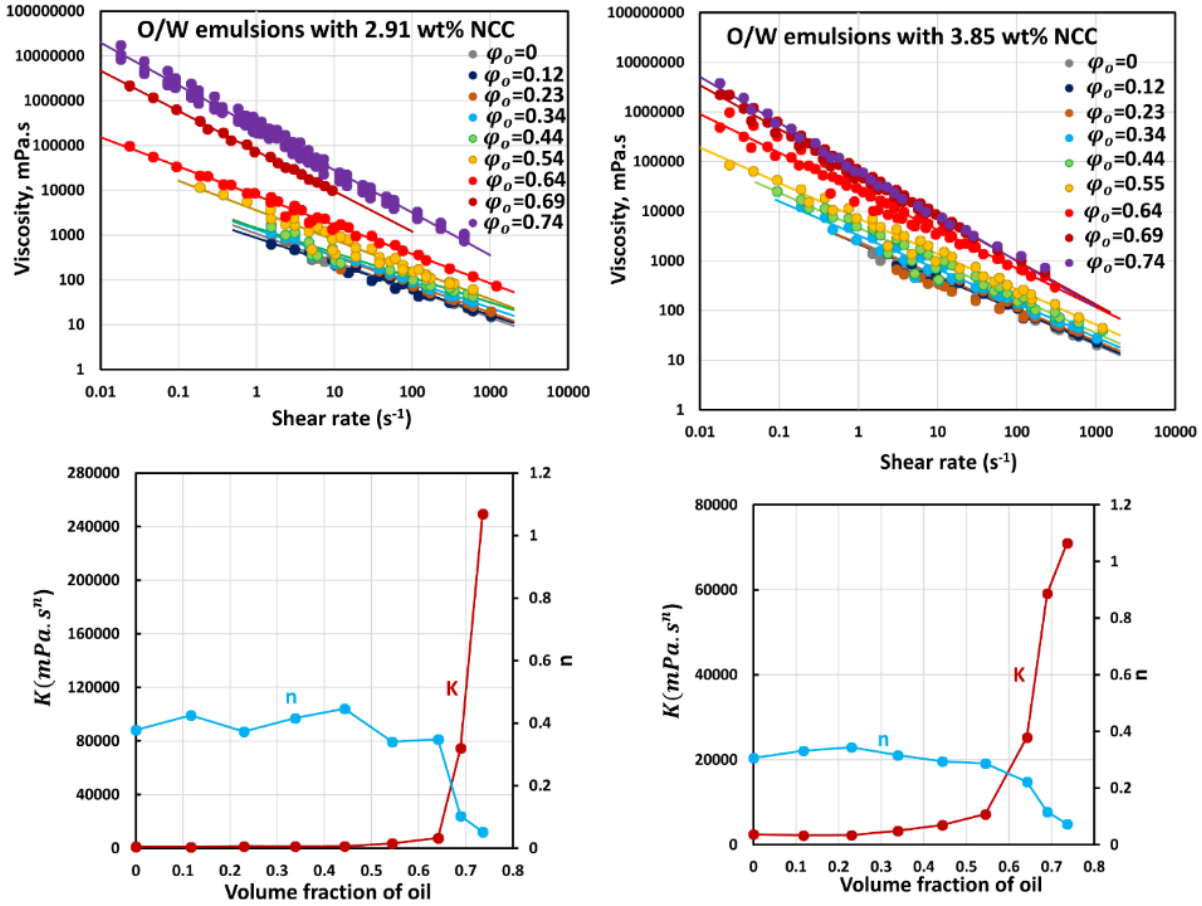

Figure 2.11. Shear thinning behavior of O/W emulsions at different vol% of the dispersed phase at fixed NCC (2.91 wt.%, and 3.85 wt.%) [19].

Pal developed a model for estimating the relative viscosity of Pickering emulsions [30]. He defined the Pickering droplet, covered with particles, as a rigid "core-shell" composite. This rigid layer around the mobile droplets protected the droplet from transmitting stress from the continuous phase. For this model, he used the effective radius, defined as follows [30] (Figure 2.7, Figure 2.12):

$$R_{eff} = R_d + h \tag{2.20}$$

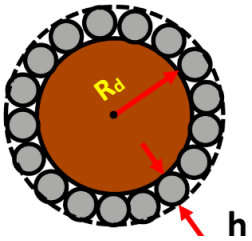

Figure 2.12. Schematic of droplets in the Pickering emulsion, R_d is the droplet radius, and h is the thickness of the particle layer[30]

h can be calculated using equation (2.8) and Figure 2.7.

The presence of particles around the droplet surface increases the total dispersed phase volume, known as effective volume fraction (φ_s)[30].

$$\varphi_s = \varphi\left(1 + \frac{h}{R_d}\right)^3 \tag{2.21}$$

The Einstein viscosity equation can be employed to estimate the relative viscosity for dilute emulsions. Effective volume fraction must be used in this equation [30], so:

$$\mu_r = \frac{\mu}{\mu_c} = 1 + 2.5\varphi_s \tag{2.22}$$

For concentrated emulsions, Pal discussed the effect of the free volume in emulsions, which allows the droplets to align under shear flow[63]. At higher volume fractions, droplets have less available space and freedom to move, resulting in higher viscosity (Figure 2.13).

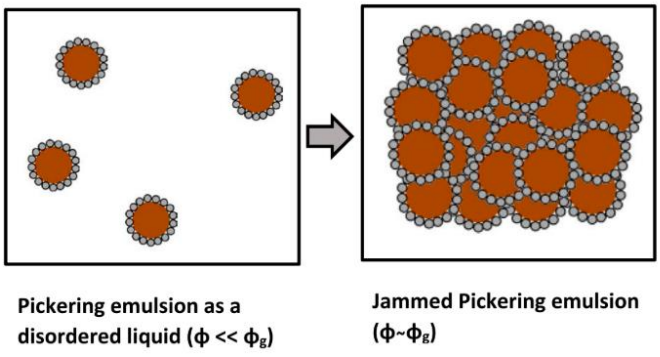

Figure 2.13. Change in free scape between droplets from dilute to the jammed Pickering emulsion [30].

Pal defined the glass-transition concentration (φ_g) and modified the equation for dilute emulsions[30]:

$$\mu_r = \frac{\mu}{\mu_c} = 1 + 2.5\left(\frac{\varphi_{eff}}{1-\varphi_{eff}}\right) \tag{2.23}$$

where μ_r is relative viscosity, μ is the viscosity of emulsion, μ_c is the viscosity of continuous phase, and φ_{eff} represents φ_s for dilute emulsions. When φ_s reaches φ_g, the amount of φ_{eff} is closed to one.

For Pickering emulsion with a volume fraction in between dilute and glass-transition concentrations, the following equation should be used to determine φ_{eff}[30]:

$$\varphi_{eff}/\varphi_s = 1 + \left(\frac{1-\varphi_g}{\varphi_g}\right)\left(\sqrt{1-\left(\frac{\varphi_g-\varphi_s}{\varphi_g}\right)^2}\right) \tag{2.24}$$

Pal determined the φ_g value, the maximum packing volume fraction of droplets, varies from 0.68 to 0.86, depending on the type of emulsions and its polydispersity [64]. For a completely monodisperse emulsion, φ_g equals 0.74.

2.5 High Internal Phase Pickering Emulsions

High internal phase Pickering emulsions, called HIPPE, form when the droplets reach their maximum packing state. As mentioned above for monodispersed spheres, the maximum packing fraction is approximately 74% (hexagonal close packing). When the emulsion reaches this state, viscosity increases sharply, and the emulsion exhibits non-Newtonian behavior [65].

The stabilization mechanism in HIPPE is a combination of a particle network in the continuous phase and the adsorption of particles at the droplet interfaces. These mechanisms make emulsions stand as a gel, which makes them an excellent choice for advanced applications. Polymeric high internal phase Pickering emulsions (PolyHIPPEs) are widely used as templates for porous material and have applications such as permeable porous materials[66], 3D printing [67], biocompatible scaffolds [15], support for catalysis [16], selective absorption of liquids [68], sensors [69], and ultra-light functional porous materials [65].

2.5.1 Preparation techniques

High internal phase Pickering emulsions are mostly prepared on a small scale using a homogenizer which is described in section 2.2.6.1, at 5000-20,000 RPM for 30 seconds to 5 minutes, producing

droplet sizes ranging from a few microns to 100 microns [70][65]. The use of a homogenizer requires high power input and may disrupt particle aggregation, leading to a non-uniform droplet size distribution. This technique is also unsuitable for large-scale production because the high shear zone is limited to a few millilitres around the homogenizer tip. As a result, large-scale production would have large areas prone to droplet coalescence.

Recently, Abdulrasaq and Ayranci [71] prepared HIPPEs in a stirred tank using PBT and RT impellers of various diameters. They found that higher energy dissipation in the impeller zone and larger impeller breakup zone reduced the droplet sizes. Due to the higher power number of RT impeller and its better dispersion geometry, it produced smaller droplet sizes compared to PBT at constant tip speed. The breakup zone is critical when maintaining constant power per volume for scale up. In this case, a larger impeller diameter is the best choice.

A few papers also used the handshaking method for HIPPE preparation [72]. However, this technique has uncontrollable and unmeasurable power input. Nevertheless, it suggests that low rotational speeds and power inputs can be sufficient to break droplets and suspend particles.

For high viscosities such as those found in concentrated emulsions, low-speed close-clearance impellers are better suited, as they handle high-viscosity mixtures effectively. Examples of such impellers include the Maxblend™ impeller [73], anchor impeller[74], Paravisc™ [75], coaxial impellers [76] and helical ribbons (single helical ribbon SHR and double helical ribbon DHR) [75]. Among these, the DHR and Maxblend™ provide the highest shear homogeneity throughout the entire volume [75]. Since the focus is on producing large droplet sizes, the DHR provides the minimum required shear with the highest homogeneity. It is also the most energy-efficient option for blending two immiscible liquids [77], as it has the shortest blend time for a given power input [77].

Very little literature exists on using low-speed impellers for producing emulsions. For instance, asphalt was successfully emulsified using an anchor impeller at 95% dispersed phase in surfactant-based emulsions with rotational speed less than 180 rpm [74], demonstrating narrow droplet size distributions and efficient processing.

2.5.2 Effect of process conditions

The hydrodynamics of the breakup zone dictate the final droplet size in the HIPPEs in both the laminar and turbulent regimes [71]. Although there is limited knowledge about the effect of processing conditions on the HIPPEs process in the laminar regime, concepts from conventional emulsions prepared in the laminar regime, such as the capillary number and viscosity ratio, can be applied since the HIPPE prepared in laminar regime. Additionally, general concepts already used in Pickering emulsions preparation in the turbulent regime, such as power consumption, revolution number, Reynolds number, and tip speed can also be explored in our study.

In the laminar flow, viscous stresses cause droplet breakup, while the interfacial forces around the droplet will limit the extent of the breakup [78]. In an idealized laminar flow with a simple shear or extension field, a droplet will break into smaller droplets if the viscous forces overcome the interfacial tension between the two phases. The capillary number (*Ca*) represents the ratio of viscous forces, generated from the shearing flow, to interfacial forces, Laplace pressure [78]:

$$Ca = \frac{\mu_c \dot{\gamma}}{2\gamma_{ow}/D_{43}} \tag{2.25}$$

where D_{43} is the volume-average droplet diameter, and $\dot{\gamma}$ is the deformation rate (shear rate) required to break up a droplet. γ_{ow} represents the interfacial tension between the two phases, and μ_c is the viscosity of the continuous phase.

Depending on the type of flow field- simple shear flow (SSF) or simple extension flow (SEF)- the capillary number is a function of the viscosity ratio (μ_d/μ_c). If the capillary number (*Ca*) goes beyond a certain critical threshold (Ca_{crit}), the droplet breaks apart, forming smaller droplets with lower *Ca* values. At the same time, these tiny droplets often merge back together, increasing their size and raising *Ca* again. As a result, over time, the system naturally shifts toward the critical capillary number, as the cycle of droplet breakup and coalescence continues. Figure 2.14 reproduced the data from previous work conducted by Grace compare with Mutsakis in the paper of Fradette et al. [79]. It illustrates how the critical capillary number (Ca_{crit}) is divided into two

regions based on different flow fields at varying viscosity ratio. It shows that simple shear alone cannot break droplets above a viscosity ratio of 3.5. However, extensional flow is always strong enough to break droplets into smaller sizes, regardless of the viscosity ratio.

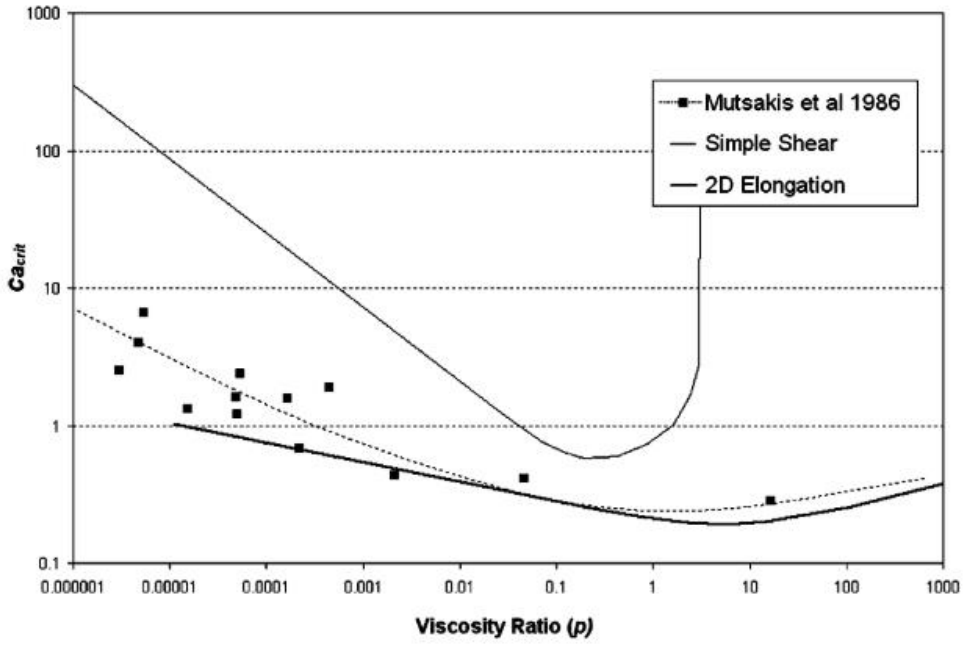

Figure 2.14. Comparison of capillary number [79]

Multiple empirical models predict the critical capillary number based on the viscosity ratio between the dispersed and continuous phases [80][81], and examine how the viscosity ratio affects the droplet breakage [82]. In these models, the *Ca* value is determined for dilute emulsions, assuming that the effect of the neighboring droplets is negligible. These studies assumed a constant viscosity for the continuous phase throughout the emulsification process. However, assuming constant continuous phase viscosity may not be accurate for Pickering emulsions, where the continuous phase can be non-Newtonian, and the presence of micro-sized particles adds complexity to the system.

The revolution number is another effective parameter for mixing two non-Newtonian liquids [83]. The revolution number is the product of rotational speed and time. It indicates how many times the droplets pass through the high shear zone, which is critical for determining the final droplet size.

The effect of tip speed, Reynolds number, and power per mass were investigated by Abdulrazaq and Ayranci [71]. They found that in general, increasing power per mass, Reynolds number, and tip speed generally resulted in higher breakage capacity and smaller droplet size [71]. They also reported that the impeller dimensions and their types have an impact on this general trend.

To sum up, most process conditions are a function of emulsion viscosity, which may exhibit behaviors such as shear thinning, shear thickening, thixotropy, and rheopexy. Therefore, the viscosity of emulsions is one of the most crucial factors that should be investigated in HIPPE preparations.

2.5.3 Rheology of High Internal Phase Pickering Emulsion

HIPPEs not only exhibit a viscoelastic behavior [84], but the continuous phase may also display complex rheological behavior. Depending on particle size, shear rate, and the repulsive force between particles, the continuous phase can exhibit both shear thinning and shear thickening [85], as well as time-dependent behavior, thixotropy, and rheopexy [86][87]. The observed behavior depends on experimental conditions and the formulation. The nonlinear rheological behavior of the concentrated suspension forming the continuous phase must be considered when calculating the viscosity ratio to estimate the capillary number.

Wu et al. produced a HIPPE gel and demonstrated that the emulsions exhibit a high storage modulus and yield stress, which improved as the droplet size decreases [88] (Figure 2.15).

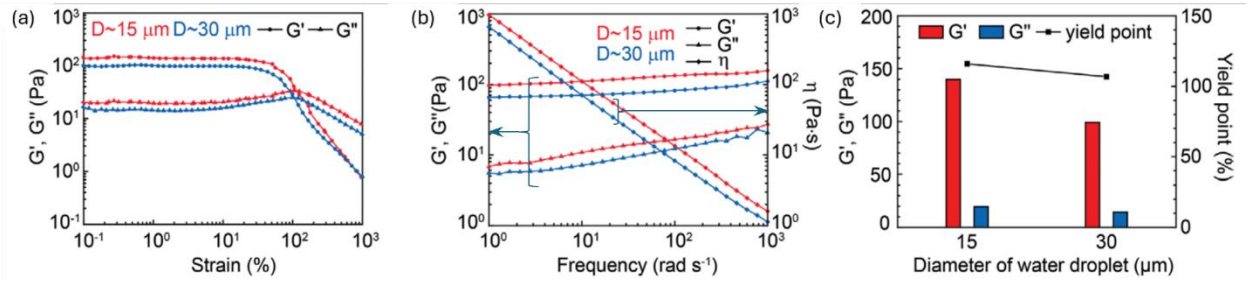

Figure 2.15. Viscoelastic properties of Pickering emulsion gels: a)Strain sweep of elastic modulus G' and viscous modulus G" with different droplet sizes at constant frequency 10 rad.s^{-1} . b) Frequency sweep of elastic modulus G', viscous modulus G" and viscosity at constant stress 1Pa. c) dependency of elastic modulus G', viscous modulus G", and yield stress on the droplet size [88].

Pal also investigated the effects of droplet size and volume fraction on the rheological properties of HIPPE [89]. They found that, by increasing the volume fraction of dispersed phase, both the

viscosity and the storage modulus increased. This effect was particularly significant in the presence of finer droplets, where the storage modulus increased substantially (Figure 2.16) [89].

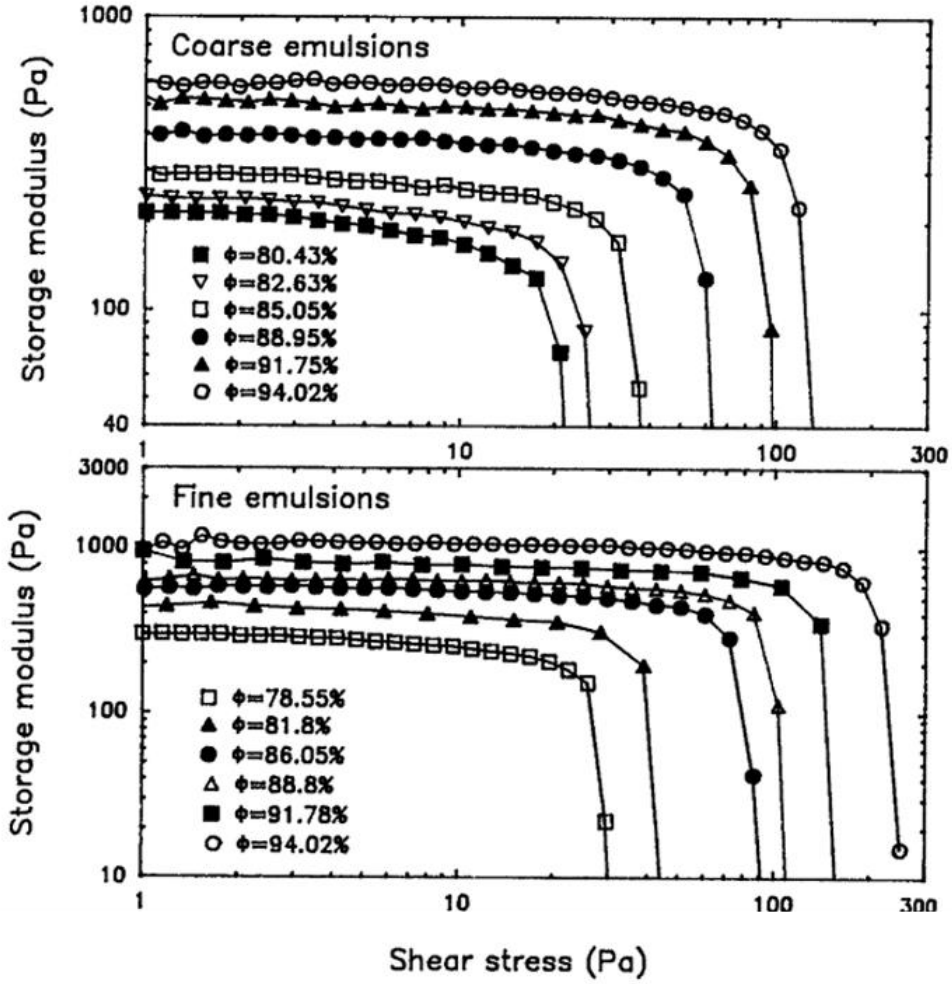

Figure 2.16. Comparison the storage modulus of HIPPEs at fine and coarse droplet size [89].

2.6 Scale-up in stirred tanks

For scale-up in any application, the first step is to determine the level of uniformity in the distribution of solids or droplets, as well as the rate of any existing reactions. Next, a reliable correlation that describe the relationship between key process parameters, mixer design, and the physico-chemical phenomena should be established. Following this, the most effective processing parameters that govern these phenomena, preferably in the dimension less form should be identified. This correlation should be employed to estimate the required process conditions in the different scale [21].

For scale-up in the stirred tanks it is essential to consider geometric design across different scales, as this affects on flow and shear distribution in the vessel. To address this, the dimensional ratios of various tanks and impeller elements can be analyzed. These include, but not limited to:

- D/T: impeller diameter (D) to the tank diameter (T); evaluates the ratio of overall pumping capacity to fluid shear.
- W/D: blade width (W) to the impeller diameter (D); investigates the ratio of microscale to the macroscale mixing process.
- C/T: impeller clearance from the vessel bottom (c)to tank diameter (T); explores the uniformity of solid distribution [21]

A schematic illustrating these tank and impeller elements is shown in Figure 2.17.

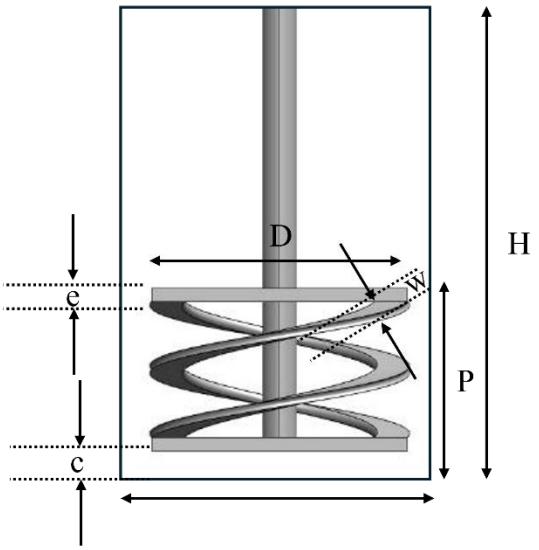

Figure 2.17. Schematic of impeller and tank design

2.6.1 Definitions for scale up in emulsification

Retaining the fluid dynamics of an emulsification process during scale-up is essential for maintaining consistent emulsion properties at all scales. This can first be achieved by running the emulsification process in geometrically similar vessels. Extrapolating emulsification conditions from one scale to the next requires the following equation to estimate the rotational speed of the impeller[21]:

$$N_2 = N_1 * \left(\frac{D_1}{D_2}\right)^{\alpha} \tag{2.26}$$

where subscripts 1 and 2 refer to the reference and the extrapolated scales, respectively. *N* is the rotational speed of the impeller, and *D* is the impeller diameter. The scale-up exponent α ranges from 0 to 2 and is directly related to the fluid mechanics that govern the emulsification [21]. Note that the expression can also be used to extrapolate mixing processes in general, not only emulsification.

A value of 0 represents constant rotational speed condition, which is used to maintain constant mixing time and constant power per volume in the laminar regime [77]. The scale-up exponent of 0 is obtained when the total power consumed during emulsification per total volume of emulsion is kept constant. In the laminar regime, the power consumed through emulsification can be calculated using the following equation:

$$P = K_P \mu N^2 D^3 \tag{2.27}$$

where *P* is the power consumed during emulsification, *N* is the impeller rotational speed, K_p is the ratio of power number ($Np = \frac{P}{\rho N^3 D^5}$) to the Reynolds number, and μ is the emulsion viscosity. Since K_p is a function of impeller design and the second scale is geometrically similar, K_p remains constant. By diving the equation 2.27 to the total volume of emulsion and considering that the volume of a cylindrical tank is directly proportional D^3,(tank height is a ratio od tank diameter), the following equation is obtained:

$$P/V = N^2 D^0 = \ constant \tag{2.28}$$

In the turbulent regime, a scale-up exponent of 0.67 is used for conditions with constant energy dissipation rate[21]. which applies to uniform particle or droplet dispersion in the turbulent regime. This value is derived from the following equation:

$$P = N_P \rho N^3 D^5 \tag{2.29}$$

where *Np* is power number, which is function of impeller design and Reynolds number. If the goal is to maintain constant power per unit volume and ensure similar flow patterns across scales, the power number should remain constant. Under these assumptions, the equation simplifies

to:

$$P/V = N^3D^2 = constant \tag{2.30}$$

Thus, in the form of equation of 2.26 the scale-up exponent is 2/3 or 0.67.

A scale-up exponent value of 1 is recommended for maintaining constant tip speed during simple blending operation [21].The tip speed obtained from the following equation:

$$U = \pi ND \tag{2.31}$$

Finally, for scaling-up droplet dispersion a constant Reynolds number criterion in the turbulent regime have been reported. This results in a scale-up exponent of 2 based on the following equation[21].

$$Re = \frac{\rho ND^2}{\mu} \tag{2.32}$$

2.6.2 Scale-up in highly concentrated emulsions

For highly concentrated emulsions (not stabilized by particles), scaling up using a constant Reynolds number as a scaling criterion has been shown to be ineffective. Using constant *Re,* during scale-up decreases the rotational speed from 1600 RPM at 100 mL to 780 RPM at 685 mL [90]. This reduction in rotational speed provides insufficient shear to break droplets, ultimately resulting in undesirably larger droplet sizes at the larger scale [90].

Gingras et al. produced emulsions through the inline SMX and helical static mixer[91]. They found that the average droplet diameter scales with specific power once equilibrium is reached, while before equilibrium, droplet size scales with the mixing energy. Meanwhile, May-Masnou et al. regarded rotational speed and power per unit volume (*P/V*) as scale-up invariants [92][93], applying, the scaling exponents of 0 and 0.67[92][93]. They found that at high rotational speed and long feeding time, the scale-up exponent of 0 resulted in similar droplet size and rheological properties. However, these studies used emulsifiers to stabilize small droplets (under 20 microns) at rotational speeds of 500-1800 RPM using pitched blade impellers, operating outside the laminar regime.

2.6.3 Scale-up in Pickering Emulsions

In the case of solid stabilized Pickering emulsions, Al-Haiek found that the scale-up factor in medium internal phase contents (<50%) emulsions operating in the turbulent regime should be between 0.67 and 1. This value is due to the combination of two simultaneous processes: the first is the simple blending of two liquids, requiring a scale-up exponent of 1, and the second is the suspension of solid, which requires α = 0.67 [56].

The key takeaway from Al-Haiek's work on the scale-up and processing of concentrated emulsions is the list of parameters to consider for the simultaneous processes. These parameters include the minimum rotational speed required to suspend particles [56] and droplets [94], the ability of particles to effectively cover the interface and ensure drop stability [48], and the capacity of the mixing system to generate interface i.e., produce droplets[48].

To ensure particles are suspended in the liquids within stirred tanks, the rotational speed must exceed the just suspended speed (N_{js}). Beyond this threshold, the number of particles available for droplet coverage decreases [48], leading to insufficient coverage [49] and the coalescence of partially covered droplets, which resulted in a non-uniform emulsion. Additionally, sufficient shear stress must be applied to ensure adequate droplet breakage and interface generation [48].

2.7 Sound absorption in porous material

When a sound wave encounters a material, its interaction—whether reflection, transmission, or absorption—depends on the material's properties. The sound absorption mechanism for the porous material is explained using energy dissipation theory. Generally, sound energy is divided into the reflection, absorption, and transmission energy [95].

$$E_i = E_r + E_a + E_t \tag{2.33}$$

where E_i represents the incident sound energy on the material, E_r is reflected energy, E_a represents the energy absorbed by material, and E_t is energy transmitted through it. The sound absorption coefficient, α, is defined as the ratio of absorbed sound energy to the incident sound energy [18] (Figure 2.18).

$$\alpha = 1 - \frac{E_r + E_t}{E_i} = \frac{E_a}{E_i} \tag{2.234}$$

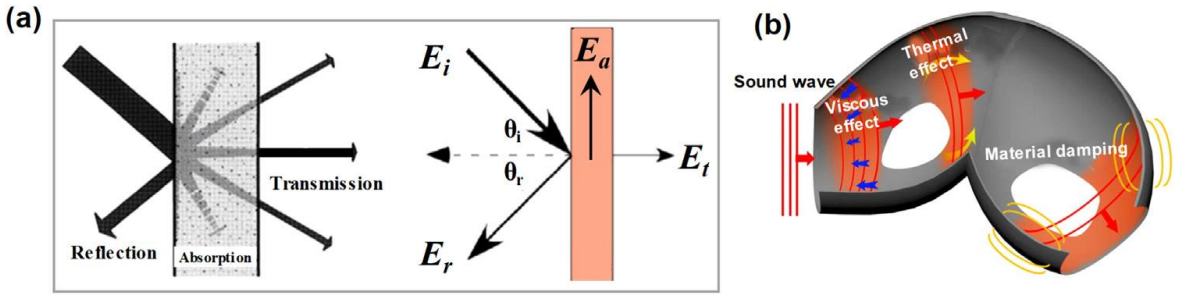

Figure 2.18. a) Schematic of different types of acoustic energy in in contact with the porous materials b) Schematic of energy dissipation in porous material [18]

In the porous material, sound energy dissipates through the following mechanisms[18]:

1. Periodic compression and release of air inside the cavity cause the pore walls to resonate, damping the sound wave by converting sound energy into mechanical energy.
2. Periodic compression and release of air inside the cavity dissipates the energy by converting it into kinetic energy and hence, thermal energy.
3. Vibration of air molecules inside the pores dissipate energy through viscous effect .

Based on these mechanisms, porous material should meet the following criteria [18]

1. Contain high number of open pores let the sound wave to penetrate.
2. Have appropriate pore size, interconnectivity, and interstices based on the desired frequency bandwidth to achieve a high absorption coefficient.
3. Include continuous channels which connect the surface and inner pores.

2.7.1 Porous material for sound absorption

Porous material is generally classified into organic, hybrid, and inorganic foam based on the chemical material involved in the foam structure. In this section, we briefly review the sound absorption performance of conventical foams [18].

2.7.1.1 Organic foam

Organic foams are widely employed in noise reduction duo their low-cost production techniques and tunable porosity and pore size, achieved by adjusting formulations. The morphology of foams is closely linked to their sound absorption performance, as the distribution of pathways within the foam structure significantly influences sound energy dissipation[18].

Polyurethane (PU) is a well-known organic foam sound absorber among polymers due to its ease of processing and its ability to produce various microstructures. Extensive research has been conducted on PU to date. Sung et al. investigated how molecular structure of isocyanate, which is the main ingredient of PU-based foam, affect the fabrication of flexible foam used as a sound absorption material[11]. They stated that the solidification rate affects the pore opening ratio. They explained that if the cavity pressure is higher than the wall strength, an open structure will form. At a low drainage flow rate (related to matrix modulus), a partially opened structure will form if the wall solidifies before rupturing. Finally, if the wall solidifies completely before the opening process begins, a fully closed structure will form (Figure 2.19).

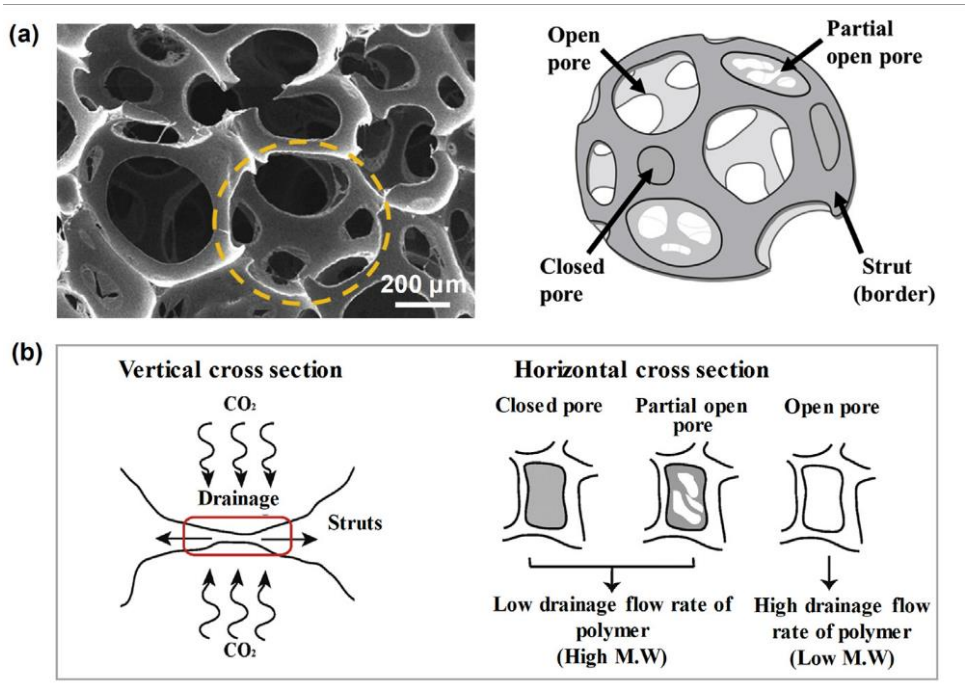

Figure 2.19. a) morphology of polyurethane, b) opening mechanism of a pore[18] [11]

Yang et al. investigated the effect of PU morphology, ranging from fully-open to semi-open structures, on sound absorption performance [96]. They also validated the Johnson-Champoux-Allard (JCA) model using experimental data and found that it deviated from test results at certain frequencies, especially for partially opened cell structures. To address this, they defined a new parameter to calculate non-acoustical properties and fitted their newly estimated sound absorption coefficient to the experimental data.

Based on the morphology investigation (Figure 2.20) and the sound absorption performance (Figure 2.21), they concluded that the partially-opened structure with a very thin membrane

(sample S6) could absorb sound energy more efficiently than a fully-open unit cell, at frequency of 500-4000 Hz [96].

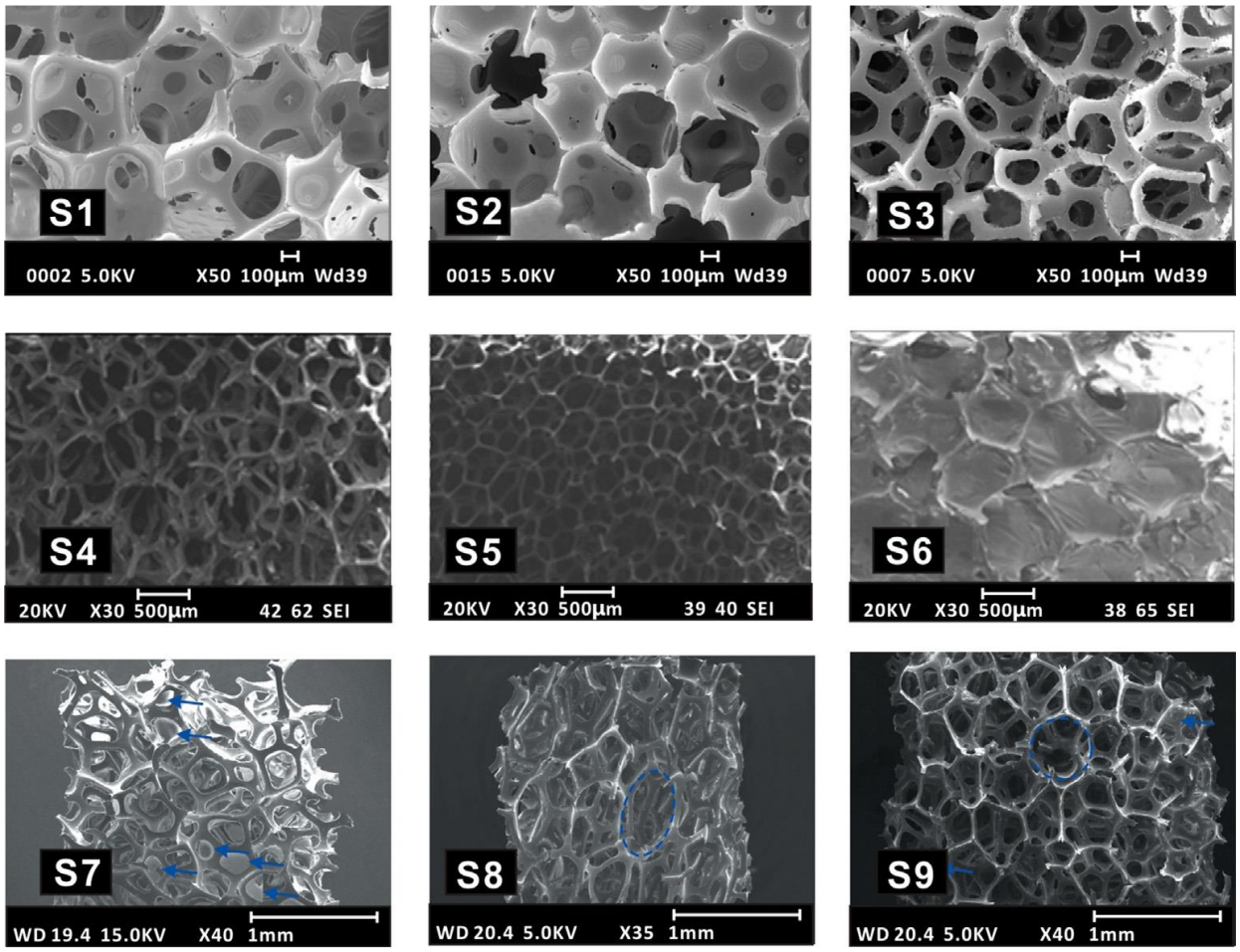

Figure 2.20.SEM image of the fully/ or partially-open structure of PU foam [96]

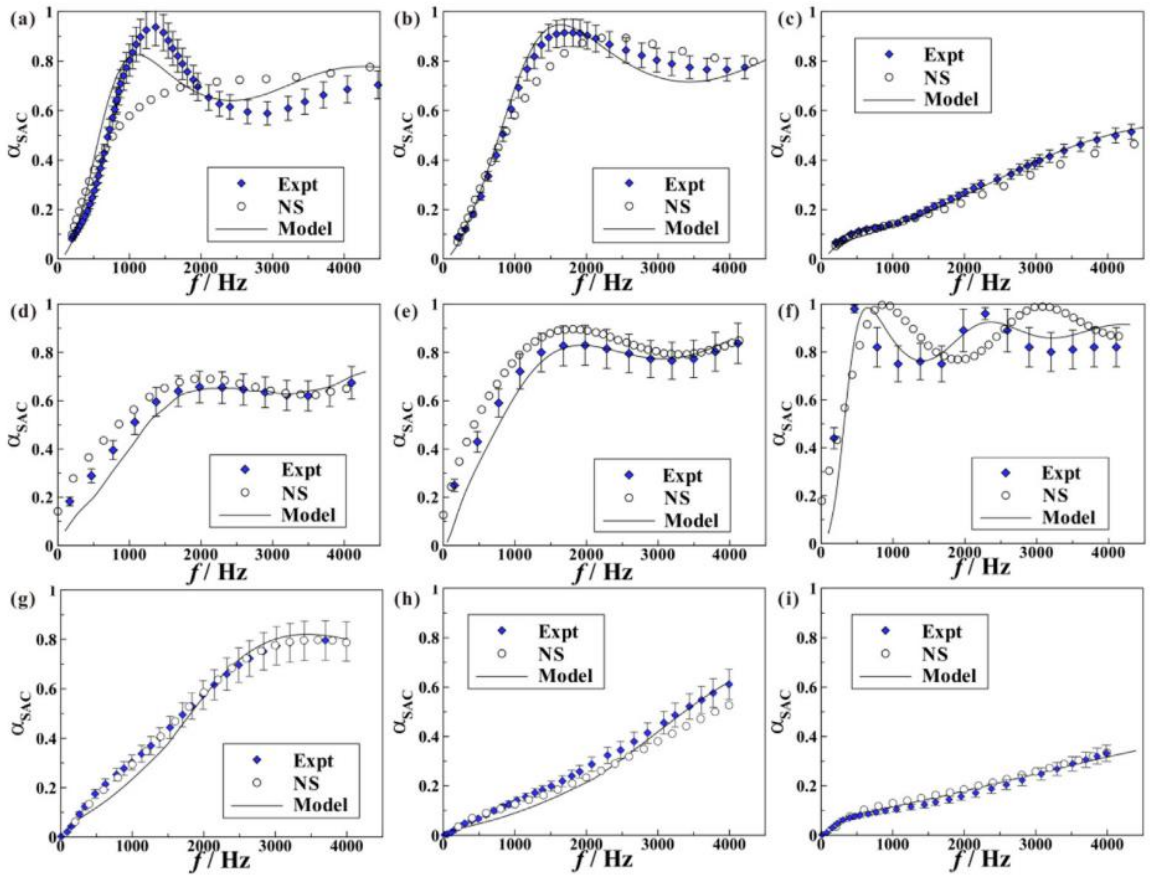

Figure 2.21. Sound absorption performance of samples in the Figure 2.20, left to right and up to down S1-S9

2.7.1.2 Hybrid foam

In addition to chemical control, incorporating particles and fibers into foams, which is called hybrid foam, dissipates sound energy more efficiently. Hybrid foams are generally produced by two techniques. The first technique begins with the preparation of a dispersion of resin and particles. Afterward, the foam is cured at the appropriate temperature. In the second technique, the prepared foam is immersed in a particle dispersion. The particles deposit inside the foam cells, forming a membrane layer, which increases tortuosity and enhances air resistivity, thereby improving sound absorption. Melamine foam/ Graphene oxide (MF/GO) is an example of this type of foam, which has been investigated by Nine et al. [97] (Figure 2.22).

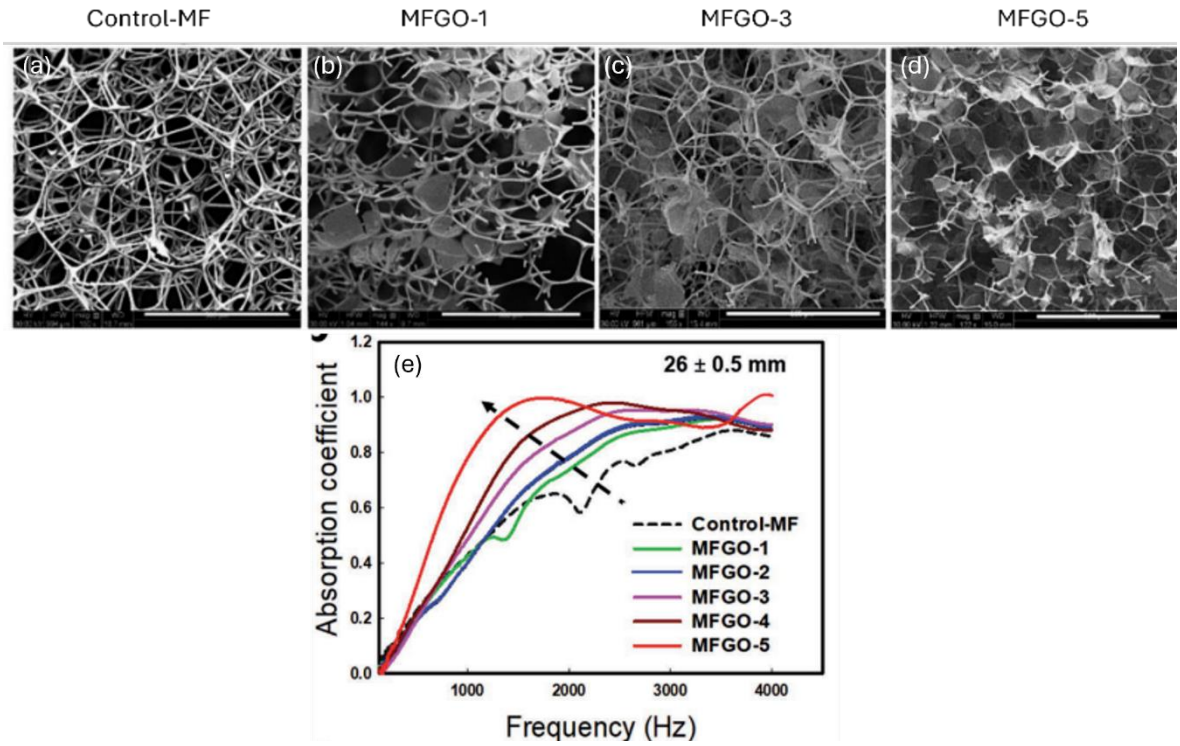

Figure 2.22. The effect of adding graphene into the melamine foam on the sound absorption performance, (a)-(d) are SEM of samples, and (e) is the sound absorption coefficient of samples. scale bar of (a)-(d) are 500 μm [97]

The particle size and distribution play a crucial role in sound adsorption. For example, hybrid foam composed of polyurethane and carbon nano tube (PU/CNT) demonstrates optimal sound absorption coefficient, near to one, performance between 400-1600 Hz when treated with ultrasonic wave for 40 min. Baferani et al. reported that ultrasonication decrease the average of pore size and increase the reticulation rate, which enhance the interaction of CNT surface with the sound waves, thereby improving sound absorption performance [98] (Figure 2.23).

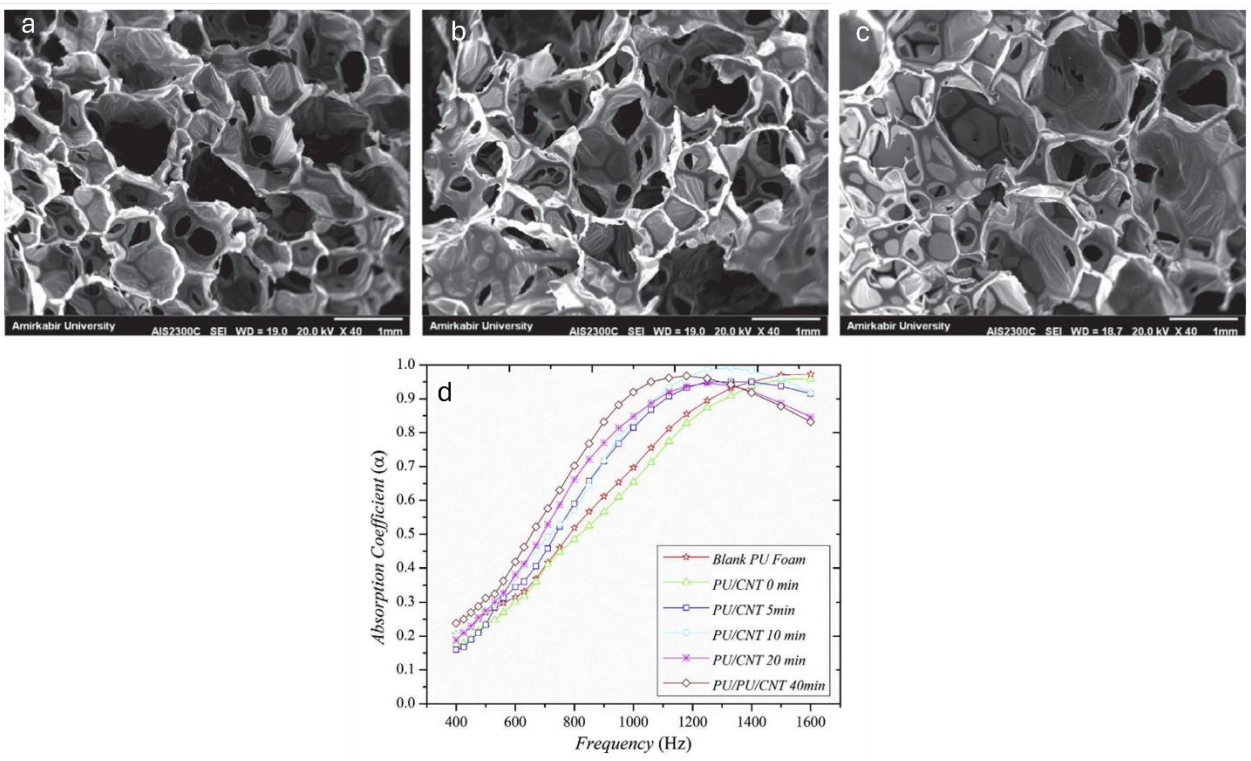

Figure 2.23. SEM image of (a) PU foam, (b) PU/CNT without sonication and (c) PU/CNT with 40 min sonication, (d) is the sound absorption coefficient of samples [98]

It has been demonstrated that the orientation of channels formed by particles and fillers in the hybrid foam significantly affects sound absorption performance [99]. When a sound wave transmitted vertically into the hybrid foam, partial reflection occurs, reducing sound absorption efficiency (Figure 2.24.a). In a parallel orientation, sound waves have higher potential for transmission through, making absorption inefficient (Figure 2.24.b). Finally, when a sound wave enters at an oblique angle, the increased travers path enhance air flow friction, maximizing sound energy dissipation (Figure 2.24.c) [99].

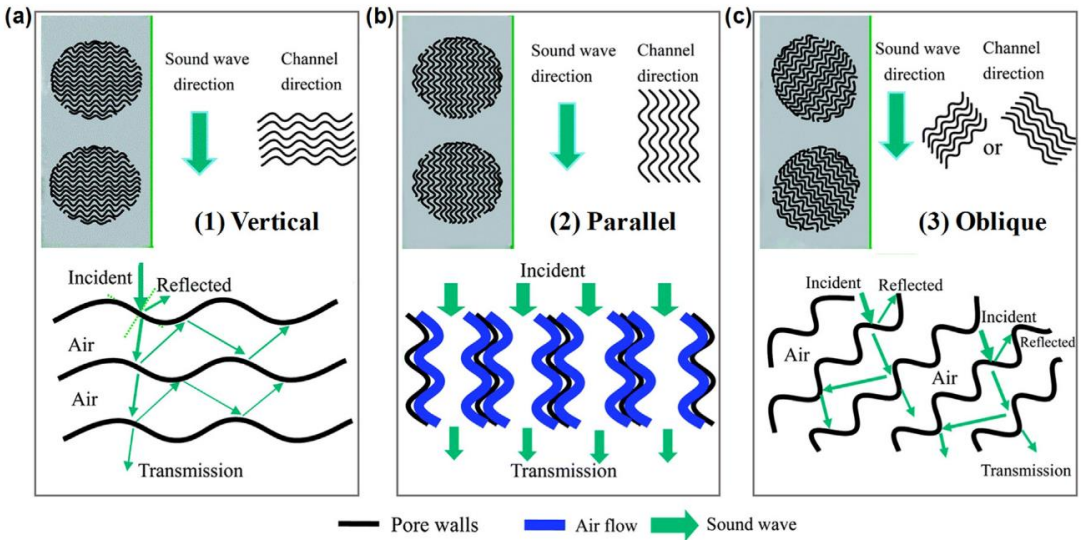

Figure 2.24. Propagation of sound wave in the hybrid foam [99]

2.7.2 Fabrication technique

2.7.2.1 Direct foaming process

Commercial acoustic materials are produced through a direct foaming process. The most well-known foam prepared using this method is polyurethane-based foams, which consists of monomers, foaming agents (mostly isocyanates), and a catalyst. The most critical parameters in this technique are the number of pores which correlated with density, as well as the size distribution of the pores, which are controlled through formulation, like manipulating the monomers, and process conditions, like increasing the foaming speed.

For instance, Gwon et al. reported that by modifying the formulation and increasing the pore wall's modulus, the pores can better tolerate the gas pressure generated by foaming agents. As a result, small holes are created, connecting neighboring pores without causing coalescence. Ultimately, a higher number of uniformly smaller pores were formed in the foam, providing a more irregular path for sound waves to dissipate, increasing the sound absorption coefficient (case 1 and 2.Figure 2.25 and Figure 2.26 [12]).

They also demonstrated that decreasing the pore wall's modulus led to pore coalescence, creating large, non-uniform pores and reducing the total number of pores within the foam. Consequently, the sound waves encountered fewer pore walls and were weakly dissipated (case 3 .Figure 2.25 and Figure 2.26 [12]).

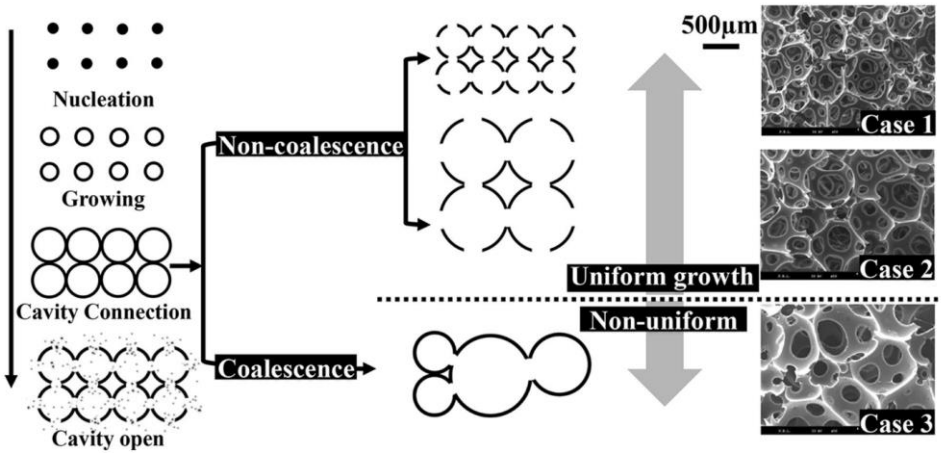

Figure 2.25. Summary of pore growth mechanism through coalescence and non-coalescence[12]

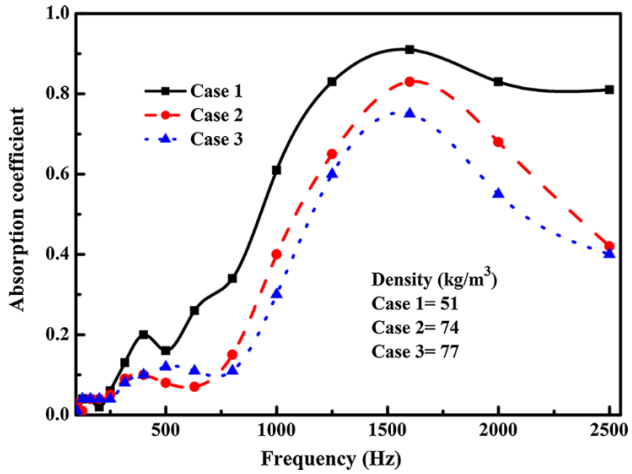

Figure 2.26. Absorption coefficient of the flexible polyurethane foam for three different case illustrated in Figure 2.25

2.7.2.2 Leaching technique

The leaching technique offers precise control over pore size and interconnectivity [100] [101]. In the leaching technique, varied sizes of salt particles are dispersed in the polymeric matrix in a layer-by-layer manner; after curing of the polymeric matrix the salt is dissolved through the leaching process. Mosanenzadeh et al.[100] showed that the sample prepared using salt particles with diameters of 500-700 microns had the highest sound absorption, as shown in (Figure 2.27) [100].

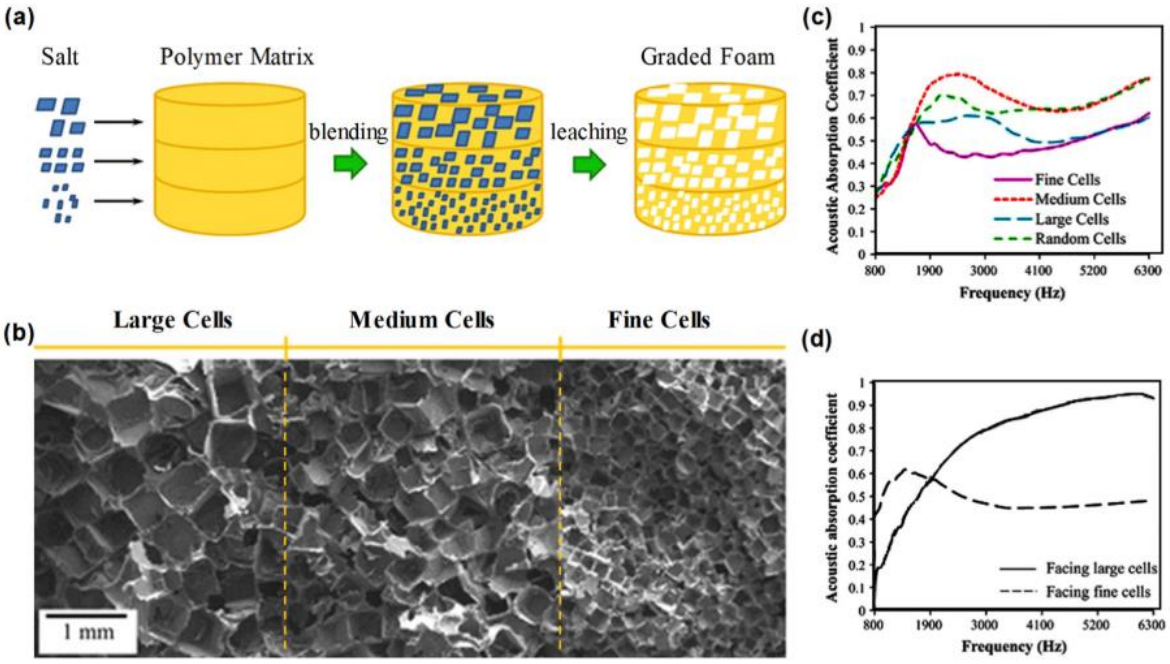

Figure 2.27. a) fabrication of gradient leaching porous material. b) SEM images of gradient foam. c) and d) sound absorption of foam [100].

2.7.2.3 Additive Manufacturing

Additive manufacturing is an emerging method for producing porous sound-absorbing material. High sound absorption can be achieved by adjusting the filament thickness, the distance between filaments (lattice parameter), and the printing orientation [102]. Analytical models for additive manufacturing suggests that the optimal morphology for maximum sound absorption involves a filling fraction of 40-50 % and a filament diameter between 50-200 microns, equal to 0.5-0.75 Dsp for Figure 2.28 [102]. However, these structures typically exhibit sound absorption peaks above 3000 Hz and require modifications to perform effectively at lower frequencies (Figure 2.28).

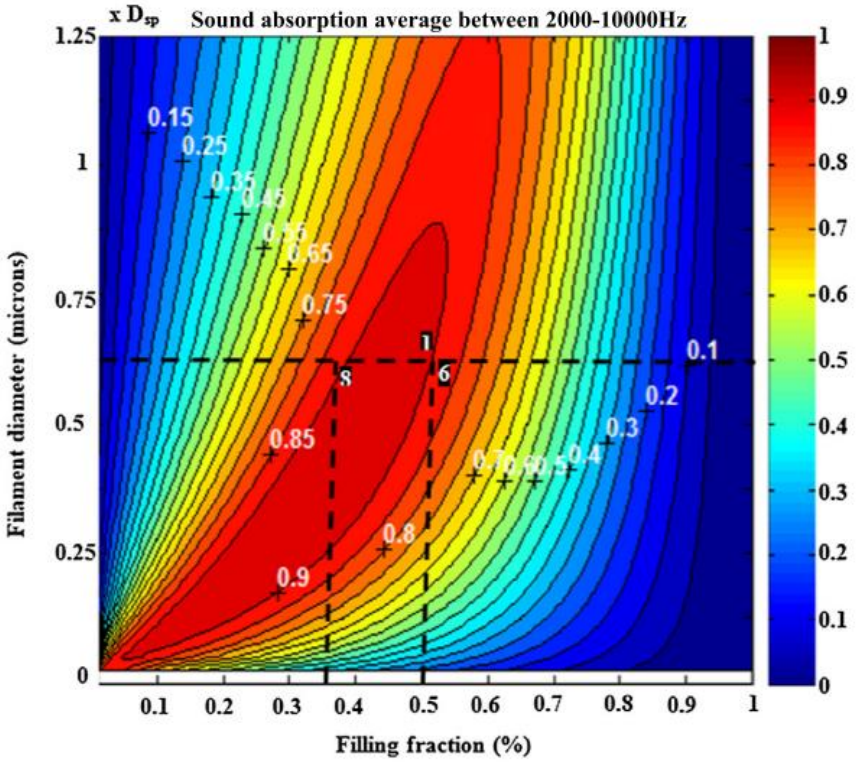

Figure 2.28. The average sound absorption at 2000-10000Hz as a function of the filling factor and filament diameter [102].

2.7.3 Sound absorption acoustic models

Numerical simulations on sound absorption in porous materials have recently attracted significant attention due to their ability to compute sound propagation in complex porous materials [96]. Since 1940s, analytical models for sound absorption coefficient have evolved significantly, and the number of physical parameters required for accurate predictions has increased. Figure 2.29 demonstrates a comparison between various numerical models of porous material, depicting the types of porous materials and the number of physical properties required for prediction [96].

The Johnson-Champoux-Allard (JCA) model and its extended models, Johnson-Champoux-Allard-Lafarge (JCAL), and Johnson-Champoux-Allard-Pride-Lafarge (JCAPL) are the most commonly used for porous materials with complex structures. These models rely on several non-acoustical properties, including open porosity (ϕ), static air flow resistivity (σ), high frequency limit of the tortuosity (α_∞), static viscous tortuosity (α_0), viscous characteristic length (Λ), thermal characteristic length (Λ'), static viscous permeability (q_0), and static thermal permeability (q_0').

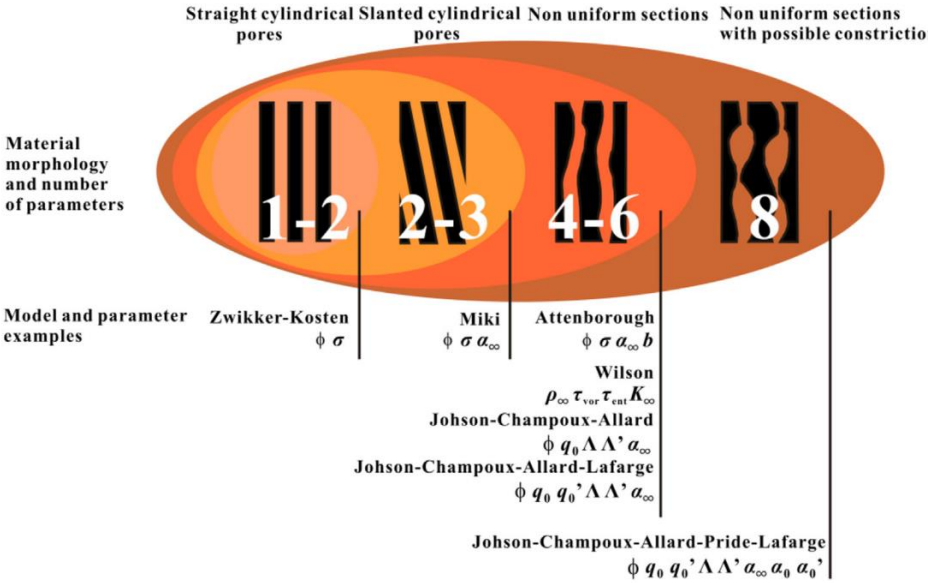

Figure 2.29. Comparison of analytical model for sound absorption of porous material with rigid skeleton [96]

Sound absorption prediction models theoretically calculate the efficiency of energy dissipation in porous sound-absorbing materials. The sound absorption coefficient can be predicted using the material's surface acoustic impedance through the following equation[103]:

$$\alpha = 1 - \left(\frac{\tilde{Z} - Z_0}{\tilde{Z} + Z_0}\right)^2 \tag{2.359}$$

where $\tilde{Z}$ is the surface impedance and Z_0 is the air impedance equals to $\rho_0 c_0$. Here, c_0 is the sound velocity in air. In the hard backing configuration, $\tilde{Z}$ is defined as:

$$\tilde{Z} = -j\widetilde{Z_c}\, cot(\tilde{k}l) \tag{2.36}$$

where l is the thickness of porous material, $\tilde{k}$ is wave number and $\widetilde{Z_c}$ is the characteristic impedance, which are defined by

$$\widetilde{Z_c} = \sqrt{\tilde{\rho}_e \tilde{K}_e} \tag{2.37}$$

$$\tilde{k} = \omega \sqrt{\frac{\tilde{\rho}_e}{\tilde{K}_e}} \tag{2.38}$$

where $\tilde{\rho}_e$ and $\tilde{K}_e$ are density and bulk modulus of the equivalent fluid. Based on the JCAPL model, these parameters defined as [104]:

$$\tilde{\rho}_e = \rho_0 \alpha_\infty \left(1 + \frac{1}{j \frac{\omega \alpha_\infty \rho_0}{\sigma \phi}} G_j(\omega) \right) \tag{2.39}$$

$$\tilde{K}_e = \frac{\gamma P_0}{\phi} \left(\gamma - \frac{\gamma - 1}{1 + \frac{1}{j \frac{\omega \rho_0 {q'}_0 P_r}{\mu \phi}} G'_j(\omega)} \right)^{-1} \tag{2.40}$$

where ω is the frequency, ρ_0 is density of air, γ is the adiabatic constant, P_0 static pressure of air, μ is the viscosity of fluid, P_r is the Prandtl number, ϕ is porosity, α_∞ is tortuosity, and σ air flow resistivity. $G_j(\omega)$ and $G_j{}'(\omega)$ are functions that defined by Johnson to correlate viscous and thermal characteristics properties:

$$G_j(\omega) = \sqrt{1 + j \frac{8 \alpha_\infty q_0}{2 \phi \Lambda^2} \frac{\omega \alpha_\infty \rho_0}{\sigma \phi}} \tag{2.415}$$

$$G'_j(\omega) = \sqrt{1 + j \frac{8 \alpha_\infty {q'}_0}{2 \phi {\Lambda'}^2} \frac{\omega \rho_0 {q'}_0 P_r}{\mu \phi}} \tag{2.426}$$

Where q_0 and ${q'}_0$ are viscous and thermal permeability, Λ and Λ' are viscous and thermal characteristic length. JCAPL model agree well with the sound absorption coefficient, especially at low frequency. However, it requires more non-acoustic parameters that cannot be obtained analytically or measured easily, making these models more complex. Accordingly, in most studies, the JCA model is employed to predict sound absorption, often with small modifications, especially for semi-open porous material.

2.7.4 Non acoustic parameters in porous material

Based on the acoustic models, the final sound absorption performance is a function of the non-acoustical properties of the porous structure [105]. These properties include porosity, tortuosity, viscous and thermal characteristic length, viscous and thermal permeability, all of which are

functions of the microstructure. Therefore, investigating the microstructure and the morphology is essential for understanding these non-acoustical parameters.

2.7.4.1 Porosity

The porosity of samples represents the proportion of its volumed filed with air. This is calculated using the following equation:

$$\phi = 1 - \frac{\rho_{sample}}{\rho_{bulk}} \tag{2.43}$$

where ρ_{sample} is calculated by measuring samples' volume and weight, and ρ_{bulk} can be experimentally obtained using a pressure difference technique (pycnometer) or fluid saturation (Archimedes' principle)[106].

2.7.4.2 Viscous Permeability (static air flow resistivity)

The viscous permeability, also known as static permeability, is a key parameter in estimating the sound absorption coefficient. It determines how easily a sound wave can penetrate a porous material. Based on Darcy's law [107], the air flow resistivity (σ) is the ratio of dynamic viscosity of air (μ) to the permeability of air in the porous structure (q_0). It can be measured experimentally or estimated numerically:

$$\sigma = \frac{\mu}{q_0} \tag{2.344}$$

2.7.4.3 Viscous and Thermal characteristic Length

Johnson, Koplik, and Dashen (1987) introduced the concept of viscous characteristic length. This parameter defines the relationship within the velocity field inside the porous material. It is function of tortuosity α_∞, viscosity of air or any liquids that is used for the test (μ), ϕ porosity, and air flow resistivity (σ). For porous material with a shape factor of c it is given by [108]:

$$\Lambda = \frac{1}{c}\sqrt{\frac{8\alpha_\infty \mu}{\phi\sigma}} \tag{2.345}$$

Allard et al. later established that thermal characteristics length is correlated with viscous characteristic length so:

$$\Lambda' = \frac{1}{c'}\sqrt{\frac{8\alpha_\infty \mu}{\phi\sigma}} \tag{2.46}$$

where c' is a coefficient related to the geometry of the pores.

2.7.4.4 Tortuosity

The tortuosity is an intrinsic property of the porous material that depends on its pore-level topology. It represents the ratio of the penetration path of air flow inside the porous material to the thickness sample. A more complex topology results in a longer penetration path and higher tortuosity. Some fully analytical and semi-analytical models predict the tortuosity factor in idealized topology. For example, for completely uniform porous structure with n pores of radius R the tortuosity factor (α_∞) is described as following equation [109]:

$$\alpha_\infty = \frac{1}{cos^2\theta} \tag{2.47}$$

where θ is the angle between the axis of the oblique pores and the normal to the surface. However, in reality, the unit cell has a complex topology and deviates from analytical prediction. Therefore, tortuosity can be measured experimentally or from inverse characterization approach from the acoustic performance.

The reflection ultrasound technique is used to experimentally measure tortuosity. In this technique, the instantaneous oblique reflection coefficient, *r(t,θ)*, of the first reflected wave at the material's surface is measured. This coefficient is obtained by ratio of the amplitude of the wave reflected from the material (A_m) to that of a rigid surface (A_r) at the same contact angle (Figure 2.30)[110].

$$r(t,\theta) = \frac{A_m}{A_r} \tag{2.48}$$

At high frequencies (60–180 kHz) and contact angles of 20–45 degrees, tests are conducted, and the average tortuosity is calculated using the following equation:

$$\alpha_\infty = \frac{z^2}{2}\left(1 + \sqrt{\left(1 - (\frac{2}{z}sin\theta)^2\right)}\right) with\ z = \frac{1+r}{1-r}\frac{\phi}{\cos\theta} \tag{2.49}$$

where ϕ is porosity and r is the reflection coefficient.

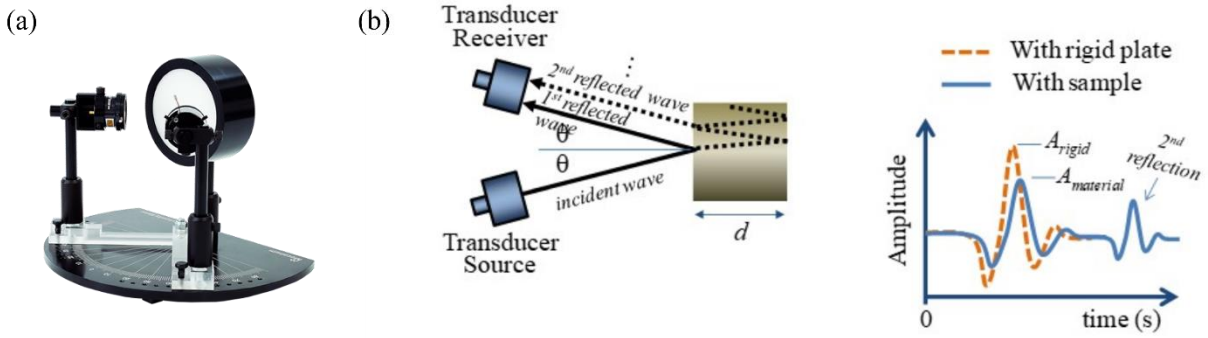

Figure 2.30. (a) reflection ultrasound instrument. (b) Schematic of instrument and reflection from mater [110].

2.7.4.5 Thermal permeability

The thermal permeability q_0' is a complex parameter representing the relationship between the pressure-time derivative and the mean temperature. Lafarge et al. reported a basic equation based on the porosity of samples and their characteristic thermal length [107]:

$$q'_o = \frac{1}{8}\phi\Lambda'^2 \tag{2.50}$$

Therefore, the non-acoustical parameter can be estimated based on the morphology analysis and the estimated unit cell. Then their can be evaluated using inverse characterization techniques through the surface impedance testing and fitted to the JCAL model.

2.7.5 Pore size and interconnectivity in porous material

The pore size and connectivity number—defined as the number of channels connecting pores to neighboring pores, allowing airflow to traverse from one pore to another—can be visualized in three dimensions using open-source pore network modeling (OpenPNM) [111]. This technique has recently been used to analyze the 3D morphology of rocks[112], and composites [113].

This model is integrated into the commercial software Dragonfly and helps determine pore size distribution, the average number of throats per pore (connectivity), the distance length between connected pores, and tortuosity. Figure 2.31 illustrates and example of 3D visualization of pore network in porous materials [113].Despite the promising potential of this technique for visualizing 3D morphology, it has not yet been used to correlate morphology with non-acoustical and acoustical parameters.

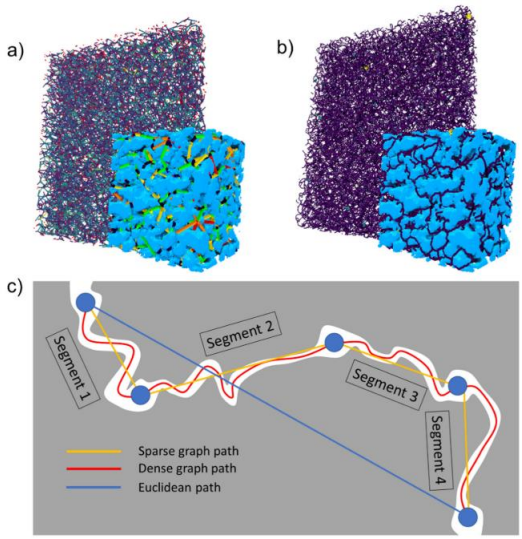

Figure 2.31. a) Sparse and b) dense graphs of pore model for a polymeric composite c) schematic of the sparse and dense graph path [113]

2.8 Summary of the literature review

The application of solid-stabilized emulsions has been extensively investigated across various fields. However, their potential in controlled foam production remains unexplored. While the effects of processing conditions on moderately concentrated Pickering emulsions in the stirred tanks have been studied, there is a lack of knowledge regarding HIPPE preparation in stirred tanks. Most studies on HIPPEs have employed homogenizers operating in the turbulent regimes, which typically result in small droplet sizes with large size distributions. Although scale-up approaches for moderately concentrated Pickering emulsions in the turbulent regimes have been stabilised, there is no existing literature addressing the scale-up of HIPPE in laminar regimes.

The literature review also revealed that the sound absorption performance of porous materials depends on factors such as pore size, interconnectivity, open porosity, and other non-acoustical properties. The final porous material produced through HIPPE technique must meet specific criteria to achieve high sound absorption efficiency.

CHAPTER 3 OBJECTIVES

This work aims to investigate a novel approach for producing acoustic porous material from high internal phase Pickering emulsions (HIPPEs). To achieve the desired sound absorption properties, the pore size-primarily prepared through HIPPE-must be sufficiently large to allow sound wave to penetrate. Achieving large droplet size, around 200-800 microns, in HIPPE is particularly challenging due to their high viscosity, and this has not been previously studied. A controllable and predicable approach for determining the required process conditions to achieve the desired droplet size across scales is necessary, emphasizing the need to define a new scale-up rule for HIPPE in stirred tank systems. Furthermore, controlling the pore size and interconnectivity of porous material produced through HIIPE preparation is a novel approach that has not yet been explored. Establishing a correlation between the final porous structure and its non-acoustical and acoustical performance in these materials warrants further investigation.

Based on these research gaps and challenges, the main objective is to develop a scalable process to prepare high internal phase Pickering emulsion that can be post-treated to produce controlled porous material. Three specific objectives are proposed:

- Production of Monodisperse Large Drop Emulsions in HIPPE
    - Develop monodisperse large-droplet HIPPEs (100-800 microns) by controlling processing conditions and formulation. This will be addressed in the 1st article.
- Scale-Up Rule for HIPPEs in Stirred Tanks
    - Determine the scale-up rule for HIPPE production in stirred tank systems, particularly in laminar regimes. This will be addressed in the 2nd article
- Acoustic Porous Material and Structure-Performance Correlation
    - Post-treat the HIPPE from our process into porous materials and establish their potential for being used as sound-proofing foams. Establish a correlation between the porous structure and the final acoustic performance. This will be addressed in the 3rd article.

CHAPTER 4 ARTICLE 1: PRODUCTION OF MONODISPERSE LARGE DROP EMULSIONS BY MEANS OF HIGH INTERNAL PHASE PICKERING EMULSIONS – PROCESSING AND FORMULATION

Authors: Mina Saghaei[1], Edith Roland Fotsing[2], Annie Ross[2], Louis Fradette[1*]

Department of Chemical Engineering, Polytechnique Montréal, Montreal

Department of Mechanical Engineering, Polytechnique Montréal, Montreal

Article history: Issue Online: 9 October 2024, Manuscript accepted:20 September 2024, Manuscript received: 16 May 2024 on Industrial & Engineering Chemistry Research

4.1 Chapter's connection to the main objective

This chapter covers article 1, where we present a novel approach for generating high internal phase Pickering emulsions with large droplets (>100 microns) and narrow size distribution. Our method combines highly concentrated emulsification with droplet stabilization by micron-sized particles. While previous studies relied on energy-intensive high-pressure mixing, limiting their applicability to fine droplets smaller than 50 microns, our approach offers a scalable and cost-effective alternative for achieving controlled large droplet size. This work provides valuable insights for both researchers and industrial applications.

My contribution to the articles includes conceptualization, methodology, experimentation, analysis, writing original draft, and literature review.

4.2 Abstract

High internal phase Pickering emulsions (HIPPE) have received significant research attention in the last two decades due to their potential for a wide range of applications. The appropriate processing of such high-viscosity emulsions, hundreds of times more viscous than that of the continuous phase, and the control of the final droplet size both remain challenges to be tackled. Our research targeted this knowledge gap by examining the influence of the emulsion formulation and the processing conditions on the final droplet size. The dispersed phase fraction (100 cSt silicon oil) ranged between 75 to 80%. The emulsions were produced in a regular mixing tank equipped

with a helical ribbon impeller rotating at low speed (100 to 150 RPM). The effective viscosity of the continuous phase was obtained from experimental torque measurements. The droplet size distributions were measured after emulsification and dilution in continuous phases. It is shown that the capillary number, obtained from the observed emulsification performance, can help predict the final droplet size. Our approach provides a straightforward methodology to generate concentrated Pickering emulsions with controlled and predictable droplet size.

4.3 Introduction

Emulsions solely stabilized by solid particles at the oil-water interface were described by Ramsden and Pickering[14] about a century ago. Their behavior and properties have been actively investigated in recent decades [23][29][114] and some applications along with them[12][18][20][34][100][101]. The substitution of solid particles for traditional surfactants in such emulsions (also known as Pickering emulsions) offers numerous advantages, making them ideal for applications in fields including biomedicine[115][116], food[26], fine chemical synthesis[117], cosmetics[27], and fine 3D structures[118][119][120].

The use of particles in replacement of chemical surfactants not only strengthens the emulsion against coalescence but also lowers the risks of harmful surfactant release to the environment. Furthermore, the solid particles can be selected to suit some specific applications of the produced emulsions[117][121][115][15][122][65].

Low-volume and energy-intensive apparatuses such as high-pressure homogenizers and ultrasonic probes are reported as emulsion generators[20]. However, high-pressure equipment produces small droplets with a considerable degree of polydispersity in the emulsion droplets[51]. Additionally, it may destroy the larger solid particles[123]. Other equipment to produce Pickering emulsions, including microchannels[124], static mixers[125][126], and membranes[53], are limited to small scales, not appropriate for applications on larger scales, as the design of such equipment poses significant challenges[20].

Large-capacity emulsification often requires the use of a high-speed rotating impeller in a mixing tank. Pitched blade turbines (PBT) have the capacity to emulsify large volumes of fluids and are known to generate larger droplets (>75 μm) compared to high-pressure homogenizers[32], [49]. They are however limited to low-viscosity emulsification.

High internal phase Pickering emulsions are referred to as HIPPE and occur when the emulsion drops reach their maximum packing state. For spheres of size, the maximum packing value is around 74% (hexagonal close packing). Different lattice structures can lead to packing fractions ranging from 34% to 60%. When the emulsion reaches this packing state, the viscosity increases sharply and remains high thereafter. Similarly to dilute emulsions, a wide variety of particle types and particle sizes, oil types, and processing conditions are employed in the preparation of HIPPEs, and can be found in reviews[65].

For high viscosities such as the ones encountered in concentrated emulsions, low-speed close-clearance impellers are more appropriate as they natively deal with high viscosity mixtures. Examples of such mixers are the Maxblend impeller[73], anchor impellers[74], Paravisc[75], and helical ribbons (Single helical ribbon SHR and double helical ribbon DHR) [75]. Very little literature exists about the use of low-speed impellers applied to the production of emulsions. For instance, asphalt was successfully emulsified using an anchor impellor at 95% dispersed phase in a surfactant-based emulsions[74]. Very narrow droplet size distributions and easy processing were demonstrated; however, they produced very fine droplet size which is not appropriated for us

The viscous stresses generate the droplet breakup in the laminar flow[81][127] while the interfacial forces around the droplet will limit the extent of the breakup. The capillary number (*Ca*) represents the ratio of viscous forces to interfacial forces (Laplace pressure) from the shearing flow:

$$Ca = \frac{\mu_c \dot{\gamma}}{2\gamma_{ow}/D_{43}} \tag{4.1}$$

where μ_c represents the viscosity of the continuous phase, $\dot{\gamma}$ denotes the shear rate, γ_{ow} is the interfacial tension between dispersed and continuous phases, and D_{43} is the diameter of a droplet. The droplet breaks if *Ca* exceeds a critical value (Ca_{crit}); the new droplets have smaller diameters and *Ca* becomes lower. Simultaneously, small droplets tend to coalesce, leading to increased diameter and *Ca*. Thus, the observed or effective capillary number of a given process will tend to "move towards" the critical capillary number if enough time is allowed for droplet rupture to occur repetitively.

Multiple empirical models predict the critical capillary number based on the viscosity ratio between the dispersed and continuous phases[80][81] and report the effect of viscosity ratio on the curvature of droplet breakage[82]. In these models, the *Ca* value is obtained for dilute emulsion, where the effect of the neighboring droplets is neglected. This literature made use of constant viscosity for

the continuous phase over the emulsification time. This assumption of constant continuous phase viscosity might not be accurate for Pickering emulsions where the continuous phase may be non-Newtonian, and the presence of micron-sized particles induces more complexity.

HIPPEs not only exhibit a viscoelastic behavior themselves[84] but also the continuous phase might reveal complex rheological behavior. Depending on the particle size, the shear rate, and the repulsive force between particles, the continuous phase can exhibit both shear thinning and shear thickening[85], as well as time-dependent behavior, thixotropy, and rheopexy[86][87]. The observed behavior is a complex function of experimental conditions and formulation. The nonlinear rheological behavior of the concentrated suspension forming the continuous phase must be considered for calculating the viscosity ratio.

Despite extensive research on the fundamentals and the properties of concentrated Pickering emulsions, there is still a lack of understanding regarding the control of the final droplet size and the impact of the processing conditions on HIPPEs in the laminar regime. This research aims to fill this gap by studying the impact of the process and the formulation on the produced droplet size. This work seeks to develop methods for precise control and estimation of droplet sizes under low shear rates.

4.4 Material and Methodology

4.4.1 Material

The dispersed phase for all emulsions was silicone oil with a viscosity of 100 cSt (Clearco Products Co. Inc., USA). The continuous phase was formed of an aqueous phase that contained dissolved Polyvinyl alcohol (PVA) (Alfa Aesar, US) in distilled water at concentrations ranging from 2 to 4%. Polyimide (PI) powder with a primary diameter of 4 microns (P84NT, Evonik Fibers GmbH) was uniformly dispersed in the continuous phase prior to any oil addition.

To create a HIPPE, the dispersed phase concentration must exceed the maximum packing fraction of the droplets. In this study, oil concentrations (dispersed phase) of 75vol% and 80 vol% were employed. While not reported here for the sake of conciseness, the torque evolution during emulsification clearly demonstrated the achievement of a concentrated emulsion state when a sharp increase in torque was indeed recorded and showed ratios of final/initial torques of 3 to 10. The continuous phase comprised aqueous solutions of PVA at 2, 3, and 4 wt.%, and adequate amounts of PI to cover the oil droplets. Based on the expected droplet size range at the target PVA concentrations, three levels of PI concentrations were determined to ensure full drop coverage.

Consequently, 6 PI vol% in two different continuous phase volumes were calculated (20-23-25 vol%, and 25-28-32 vol.%) for samples containing 75% and 80% oil, respectively. All emulsions were prepared based on the full factorial design of all variants summarized in Table 4.1.

Table 4.1.Table of variants and level for formulation

	Level 1	Level 2	Level 3
PVA solution (wt.%)	2	3	4
PI (g)	0.7	0.8	0.9
Oil (Vol%)	75	80	(-)

The PI volume fraction, which is employed for all results, is calculated based on its volume in the continuous phase. The density of PI is 1.4 g/cm^3, and the volume of the continuous phase is 2 mL and 2.5 mL for emulsions prepared with 80 vol%, and 75 vol%, respectively.

4.4.2 Emulsification

4.4.2.1 Emulsification Setup and Procedure

The high internal phase Pickering emulsions were prepared using a 3D-printed double-helical ribbon within a 20 mL tank. The required quantity of particles was initially dispersed in the PVA solution by subjecting the mixture to 100-150 RPM for one minute. Subsequently, the oil was injected at a constant flow rate of 2.5 mL per minute, while agitation was maintained. The oil injection port was located at the base of the side wall of the tank (see Figure 4.1). This configuration allowed the oil to be injected at the bottom of the tank, in the most favorable zone for emulsification at low impeller speed. The torque meter recorded data during the mixing process for future calculations. The dimensions of the apparatus are given in Figure 4.1. These dimensions are representative of efficient ribbon designs, as recommended from the literature[21].

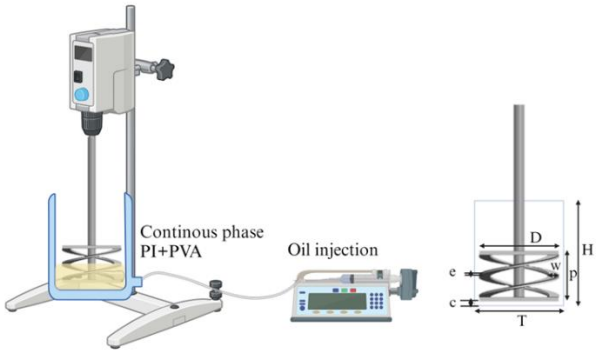

	D	T	H	P	c	e	w
(cm)	2.7	2.9	4.3	1.8	0.1	0.1	0.4

Figure 4.1Schematics and dimensions of the setup.

4.4.2.2 Processing conditions

To examine the impact of the emulsification time on the droplet size, three pre-established revolution number (*nr*) of the impeller were applied consistently during the emulsification process. The revolution number corresponds to the rotation speed multiplied by the emulsification time. This approach is justified by the fact that the HIPPE emulsification process operates in the laminar regime due to the very high viscosity of the concentrated emulsion. In this viscous flow regime, it is the amount of shear stress exerted on the emulsion that is expected to dictate the drop size reduction process. Exploiting the very high viscosity and the laminar regime, we can relate the number of rotations of the impeller to the potential of droplet rupture. The maximum torque value measured at the end of the emulsification step allows us to access average stress which in turn is related to the energy consumption.

Two values of rotation speeds, chosen for their ability to supply ample pumping capacity within the tank, were employed. The first selected revolution number is much larger than the dimensionless mixing time reported for helical ribbons in the literature[128]. Six process conditions (C1-C6) corresponding to each formulation, and three replication runs were conducted for each experiment. The list is presented in

Table 4.2.

The emulsions being viscous with non-Newtonian behavior, the shear rate is defined as per the Metzner and Otto concept following[21]:

$$\dot{\gamma} = K_s N \tag{4.2}$$

where $\dot{\gamma}$ is the shear rate, N is the impeller rotation per second, and K_s is the Metzner and Otto constant. K_s represents the capacity of a given impeller geometry to generate shear at a given rotation speed. Despite being called a "constant", this impeller characteristic may sometimes vary with the flow behavior index of the fluid (n) in the power-law expression of the viscosity[28]. Based on the published values[129],[130] from the literature and the double helical ribbon geometry used here, we assumed an average K_s value of 30 from the Brito-De La Fuente et al. [130] for a similar geometry and considering the flow behavior index (n) between 0.6-0.8.

Table 4.2. Process conditions

Condition number	**Rotation speed (*N*(RPM))**	**Revolution number (*nr*)**	**Emulsification time (min)**
C1(100/800)	100	800	8
C2(100/1600)		1600	16
C3(100/2400)		2400	24
C4(150/800)	150	800	5.33
C5(150/1600)		1600	10.66
C6(150/2400)		2400	16

4.4.3 Methodology

This section introduces the equations used for estimating the viscosity of the continuous phase for two different approaches: formulation and in-situ torque measurement. For formulation-based viscosity estimations, the measurements of PI particle size distribution (PI PSD), the zeta potential at different PVA concentrations, and the PVA viscosity are required. For torque-based viscosity, the emulsion's torque is recorded during mixing and is correlated to the continuous phase viscosity through analytical equations.

4.4.3.1 Emulsion characterization

4.4.3.1.1 Determining droplet size and particle size

Particle and droplet sizes were assessed using dynamic laser scattering (DLS) with the Mastersizer 3000 instrument from Malvern Panalytical, UK. The Malvern software provided various droplet size parameters, including D_{10}, D_{50}, and D_{90}, which represent sizes at which 10%, 50%, and 90% of the volume of all droplets are smaller, respectively. Additionally, the mass-weighted average size (D_{43}) was reported, which best represents the total droplet size within the emulsion. It is given by:

$$D_{43} = \frac{\sum n_i d_i^4}{\sum n_i d_i^3} \tag{4.3}$$

where n_i is the number of droplets at each size class (d_i).

4.4.3.1.2 Determining fractal dimension of particle

To identify the particle aggregation structure after emulsification, a 2 mL sample of the produced emulsion was collected from the mixing tank and diluted with water. The dilution was performed in a 20 mL tank with the DHR rotating at 100 or 150 RPM for one minute. Free particles were collected at the bottom of the tank once the agitation was stopped, and the mixture had settled. The fluid used to transport the samples during analysis had the exact same composition as the continuous phase (PVA solution at different percentages) to minimize agglomeration or dispersion due to ionic strength changes.

The slope of the log-log intensity-scattering angle (*I vs. q*) graph obtained from the DLS corresponds to the fractal dimension, D_f in the following equation [131],[132].

$$I(q) \propto q^{-D_f} \tag{4.4}$$

The slope is estimated in the domain where $Rg*q > 5$ where the relation is linear [131]. R_g is the particle gyration radius (half of D_{43}), q is the scattering angle, and I is the scattering intensity.

The compactness of aggregation is represented by the structure prefactor, k_g (Eq (4.5)):

$$n_p = k_g \left(\frac{R_g}{r_0}\right)^{D_f} \tag{4.5}$$

where the aggregate's particle number is n_p, and the primary particle's radius, r_0, was set at 0.33 microns based on minimum D_{10} which was observed for the PI particle at PVA 4 wt.%. The cubic ratio of R_g / r_0 is used to estimate n_p, since a fully spherical aggregate with a gyration radius R_g contains n_p individual spheres of radius r_0.

4.4.3.1.3 Scanning electron microscopy

Two scanning electron microscopes were used to study and characterize the morphology of the polyimide particles: Tabletop SEM Hitachi at 5-15kV, for statistical analysis, as well as Ultra-high-resolution SEM Hitachi (Regulus 8220) at 2kV for a more accurate description of the texture at higher resolution. Polyimide particles were analyzed before any process and after the

emulsification process. A 2 mL sample of the produced emulsion was collected from the mixing tank and diluted with water. The dilution was performed in a 20 mL tank with the DHR rotating at 100 or 150 RPM for one minute. The samples were then frozen at -80 ˚C for one hour and subjected to freeze-drying for 5 days.

4.4.3.1.4 Zeta potential of particle dispersion in PVA solutions

The particle's zeta potential is obtained using a Zetasizer (Malvern Panalytical, UK). First, the natural pH of the PVA solutions (2, 3, and 4 wt.%) was measured at 6.08, 5.88, and 5.7, respectively. At a concentration of 5 mg/mL and a temperature of 25°C, at least three distinct samples of each suspension were measured. Folded capillary cells DTS1070 were utilized. The equipment determined the electrophoretic mobility, and the software subsequently applied the Smoluchowski model to calculate the zeta potential.

4.4.3.1.5 Surface and interfacial tension

To measure surface and interfacial tension between two liquids, the Wilhelmy plate method was employed (DCAT 25, Data Physics Instruments).

4.4.3.1.6 PVA viscosity

The viscosity of the PVA solution was measured using a rheometer (MCR 501, Anton Paar) with double gap geometry (DG). The viscosity was determined by means of a shear sweep ranging from 0.1 to 100 s^{-1}.

4.4.3.2 Estimating the viscosity of continuous phase

4.4.3.2.1 Formulation-based approach

To estimate the viscosity of the continuous phase based on the formulation, the intrinsic viscosity of the particle suspension in the continuous phase is determined by the Smoluchowski, Krasno-Ergen Equation for large double-layer colloidal suspensions [133]:

$$[\eta] = 2.5\left(1 + \frac{3\xi^2\zeta^2}{K\mu_c R_g^2}\right) \tag{4.6}$$

where ξ is the absolute permittivity in electromagnetism, ζ the zeta potential of the particles, K is the specific conductivity of the continuous phase, R_g is the particle radius, and μ_c is the viscosity of the continuous phase alone.

The calculated intrinsic viscosity $[\eta]$, based on (Eq.4.6) were summarized in Table 4.3.

Table 4.3. Properties of the continuous phase

PVA wt.%	**Zeta potential (mV)**	**Conductivity (mS/cm)**	**Permittivity (*10e-10)[a]**	**Particle radius[b] (µm)**	**Viscosity of PVA solution (mPa.s)[c]**	**$[\eta]$**
2	26.68 ± 2.85	0.309	6.9	2.53±0.18	7.3±0.8	2.500
3	55.47 ± 5.8	0.39	6.8	1.31±0.07	23.1±1	2.501
4	132.98 ± 14.9	0.53	6.8	0.83±0.13	61.2±3	2.503

a Obtained from ref [134]
b Particle size for suspension of PI at different PVA solution
c Measured by rheometer; viscosity is constant at 0.1-100 s^{-1}

The concentrated suspension viscosity is determined using the equation used by Pal[135]:

$$\eta_r = [1 - k\varphi]^{-[\eta]} \tag{4.7}$$

where $\eta_r$is the relative viscosity. The value of k is obtained as follows:

$$k = 1 + \left(\frac{1 - \varphi_m}{\varphi_m^2}\right)\varphi \tag{4.8}$$

Here, φ_m is the maximum sphere packing factor. Assuming random close packing for polyimide particles after obtaining the PSD, φ_m is estimated at 0.637[135]. By substituting Eq (4.6) and (4.8) into Eq (4.7), the relative viscosity of the continuous phase was estimated. The result from Eq (4.7) multiplied by the measured PVA viscosity allows the calculation of the complete continuous phase viscosity. This calculation was performed at the three PVA concentrations used in this work.

4.4.3.2.2 Torque measurement approach

To estimate the viscosity of the continuous phase, we first need to measure the emulsion viscosity. During the mixing procedure, the torque's evolution over time is recorded. There is a correlation between the amount of torque and the viscosity of samples. In the laminar flow regime, for any

specific impeller geometry, the product of Reynolds number (*Re*) and the power number *Np* is a constant and is expressed as [21]

$$K_p = Np * Re = \frac{2\pi N(\Gamma - \Gamma_0)}{\eta_e * N^2 D^3} \tag{4.9}$$

where η_e is the emulsion viscosity at a specific rotation speed (*N)*, *D* is the impeller diameter, and Γ is the torque obtained from the torque meter and Γ_0 is the torque value for empty tank which corresponds to the mechanical friction within the micing system. The useful value of Γ is measured when the torque reaches a plateau at the end of the emulsification process. This maximum value is employed to calculate η_e. In the laminar regime, the K_p value is simply the proportionality constant between *Re* and *Np* and represents the capacity of the impeller's geometry to consume power during rotation.

The relative viscosity of the emulsion was estimated by employing again the Pal equation [135]. In this situation, the value of φ_m is the maximum close-packed droplet volume fraction. Depending on the emulsion uniformity[135], it is between 0.68 and 0.86. For close-packed monodispersed spherical droplets, the φ_m value should be 0.74[64]. In our case, owing to the polydispersity of the prepared HIPPEs, the φ_m value of 0.86 is selected. (Detailed information is given in the supporting information)

$$\eta_r \left[\frac{2\eta_r + 5p}{2 + 5p}\right]^{\frac{3}{2}} = \left[1 - \left(1 + \left(\frac{1 - \varphi_m}{\varphi_m^2}\right)\varphi\right)\varphi\right]^{-2.5} \tag{4.10}$$

By substituting $\eta_r = \frac{\mu_e}{\mu_c}$ and $p = \frac{\mu_d}{\mu_c}$, where η_e is obtained from Eq.4.8 and $\eta_d$is 0.0966 (Pa.s), the viscosity of the continuous phase viscosity is estimated.

4.5 Results

4.5.1 Effect of particle volume fraction and viscosity modifier (PVA) on droplet size

Under comparable processing conditions, the droplet size is generally more impacted by the PVA concentration than the PI concentration. Figure 4.2 illustrates this general trend where droplet size is more impacted by the PVA concentration vs the PI vol% at the C1(100/800) condition.

With 75% dispersed phase (Figure 4.2-a) and 20 vol% of PI, D_{43} decreased from 1100 to 400 microns by increasing the PVA content from 2 to 4 wt.%, respectively. The increase in oil volume from 75% to 80% (Figure 4.2-b) leads to a sharp decrease in droplet size. For instance, at a constant PI of 25 vol% and for PVA concentration of 2 wt.%, the droplet size decreases from 900 to 600 microns with this change in oil from 75% to 80%. However, for emulsions prepared using PVA 4 wt.%, increasing the oil vol% did not result in such a sharp reduction in droplet size when 80% was used. It reveals that the droplet reaches its minimum size even at 75 oil vol% with 25 vol% of PI. Beyond this volume fraction, there is no further reduction in droplet size with increasing particle content. It means the system has reached its maximum size reduction capacity. During our preliminary experiments, we ran emulsification tests with 28% PI and 75% oil. The D_{43} obtained then was comparable to the D_{43} obtained at 25% and supports our statement that the minimum size is achieved at 25% PI when using PVA 4%. This observation made us confident that the minimum size of the drops was obtained at the conditions we are using. Moreover, the droplet size does remain constant at PVA 4% and higher oil concentration.

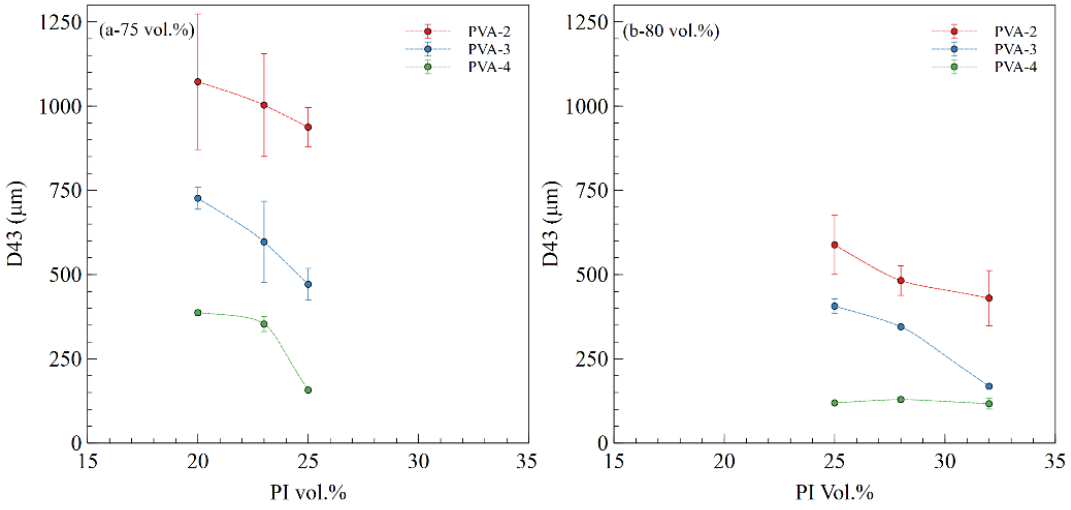

Figure 4.2. D_{43} for samples prepared under condition C1(100/800) for 2, 3, and 4 wt.% PVA; (a) 75% oil, (b) 80% oil. The results shown are based on the volume fraction of PI in the continuous phase at predetermined levels (from Table 4.1).

4.5.2 Effect of process conditions and viscosity modifier (PVA) on droplet size

Figure 4.3 illustrates the effect of the revolution number at three PVA percentages on the droplet size. It reveals that at constant PI vol%, increasing *nr* reduces the droplet size down to a minimum; however, the decline in D_{43} depends on PVA wt.%, oil volume, and rotational speed. For instance, in Figure 4.3-a, D_{43} is almost constant between 1600 and 2400 revolutions for PVA concentrations of 2wt.% and 4wt.%; whereas, at this revolution number for emulsion with PVA 3 droplet size decreases sharply from 600 to 250 microns.

It is also observed that the final value of D_{43} at *nr* of 2400 is a function of the viscosity ratio. PVA-4, which has the highest continuous phase viscosity shows the minimum D_{43} for all rotation speeds and oil volume content. Higher oil volume content leads to a minimum D_{43} even at the beginning of the process at 800 revolutions. These findings indicate that impeller speed is less important than the formulation since continuous phase viscosity determines the minimum droplet size. We mentioned earlier that deformation is the leading breakup mechanism in the viscous flow regime and the results shown here are going along that line.

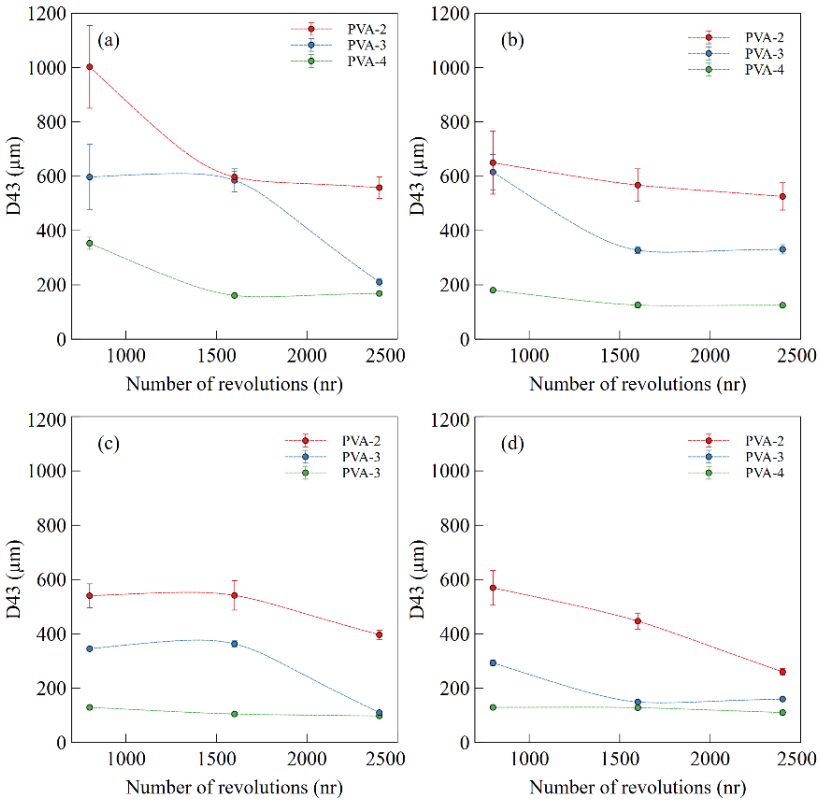

Figure 4.3. Evolution of D_{43} with respect to the revolution number while varying oil fraction, PI, and impeller speed; (a) 75% oil, 23% PI, 100 RPM; (b) 75% oil, 23% PI, 150 RPM; (c) 80% oil, 28 % PI, 100 RPM; (d) 80% oil, 28% PI, 150 RPM.

4.5.3 Effect of formulation on the viscosity of the continuous phase

In the methodology section, Table 3, we demonstrated that adding PVA changes the continuous phase conductivity, and alters the particle radius and zeta potential. The intrinsic viscosity of the continuous phase is calculated based on equation 4.6 and summarized in Table 4.3.

Figure 4.4 presents the effect of PI vol% on the continuous phase viscosity, which is calculated based on Eq 4.7 and Eq (4.8). In general, higher particle volume fraction increases the viscosity of the continuous phase, which is also amplified with higher PVA content. The presence of PVA exerts a more pronounced impact than the PI volume fraction. Specifically, for the same PI volume fraction, the viscosity of the continuous phase at PVA 4 wt.% is tenfold higher than that at PVA 2 wt.%.

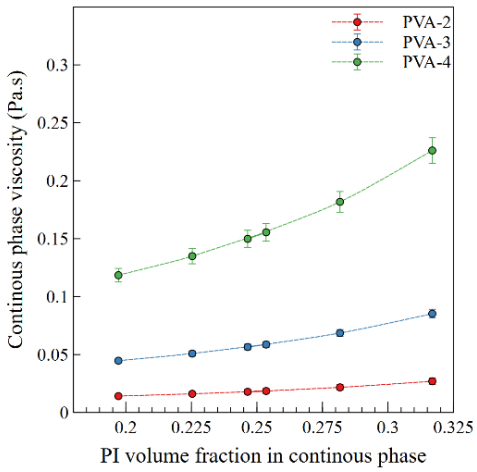

Figure 4.4. Effect of PI volume fraction and PVA content on the viscosity of continuous phase.

4.5.4 Effect of process conditions on the viscosity of the continuous phase

The effective viscosity of the continuous phase is obtained through the steps described in section 4.4.3.2.1. The evolution of the effective viscosity of the continuous phase (μ_c) is plotted as a function of the revolution number **(**Figure 4.5). The results are categorized into four groups with two values of oil volumes and rotation speed. Each point represents the average of continuous phase viscosity for different PI concentrations under constant conditions. The results show that the variation of viscosity with *nr* is not constant at each PVA concentration. The viscosity of PVA 2 wt.% is almost constant, whereas PVA 3 and 4 generally exhibit radical changes with a changing revolution number.

The increased viscosity observed for PVA 4 in Figure 4.5-c for 2400 revolutions can be attributed to the generation of very fine droplets and the formation of a strong network of continuous phases around these droplets. Conversely, the decrease observed in Figure 4.5-d for 2400 revolutions might be linked to particle contamination resulting from prolonged exposure to high shear. Contaminated particles are unable to stabilize oil droplets effectively, leading to excess oil observed in the emulsification process, consequently reducing the viscosity.

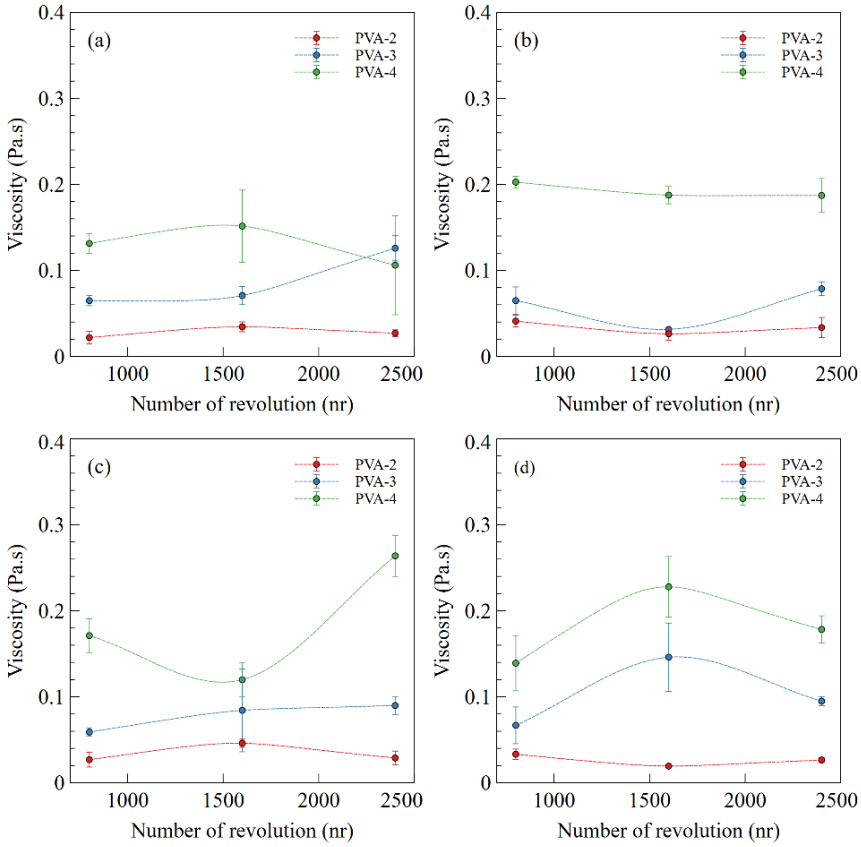

Figure 4.5.Viscosity of continuous phase as a function of *nr*; (a) 75% oil, 23% PI, 100 RPM; (b) 75% oil, 23% PI, 150 RPM; (c) 80% oil, 28% PI, 100 RPM; (d) 80% oil, 28% PI, 150 RPM. Note: The lines joining the data points in the graphs serve as a visual guide and do not represent any specific trend.

4.5.5 Size evolution of the remaining particles in the continuous phase

The size distribution (PSD) of the remaining (unattached) PI particles was measured after emulsification. We observed that certain groups of operating conditions generated comparable PI PSD, with peaks at similar particle size. Figure 4.6 presents the PSD of these remaining particles according to three distinct groups of conditions that we were able to differentiate. Generally, the three groups offer PSDs with two clear peaks. The first peak (P1, smaller sizes) is the same under all conditions and for all experiments. It corresponds to the individual particle size from provided by the supplier. The second peak shifts to smaller particle sizes with extended processing durations (higher *nr*), higher shear rates (higher RPM), or higher oil and PVA concentrations. This size reduction of the larger particles indicates that the processing conditions break down larger aggregates to generate finer particles.

To illustrate our observation, we use what we determined as Group 1 (G1). For that group, similar particle size distributions with the second peak at 4.2 μm were obtained for unattached particles from emulsions prepared under C1(100/800) conditions at three different PVA percentages. The combination of low to moderate PVA concentration and prolonged processing time (C3 and C6) shifts the PI PSD to a smaller particle size and the second peak occurred at 4.0 μm. The emulsions prepared with this particle size are placed in Group 2 (G2). Finally, a high-intensity process (higher RPM and *nr*) or higher viscosity (higher PVA and oil) yields finer particles with P2 at 3.7 μm; these emulsions are categorized in Group 3 (G3). Further emulsions, which were prepared under similar conditions also showed the same results. The details of formulations and processes are summarized in supporting information Table A.2.

The shift of PI PSD from G1 to G3 decreases the D_{43}, which is considered as a double gyration radius of the particle. From the Mastersizer data, the average of D_{43} for G1 to G3 is 3.69 ± 0.03, 3.41 ± 0.01, and 3.37 ± 0.03, respectively.

The reduction of particle size with higher PVA content is attributed to its role as an electrolyte in the continuous phase, increasing the zeta potential of particle dispersion and inducing a repulsive interaction that diminishes particle aggregation sizes[136].

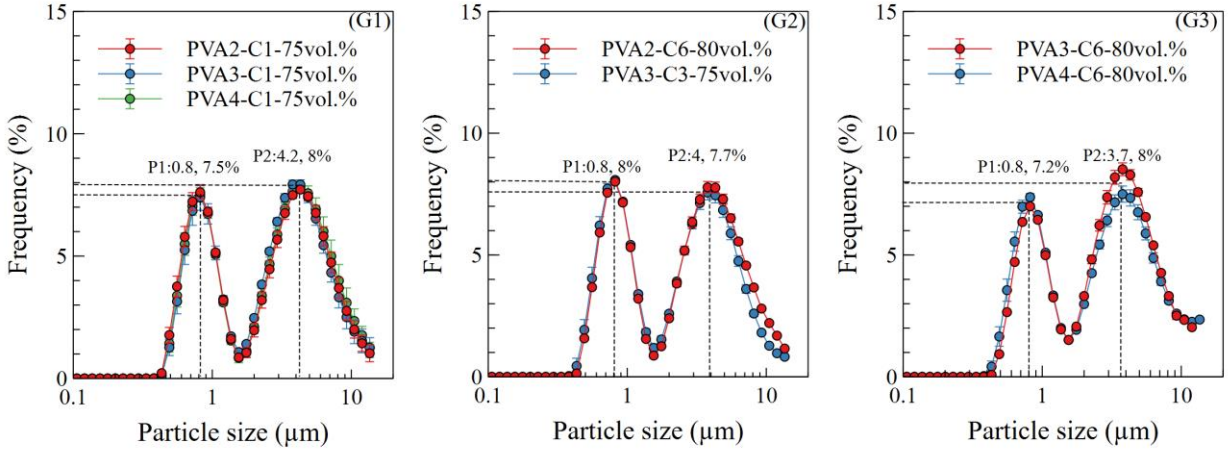

Figure 4.6. The size distribution of PI particles in three defined groups G1 (low to high viscous (PVA2,3,4 wt.%) low-intensity process(100 RPM or 800 *nr*)); G2 (Medium viscous (PVA 2, 3 wt.%) medium intensity process(150 RPM for PVA 2 wt.%, 100 RPM PVA 3)); G3 (high viscous (PVA 3,4 w.%, 80.oil vol.%) high intensity process (2400 *nr* and 150 RPM))

To further characterize the PI aggregates and quantify their compactness, we also measured the fractal dimension and structure prefactor using the correlation between the light intensity and the scattering angle (Eq(4.4)), which obtained through Mastersizer results. Based on the processing conditions and formulation, the same three groups as the ones based on PSD were investigated. Figure 4.7 shows the intensity versus the scattering angle for determined groups. The intensity is a linear function of the scattering angle with D_f corresponding to the exponents on q. It can be noted that group G2 exhibits the lowest D_f value, while group G3 has the highest. A lower D_f value indicates an important presence of non-spherical aggregates in the emulsification process. Under shear, the aggregates can orient and/or aggregate further depending on the emulsion formulation and process conditions. The aggregation explains the high sensitivity of continuous phase viscosity and the large variation of droplet size under shear.

Table 4.4 shows a decrease in the structure prefactor value from G1 to G3, suggesting the reduced compactness of aggregates in G3. A lower compactness enables PVA solutions to penetrate, forming a network with aggregates. This strengthens the continuous phase, facilitating the breakdown and the stabilization of finer droplets. It is worth noting that the values of D_f and k_g are aligned with those found in references dealing with micro-spherical latex[137].

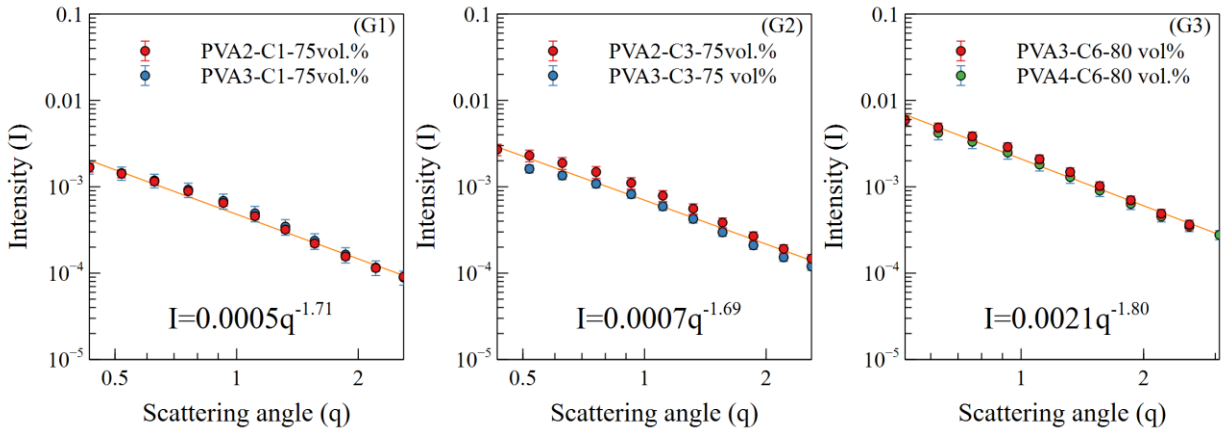

Figure 4.7 Light intensity (I) versus scattering angle (q) for samples in the three groups

Table 4.4. Grouping of particles following their characterization based on Eq 4.5

	Conditions [a] **RPM/nr/oil vol%/PVA wt.%**	***Df***	***Rg (μm)***	***np***	k_g
G1	100-150/800-1600/75/2	1.71	1.85±0.015	175±4	9.21±0.25
G2	100/2400/75-80/3	1.69	1.70±0.005	138±1	8.6±0.08
G3	150/1600-2400/80/4	1.80	1.67 ±0.015	129±3	6.99±0.22
a : The details of conditions were summarized in supporting information in **Table A.2**					

4.5.6 Scanning electron microscopy (SEM) of particles

To visualize the effect of process conditions on the particle size and fractal dimensions, SEM images of freeze-dried diluted particles were obtained. Although water evaporation during freeze-drying affects the interaction between PVA and PI particles, comparing the three different processes provides a clear understanding of the particles' shape and size. For consistency, the details of statistical analysis and additional images are provided in the supporting information (Appendix A.6); a few images for illustrating the effect of PVA on the particles' morphology are shown in Figure 4.8.

A comparison between Figure 4.8-a and Figure 4.8-b illustrates that PVA forms a network that surrounds each particle. The surface morphology of both pure and PVA-modified particles as depicted in Figure 4.8-c and Figure 4.8-d, confirmed that each PI particle comprises hundreds of nanometer-size particles. This structure allows PVA chains to penetrate due to its porosity.

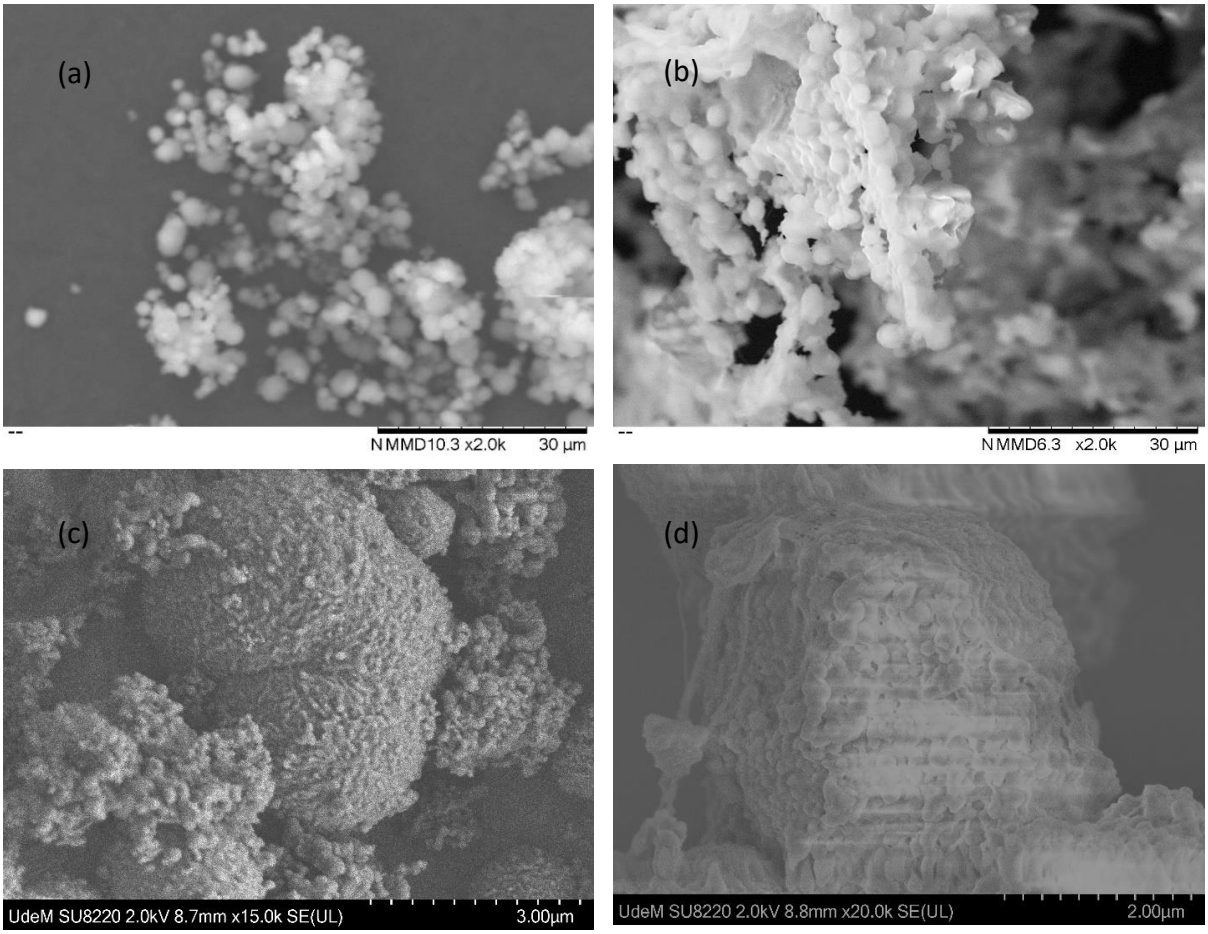

Figure 4.8. SEM image of a) pure PI particles and b) PVA-PI particles; ultra-high resolution SEM c) pure particles and d) PVA-PI particles

Table 4.5 shows that the particle size decreased by higher PVA%, prolonged emulsification process, and higher rotation speed; from G1 to G3. The aspect ratio of particles which is correlated to the fractal dimension, is also decreased by these conditions. These findings confirmed our results obtained from the Master sizer showing that particle size reduced through these process conditions from G1 to G3.

Table 4.5. Statistical analysis of microscopic image

Process conditions	**Size (µm)**	**Aspect ratio**
G1	3.34±0.81	1.26±0.16
G2	2.68±0.86	1.15±0.11
G3	2.29±0.45	1.10±0.1

4.5.7 Correlation of the capillary number with the viscosity ratio

Figure 4.9 compares the fitting curve of *Ca* versus the viscosity ratio *p*. The left part (a) is obtained based on the formulation approach and the torque approach is on the right (b). In Figure 4.9-a all samples with constant PVA-oil formulation exhibit constant *p* value, as the viscosity was solely calculated based on formulation. The calculation of *Ca* is also based on this viscosity. The low regression coefficient (R^2=0.38) observed in Figure 4.9-a indicates the limitation of this approach to accurately estimate *Ca*. It is worth mentioning that for both Figure 4.9-a and Figure 4.9-b, the interfacial tension decreases slightly with increasing PVA concentration. The interfacial tension between silicon oil (100 cSt) and the three PVA solutions is provided in the supporting information Table A.1.

The viscosity of the continuous phase, estimated solely on the formulation (Section 3.3), leads to a poor correlation between *p* and *Ca*. The data in Figure 4.9-a fits on Ca= -0.005log(p)+0.0165 with R^2 equals to 0.38, while in Figure 4.9-b, by categorizing data, the correlation matches measurements with R^2 equals to 0.93, and 0.8 was obtained for G1 and G3, respectively. From G1 to G3 the logarithmic slope increased from -0.01 to -0.006, and their intercept decreased from 0.032 in G1 to 0.02, and 0.013 in G2 and G3, respectively. The approach used here clearly helps represent the behavior of the concentrated emulsions and allows for a fine representation of the droplet size obtained in the concentrated conditions.

To gather all conditions together, we use the same three groups as presented in 4.5.5. The process conditions and formulation were summarized in Table A.2 of the supporting information. In Figure 4.9-b, both *nr* or RPM and PVA or oil concentration increase from G1 to G3. These conditions lead to smaller PI particles consequently increasing the emulsion's capacity to stabilize droplets. Due to smaller individual particles/agglomerates with the same overall PI vol%, more particles are available for stabilizing finer droplets which results in a shift of the Ca-p curve towards lower values.

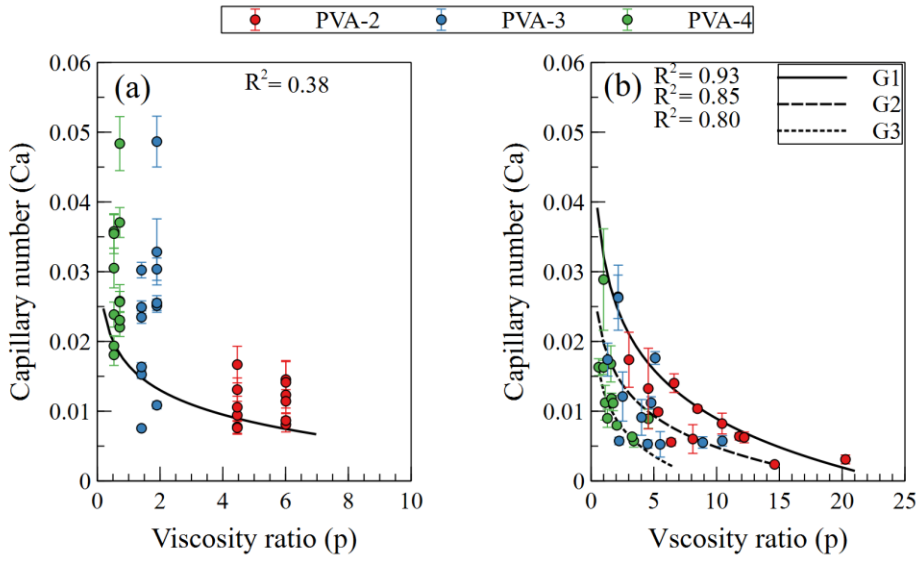

Figure 4.9. Capillary number vs. viscosity ratio (p). (a) calculated based on formulation-approach viscosity; (b) calculated based on torque-approach viscosity.

4.5.8 Estimating the droplet size based on the capillary number and viscosity ratio

The droplet diameter (d) was estimated using the following equation by substituting the fitting curve parameters obtained from section 4.5.53.6 and their corresponding viscosity ratio (p):

$$Ca = a\log(p) + b = \frac{\eta\dot{\gamma}}{2\gamma_{ow}/D_{43}} \tag{4.11}$$

Figure 4.10 compares the estimated and measured droplet sizes. In Figure 4.10-a, values are estimated solely from the formulation while in Figure 4.10-b, values are determined using the process viscosity obtained from the torque measurements. The variability is clearly reduced when predicting the droplet size using the process viscosity (torque) compared to the size predicted using the formulation approach. This observation reveals that variations in factors such as the revolution number, rotation speed, PVA wt.%, and oil concentration affect the ratio of viscous force to interfacial tension (Ca). Therefore, to accurately determine the Ca number and droplet size it is imperative to incorporate the real viscosity of the continuous phase.

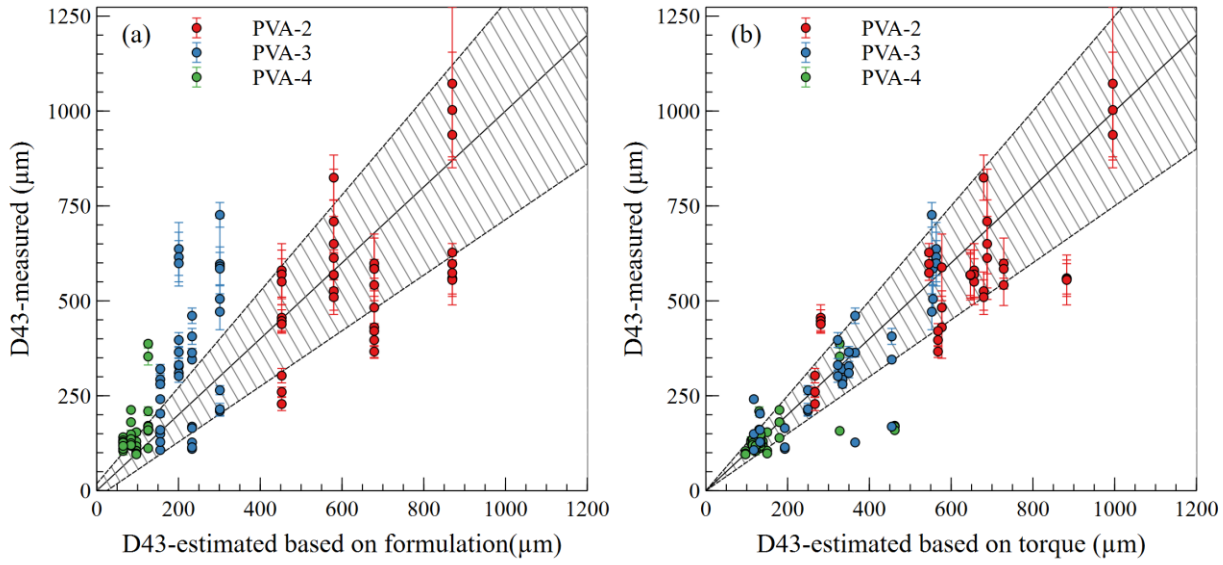

Figure 4.10. Measured droplet size vs. estimated droplet size; (a) estimates based on formulation, (b) estimates based on torque measurement. The hatched area represents the ±25% variation from the line of perfect experimental to estimated match.

4.6 DISCUSSION

We demonstrate that HIPPE can be generated with a controlled droplet size selected *a priori*. We take advantage of the highly viscous systems provided by high concentrations of dispersed phase to reduce the droplet size instead of using high-intensity mixers. The results also reveal that the PVA concentration, the revolution number (*nr*), shear rate, and oil volume all altered the viscosity of the continuous phase. Our results indicate that assuming a constant viscosity of the continuous phase over different process conditions might lead to prediction errors. It is rather crucial to consider the continuous phase viscosity variations in high internal phase emulsions.

Based on the literature, the critical capillary number is a function of the viscosity ratio (p) and the type of flow. In a simple shear flow, Ca decreases with p until it reaches a minimum value (0.5-1) at $0.1<p<1$. After this minimum, it increases sharply. It is generally agreed that droplet breakage is impossible at $p>3.5$ within a simple shear flow[78]. Conversely, in elongational flow, Ca decreases with p and it reaches its minimum (0.1-0.5) at $p>10$[138][139]. In such flow, droplet breakage is considered feasible at all p ranges.

There is a lack of knowledge for estimating *Ca* in highly concentrated emulsions, especially emulsions where droplets are covered by particles as is the case in HIPPE. The calculated *Ca* values decrease from 0.03 to 0.005 when the *p-value* increases from 1 to 20. Drops breakage can therefore originate from a combination of simple shear and elongational flows. This is the very nature of tank mixing where simple flow fields (shear and/or elongational) do not exist alone but in combination and at various degrees. Considering that emulsification in HIPPEs occurs in the presence of very high (overall) viscosity, in the laminar regime, it is reasonable to assume that most of the droplet rupture will originate from elongation. The fact that drops size reached small values, even at high viscosity ratios, is an additional argument in favor of a generally elongational flow field in the tank.

The *Ca* results obtained for HIPPEs are much smaller than the minimum *Ca* reported for elongational flow, 10 times smaller than Grace's results[78]. This might be attributed to the high interaction between droplets in the HIPPE emulsions and the stabilization process, which involves particle absorption. The *Ca-p* curves shift to the lower amount by decreasing the particle size. From G1 to G2 finer particles stabilize smaller droplets, leading to lower *Ca* at a fixed viscosity ratio

The structure of the particles at all formulations and process conditions plays a crucial role in determining the capillary number. From G1 to G3 in Figure 4.9, *Ca* shifts to a lower value by decreasing the k_g and R_g. It reveals that the lower compactness of aggregates (k_g) enhances the penetration of PVA chains into the aggregates, thereby increasing droplet stability. Additionally, using finer particles, smaller *Rg*, provides more coverage potential for stabilizing small droplets. Consequently, this leads to the formation of finer droplets at a lower *Ca*.

The lowest fractal dimension (D_f) belongs to G2 (Table 4.4), which means that the aggregated structure is far from the spherical likelihood. It is reported that suspension containing plate-like aggregates exhibits complex non-Newtonian behavior owing to the potential of clustering or orientations[81]. Therefore, the continuous phase containing this type of particle is more sensitive to shear rate.

On the other hand, the intermediate *kg* value in G2 allows PVA chains to penetrate. The penetration of PVA chains leads to the clustering or networking of particles depending on the process conditions. So, the capillary number of the emulsions stabilized with these particles fits into the G2 curve, which lies between the other curves with the largest and finest particles.

In conclusion, the structure of the particles, which is determined by D_{43}, D_f, and K_g, is the key factor for distinguishing three curves in the *Ca*-*p* graph. The finer and less dense the particles, the finer droplets are obtained, resulting in a shift of the *Ca*-p curve to a smaller value.

4.7 CONCLUSION

The droplet size can be tailored in HIPPEs through formulation and process conditions. It showed that the evolution of particle aggregation structure, which is influenced by the revolution number of the impeller, the shear rate, and varying PVA concentrations, significantly impacts the final droplet size. Furthermore, this study highlights the fact that the capillary number is a function of the effective viscosity of the continuous phase, and it changes with process conditions, emulsification time, and formulation. As a result, by considering both particle structure and the effective viscosity of the continuous phase, a correlation of *Ca* vs *p* was obtained for three groups of emulsions. Using these curves, one can estimate the required continuous phase viscosity and process conditions to achieve the desired droplet size.

The use of the effective viscosity of the continuous phase helps determine accurate estimates of the capillary number (*Ca*). The effective viscosity of the continuous phase obtained through in-situ torque monitoring during the emulsion preparation reveals that both formulation and the process impact the viscosity of the continuous phase. The torque in-situ technique is beneficial for inverse engineering approaches, to estimate the correct continuous phase viscosity or shear rate to achieve the desired droplet size.

The fractal dimension (D_f), compactness of particles (k_g) and particle radius (R_g), which are affected by PVA content, process conditions and emulsification time, play crucial roles in explaining the final droplet size at the conditions explored. The continuous phase's effective viscosity, impacted by particle shape and size, supports the estimation of the capillary-viscosity ratio, leading to a more precise prediction of droplet size.

In summary, this investigation offers a better understanding of the relationship between capillary number-viscosity ratios, particle properties, and processing parameters. The ability to modulate emulsion characteristics through the adjustments of key factors provides valuable insights for the design and optimization of emulsion systems with tailored properties.

4.8 ACKNOWLEDGMENTS

The authors gratefully acknowledge financial support by the “Natural Sciences and Engineering Research Council of Canada” (NSERC) and “Optimizing Power Skills in Interdisciplinary, Divers & Innovative Academic Networks” (OPSIDIAN), which is also partly founded by NSERC

CHAPTER 5 ARTICLE 2: SCALE-UP OF HIGH INTERNAL PHASE PICKERING EMULSION IN STIRRED TANK

Mina Saghaei[1], Edith Roland Fotsing[2], Annie Ross[2], Louis Fradette[1]*

1.Department of Chemical Engineering, Polytechnique Montréal, Montreal, Quebec H3C 3A7, Canada
2.Department of Mechanical Engineering, Polytechnique Montréal, Montreal, Quebec H3C 3A7, Canada

Submitted March 7, 2025 to Chemical Engineering Research and Design

5.1 Chapter's connection to the main objective

This chapter covers article 2, where we established an appropriate scale-up exponent for HIPPE production in the laminar regime. We systematically investigated the effects of hydrodynamic criteria that remain constant throughout the emulsification process while scaling up by a factor of 3000. Our finding revealed that the most appropriate hydrodynamic criterion for maintaining consistent droplet size across scales is constant power per volume in the laminar regime. These findings address the challenges and knowledge gaps associated with the mixing of complex HIPPE and offer valuable insights for versatile industrial applications.

My contribution to the articles includes conceptualization, methodology, experimentation, analysis, writing original draft, and literature review.

5.2 Abstract

This study investigates the effect of the scale-up exponent on droplet size in high internal phase Pickering emulsions (HIPPEs) within the laminar regime. Through systematic analysis, we demonstrate that a scale-up exponent of zero, which maintains a constant shear stress, results in consistent droplet size across all scales. We explore the relationship between droplet size, power-law index, consistency index and Metzner-Otto constant, establishing a correlation that accurately predicts the required power per unit volume for achieving the desired droplet size.

Further analysis of the relationship between D_{32} and specific energy reveals that droplet size decreases with increasing specific energy until reaching an equilibrium droplet size. Beyond the equilibrium point, D_{32} correlates with power per volume (P/V). These two curves can serve as a

predictive tool for estimating the required *P/V* and revolution number to achieve target droplet sizes. Our findings suggest that emulsion viscosity, rotational speed, and revolution number are crucial parameters for controlling droplet size, thereby optimizing HIPPEs for industrial-scale applications.

5.3 Keywords:

Solid stabilized emulsion, Industrial-scale design, stirred vessel, Helical ribbon impeller, HIPPEs' rheology, Estimating energy dissipation rate.

5.4 Highlights:

- ✓ A scale-up exponent of zero ensures the constant droplet size across scales in HIPPEs.
- ✓ Rheological characteristics of emulsion correlate with droplet size.
- ✓ Required power per volume for target droplet size is estimated from emulsion rheology.
- ✓ Droplet size scales with energy and power per volume.

5.5 Introduction

Solid stabilized emulsions (SSE), commonly referred to as Pickering emulsions, have found widespread applications across numerous industries in the last twenty years, after being disregarded for decades from the first introduction by Pickering [14]. Application sectors include the food, where starch, soy protein and other substances act as interface-stabilizing agents [26][42]; polymerization process, where nanoparticles stabilize the polymeric phase[140]; pharmaceuticals, where chitosan-based emulsion is used for drug delivery [20]; cosmetics, where the particles stabilize lipophilic actives for skin care products [27]; and oil industries where SEEs are used in crude oil production and treatment [141]. This widespread number of applications arises from the properties of the particles involved in stabilizing the interface; particles can be tailored and adapted in each case, providing distinct features in the resulting emulsion structure [28][142][20][143][123].

Specifically, HIPPEs which are characterized by internal phase volume content exceeding 75 vol.%, have gained broad usage in diverse applications in recent years. For example, they find applications in 3D-printed bone tissues, self-healing materials, super absorbents and catalysts [65]. The pore structure, permeability and mechanical properties of HIPPEs can be tailored by adjusting

the internal phase volume fraction, the particle size, the interface chemistry and the particle concentration.

By increasing the dispersed phase volume and decreasing the droplet size, the viscosity of HIPPEs increases sharply [144][64][135]. These emulsions exhibit different rheological behaviors during mixing, attributed to their complex morphology and their dependence on droplet size. HIPPEs may demonstrate shear-thinning behavior [19] when low shear forces are applied, allowing the emulsion to slide within the shear field without droplet breakage. Conversely, they may exhibit shear-thickening behavior [62] under higher shear forces that result in droplet breakage. Additionally, rheopectic behavior [145] can occur when, at a constant shear rate, droplet breakage over time leads to a gradual increase in viscosity.

Despite extensive research on Pickering emulsions' formulation [32][49], few studies investigated their processing conditions [20]. Albert et al. reviewed conventional emulsification processes that can be used in Pickering emulsification, outlining the rotor-stator mixer and high-pressure homogenizer as the most viable options for SSE industrialization [20]. These mixers consume elevated specific energy, and potential issues such as particle destruction during processing, final emulsion polydispersity and temperature increase of the emulsion were identified as processing challenges. Temperature management is a common processing limitation, particularly in the preparation of viscous emulsions [20]. The review did not provide insights into the processing of very concentrated emulsions.

To process emulsions in the laminar flow regime, where the viscosity of the fluid(s) is a hundred times higher than that of water, close-clearance impellers generally show good performance in achieving suspension of particles within liquids [75]. Among the well-known impellers, the Paravisc™, the helical ribbon, the double helical ribbon (DHR), the Maxblend™ and the anchor impellers, the DHR is the most energy-efficient one for blending two immiscible liquids [77]. This performance is due to its shortest blend time for a given power input [77].

According to literature, all mixing scale-up procedures in both turbulent and laminar regimes begin by maintaining a constant hydrodynamic properties as the scaling criterion. These hydrodynamic properties include power per volume, mixing time, off-bottom suspension speed, maximum shear at the impeller tip, and equal viscous/inertial force [21]. By ensuring geometric similarity and using

a constant formulation, these criteria establish simplified correlations between rotational speed (*N*) and impeller diameter (*D*).

For example, in the laminar regime, maintaining constant power per volume results in $N_2=N_1$ [77]. In the turbulent regime, maintaining constant power per volume leads to the relationship $N_2^3D_2^2=N_1^3D_1^2$ [21]. Similarly, maintaining constant tip speed results in $N_2D_2=N_1D_1$, and constant Reynolds number leads to $N_2D_2^2=N_1D_1^2$. So, in general, to extrapolate the rotational speed in similar tanks, from scale1 to the scale 2, the following equation is used by considering a scale up exponent of α [21]:

$$N_2 = N_1 * \left(\frac{D_1}{D_2}\right)^{\alpha} \tag{5.1}$$

A value of 0 represents constant speed conditions applicable for constant mixing time and constant power per volume in the laminar regime [77]. A value of 1 is recommended for maintaining constant tip speed for simple blending, as well as shear-controlled droplet size [21]. In the turbulent regime, for constant energy dissipation rate, a scale-up exponent of 0.67 [21] is applicable for turbulent droplet dispersion. Finally, for constant Reynolds number (*Re*), a scale-up exponent equal to 2 is recommended [21].

For highly concentrated emulsions (not stabilized by particles), scaling up using a constant Reynolds number as the criterion has proven ineffective. Maintaining constant *Re,* while scaling up, decreases the rotational speed from 1600 RPM at 100 mL to 780 RPM at 685 mL [90]. This reduction in rotational speed provides insufficient shear to break droplets, ultimately resulting in undesirable larger droplet sizes at the larger scale [90]. Gingras produced emulsions through the inline SMX and helical static mixer [91] and found that the average droplet size scales with the specific power once equilibrium is reached; before reaching equilibrium, the droplet size scales with the specific energy. Meanwhile, May-Masnou et al. regarded rotational speed and power per unit volume (*P/V*) as scale-up invariants [92][93], applying the scale-up exponents of 0 and 0.67 [92][93]. These studies used emulsifiers to stabilize small droplets (under 20 microns) at a speed of 500-1800 RPM with pitched blade impellers, which operated outside the laminar regime.

In the case of solid stabilized Pickering emulsions, Al-Haiek et al. revealed that the scale-up factor in medium internal phase content (<50%) emulsions, operated in the turbulent regime) should be between 0.67 and 1. The reason for such values arises from the combination of two processes at

once, the first being a simple blending of two liquids, that require alpha = 1 for scaling up and the second is the solid suspension [56], which require alpha = 0.67 [21].

The most important learning from Al-Haiek's work on scale-up and the processing of concentrated emulsions is the list of parameters to consider due to the combined processing taking place all at once. These parameters cover the minimum rotational speed for suspending particles [56] and droplets [94], the capacity for the particles to cover the interface effectively and sufficiently to ensure drop stability [48], and the capacity of the mixing system to generate interface, i.e., produce drops [48].

To sufficiently suspend particles in the liquids inside stirring tanks, the rotational speed must exceed the just suspended speed (N_{js}). Beyond this threshold, fewer particles are available for droplet coverage [48], leading to insufficient coverage [49], and the coalescence of partially covered droplets, resulting in a non-uniform emulsion. Additionally, sufficient shear stress must be applied to ensure adequate droplet breakage and interface generation [48].

Despite an extensive body of literature published on droplet size prediction in emulsions using various impeller designs, and operating in laminar and/or turbulent flow regimes, there remains a knowledge gap regarding the scale-up rules applicable to high internal phase Pickering emulsions (HIPPEs). These emulsions pose specific challenge which arises due to the combination of high viscosity of these emulsions and the need for effective particle suspension inn the laminar regime during the emulsification process.

Our research aims to address this gap by identifying the optimal scale-up rule for HIPPEs. Given that the emulsions process involves both particle suspension and liquids dispersion under highly viscous conditions, the double helical ribbon impeller is particularly well-suited for this process. This work focuses on developing methods to control and estimate droplet sizes before and after equilibrium state, ultimately achieving consistent droplet sizes in tank scales from 1 to 3000 times in scale.

5.6 Material and Methods

A systematic investigation evaluated the effect of the scale-up exponent and revolution number on the droplet size in HIPPEs with a constant formulation. The study commenced by determining the optimal scale-up factor for HIPPEs, exploring three scale-up exponents for 0.01 -30 L scales. The most appropriate exponent was selected based on the consistency of droplet size across different

scales, and the findings were validated on a larger scale. Power consumption during emulsification was measured through in situ torque measurements and compared to the estimated power derived from the viscous shear stress. Finally, the correlation between power and energy consumption with the droplet size was analyzed.

5.6.1 Material

The oil phase consisted of pure silicone oil with a viscosity of 200 cSt at 25 °C (Clearco Products Co. Inc., USA). The oil phase, always constituting 80 vol.% of the total volume, was injected from the bottom of the tank at a controlled speed. To neutralize the potential impact of the oil injection rate and mitigate the risk of phase inversion, which may occur with fast injection relative to the rotational speed, a constant ratio between the oil injection rate and rotational speed was maintained. Additionally, it was crucial to complete the oil injection process within the same proportion of the total emulsification time across all processes and scales. Consequently, the oil injection speed was adjusted based on the total oil volume, rotational speed and initial revolution number. The injection speed for each scale and rotational speed was calculated using the following equation.

$$Injection\ speed = \frac{Voil * N}{800} \tag{5.2}$$

800 revolution number is the minimum revolution number to reach the periodic emulsion which obtained through preliminary tests. The aqueous phase was prepared using deionized water in which polyvinyl alcohol (PVA) in solid powder form (Alfa Aesar, US) was dissolved with 3 wt%, which is a medium concentration that we used in our previous work (2-4 wt% [146]).

The particles used for all experiments were made of Polyimide (PI) with a primary diameter of 4 microns (P84NT, Evonik Fibers GmbH). The particle concentration was adjusted to ensure sufficient coverage of the expected smallest oil droplet, leading to a PI particle-to-oil weight ratio of 0.1, which is a medium ratio based on our previous work [146].

5.6.2 Experimental methods

5.6.2.1 Emulsification setup

Emulsification was performed using a double helical ribbon (DHR) at four different scales while maintaining geometrical similarity. The impellers were fabricated using 3D printing with polylactic

acid (PLA). The detailed geometrical characteristics of the emulsification setup are presented in Figure **5.1**and Table **5.1**.

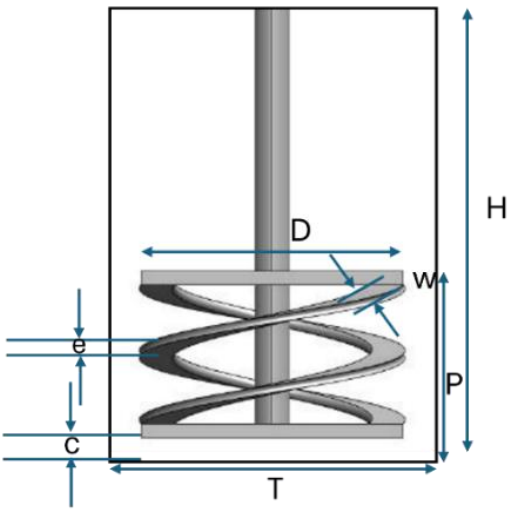

	D/T	w/D	e/D	P/D	c/D	H/D
Similar geometry	0.94	0.15	0.03	0.67	0.03	1.6

Figure 5.1. Schematic impeller and tank dimensions

Table 5.1. Scales and the impeller diameter

	Scale1 (Small; S)	Scale 2 (Medium; M)	Scale 3 (Large; L)	Scale 4 (Giant; G)
Total volume (mL)	10	100	1000	30000
Diameter (cm)	2.7	5.5	12.5	34.5

5.6.3 Droplet measurements

Droplet sizes were measured using dynamic laser diffraction (DLS) with the Mastersizer 3000 (Malvern Panalytical, UK). A sample of the emulsion at each *Nr* was taken and diluted in the 300 mL vessel of Mastersizer which contains PVA 3 wt.%. In the size distribution graph of the preliminary test, two peaks are observed: a smaller peak below 10 microns, corresponding to the particles, and a larger peak ranged from 20-50 microns, corresponding to the droplets. In all main measurements, the effect of particle on the overall averaged droplet size was eliminated by limiting

the size domain to 10-3000 microns. The same procedure was employed for all samples to avoid any potential biases. Among the data provided by the Malvern software, the Sauter mean diameter (D_{32}) was reported as the most representative measure of the droplet size under each process condition. It is defined as the ratio of the sum of the cubic power of each droplet size (denoted by index *i*) multiplied by its percentage (n_i), to the sum of the square of each droplet size multiplied by its percentage:

$$D_{32} = \frac{\sum n_i D_i^3}{\sum n_i D_i^2} \tag{5.3}$$

5.6.4 Power measurements

The power consumed during each emulsion preparation was recorded via in-situ torque measurement. Power was calculated using the following equation:

$$P = 2\pi N\Gamma \tag{5.4}$$

where Γ (N.m) represents the torque, N (1/s) is the rotational speed of the impeller, and P (W) is power. Time integration of the power provides an experimental value of the energy consumption during the emulsification process.

5.7 Theory and calculations

5.7.1 Selection of scale-up exponent

As previously discussed, constant Reynolds number lead to weak particle suspension at larger scales; consequently, droplets were different in both scales.[56] In this study, we assumed that the HIPPE production process occurs in a laminar regime due to its high viscosity, or in a transitional regime when high rotational speed and large impeller are employed. So, the constant power per unit volume was selected as a scale-up criterion for both flow regimes. Additionally, a constant tip speed which leads to constant shear at the edge of the impeller was employed.

Three scale-up exponents were evaluated to determine the most appropriate exponent for HIPPEs based on the evolution of droplet size over the revolution number. The first exponent was derived from the condition of constant power per unit volume in the laminar flow:

$$P = K_p \mu N^2 D^3 \tag{5.5}$$

where K_p is the ratio of power number ($Np = \frac{P}{\rho N^3 D^5}$) to the Reynolds number, and μ is the emulsion viscosity.

Considering that the volume of a cylindrical tank is in direct relation with D^3. So:

$$\frac{P}{V} \sim K_p \mu N^2 D^0 = const \tag{5.6}$$

It means that the exponent α is 0 in the following equation

$$N_2 = N_1 * \left(\frac{D_1}{D_2}\right)^0 \; i.e \; N_2 = N_1 \tag{5.7}$$

The second option is to work at constant power per unit volume, where the Reynolds number ranges between 10 and 1000. In this case, the power per unit volume is

$$\frac{P}{V} = N_p \rho N^3 D^2 \tag{5.8}$$

where Np is the power number and ρ is the emulsion density. This equation leads to the exponent α equals 2/3 and the scale-up expression becomes:

$$N_2 = N_1 * \left(\frac{D_1}{D_2}\right)^{\frac{2}{3}} \tag{5.9}$$

This approach (Equation 5.9) is normally applicable to the transient flow regime. At the beginning of the scale-up selection, the type of flow regime is unclear, so all potential approaches, including laminar flow, transitional flow and turbulent flow should be considered.

The third scale-up rule is to maintain a constant tip speed between scales, which results in exponent α equal to 1:

$$N_2 = N_1 * \left(\frac{D_1}{D_2}\right)^1 \; i.e. (ND)_2 = (ND)_1 \tag{5.10}$$

In the laminar flow regime, the DHR is assumed to produce the same amount of fluid motion per revolution, regardless of the scale. Consequently, the fluid motion history is identical after similar revolution number (*Nr*), as the deformation history remains the same. This suggests that it is the total deformation that governs droplet size and distribution, rather than just the level of shear or emulsification time [146]. Based on this principle, we consistently applied five pre-established

numbers of revolutions (*Nr*: 800, 1600, 2400, 3200, 4000), calculated as the product of the impeller speed (*N*) and the processing time. As soon as the oil fraction goes above 40 or 50% (and long before reaching 75 or 80%), the viscosity of the emulsion increases sharply. This increase is recorded using the in-situ torque meter. Once these viscous conditions have been reached, the flow regime becomes laminar, as proven by the torque curve over *N* (see result section). We employed three rotational speeds, selected for their ability to ensure sufficient suspension capacity of the particles within the tank. A full factorial design of experiment was employed for all factors and levels; resulting in 45 runs with 3 repetitions for each scale; details are presented in Table 5.2.

Table 5.2. Factors and levels for process conditions

Factors	Level1	Level2	Level3	Level4	Level5
N_{ref}[a]	100	150	200		
α	0	0.67	1		
Nr	800	1600	2400	3200	4000

a: N_{ref} is the rotational speed employed in the smallest scale

5.7.2 Emulsification power from the viscosity and shear rate

The breakage capacity of the mixing system during HIPPE emulsification in the laminar regime can be characterized by the deformation rate, estimated using the Metzner-Otto relation [77]. This relation provides a basis for estimating the power consumption based on viscosity and rotational speed [77].

$$P/V \cong K_p \mu N^2 \tag{5.11}$$

Here, K_p is the power constant, obtained from power curve of DHR impeller for a Newtonian fluid at *Re=1*. The power curve is a plot of power number (*Np*) versus Reynolds number (*Re*). The power

number is calculated based on the torque (Γ), emulsion density (ρ), rotational speed (N), and impeller diameter (D):

$$Np = \frac{P}{\rho N^3 D^5} = \frac{2\pi N\Gamma}{\rho N^3 D^5} \tag{5.12}$$

The Reynolds number is calculated as:

$$Re = \frac{\rho N D^2}{\eta} \tag{5.13}$$

where η is the viscosity of Newtonian fluid. For the impeller geometry used in this work (DHR), the $K_p$value was determined experimentally and is constant at 324 across all scales.

The emulsion viscosity (μ) was obtained from the power-law equation:

$$\mu = k\dot{\gamma}^{n-1} \tag{5.14}$$

where n is power-law index, k is the consistency index, and $\dot{\gamma}$ is the effective shear rate, expressed as:

$$\dot{\gamma} = K_s N \tag{5.15}$$

where K_s is Metzner-Otto constant [77]. Substituting Equation (5.15) into Equation (5.14), the viscosity Equation becomes:

$$\mu = kK_s^{n-1}N^{n-1} \tag{5.16}$$

The value of kK_s^{n-1}, and n were determined experimentally. A plot of torque-to-rotational-speed ratio (Γ/N) versus rotational speed (N) was recorded as N increased. The n and kK_s^{n-1} values were obtained from the exponent and slope of the (Γ/N) versus N curve [147].

$$2\pi N\Gamma = K_p \mu N^2 D^3 \tag{5.17}$$

$$\frac{\Gamma}{N} = \left(\frac{K_p D^3 k K_s^{n-1}}{2\pi}\right) N^{n-1} \tag{5.18}$$

By substituting experimentally determined values of kK_s^{n-1}, and n into Equation (5.16), the viscosity of emulsions at each rotational speed were calculated. Finally, substituting the viscosity and Kp into Equation (5.11) allows the required power for all scales to be estimated.

5.8 Results

5.8.1 Effect of scale-up on droplet size

Figure 5.2 illustrates the evolution of the average D_{32} with the three scale-up exponents considered in our work. The curves in each graph cover 5 revolution number (*Nr)*, three different reference rotational speeds, and the three tank sizes used (S, M, L). The overall trend is that D_{32} decreases with the revolution number until it reaches a minimum plateau value. The time (or *Nr*) to reach the plateau value, the drop size value on the plateau, and the change in the droplet size during processing are all determined by the process conditions. The final D_{32} plateau value is the same for all scales, regardless of N_{ref}. In fact, a higher initial N_{ref} results in a smaller initial D_{32} (at Nr=800), and diminishes the rate of decrease in D_{32} over *Nr*, with the final D_{32} being the same when *Nr* is large enough to reach the plateau value.

Looking closer at the first row of graphs in **Figure 5.2** where the scale-up exponent α equals 0 (i.e. constant rotational speed across the three scales), a very tight overlap of the droplet evolution and droplet size is observed across all three scales, and for each reference rotational speed (N_{ref}. 100, 150, and 200 RPM). On the lower rows of **Figure 5.2**, as the scale-up exponent α increases to 0.67 and 1.0, the curves overlap is gradually broken and the three curves spread more and more apart with increased α values. An increase in exponent α (from 0) decreases the rotational speed as the scale grows. The decrease in rotational speed results in lower droplet breakage capacity, which in turn leads to the formation of larger droplets. As a result, the largest droplet size was obtained at α equal to 1 and scale L (largest).

The similarity in droplet size suggests that a scale-up exponent of zero, i.e. scaling up at constant rotational speed, is the most appropriate method to retain the emulsification performance across scales when processing HIPPEs with a constant formulation. Working with geometrically similar systems at all scales requires keeping a constant rotational speed to retain the same emulsification capacity as the scale increases. Derived from this observation at the three scales, it appears that the key factor in controlling the droplet size during scale-up is regulating the stress rate or power per volume (*P/V*). This parameter is thoroughly analyzed across all three scales and process conditions in the next section.

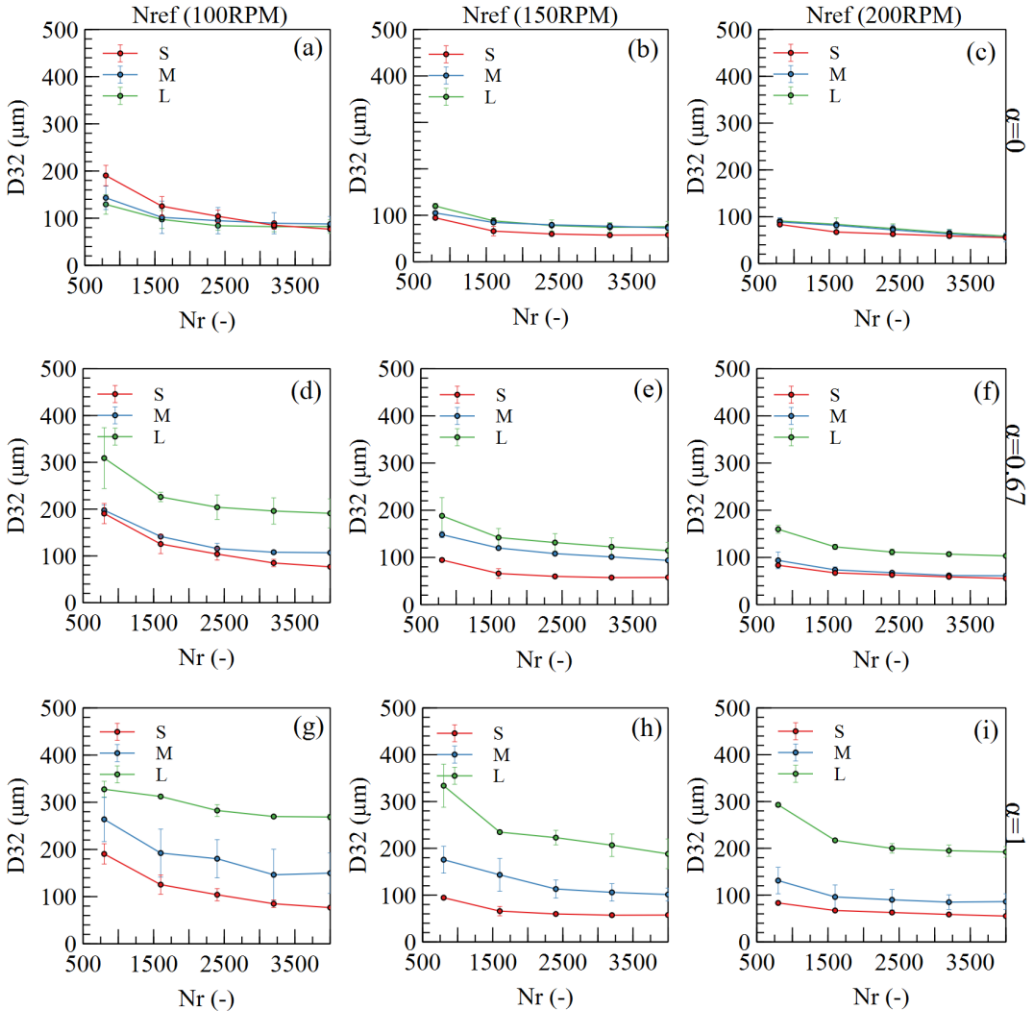

Figure 5.2. The evolution of droplet size over the revolution number (Nr) for three scale-up exponents and three system sizes (S, M, L). (a), (b), (c) α=0 (N2=N1). (d), (e), (f) α= 0.67 (N2/N1 =(D1/D2)0.67 (g), (h), (i) α=l 1 (N2/N1 =D1/D2). Left-side graphs (a), (d), and (g) were prepared at Nref=100 RPM; Middle graphs (b), (e), and (h) were prepared at Nref=150 RPM; right-side graphs (c), (f), and (i) were prepared at Nref=200 RPM

5.8.2 Effect of scale-up on Power per unit volume

Figure 5.3 shows the evolution of power per unit volume (*P/V*) as a function of the revolution number (*Nr*) across all the process conditions and scales. From top to bottom, the scale-up exponent increases, meaning that rotational speed decreases with the increasing scale diameter. From left to right, the reference rotational speed- corresponding to the rotational speed of the smallest scale- increases from 100 to 200 RPM. The *P/V* rises with the revolution number and reaches a constant

value across all conditions and scales, which is attributed to the equilibrium droplet size being reached at a higher revolution number.

When the exponent α is zero, the power per unit volume (*P/V*) remains consistent across all scales for each N_{ref}. As α increases, the spread of the (*P/V*) curves become more pronounced, although the aim is to maintain them on top of each other. For instance, at α = 0.67, the *P/V* of the medium scale (M) and large scales (L) are roughly 0.4 and 0.1 of the *P/V* for the small scale (S), respectively. These values decrease further at α=l, where the *P/V* of the medium and large scales reaches 0.2 and 0.03 of *P/V* for small scale (S), respectively. (see supporting information Figure S.1)

The evolution of power per volume agrees with the changes observed in the droplet size reported for the same conditions (Figure 5.2). Thus, scale-up using an exponent of 0 appears to be the most reliable procedure to ensure consistent droplet size when working with HIPPE with similar formulations, as it results in a constant *P/V*. The loss in reproducibility of the power with increasing scales at higher exponents is attributed to the larger droplet size produced. These larger drops are generated due to ineffective particle suspension and reduced droplet breakage capacity at lower rotational speeds as scale increases, resulting in lower viscosity and power consumption. This indicates a direct correlation between the droplet size and emulsions' viscosity.

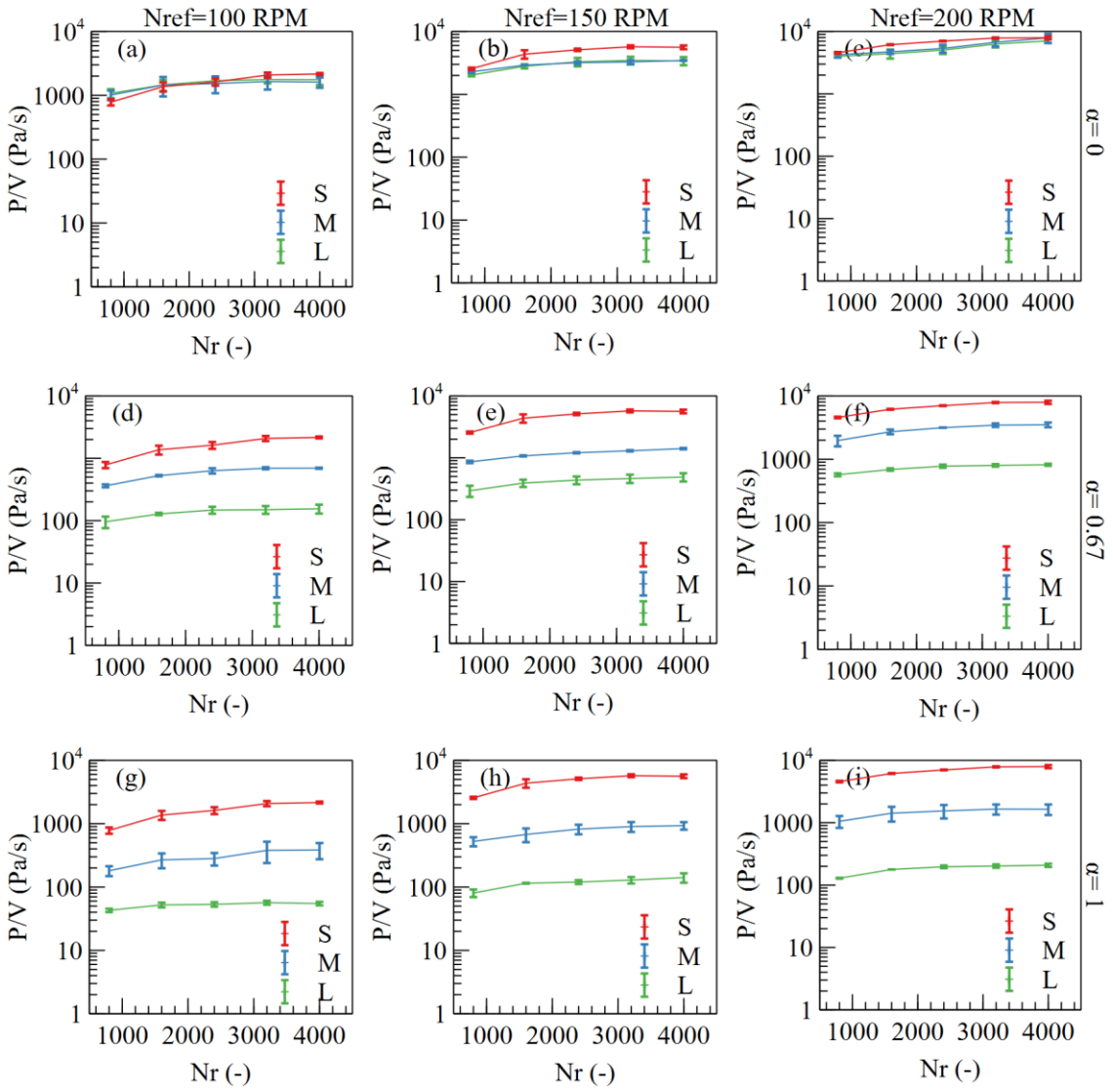

Figure 5.3. The evolution of P/V over the revolution number (Nr), for three scale-up exponents and three system sizes (S, M, L). (a), (b), (c) α=0 (N_2=N_1). (d), (e), (f) α=0.67(N_2/N_1=(D_1/D_2))$^{0.67}$. (g), (h), (i) α=1 (N_2/N_1=D_1/D_2).). Left-side graphs (a), (d), and (g) were prepared at N_{ref}=100 RPM; Middle graphs (b), (e), and (h) were prepared at N_{ref}=150 RPM; right-side graphs (c), (f), and (i) were prepared at N_{ref}=200 RPM

5.8.3 Linking the rheological characteristic and the D_{32}

By determining the shear rate and viscosity, one can estimate the specific power *P/V* (Equation(5.11)). However, accurate measurements of both viscosity and shear rate are crucial for this estimation, as Pickering emulsions exhibit complex non-Newtonian behavior.

In our case, the rheopectic and shear thickening behavior were observed during the mixing process. Droplets became progressively smaller over time at a constant rotational speed, until reaching a

minimum threshold for D_{32}. Increasing the rotational speed in the prepared emulsion further reduced droplet size and altered the morphology and structure, resulting in shear thickening behavior. These two phenomena occurred in an unsteady state, where the droplet size decreased during mixing.

Additionally, shear thinning behavior was observed as the rotational speed gradually increased before reaching the rotational speed that was employed for the preparation of the emulsion. Under these conditions, the morphology and droplet size remained unchanged, and the viscosity of the emulsion decreased with the shear rate due to the slight slipping of droplets and the alignment of fluid in the direction of flow. So, at each D_{32}, in a steady state condition, emulsions exhibit shear-thinning behavior, and its viscosity is calculated from the Power-law equation.

To estimate the required power per volume (*P/V*) for achieving a target droplet size, we first determine the power constant (K_p). Then, the power-law index (*n*), consistency index (*k*), and Metzner and Otto constant (K_s) are derived from the correlation between torque and rotational speed, as described in the Equation (5.18). The viscosity is then calculated using Equation (5.16) Finally, by substituting these values into Equation (5.11), the required *P/V* for target droplet size is determined.

Figure 5.4 illustrates the evolution of Γ/N as a function of N for emulsions prepared in the medium scale, considering three different reference rotational speed (Nref) values and three scale-up exponents (α). The plot shows that Γ/N decreases according to the power equation $\frac{\Gamma}{N} = M * N^{n-1}$. At each Nref, the values of M and n decrease as α increases. Moving from Figure 5.4-a to Figure 5.4-c, where Nref increases at a constant α, the values of M and n also increase. The M value is related to the consistency index (k), power-low index (n), power constant (K_p), Metzner and Otto constant (Ks), and the impeller's diameter D, through the following equation.

$$M = \frac{D^3 K_p k K_s^{n-1}}{2\pi} \tag{5.19}$$

It is worth mentioning than the value of power-law and consistency indexes were validated using rheometer results. The detailed results are summarized in the appendix.

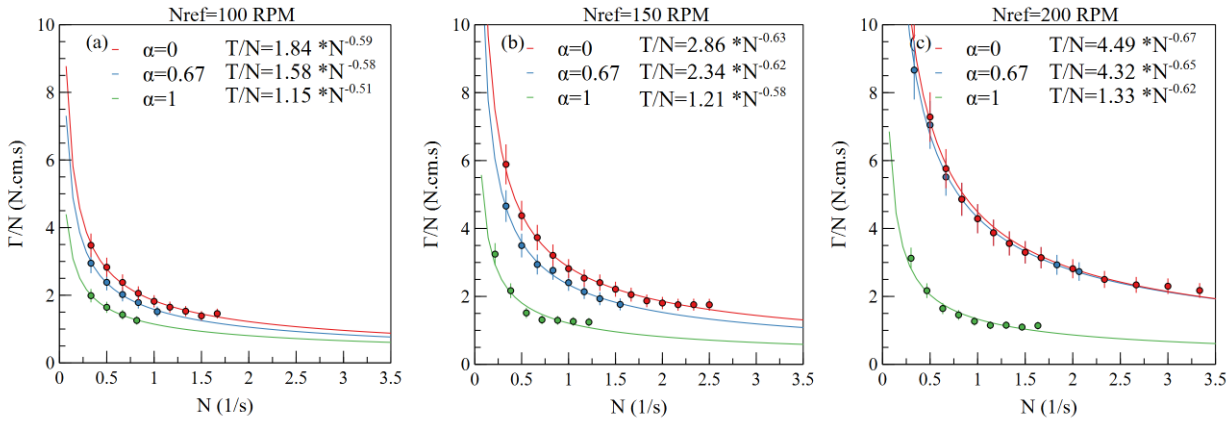

Figure 5.4. Torque/ rotational speed versus rotational speed for medium-scale with different scale-up exponents. (a) N_{ref}=100 RPM, (b) N_{ref} =150 RPM, (c) N_{ref}=200 RPM

The same procedure was applied to other scales, and the results show that, regardless of α and N_{ref}, the values of n and kK_s^{n-1} for all emulsions are a function of D_{32}. (The graph illustrating this correlation is provided in supporting information Figure S.2). This observation implies that n and k are intrinsic material properties, independent of process conditions. As a result, the viscosity of the emulsion can be estimated based on the target droplet size using the two correlations. By substituting these relationships into Equation (5.16), the viscosity can be calculated, and the required power can finally be determined using Equation (5.11).

5.8.4 Measured vs estimated power per unit volume

We compared the power per unit volume measured via torque measurement ($P/V(\Gamma)$) with the power estimated through the viscous stress rate ($P/V(\mu)$). The correlations between D_{32}, n, k, and K_s were employed to estimate power from the droplet size obtained at all scales, scaleup exponents, and rotational speed in all the revolution number (Nr). Results for α=0 are shown in Figure 5.5 and the two other exponents are presented in the supporting information, Figure S.3.

Figure 5.5 compares the estimated and measured power per volume (P/V) at constant α=0 across all scales (S, M, L) and three reference rotational speeds (N_{ref} = 100, 150, 200 RPM, in Figure 5.5-a, Figure 5.5-b, and Figure 5.5-c, respectively). These graphs indicate that the estimated P/V ($P/V(V)$) slightly deviated from the measured P/V ($P/V(\Gamma)$); with the deviation decreasing as the rotational speed increases. At a constant rotational speed of 100 RPM (Figure 5.5-a), the estimated power for the small scale is 81% of the measured power. This discrepancy can be attributed to the

larger portion of the power consumed for particle suspension, which was not accounted for in our estimation.

From the comparison between the consumed power and the specific just suspended power P_{js}, calculated using Ayranci et al.'s equation [148] (see supporting information), it was found that only at a small scale with N=100 RPM does the P/P_{js} ratio falls below one (Supporting information Figure S.3). This indicates that, under this condition, particles are not fully suspended, and a large portion of total power is consumed for particle suspension. At larger scale and higher rotational speed, the P/P_{js} ratio exceeds one, meaning that more power is allocated to emulsification, resulting in closer alignment between the estimated and measured P/V values.

At other rotational speeds, when all scales exceed the just-suspended power threshold, the deviation between the estimated and the measured power is relatively consistent across scales, ranging between 4-8%. This deviation is due to the elongational flow present during HIPPE production in the laminar regime with DHR, whereas our estimation assumes a simple shear flow for the emulsification process.

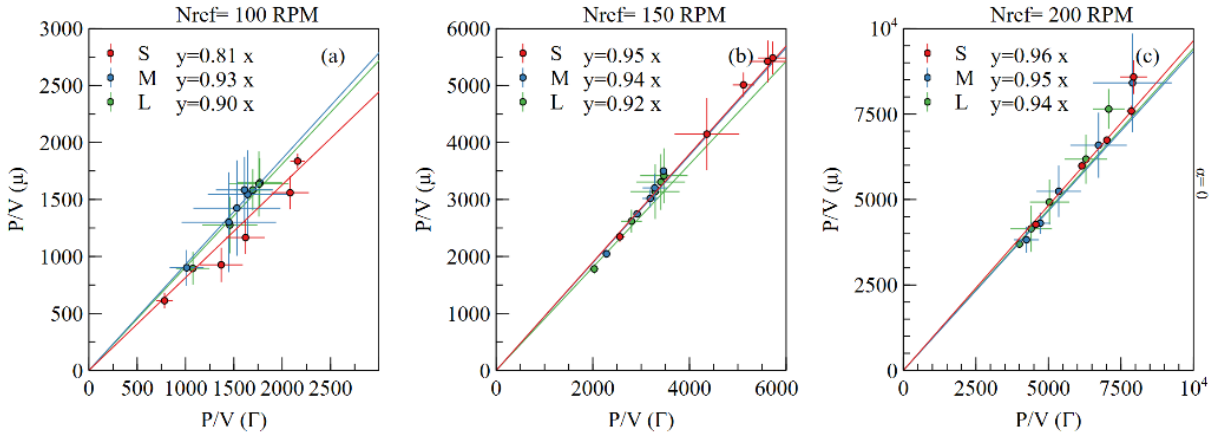

Figure 5.5. Comparison of the measured P/V(P/V(Γ)) with the estimated P/V (P/V(μ)) at scale-up exponent 0: (a), (b), and (c) Nref= 100, 150, and 200 RPM, respectively. Equations Infront of each legend represent the equation of P/V (μ) versus P/V(Γ)

5.9 Validation

We aim to validate the developed scale-up procedure by producing a HIPPE at a much larger scale than the ones used in our experiments and adjusting the formulation to confirm the effect of

constant *P/V* on D_{32}. Three approaches are explored; the first approach involves maintaining a constant emulsion formulation and scale-up exponent to achieve a consistent D_{32} across scales. In the second approach, we compare the droplet size and *P/V* of emulsions prepared at similar low rotational speeds for two scale G and L. Finally, in the third approach, we adjust both formulation and rotational speed to achieve equivalent *P/V* and D_{32}.

Emulsions were first prepared under selected conditions at a larger scale of 30 L, referred to as scale G, which is 3,000 times larger than the smallest scale used in our initial experiments. A scale-up exponent of zero was applied only for N_{ref}=100, for this large tank, due to limitations in the experimental torque measurement, which hampered the maximum speed at this scale. Figure 5.6 compares the droplet size (D_{32}) and *P/V* of emulsions prepared across all scales. The results indicate that, although there is a slight discrepancy in D_{32} at the onset of the emulsification (*Nr* 800), consistent D_{32} values were achieved across all scales after *Nr* =3200 (Figure 5.6-a). A similar trend is also observed for *P/V* (Figure 5.6-b), which validated our conclusion that applying a scale-up exponent of zero in the HIPPE production within the laminar mixing process yields consistent *P/V* values and similar droplet size across scales.

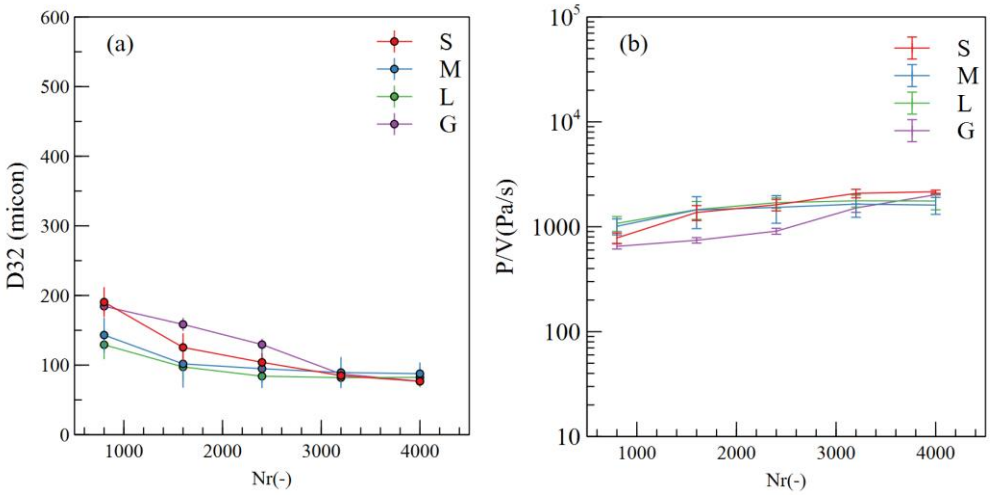

Figure 5.6. Evolution of D_{32}, and P/V over revolution number Nr for **α=0** and N_{ref}=100 RPM.

The second approach aims to compare D_{32}, and *P/V* of emulsions prepared at two different scales using similar low rotational speeds to produce larger droplet sizes. For this purpose, at scale G, an α=0.67 was employed for N_{ref}=150 and 200 RPM, resulting in *N* values of 27 and 36 RPM, for G

2-α0.67, and G3-α0.67, respectively. The D_{32} and *P/V* of these emulsions were compared with those of emulsions prepared at scale L at speeds of 21 RPM (L_1-α_1) and 35 RPM (L_1-$\alpha_{0.67}$). Figure **5.7**-a shows that similar rotational speeds, *N*= 21-27 RPM, and *N*=35-36 RPM, produce relatively similar droplet sizes across the scales over the revolution number.

A similar trend was observed for *P/V* (Figure **5.7**-b), for each rotational speed, *P/V*, for both emulsions it first increases until the revolution number in which droplets reach their equilibrium size, then reach a plateau. These findings further confirm that similar rotational speed resulted in comparable droplet sizes, leading to similar rheological behavior and viscosity, and ultimately consistent *P/V* values.

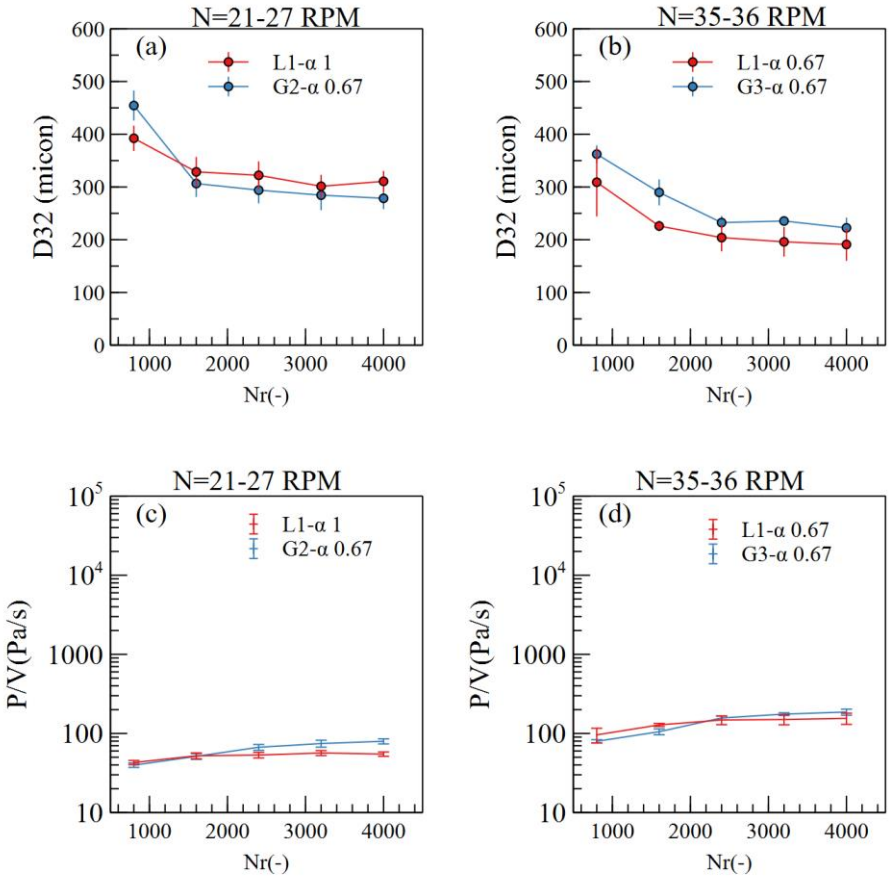

Figure 5.7. Evolution of D_{32}, and P/V over revolution number (a, c) emulsified at N=21-27 RPM; (b, d) emulsified at N=35-36, index number corresponds to the level of reference rotational speed: 1,2,3 corresponds to 100,150,200 N_{ref}.

In the third approach, similar *P/V* and D_{32} values were achieved by varying formulations and rotational speeds. For this approach, we used the data from our previous work [146], where emulsions were prepared at constant PI concentration but with different continuous phase viscosity, adjusted by modifying the PVA concentration. A summary of this work, illustrated in Figure 5.8, shows that the D_{32} of an emulsion prepared with higher continuous phase viscosity and lower rotational speed (i.e. 3 wt% PVA at 100 RPM) was similar to that of an emulsion prepared with a higher rotational speed and lower viscosity (i.e. 2 wt% PVA at 150 RPM, Figure 5.8-a). Similar results were observed for emulsions with 4 wt.% PVA at 100 RPM (Figure 5.8-b) and 3 wt.% PVA at 150 RPM (Figure 5.8-b). This trend was also consistent for the *P/V* at each corresponding emulsion (Figure 5.8-c and Figure 5.8-d). These findings confirmed that, in cases where rotational speed is limited, a higher continuous phase viscosity provides sufficient power to achieve similar droplet size.

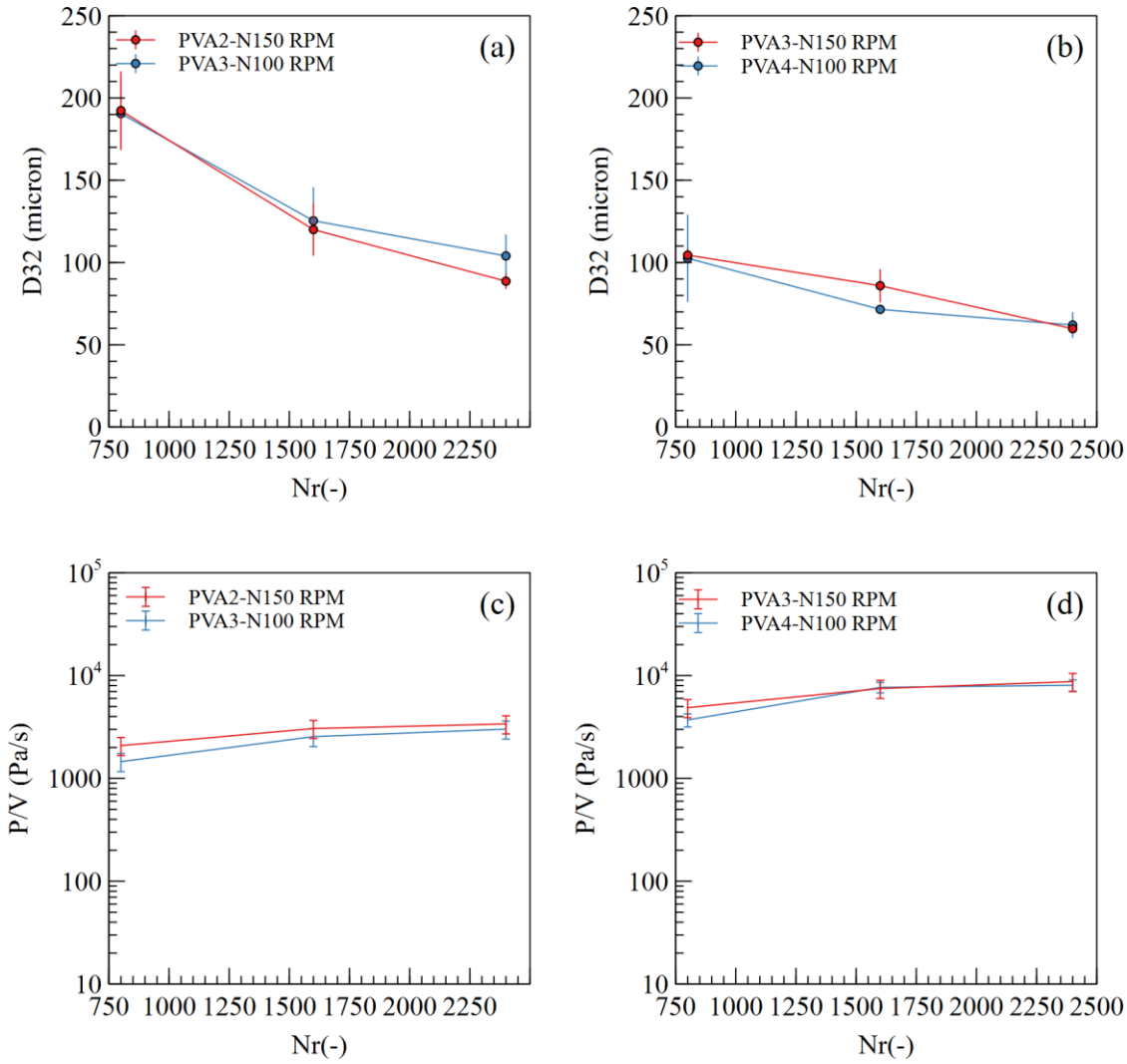

Figure 5.8. Evolution of D_{32}, and P/V over revolution number; (a) and (c) emulsions were prepared by lower viscosity or rotational speed; (b) and (d) emulsions were prepared by higher viscosity or rotational speed

5.10 Discussion

We demonstrated that the most appropriate scale-up exponent for HIPPEs in the laminar regime is 0 (zero). At this exponent, maintaining constant rotational speed results in a consistent stress rate, leading to an overlapping average of D_{32} across scales. Torque analysis revealed that emulsions prepared with this scale-up exponent exhibit similar viscosity and consistent *P/V*. Under all process conditions, droplet size decreased with emulsification time.

Combining the emulsification time with *P/V* yields specific energy (*e/V*), a key parameter for controlling D_{32} during the transitional phase before reaching the equilibrium droplet size. [91][149][74] It has been shown that droplet size decreases with specific energy until equilibrium is reached, after which *P/V* governs D_{32} [91][149][74]. We observed similar behavior in our emulsions prepared at constant rotational speed and *P/V*.

Figure 5.9 compares the dependency of D_{32} on the *e/V* and *P/V* for emulsions prepared at three rotational speeds -100, 150, and 200 RPM- across all scales. The results demonstrate that D_{32} follows a power-law correlation with both *e/V* and *P/V*. These curves can be used to estimate the required power or energy to achieve the target droplet size.

Figure 5.9-a illustrates the reduction of D_{32} as a function of specific energy, with data points aligning along two curves for *N*=100 RPM and 200 RPM. Covariance analysis yields a *p-value* of $4.2*10^{-19}$ (Supporting information Table S.1), indicating a strong dependency of D_{32} on *e/V*. At low e/V the data points are also dependent of rotational speed; however, this dependency diminishes at higher *e/V* values (i.e. longer emulsification time), suggesting that the equilibrium D_{32} has been reached.

Figure 5.9-b illustrates the reduction of D_{32} as a function of power per volume, with data points fitting within two curves for *Nr*=800 and 4000. Covariance analysis obtained a *p-value* of $5.2*10^{-18}$ (Supporting information Table S.1) indicating a strong dependency of D_{32} on *P/V*. The observed deviation for *N*=100 RPM and *Nr*=800 (S1, and G1 on the *Nr*=800 line) corresponds to the droplet sizes that have not yet reached equilibrium. However, these points fit the line for *e/V*, as illustrated in Figure 5.9-a. This behavior can be attributed to the fact that, at low rotational speed and at the beginning of emulsification (Nr=800), droplets have not yet reached their equilibrium size. Under these conditions, D_{32} shows a strong correlation with *e/V* rather than *P/V*.

In summary, these analyses indicate that D_{32} correlates with *e/V* before equilibrium is reached and with *P/V* once equilibrium is achieved. These findings align with previous studies that established correlations of droplet size with *P/V* and *e/V* for emulsions stabilized with emulsifiers [91][149][74]. From these two curves, once the relevant equilibrium state is identified, the corresponding correlation can be used to estimate the energy or power required to achieve the desired D_{32}.

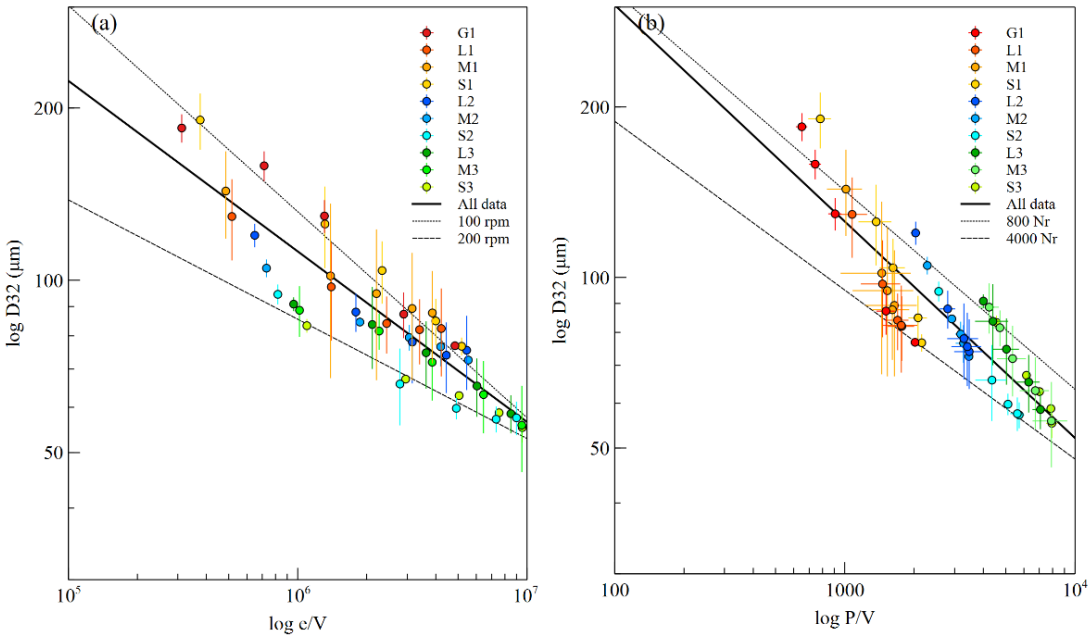

Figure 5.9. Evolution of D_{32} with (a) e/V, and (b) with P/V at constant rotational speed; indexes 1, 2, and 3 refer to rotational speeds of 100, 150, and 200 RPM, respectively. Scales G: 30 L, L:1 L, M:100 mL, S: 10 mL

5.11 Conclusion:

Our study investigates the effect of the scale-up rules on high internal phase Pickering emulsion in laminar mixing flow, leading to the following conclusions:

- A scale-up exponent of α=0 (constant rotational speed) is a practical approach for achieving consistent droplet size across scales from 10 mL to 30 L.
- At α=0, maintaining constant *P/V* across scales ensures consistency in droplet breakage and results in similar droplet sizes.
- Constant *P/V* can be achieved either by maintaining a constant rotational speed with preestablished formulation or by increasing the continuous phase viscosity when rotational speed increases are limited.
- A reliable correlation exists between droplet size and emulsions rheology, enabling accurate estimation of *P/V* based on viscosity.
- D_{32} evolves with specific energy input per volume (*e/V*) before the equilibrium droplet size is reached and then correlates directly with *P/V* once the equilibrium is achieved.

This correlation serves as a predictive tool in emulsion production, allowing engineers to estimate the required power and energy to achieve target droplet size based on lab-scale data. While this correlation is derived from a constant formulation, further research on variable formulations at a large scale is recommended to examine how changes in viscosity affect these relationships. Finally, investigating the impact of the impeller-to-wall gap could enable reductions in rotational speed while maintaining a constant shear rate. This could support efficient and consistent production across scales and further optimize the scalability of HIPPE productions.

5.12 Declaration of Competing Interest

The authors declare that they have no competing financial interests.

5.13 Funding

This work was support by the “Natural Sciences and Engineering Research Council of Canada” (NSERC 2020-06326) and “Optimizing Power Skills in Interdisciplinary, Divers & Innovative Academic Networks” (OPSIDIAN), which is also partly founded by NSERC.

5.14 Acknowledgments

The authors acknowledge the assistance of interns who contributed to sample preparation: Parinaz Nouraei , Margot Gebel , Mohamed Alioune Diagne. They are also grateful for the technical support provided during setup preparations by Sebastien Chenard, and Alejandro Velez Garcia.

CHAPTER 6 ARTICLE 3: HIGH-INTERNAL-PHASE PICKERING EMULSIONS FOR ENHANCED SOUND-ABSORBING MATERIALS

Mina Saghaei [1], Edith Roland Fotsing*[2], Louis Fradette[1,3], and Annie Ross[2,3]

[1]Chemical Engineering Department, Polytechnique Montréal, (Québec), Canada, H3C 3A7

[2] Laboratory for Acoustics and Vibration Analysis (LAVA), Mechanical Engineering Department, Polytechnique Montréal, (Québec), Canada, , H3C 3A7

[3]Research Center for High Performance Polymer and Composite Systems (CREPEC), Department of Mechanical Engineering, McGill University, 817 rue Sherbrooke Ouest, R.270, Montréal (Québec) Canada, H3A 0C3

*edith-roland.fotsing@polymtl.ca

Submitted February 18, 2025, to Journal of Material Science

6.1 Chapter's connection to the main objective

This chapter covers article 3 which we aimed to introduce HIPPE templates as a novel approach for producing acoustic porous materials. We demonstrated that the porous structure can be effectively controlled through a straightforward process using an environmentally friendly formulation. The pore size is precisely determined by the original droplet size, meaning that the process conditions during the emulsification directly affect the final pore size. The key advantage of this approach is its versatility: depending on the target frequency range for sound absorption, the pore size can be controlled during the emulsification process, making this method highly adaptable to specific acoustic application.

My contribution to the articles includes conceptualization, methodology, experimentation, analysis, writing original draft, and literature review.

6.2 Abstract

This paper introduces a novel approach for producing acoustic porous materials using solid-stabilized emulsion templates. The technique allows for precise control of pore size through straightforward emulsification processing conditions, highlighting its potential for developing multifunctional acoustic foams. The microstructure of the porous material was investigate using X-ray microtomography and open pore network modelling. The correlation between processing conditions, porous microstructure, and acoustic performance was determined. The findings reveal

that desired sound absorption performance can be achieved by adjusting the rotational speed during emulsification, which affects droplet size and ultimately results in targeted pore size, connectivity, and tortuosity. Notably, nearly perfect sound absorption coefficient at 1100 Hz was achieved for samples with largest pores, highest porosity, and greatest connectivity. Furthermore, samples with medium porosity and pore size, but the highest tortuosity, exhibited maximum sound absorption below 500 Hz, despite a low sample thickness of only 3cm. This performance is particularly notable, as it is challenging to achieve with conventional acoustic foams, demonstrating the potential of this novel approach for developing high-performance acoustic materials.

Keywords: Highly concentrated solid stabilized emulsion, Pickering emulsion, porous material, sound absorption

6.3 Introduction

In recent decades, the alarming rise of health problems caused by noise pollution has become a serious concern, largely driven by the rapid growth of the transportation industry [150]. Prolonged exposure to noise-polluted environment can significantly disrupt daily life leading to insomnia, cardiovascular diseases and other serious health issues [150]. In response to these concerns, new regulations in the United States (14 CFR Part 36, updated 2023) have been implemented to reduce noise levels in transportation systems, thereby creating a growing demand for innovative and effective sound-absorbing materials.

Recent advancements in polymer foams have sparked significant interest in their potential applications in sound dissipation. The latest generation of porous acoustic liners offers several advantages, including reduced spatial requirements and simplified design [4]. However, the foaming processes used to manufacture these materials often rely on hazardous ingredients and chemical reactants, which can have negative environment and health implications. The implementation of health, safety, and environmental (HSE) measures to protect both operators and the public can substantially increase production costs, making these materials less competitive.

Emerging methods such as the leaching process [101] and additive manufacturing [102], which offer precise control over pore size and interconnectivity. The leaching process using particles with diameters of 500–700 microns has been found to yield maximum sound absorption around 3000 Hz [101]. Additive manufacturing of acoustic periodic materials has also achieved high sound absorption when finer filaments and smaller lattice parameters are used [102]. Predictive analytical

models for acoustic micro-lattices produced via additive manufacturing indicate that the microstructure for maximum sound absorption includes a filling factor of 40-50 % and filament diameter between 50-200 microns [102]. However, these structures typically exhibit sound absorption peaks above 2000 Hz, requiring modifications to perform well at lower frequencies.

Polymeric emulsion templating approaches have gained significant attention in recent years for producing porous structure [68][151] with applications in various fields including tissue engineering [152], catalysis [153], membrane separation [154] and acoustic applications [155]. This approach involves using high concentrations of monomers in the polymerized continuous phases, along with substantial emulsifiers to stabilize droplets as dispersed phases. However, the use of monomers and emulsifiers not only raises production costs due to required safety measures but also raises health concerns for end users, leading to restrictions in some industries.

Surfactant-free solid-stabilized emulsions (SSE), also known as Pickering emulsions, -named after the pioneering researcher who first describe them [3]- are formed through the spontaneous absorption of particles at the interface of two immiscible phases [23]. A wide range of mineral, organic, and polymeric particles, with suitable contact angles, can locate at the interface of two phases. The stability of Pickering emulsions is achieved by preventing coalescence through the formation of a steric particle barrier around the droplets, which is more effective than traditional chemical emulsifiers [23]. Furthermore, capillary forces and particle interactions at the interface contribute to stability by creating a close-packed particle network [31]. The unique characteristics of Pickering emulsion, including ease of formation with sufficient mixing, long-term stability, control over droplet size, and adjustable surface chemistry, have garnered significant attention from researchers across various fields [28]. Applications for these emulsions are diverse and widespread, encompassing fields such as drug delivery [24][156], catalysis [157], food technology [158][26], photocatalysis [159], oil recovery [160] antibacterial activity [161], and the cosmetics [162].

High internal phase Pickering emulsion (HIPPE), which contains over 75 vol % of the internal phase, have recently been employed as templates to create porous materials for industrial applications including, filtration membranes [17], porous scaffolds [163], and other uses that require micro-, meso-, and macro-porous structures [140]. The porous structure is formed through a process of liquid evaporation and particle sintering, resulting in materials with high porosity and

extensive interconnectivity. This unique combination of properties makes HIPPE templated materials promising candidates for high sound absorption applications.

This study explores the application of high internal phase solid-stabilized emulsions as a novel approach to produce controlled porous structures optimized for sound absorption. The sound absorption performance of these porous structures is closely related to their morphology, which can be tailored through the manipulation of emulsification processing parameters. A significant technical challenge in controlling droplet size reduction is achieving large droplets in the range of 200-800 microns, which is approximately two orders of magnitude larger than those obtained through polymeric emulsion templating [155]. This challenge is particularly pronounced when working with highly viscous emulsions. By utilizing polymeric particles as stabilizers, we are able to eliminate the need for monomers and achieve highly interconnected porous structures through a simple and efficient process involving spontaneous evaporation and sintering of polymeric particles, without the requirement for foaming agents. A notable advantage of these porous materials is their high sound absorption, achieved through a simple and environmentally friendly manufacturing approach. More specifically, the study examines the impact of key parameters such as pore size, porosity, and interconnectivity on the tortuosity, sound absorption, and normalized acoustic impedance. To achieve this, three distinct process conditions were employed to produce three types of porous materials with varying pore sizes and interconnectivity levels. A comprehensive investigation was conducted to establish the correlation between the microstructure parameters and the acoustic properties.

6.4 Material and method

6.4.1 Materials

All emulsions are prepared in total volume of 1 liter comprising 80 vol.% dispersed phase which consists of pure silicone oil with a viscosity of 200 cSt at 25˚C (Clearco Products Co. Inc., USA) and 20 vol.% continuous phase. This continuous phase is a mixture of distilled water, 40 wt.% Polyimide (PI) powder with a median size (d50) of 4 microns (P84NT, Evonik Fibers GmbH), and 3 wt.% polyvinyl alcohol powder (PVA, Alfa Aesar, US). Polyimide was selected for its superior thermal and chemical resistance, which is crucial for the potential end use of the porous structure as an acoustic absorbing material in the aerospace industry.

6.4.2 Emulsification setup

The concentrated Pickering emulsions were prepared using a custom- designed 3D-printed double-helical ribbon (Figure 6.1) immersed in a 2 L tank, which was half filled with material. Oil injection process was facilitated by pushing the silicone oil through a syringe inserted into a hole located on the side of the tank (Figure 6.2). In the initial stage, the specified quantity of particles was uniformly dispersed in PVA solutions by subjecting the mixture to a designated speed for one minute. Subsequently, the oil was injected from the bottom of the tank at a speed proportional to the total oil volume and rotational speed. The torque meter continuously measured the torque during the mixing process, providing valuable insights into the emulsification dynamics.

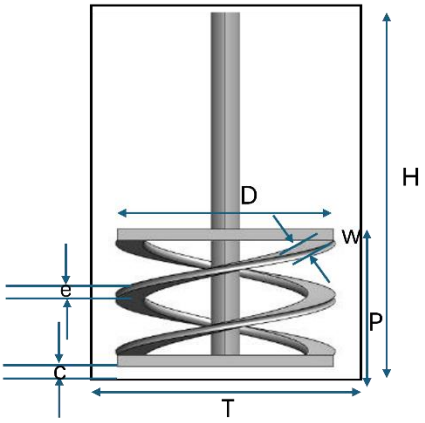

	D	T	H	P	c	e	w
Unit (cm)	12.5	13.3	20	8.38	0.38	0.38	1.88

Figure 6.1. Dimension of impeller and tank

1. Computer
2. Torquemeter
3. Emulsion
4. Impeller
5. Power

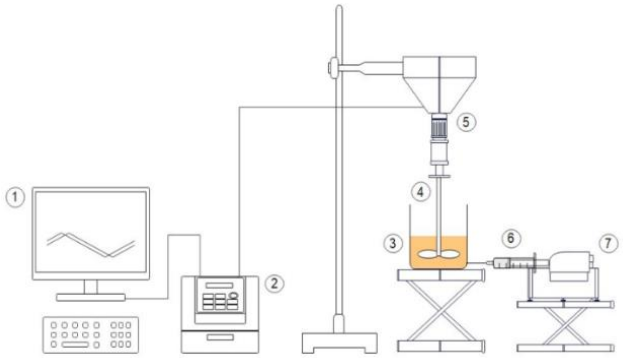

Figure 6.2. Schematic of the setup.

6.4.3 Sample preparation

Three distinct levels of rotational speeds were chosen for their ability to provide sufficient pumping capacity within the tank. The total revolution number, calculated as the product of processing time and rotational speed, was maintained constant at 4000 for all rotational speeds. To ensure reliability and reproducibility, all samples at each process condition were replicated three times. A summary of the process conditions is presented in Table 6.1. It is worth mentioning that different formulation and process conditions were investigated in our previous work [146]. In this study, we focused on applying 3 levels of rotational speed while keeping the formulation and revolution number constant.

A specific mold (14 cm diameter and 7 cm thickness) is used to prepare the samples for acoustic performance measurements. The emulsions are poured into this mold and allowed to settle at room temperature for a period of 24 hours. Subsequently, the mold is placed in an oven where the water is evaporated through a controlled temperature ramp, increasing gradually at a rate of 10˚C/h. Once the water has evaporated, the temperature is further increased to 350˚C at a rate of 50˚C/h, and maintained at this final temperature for 5 hours to ensure complete evaporation and stabilization of the sample. Finally, all samples were cut 2 cm from each side (top, bottom, and circumference) to eliminate side effects for all experiments, resulting in samples with 10 cm diameter and 3 cm thickness.

Table 6.1. Processing conditions

Samples	**P1**	**P2**	**P3**
Rotational speed (RPM)	20	35	42
Time (minute)	200.0	114.3	95.2
Revolution number	4000	4000	4000
Sample thickness (cm)	3.00±0.10	3.00±0.10	3.00±0.10

6.4.4 Characterization

The droplet size of emulsions was measured by laser diffraction technique (Malvern Mastersizer 3000) which generates droplet size distribution (DSD) plots. The Malvern software also reported the D_{10}, D_{50}, D_{90} values, which represent the droplet size at which 10%, 50%, and 90% of droplets

are smaller than the respective sizes. These values offer a quantitative description of the droplet size distribution, allowing for a detailed analysis of the emulsion's characteristics.

The bulk density of the material was determined using a gas pycnometer (AccPYc 1340). A small sample of the final porous structure, weighing less than 3 grams, was placed into a 10-cc cylinder. The pycnometer measures the difference in the total volume occupied by helium gas and calculates the bulk density, ρ_b.

The density of porous material (ρ_m) was calculated based on the sample's weight and volume. The porosity was then determined using the following equation:

$$\phi = 1 - \frac{\rho_m}{\rho_b} \tag{6.1}$$

The sound absorption coefficient and normalized impedance were determined using a 100 mm conventional impedance tube (Mecanum Inc, Sherbrooke, Canada) in accordance with the standard procedures outlined in ISO 10534-2 and ASTM E2611. The samples were prepared with a 10 cm diameter and a thickness of 3 cm and were tested over a frequency range of 35-1800 Hz by using impedance tube (Figure 6.3).

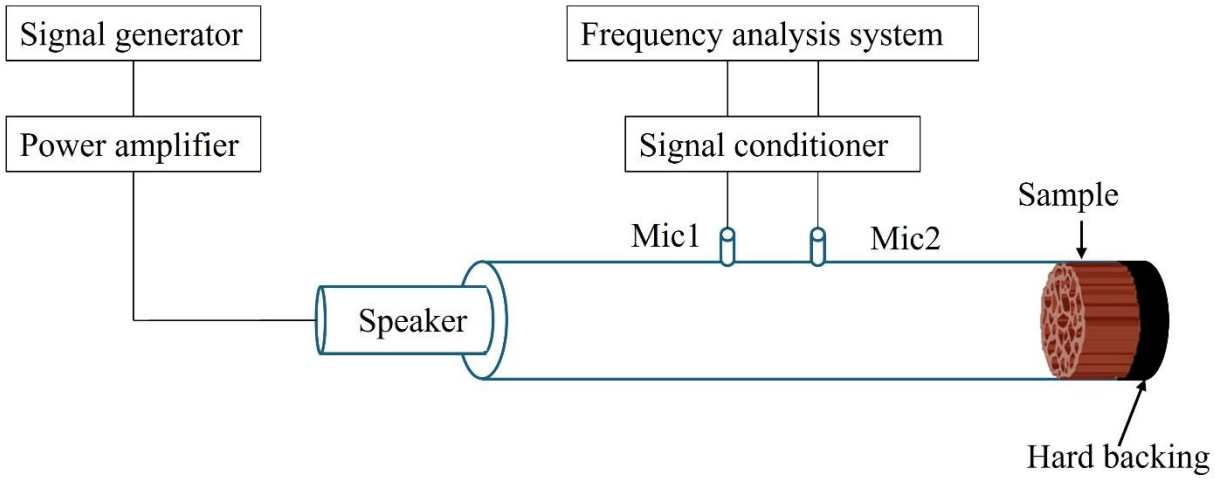

Figure 6.3. Schematic of impedance tube

The tortuosity of the samples was measured using the ultrasound reflection technique (Mecanum Inc, Sherbrooke, Canada), which is based on the principle of measuring the instantaneous oblique reflection coefficient of the first reflected wave at the surface of the porous material. The ultrasound reflection test was conducted at four different incident angles ranging between 20˚ and 45˚, and the

average of all measurements was reported. To account for inhomogeneity, samples were rotated in order to measure tortuosity at four different locations.

Additionally, an alternative method was used to estimate the tortuosity from the reconstructed 3D images obtained from microtomography measurements in the Dragonfly software. This method involves segmenting the pore region of interest based on voxel intensity, defining the inlet and outlet regions as small cubes and then calculating the tortuosity of porous structure by analyzing multiples pathways that an imaginary flow can travel between the inlet and outlet. Figure 6.4 illustrates an example of the selection of the inlet and outlet on the cross-sectional view of sample using the commercial software Dragonfly.

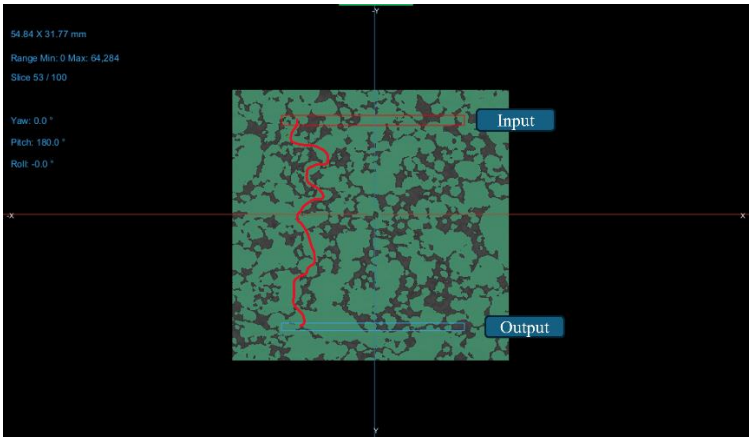

Figure 6.4. Determination of the tortuosity, from the pore region of interest (ROI) using the commercial software Dragonfly

The 3D microstructure of porous material was characterized using X-ray computerized tomography (Micro-CT) on a ZEISS Xradia 520 Versa. The image resolution was set to 20.6 μm/pixel for P1, 12.5 μm/pixel for P2, and 10.2 μm/pixel for P3 samples. Samples were rotated over a range of 0˚-180˚, and 1000 projections were captured. The 3D volume of samples was reconstructed using advanced projection algorithms and visualized using commercial software Dragonfly version 2022.1.0.12 (Comet Technologies, Canada Inc). The segmentation routine was applied in the 3D microstructure, where each voxel point was assigned a grey level high-intensity voxels were identified as material region of interest (ROI), and low-intensity voxels were considered pores ROIs. To quantify the pore volume, and interconnectivity, an open-source workflow called Open Pore Network Modelling (Openpnm) was employed. Details of this open-source workflow are described in the literature by Gostick [111].

To gain a comprehensive understanding of the microstructure of porous materials, it is essential to determine several key parameters, including pore diameter, connectivity number, conduit length, and total length. These parameters provide valuable insights into the internal structure and topology of the porous material, enabling a deeper understanding of its properties and behavior. The equivalent pore diameter is a parameter that represents the diameter of hypothetical spherical pore that has the same volume as the actual pore. This value is calculated using the following equation:

$$d_{equivalent} = \left(\frac{6V}{\pi}\right)^{\frac{1}{3}} \tag{6.2}$$

where V is the volume of actual pore, determined using the Dragonfly software.

The conduit length is defined as the distance that a fluid or particle travels between two connected pores passing through the throat linking them. It is quantified as the center-to-center physical distance between two pores. The total length represents the cumulative sum of all conduit lengths that the flow traverses, from the entrance of an open pore to the end of the flow path. A schematic illustration of these lengths is provided in Figure 6.5 which helps visualize the concept of conduit and total lengths in the context of pore connectivity.

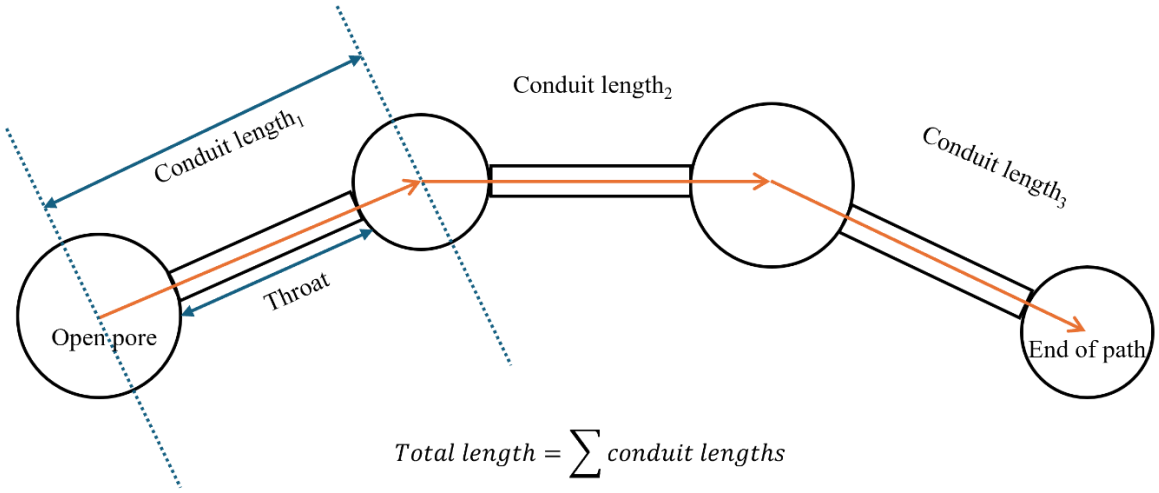

Figure 6.5. Schematic of conduit and total lengths in interconnected porous materials

Connectivity number is a structural parameter that quantifies the number of connections (throats) a single pore has with other pores in the network [164]. It is a key metric that describes the degree of connectivity between pores within the porous material, providing insight into how well-

connected the pore network is. The connectivity number can vary depending on the preparation process used, highlighting the importance of controlling and optimizing the fabrication conditions to achieve the desired pore network architecture.

6.5 Results and discussion

6.5.1 Process and microstructure analysis

The droplet size distribution of emulsions prepared at different rotational speeds was measured using a Mastersizer with three replications performed for each process. The size distribution data of all replications were averaged and reported in Figure 6.6. In this figure, the left vertical axis represents the percentage of droplets in each size class, while the right vertical axis corresponds to the cumulative curve. From this cumulative curve, the parameters D_{10}, D_{50}, and D_{90} were derived, which represent the droplet sizes at which 10%, 50%, and 90% of droplets are smaller than these values, respectively. The distance between D_{10} and D_{90}, known as the width of droplet size distribution (DSD), is a critical factor in determining the overall droplet size range within the emulsion, as it provides insight into the polydispersity of the droplet population.

Figure 6.6 also illustrates the effect of increasing rotational speed on the (DSD) of the emulsions. As the rotational speed increases from P1 to P3, the D_{50} value, corresponding to the median droplet size, shifts toward smaller size classes. Specifically, the D_{50} values are 388, 231, and 107 microns for emulsions prepared under conditions P1, P2, and P3, respectively. Furthermore, the width of DSD, calculated as D_{90}-D_{10}, narrows with increasing rotational speeds with values of 401, 275, 220 microns for emulsions prepared under conditions P1, P2, and P3, respectively. This trend suggests that higher rotational speeds enhance the droplet breakage capacity during emulsification, resulting in smaller droplets. When sufficient particles are present to stabilize the droplets, these smaller droplets are fully stabilized and rigid, preventing coalescence after mixing.

It is important to note that the mechanism of droplet breakage and stabilization in the Pickering emulsions leads to unimodal Gaussian size distributions, which were observed for all process conditions.

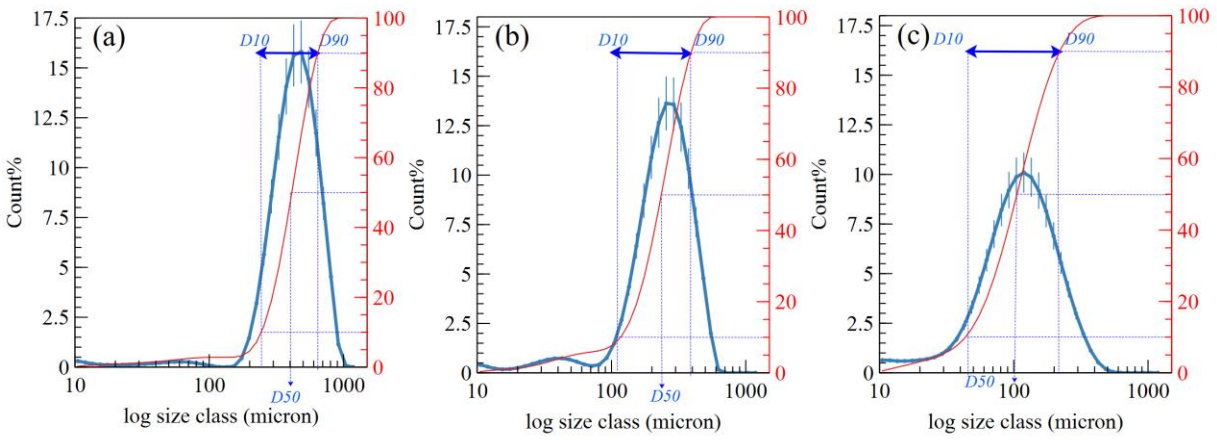

Figure 6.6. Comparison of droplet size distribution prepared at different rotational speeds: P1=20RPM, P2=35RPM, and P3=42RPM. The blue curve is the cumulative curve for determining D10 and D90.

Following the evaporation of oil and water, the 3D microstructure of the resulting samples was analyzed using X-ray computerized tomography (micro-CT). Cross-sectional of samples prepared under three different process conditions are compared in Figure 6.7 In these images, the black regions represent pores, while the whiter areas indicate the material remaining after evaporation of the liquid. The pore shapes are both spherical and nonspherical, with the nonspherical ones forming through the connection of adjacent spherical pores. The varying process conditions resulted in three distinct morphologies.

As shown in Figure 6.7a, the samples prepared under P1 condition contains the largest pores, and the least amount of remaining material compared to the other process conditions. In contrast, the samples prepared under condition P2 (Figure 6.7b) exhibit two distinct phases in the remaining material: a brighter, spherical phase, comparable in size to the smaller pores, and a grey, nonspherical phase. The brighter spherical phase can be identified as pores partially covered with residual silicon oil trapped within them. It worth mentioning that this assumption has been verified by comparing the bulk density. We observed lower density when the number of covered pores were increased, which is due to the lower density of silicon oil compared to pure PI (further explanation are provided in the next section). The grey, nonspherical phase corresponds to PI particles that have sintered together to from the continuous phase.

The cross-sectional image of the samples prepared under condition P3 (Figure 6.7c) reveals a microstructure that is similar to that of P2 samples, with three distinct phases present. However, the P3 sample exhibits the smallest pore sizes, the highest amount of remaining material, and a

greater number of pores containing trapped silicon oil. It is noteworthy that the linear pore shape can be attributed coalescence of smaller pores, which merge, to form linear pores. This suggests that condition P3 leads to a more complex and interconnected pore network.

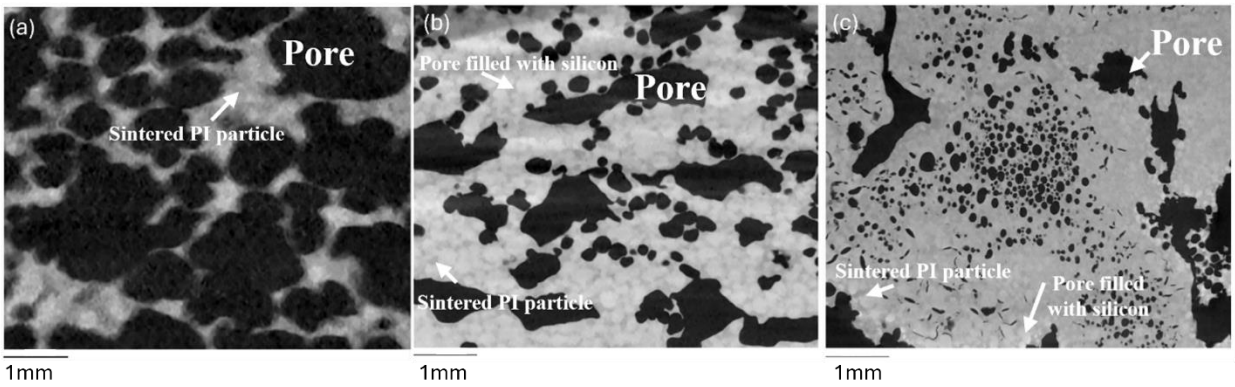

Figure 6.7.Cross-section of samples prepared under (a)P1, (b)P2, (c)P3 process conditions

3D structure of samples was reconstructed using commercial Dragonfly software. An open-source workflow for pore network modelling (OpenPNM) was employed within the Dragonfly to gain deeper understanding of average pore size distribution, and their connectivity. A constant volume of samples (width 6.5 mm, height 5.5 mm, depth 1 mm) was selected for all samples to ensure consistency in the analysis. The region of Interest (ROI) for pores was determined based on the intensity of the dark phase for each sample, allowing for accurate identification of the pore network. The selected pore ROI were then processed using OpenPNM, which labelled all pores and calculated their equivalent pore diameter. The equivalent pore diameter refers to the diameter of a hypothetical spherical pore that has the same volume as the actual pore within the material.

Figure 6.8 shows the size distribution of equivalent pore diameters alongside the droplet size distribution of the emulsions from which they were prepared. It is observed that under all process conditions, pore size distribution shifts slightly toward larger size class relative to the droplet size. However, this variation is negligible, as the peak of their size distribution occurred within very similar size classes. These findings demonstrate the robustness of the process; wherein stabilized droplets remain intact during liquid evaporation without collapsing and bursting

It is worth mentioning that the count percentage of pores and droplets does not perfectly match. The mismatch arises from their differing natures: droplets in HIPPE exhibit a perfect Gaussian distribution, whereas pores have a potential to merge during evaporation. As a result, the

percentage of pores within each size class may differ from that of their original droplet size. Despite some merging, the pore size distribution closely resembles the droplet size distribution, indicating that minor droplets coalescence does not significantly shift the overall pore size distribution toward large size class.

Comparison all process conditions reveals that samples prepared under condition P1 has significantly larger pores in comparison to two other processes. The larger droplet sizes in the emulsion provide more flexibility for droplets, resulting in the formation of larger pores. Specifically, samples prepared under condition P1 (Figure 6.8a), exhibit pore size exceeding 1000 microns, formed by the merging of multiple pores during evaporation. In contrast, the phenomenon is rarely observed for samples prepared under conditions P2 and P3 as their smaller droplets are less flexible due to the strong network of particle surround them. As a result, the oil droplets have less potential to merge to neighbor droplet.

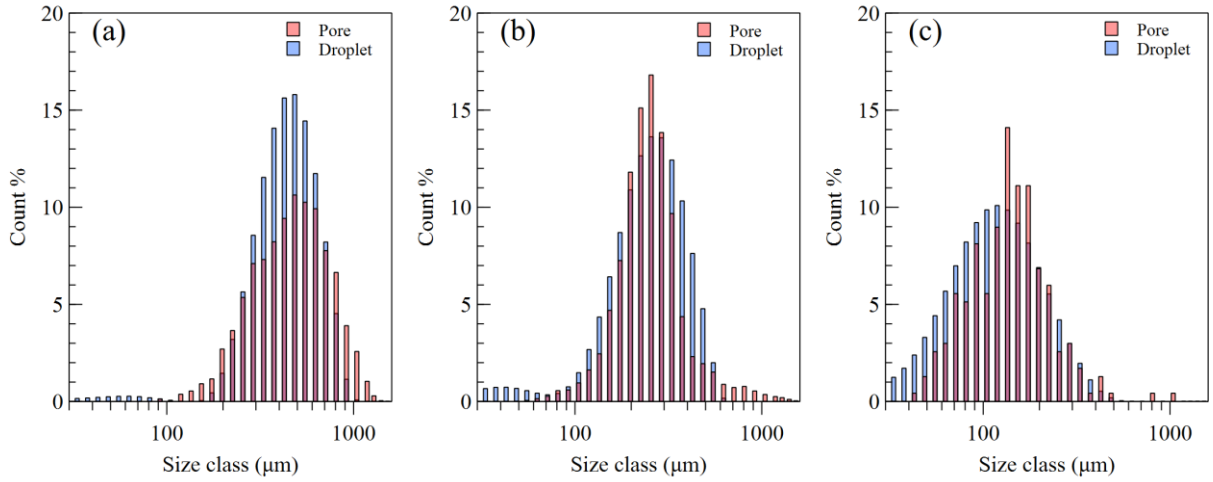

Figure 6.8. The size distribution of equivalent pore diameter and droplet diameter; (a) P1, (b) P2, (c)P3.

The pore connectivity and the total length within the selected 3D volume for each sample were also determined using OpenPNM. Connectivity number, which determines the number of connections (throats) a single pore has with other pores in the network, was calculated for each sample. Figure 6.9 illustrates the 3D view of a selected volume and their corresponding connectivity. The results reveal that, that the connectivity number decreases from P1 to P3, which is consistent with the cross-sectional view shown in Figure 6.7. The trend suggests that the number of closed pores, covered with residual silicon oil, increases as the rotational speed increases and droplet size decreases, which ultimately reduce the connection between pores. In the small pores, the trapped

silicon oil has limited space to evaporate and during the high temperature evaporation process; it solidifies and remains in the pores.

As shown in Figure 6.9a sample prepared under condition P1 has the highest connectivity, with a maximum value of 31. In contrast, the maximum connectivity number for samples prepared under P2 and P3 conditions are 26 and 22, respectively. The mean connectivity values for P1, P2, and P3 are approximately 4, 3, and 2, respectively. This indicates that most of the pores in all samples are connected to at least three neighbouring pores, making these structures highly suitable for sound absorption applications where high degree of open, interconnected pores is required.

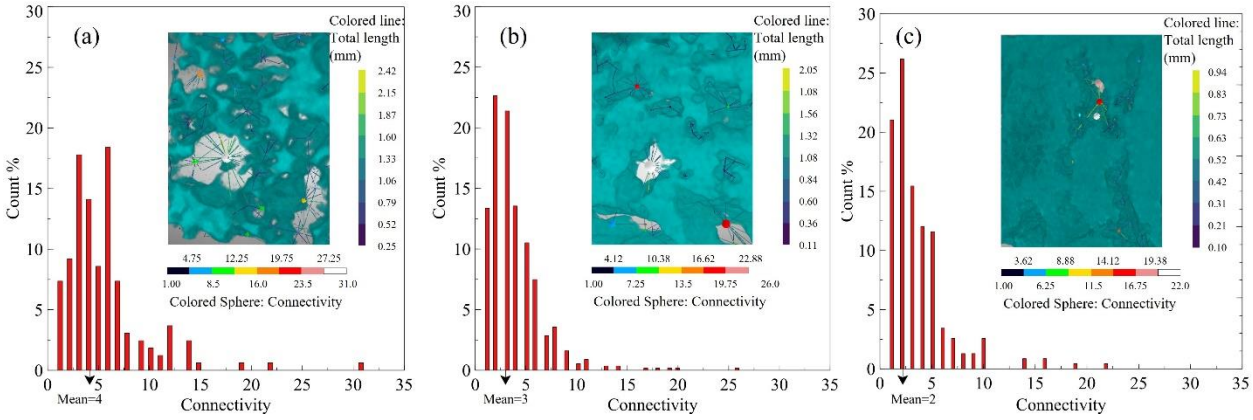

Figure 6.9. 3D view of selected volume of samples and their connectivity number prepared under (a, d) P1, (b, e) P2, and (c, f) P3.

The total length of pores is another important factor in open porous structures as it represents the sum of the lengths of connected pore and is considered the pathway through which sound waves travel, passing from an open pore to another one. It is accepted the acoustic energy dissipation through viscous friction and thermal exchange will be improved with increasing the length of throats and the connectivity number. Figure 6.10 shows the histogram of the total lengths for all samples, indicating that the distribution of total lengths shifts toward smaller size classes from P1 to P3. The results reveal that emulsions with largest droplet size (P1) leads to the longest total lengths, with an average of 788 μm. In contrast, emulsions with smaller droplet sizes (P2 and P3) exhibit shorter total lengths, averaging of 343μm and 308μm, respectively, which is attributed to their finer pores and lower connectivity. This suggests that the total length of pores is strongly influenced by the droplet size and pore structure, with larger droplets and higher connectivity leading to longer total lengths.

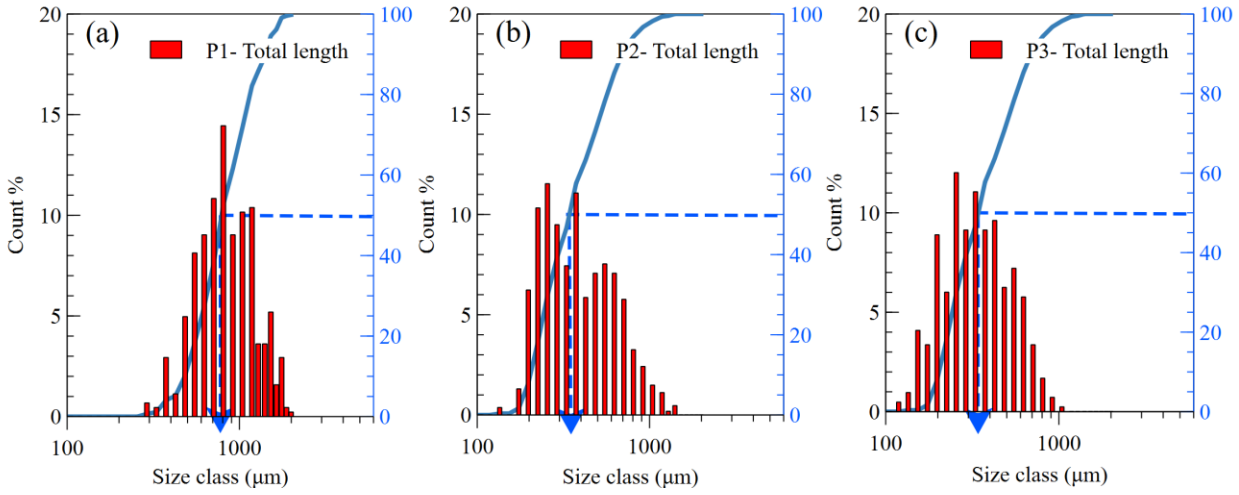

Figure 6.10. Total length porous structures. (a) P1, (b) P2, (c) P3.

The porosity of the samples was determined using Equation (6.1), by measuring the bulk density with a pycnometer. The experimental data are summarized in Table 6.2 Additionally, the porosity of the samples was calculated through the reconstructed 3D microstructure by averaging the volume ratio of pore region of interest (ROI) to the total selected volume in different sections of each sample. These calculated values are compared with the experimental values in Table 6.2. The results show that the porosity decreases from P1 to P3 which is consistent with the cross-sectional view in Figure 6.7 showing a decrease in the number of open pores as the process conditions change from P1 to P3.

Table 6.2 also indicates that the bulk density of the samples varies across different process conditions. This confirms our assumption that decreasing the pore size leads to more trapped silicon oil, resulting in pores filled with solidified silicon. Since silicon oil has lower density (ρ = 0.96 g/cm³) compared to pure polyimide particle (ρ=1.42 g/cm^3), this trapping reduces the total bulk density. Specifically, P1 has a bulk density (ρ=1.37 g/cm^3) closest to that of polyimide particles, indicating that no residual silicon oil remains in its structure. In contrast, P2 and P3, with bulk densities of 1.28 and 1.19g/cm^3, respectively, confirm an increasing amount of residual silicon oil in the structure. This findings suggest that low rotational speed during emulsification process, which resulted in large droplet size, would be beneficial for higher porosity.

Tortuosity is another key factor for sound absorption, particularly at low frequency [105]. It refers to the complexity or "twistiness" of a porous material's microstructure, describing the extent to which a sound wave deviated from a straight-line path due to the geometry and connectivity of the

pore network [165]. Physically, tortuosity is defined as the ratio of actual pathway length to the direct distance between two points. According to the ultrasound reflection measurement method, the average tortuosity was measured at four contact angle and reported in Table 6.2. Additionally, the tortuosity of samples was measured from the reconstructed 3D microstructure and compared with experimental values.

The results show that samples prepared under condition P2 exhibits the highest tortuosity in both experimental measurement and simulations, while samples prepared under condition P1 has the lowest tortuosity, and P3 falls in between. This trend can be attributed to the higher connectivity number in P1, which provides more direct connections between pores, thereby reducing tortuosity. The results also indicate that the porosity is another key factor in determining tortuosity. Although P2 and P3 have approximately the same connectivity number, the higher porosity of P2 results in greater tortuosity compared to P3.

It is worth noting that close agreement between experimental and simulation values for tortuosity and porosity validates the accuracy of the pore ROI segmentation

Table 6.2. Porosity and tortuosity of samples

Sample	Bulk density	Porosity (Experimental)	Porosity (simulated)[a]	Tortuosity (Experimental)	Tortuosity (simulated)[a]
P1	1.37±0.07	73%±1	73%±2	1.18±0.20	1.08±0.1
P2	1.28±0.03	62%±2	59%±3	1.88±0.23	1.54±0.18
P3	1.19±0.07	54%±1	50%±4	1.35±0.30	1.20±0.2

a. Obtained from 3D reconstructed microstructure in Dragonfly

6.5.2 Sound absorption analysis

The sound absorption of porous samples prepared under each process condition was measured using an impedance tube. For each process, we averaged the data from three replicated samples with a thickness of 3 cm, and the results are compared in Figure 6.11. The tests were conducted with the incident sound wave impinging on both the top surface (upper layer of the emulsion samples during evaporation) and the bottom surface.

The results show that samples prepared under condition P1 exhibit the highest sound absorption, particularly between 900-1200 Hz (Figure 6.11a). In contrast, the maximum sound absorption for samples prepared under P2 and P3 is approximately 0.6 for the top surface, occurring at 400-600 Hz (Figure 6.11a).

Generally, the bottom surface shows lower sound absorption at higher frequency compared to the top surface. However, an exception is observed in samples prepared under condition P2 (Figure 6.11a), where the sound absorption of the bottom surface between 700-1000 Hz is higher than that of the front surface. These variations can be attributed to the differences in pore size and interconnectivity resulting from varying process conditions. Furthermore, each sample exhibits a gradient in pore size and interconnectivity from top to bottom, with larger pores located at the top and smaller pores at the bottom. This gradient formed during the evaporation process for all samples. The smaller pores at the bottom lead to higher reflection, reducing the penetration and absorption of sound waves through the porous structure.

The real and the imaginary parts of the normalized acoustic impedance of the samples are compared in Figure 6.11b and Figure 6.11c, respectively. The imaginary part (reactance) represents the inertia effect and the elasticity of air in the porous media, while the real part (resistance) accounts for the opposition to the sound wave propagation [101]. The higher the reactance and resistance response, the lower the resulting sound absorption coefficient.

Figure 6.11 shows that P1 exhibits the lowest resistance at all frequencies. In contrast, samples prepared under P2 show higher resistance especially between the 800-1200 Hz range. Furthermore, samples prepared under P3 exhibit the highest resistance at all the frequencies, and highest negative value of reactance after 1000 Hz.

The impedance results align well with the sound absorption results. As resistance increases and reactance decreases, the sound absorption coefficient decreases, indicating that varying process conditions alter pore size, porosity, interconnectivity, ultimately affecting the acoustic absorption performance.

Correlating the process conditions, porous structure, and acoustic performance reveals that increasing the rotational speed decreases droplet size, leading to smaller pores and more closed pores filled with solidified silicon oil. Consequently, sample P2 and P3 exhibit lower porosity and connectivity but higher tortuosity compared to P1. This increased tortuosity enhances sound

absorption at lower frequencies (~500 Hz), while the higher porosity and connectivity of P1 samples enable better sound absorption at higher frequencies (~1100Hz). The large droplet and pore size in P1 samples allow for more effective evaporation, creating interconnected pore networks with throats and channels. This highly porous structure contributes to nearly perfect sound absorption at higher frequencies. In contrast, the low porosity of P3 samples limits their maximum sound absorption to 0.5. These findings demonstrate that the emulsification process can be tailored to control the microstructure and acoustic properties of the porous material, with tortuosity playing a key role in low-frequency absorption and porosity favoring high-frequency absorption.

It is worth noting that the error bars that observed in Figure 6.11 arise from slight differences in the porous structure due to the nature of evaporation. However, the trend of sound absorption performance remains consistent among the samples in each process.

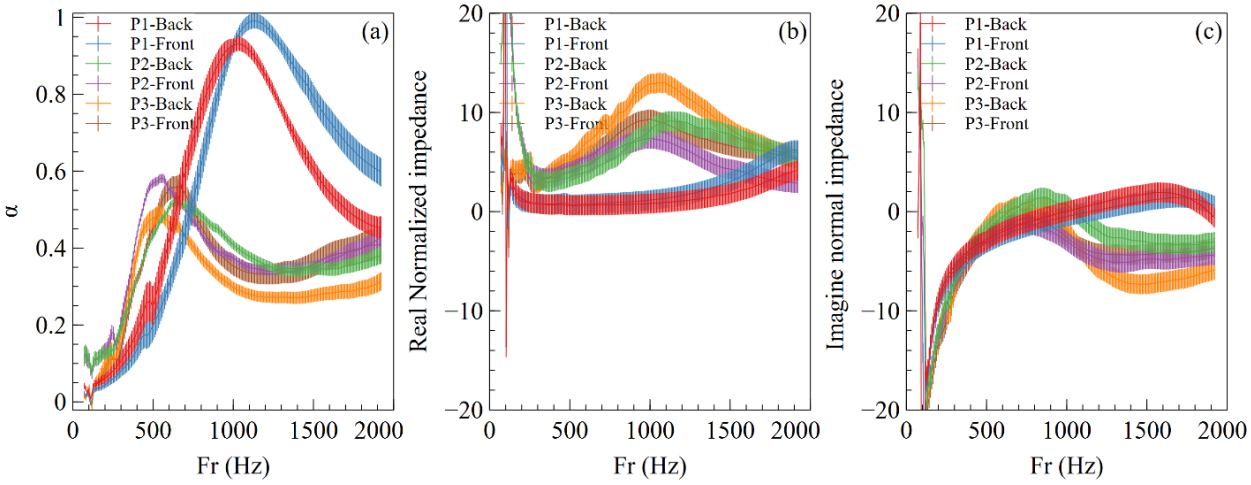

Figure 6.11. Acoustic performance of samples from front and back surface, (a) sound absorption coefficient, (b) Real normal impedance, (c) Imaginary normal impedance. The error bar represents the average of three sample in each process

Traditional porous materials such as melamine foam and glass wool exhibit a broadband response to sound absorption for mid to high frequencies with the first peak of absorption appearing at the so-called quarter-wave resonance according to the following equation[166]:

$$f = \frac{c}{4T} \tag{6.3}$$

where c is speed of sound in air, 340 m/s, and T is the thickness of samples.

Foams produced by the novel approach presented in this work demonstrate outstanding acoustic performance, particularly at frequencies lower that the quarter-wave resonance. For instance, the first absorption peaks for sample P1 and P2 are located at 1100 Hz, and 500 Hz, respectively. These frequencies would correspond to the absorption peaks of traditional foam with a thickness of 7 cm and 17 cm, respectively. The thickness of samples in this study is only 3 cm, suggesting that porous materials produced by HIPPE exhibit the so-called subwavelength behaviour. Although the sound absorption at 500 Hz is about 0.6, this foams can obtained higher absorption by increasing porosity and open pore connectivity. This unique characteristic provides significant advantages, such as achieving low-frequency sound absorption with minimal added mass. This is particularly valuable for applications where weight and space are critical constraints, offering a lightweight and compact solution for acoustic performance.

6.6 Conclusion

This study pioneers the production of acoustic porous material from HIPPE and examines the impact of process conditions on the droplet size, final porous microstructures, and the resulting sound absorption performance. The study demonstrates that this novel technique not only enables precise control over the pore size based on the original droplet size but also eliminates the need for foaming agents and monomers by utilizing polymeric particles as stabilizers. Furthermore, highly interconnected porous structure is achieved through spontaneous evaporation and particle sintering.

The strong correlation between process conditions, porous structure, and acoustic performance is established by comparing samples prepared under different conditions. The results show that the highest porosity and connectivity are achieved in sample which has the largest droplet and pore size, ultimately exhibiting a nearly perfect sound absorption around 1100 Hz. Moreover, the highest tortuosity with intermediate porosity, is found in the sample which has smaller droplet and pore size, demonstrating a sound absorption coefficient of 0.6 around 500 Hz. This sound absorption performance is achieved with a samples thickness of just 3 cm , demonstrating the potential of HIPPE-based porous structures to exhibit subwavelength behavior in sound absorption. The first absorption peak at 500 Hz and 1100 Hz, occur within this remarkably thin structure, offering a solution for applications where space and weight constraints are critical.

In conclusion, the HIPPE production approach offers a straightforward and versatile technique for creating acoustic porous materials. By simply adjusting the process conditions, such as increasing or decreasing the rotational speed during emulsification, it is possible to achieve the desired sound absorption properties. The ability to tailor the pore size and structure of the porous materials through careful control of the emulsion formulation and processing conditions offers a wide range of possibilities for designing materials with specific properties and applications. This study provides a foundation for future research into the development of novel porous materials with optimized properties and underscores the potential of HIPPE as a versatile and powerful tool for creating advanced materials.

CHAPTER 7 GENERAL DISCUSSION

This thesis pioneers a novel approach for producing acoustic porous materials using high internal phase Pickering emulsion. This method requires identifying the appropriate formulation and process conditions to achieve the desired pores size and, ultimately, the target sound absorption performance. The findings of this thesis advance the understanding of the production and scale-up of HIPPE in the laminar regime, while also demonstrating their potential as templates for acoustic porous materials. This work provides a comprehensive analysis of the process-structure-property relationship in HIPPEs.

Although the production of large droplets in this viscous emulsion is challenging, as it naturally tends to produce small droplets, we were able to control large droplet size by systematically investigating the effects of formulation and processing conditions. In the production of large-droplet HIPPEs, we determined its scale-up rules in the laminar regime, which never reported in the literature. Finally, the impact of droplet size on the porous structure and its corresponding sound absorption performance is well investigated using 3D visualization and is correlated with non-acoustical properties of porous material. The ability to precisely control pore size from droplets in an emulsion through a straightforward process highlights the versatility and industrial potential of this approach.

7.1 Challenges and Key Insights

Our approach in producing porous material form HIPPE for acoustic application encountered several challenges, such as identifying the appropriate particle with optimal contact angle at the oil-water interface, determining its concentration, and ensuring its high thermal resistance during evaporation of liquids at temperature close to 350˚C. Based on the literature, particles with contact angle close to 90˚ at the oil-water interface provide maximum stability. Recent studies by Tsabet [48] and Wang [46] showed that once the particle concentration exceeds the amount required to fully cover the droplet surface area, the final droplet size becomes predominantly controlled by processing conditions. Accordingly, the three levels of particle concentration were selected to ensure the desired pore size (100-800 microns) was achieved for optimal acoustic performance.

The selection of oil type, its viscosity and concentration are also posed challenges. Oil polarity [33] and viscosity [32] significantly affect final droplet size. To align with environmentally friendly

goals of this project, silicon oil was selected for its inertness and compatibility with both particle and continuous phase. While volatile and polar oils evaporate easily during curing, they destabilize emulsions by altering particle wettability, cause droplet collapse or bursting due to rapid evaporation and pose safety hazards in the work environment.

Through a combination of literature review and preliminary tests, we optimized the viscosity of silicon oil. We found that low-viscosity silicon oil in HIPPEs led to excessively large, flexible droplets prone to migration to the surface during curing, resulting in phase inversion and non-porous final structure. The optimal silicon oil viscosity for achieving maximum porosity and precise pore size control was determined to be in the range 100-200 cSt.

During evaporation, particles need to remain stable at their positions around the droplets. Additionally, the viscosity of continuous phase should be adjusted to provide sufficient power in the laminar regime. Preliminary tests and literature review indicated that polyvinyl alcohol (PVA) at concentrations of 2-4 wt.% is ideal for Pickering emulsions [167]. Additionally, we found that PVA decomposition and shrinkage during curing created several small holes in the pore walls, which are critical for achieving pore connectivity in acoustic applications.

Polyimide particles were selected for ideal contact angle ($\sim 90^{\circ}$ at the oil-PVA solutions interface), ability to sinter during curing and high thermal resistance. Using the capillary rise technique, the contact angle of Polyimide particles at oil-PVA solution interface were confirmed, ensuring optimal emulsion stability during storage and evaporation.

7.2 Key Findings

Overall, this project successfully demonstrated a novel approach to controlling pore size and interconnectivity, ultimately achieving the target sound absorption through the HIPPE production method. The first paper showed that although producing large droplets in HIPPEs is challenging due to their high viscosity, which naturally results in smaller droplets, large droplet sizes can still be achievable by optimizing the formulation and process conditions. This was accomplished by carefully selecting processing conditions and production equipment. While extensive research focused on the effect of processing conditions in the turbulent regime on droplet size, limited studies have addressed processing conditions in the laminar regime. These studies only employed microchannels for production HIPPEs, which are impractical for industrial applications. For this project, we employed a stirred vessel with a double helical ribbon impeller, which is widely used

for high viscosity mixing in industry. Although the Maxblend and the SuperBlend mixers could also be used for mixing HIPPEs, their small gap design could produce smaller droplets, making them less suitable for the intended application.

We also introduced a modified capillary number to describe droplet size correlation with processing conditions. Unlike prior assumptions in the literature, where a constant continuous phase viscosity is considered for capillary number estimation, our study accounted for the actual continuous phase viscosity, which depends on particle aggregation and processing conditions. Compared to previous studies by Bentley[139] and Grace[78], which reported capillary number value of 0.1 and 0.5 for elongational and simple shear flow involving a single drop, respectively, we found effective capillary numbers in the range of 0.005 and 0.03, emphasizing the significant impact of neighboring droplets and particle interactions on the drop equilibrium size in HIPPE.

The second paper addressed the knowledge gap in scaling up HIPPEs in the laminar regime. It demonstrated that, depending on the hydrodynamic criteria for scale-up, the rotational speed correlates with the impeller diameter, governed by different scale-up exponents (α). This relationship is summarized as $N_2 = N_1(\frac{D_1}{D_2})^{\alpha}$. We systematically investigated the exponents 0, 0.67, and 1, corresponding to constant power in the laminar regime, constant power in the turbulent regime, and constant tip speed, respectively.

Al-Haiek [56] established scale-up rules for Pickering emulsion in the turbulent regime, determining a scale-up exponent of 0.8 for emulsions which is between α 0.67 and 1. Al-Haiek established that this value is valid since the solid-stabilized emulsion is a balance of two main component of which are droplet dispersion and particle suspension which required α=0.67 and 1, respectively. It is worth mentioning that Al-Haiek emulsification process included less than 60 vol% internal phase and used a 4-blade pitched-blade-turbine (PBT) and a 6-blade Rushen-turbine (RT) in the turbulent regime, while our study focused on high internal phase (> 74 vol.%) in the laminar regime. In contrast to Al-Haiek's findings, our research demonstrated that the most appropriate scale-up exponent for HIPPEs in the laminar regime is α=0, indicating that maintaining a constant rotational speed across all scales is necessary to achieve similar droplet size, provided that the geometry and the formulation remain constant across scales

Maintaining constant RPM at increasing scales may become unrealistic to reach industrial production. Challenges in maintaining high rotational speed at pilot scales due to equipment limitations were addressed by decreasing the gap between the impeller and tank walls to increase shear rates. The smaller gap allowed for higher shear rates and provided sufficient breakage capacity, without increasing the rotational speed at the level required by the $\alpha=0$ relationship. Adjusting the formulation by increasing the continuous phase viscosity was another effective strategy generating sufficient power for droplet breakage. Ultimately, maintaining constant power per volume was identified as the key factor for achieving consistent droplet size across scales. This finding is key to successful scaleup of HIPPE processing equipment and constitutes a very effective guideline for producers.

The third paper introduced a novel approach for producing acoustic porous materials from HIPPEs. Acoustic porous material should have open pores with high connectivity to allow sound wave penetration and high viscous and thermal dissipation. Higher number of open pores and porosity in the porous material let the sound wave to penetrate, which is essential for achieving higher sound absorption. Moreover, the complexity in the morphology and topology of porous structure increases the tortuosity of sample, which is beneficial for sound absorption at low frequency. We demonstrated the potential of HIPPE in controlling pore size, porosity, and tortuosity. By simply adjusting the rotational speed, we created porous structures with varying pore size, porosity, connectivity, and tortuosity, which ultimately impacted the sound absorption performance. Samples with highest tortuosity exhibited the highest sound absorption coefficient at 500 Hz. However, at higher frequencies, their absorption coefficient sharply decreases due to low porosity. Conversely, samples with the largest pore size, highest porosity, and highest connectivity demonstrated the maximum sound absorption coefficient at 1000 Hz, as their structure allowed sound wave to penetrate effectively with minimal resistance.

The state-of-the-art X-ray micro-CT scan tool facilitates the microstructure analysis in 3D reconstructed view of samples. For the first time, we utilized the open-source workflow Open Pore Network Modeling (Open PNM) within the Dragonfly software to analyze reconstructed 3D images of the acoustic porous structures. The combination of 3D scans and software analysis tools allowed us to obtain the pore size distribution throughout the entire 3D structure, as well as visualize and analyze the connectivity among pores. Additionally, the tortuosity and porosity of

each sample were calculated using OpenPNM, closely aligned with the experimental values, confirming the accuracy and validity of the network analysis.

In this third phase of our work, we observed that some oil droplets became trapped in small pores, and the silicon oil solidified at high temperatures during the preparation of the porous structure. This trapped and solidified oil resulted in closed pores leading to reduced porosity and reduced pores connectivity. The results on the sound-proofing characteristics were a lower (20% lower than the best sample) sound absorption at high frequencies. This highlights the need for further formulation optimization to reduce the risk of closed pores and enhance sound absorption across a wider frequency range.

The concept of increasing tortuosity to enhance sound absorption at lower frequencies has been explored in studies on hybrid foams. However, our findings show a significant improvement in absorption. For example, while polyurethane-carbon nanotube (PU/CNT) foams achieved a sound absorption coefficient of 0.3 at 500 Hz and melamine-graphene hybrid (MF-GO) foams reached 0.4 [97], our samples with the highest tortuosity attained 0.6 [98], a 50% increase over MF-GO foams.

The findings from these three papers demonstrate that controlling process conditions and formulation in HIPPE production to achieve target acoustic performance in porous materials is a straightforward and environmentally friendly approach—one that has not been previously reported in the literature. This research also highlights the versatility of HIPPEs as templates for the simple and cost-effective production of high-performance acoustic materials. By enabling precise control over pore size through straightforward adjustments to processing conditions, our HIPPE-based approach shows promise for diverse industrial applications. However, further optimization of the formulation is necessary to eliminate closed pores and improve the sound absorption coefficient across a broader frequency range.

CHAPTER 8 CONCLUSION AND RECOMENDATIONS

8.1 Conclusion

This thesis investigated a novel approach for producing acoustic porous materials from high internal phase Pickering emulsions (HIPPEs). The first objective focused on producing monodisperse large droplet from HIPPE by controlling processing conditions and formulation. It was found that the particle aggregation structure, influenced by the revolution number of the impeller, the shear rate, and varying PVA concentrations, play critical role in droplet size. Finer particles stabilized smaller droplets, while larger particles resulted in larger droplets. By studying particle aggregation under different process conditions and formulation, it was determined that the fractal dimension (D_f), compactness of particles (k_g) and particle radius (R_g) are affected by PVA content, process conditions and emulsification time. These factors are crucial for controlling the final droplet size at the explored conditions. In the first paper, published in *Industrial and Engineering chemistry research* journal it was demonstrated that the effective viscosity of the continuous phase, which is measured through in-situ torque meter and varies with process conditions, emulsification time, and formulation, leading to more accurate calculation of capillary number and viscosity ratio, resulted in accurate prediction of droplet size. Employing a modified capillary number based on actual viscosity of the emulsion provides and effective tool for controlling droplet size in industrial emulsion production. These findings enhance the understanding of the relationship between capillary number-viscosity ratios, particle properties, and processing parameters. The ability to adjust emulsion characteristics by modifying key factors offers valuable insights for the design and optimization of emulsion systems with tailored properties.

The second paper of this thesis, submitted in *Chemical Engineering Research and Design* journal examines the impact of the scale-up rules on high internal phase Pickering emulsion in laminar mixing flow. The findings reveal that a scale-up exponent of $\alpha=0$ (constant rotational speed) is a practical approach for achieving consistent droplet size across scales ranging from 10 mL to 30 L. At this scale-up exponent, maintaining constant *P/V* ensures consistent droplet breakage and results in similar droplet sizes. Constant *P/V* can be achieved either by maintaining a constant rotational speed with a preestablished formulation or by increasing the continuous phase viscosity when equipment limitations prevent rotational speed increases. This paper also reported that a strong

correlation between droplet size and emulsion rheology allows for accurate estimation of *P/V* based on viscosity. This study also demonstrated that D_{32} evolves with specific energy input per volume (*e/V*) until equilibrium droplet size is reached, after which it correlates directly with *P/V*. This correlation between energy, power and droplet size, along with the identification the appropriate scale-up exponent, provides valuable predictive tool for emulsion production. Engineers can use this framework to estimate the required power and energy to achieve target droplet size based on lab-scale data, supporting efficient and consistent production across scales. This approach enhances the scalability of HIPPE productions while ensuring process optimization and product quality.

The third paper, submitted to *Journal of Material Science* examined the impact of process conditions on the droplet size, final porous microstructures, and the resulting sound absorption performance. The study demonstrates that this novel technique not only enables precise control over the pore size based on the original droplet size but also eliminates the need for foaming agents and monomers by utilizing polymeric particles as stabilizers. Furthermore, highly interconnected porous structure is achieved through spontaneous evaporation and particle sintering.

The strong correlation between process conditions, porous structure, and acoustic performance is established by comparing samples prepared under varying process conditions. The results show that the highest porosity and connectivity are achieved in samples with large pores, which are obtained with low rotational speed, ultimately exhibiting a nearly perfect sound absorption around 1100 Hz. In contrast, samples with smaller pore size exhibit the highest tortuosity with intermediate porosity, and have a sound absorption coefficient of 0.6 around 500 Hz. This sound absorption performance is achieved with a samples thickness of just 3 cm , demonstrating the potential of HIPPE-based porous structures to exhibit subwavelength behavior in sound absorption offering a solution for applications where space and weight constraints are critical.

In conclusion, the HIPPE production approach offers a straightforward and versatile technique for creating acoustic porous materials. By simply adjusting the process conditions, such as increasing or decreasing the rotational speed during emulsification, it is possible to achieve the desired sound absorption properties. The ability to tailor the pore size and structure of the porous materials through careful control of the emulsion formulation and processing conditions offers a wide range of possibilities for designing materials with specific properties and applications. This study provides a foundation for future research into the development of novel porous materials with

optimized properties and underscores the potential of HIPPE as a powerful tool for creating advanced materials.

8.2 Recommendation

Based on the findings of this research, several recommendations are proposed to guide future studies:

8.2.1 Correlation Between Droplet Size and Processing Conditions

This work established a correlation between the droplet size distribution and the processing conditions using a modified capillary number. The improvement involves considering the actual viscosity of the continuous phase, measured in-situ through torque measurements, rather than assuming constant viscosity. The findings reveal that decreasing particle size shifts the capillary-viscosity ratio curve toward smaller *Ca* number. While this study focused on three group of particles (radius of 1-2 micron), further validation with other particles, especially nano particles commonly used in their Pickering emulsions, would be beneficial. This investigation could help develop a master curve to better understand the effect of particle size and shape on the capillary number, ultimately advancing the control of droplet size in HIPPE productions.

8.2.2 Extension of the Scale-up Exponent to Other Mixers

Our experiments involved only one geometry of mixer i.e., the double helical ribbon. Other mixers, such as the SuperBlend and the Maxblend mixers demonstrated effectiveness in mixing highly viscous materials within the laminar flow regime. Further validation of the scale-up exponent ($\alpha = 0$) for these impellers is essential, particularly for producing HIPPEs with fine droplet sizes. This investigation could provide valuable insights into the effect impeller design on power consumption, enabling to optimization of process conditions to achieve target droplet size across different type of impellers.

8.2.3 Simulation Studies

At present, with the current numerical tools, simulating the complex Pickering emulsification process remains far beyond what is feasible. Such a simulation would need to account for multiple intricate phenomena, including particles entering and stabilizing curved droplet interfaces, coalescing semi-stabilized droplets, droplet breakage in high-shear zones, and particle suspension

within two-phase fluid mixing. However, advancement in next-generation numerical tools capable of simulating this Pickering emulsification process, would offer significant benefits in terms of time and cost savings. While experimental validation is still necessary to confirm the accuracy of simulated data, the number of required experiments would be reduced compared to fully experimental approaches, thereby enhancing efficiency, and enabling faster optimization of Pickering emulsification process.

8.2.4 Improvement of Acoustic Simulations

For acoustic performance prediction, some commercial software such as Geodict can be used to perform inverse characterization of microscopic structures. However, its inability to simulate tortuosity in alignment with experimental data suggests that modifications—such as accounting for semi-open pore structures—could improve the reliability of the simulation outputs.

In summary, this thesis introduces a novel and environmentally friendly approach to creating acoustic porous materials from HIPPEs, laying the groundwork for future developments in both fundamental research and industrial applications. By addressing current challenges and building on the recommendations provided, this work contributes significantly to advancing the field of HIPPEs and their diverse applications.

REFERENCES

[1] W. Konopka, M. Pawlaczyk-Łuszczyńska, and M. Śliwińska-Kowalska, “The influence of jet engine noise on hearing of technical staff,” *Med. Pr.*, vol. 65, no. 5, pp. 583–592, 2014, doi: 10.13075/mp.5893.00045.

[2] J. Vos and M. M. J. Houben, “Annoyance caused by the low-frequency sound produced by aircraft during takeoff,” *J. Acoust. Soc. Am.*, vol. 152, no. 6, pp. 3706–3715, 2022, doi: 10.1121/10.0016596.

[3] J. Ivošević, E. Ganić, A. Petošić, and T. Radišić, “Comparative uav noise-impact assessments through survey and noise measurements,” *Int. J. Environ. Res. Public Health*, vol. 18, no. 12, 2021, doi: 10.3390/ijerph18126202.

[4] X. Ma and Z. Su, “Development of acoustic liner in aero engine: a review,” *Sci. China Technol. Sci.*, vol. 63, no. 12, pp. 2491–2504, Dec. 2020, doi: 10.1007/s11431-019-1501-3.

[5] B. S. Beck, N. H. Schiller, and M. G. Jones, “Impedance assessment of a dual-resonance acoustic liner,” *Appl. Acoust.*, vol. 93, pp. 15–22, 2015, doi: 10.1016/j.apacoust.2015.01.011.

[6] Y. Tang *et al.*, “Hybrid acoustic metamaterial as super absorber for broadband low-frequency sound,” *Sci. Rep.*, vol. 7, no. July 2016, pp. 1–11, 2017, doi: 10.1038/srep43340.

[7] Y. Li and B. M. Assouar, “Acoustic metasurface-based perfect absorber with deep subwavelength thickness,” *Appl. Phys. Lett.*, vol. 108, no. 6, 2016, doi: 10.1063/1.4941338.

[8] C. Chen, Z. Du, G. Hu, and J. Yang, “A low-frequency sound absorbing material with subwavelength thickness,” *Appl. Phys. Lett.*, vol. 110, no. 22, 2017, doi: 10.1063/1.4984095.

[9] Y. Tao, M. Ren, H. Zhang, and T. Peijs, “Recent progress in acoustic materials and noise control strategies – A review,” *Appl. Mater. Today*, vol. 24, p. 101141, 2021, doi: 10.1016/j.apmt.2021.101141.

[10] J. H. Park *et al.*, “Optimization of low frequency sound absorption by cell size control and multiscale poroacoustics modeling,” *J. Sound Vib.*, vol. 397, pp. 17–30, Jun. 2017, doi: 10.1016/j.jsv.2017.03.004.

[11] G. Sung, S. K. Kim, J. W. Kim, and J. H. Kim, “Effect of isocyanate molecular structures

in fabricating flexible polyurethane foams on sound absorption behavior," *Polym. Test.*, vol. 53, pp. 156–164, Aug. 2016, doi: 10.1016/j.polymertesting.2016.05.028.

[12] J. G. Gwon, S. K. Kim, and J. H. Kim, "Development of cell morphologies in manufacturing flexible polyurethane urea foams as sound absorption materials," *J. Porous Mater.*, vol. 23, no. 2, pp. 465–473, Apr. 2016, doi: 10.1007/s10934-015-0100-0.

[13] A. Shi, X. Feng, Q. Wang, and B. Adhikari, "Pickering and high internal phase Pickering emulsions stabilized by protein-based particles: A review of synthesis, application and prospective," *Food Hydrocoll.*, vol. 109, p. 106117, Dec. 2020, doi: 10.1016/j.foodhyd.2020.106117.

[14] S. U. Pickering, "CXCVI.—Emulsions," *J. Chem. Soc., Trans.*, vol. 91, no. 0, pp. 2001–2021, 1907, doi: 10.1039/CT9079102001.

[15] T. Yang, Y. Hu, C. Wang, and B. P. Binks, "Fabrication of Hierarchical Macroporous Biocompatible Scaffolds by Combining Pickering High Internal Phase Emulsion Templates with Three-Dimensional Printing," *ACS Appl. Mater. Interfaces*, vol. 9, no. 27, pp. 22950–22958, Jul. 2017, doi: 10.1021/acsami.7b05012.

[16] A. M. B. Rodriguez and B. P. Binks, "Catalysis in Pickering emulsions," *Soft Matter*, vol. 16, no. 45, pp. 10221–10243, 2020, doi: 10.1039/d0sm01636e.

[17] S. Nagarajan *et al.*, "Porous Gelatin Membrane Obtained from Pickering Emulsions Stabilized by Graphene Oxide," *Langmuir*, vol. 34, no. 4, pp. 1542–1549, Jan. 2018, doi: 10.1021/acs.langmuir.7b03426.

[18] L. Cao, Q. Fu, Y. Si, B. Ding, and J. Yu, "Porous materials for sound absorption," *Compos. Commun.*, vol. 10, pp. 25–35, Dec. 2018, doi: 10.1016/j.coco.2018.05.001.

[19] S. Kinra and R. Pal, "Rheology of Pickering Emulsions Stabilized and Thickened by Cellulose Nanocrystals over Broad Ranges of Oil and Nanocrystal Concentrations," *Colloids and Interfaces*, vol. 7, no. 2, p. 36, Apr. 2023, doi: 10.3390/colloids7020036.

[20] C. Albert, M. Beladjine, N. Tsapis, E. Fattal, F. Agnely, and N. Huang, "Pickering emulsions: Preparation processes, key parameters governing their properties and potential for pharmaceutical applications," *J. Control. Release*, vol. 309, pp. 302–332, Sep. 2019, doi: 10.1016/j.jconrel.2019.07.003.

[21] N. J. Edward L, Paul (Merck & Co., Inc. Rahway, M. Victor A, Atiemo-Obeng (The Dow Chemical Company Midland, and C. Suzanne M, Kresta (University of Alberta Edmonton, Eds., *HANDBOOK OF INDUSTRIAL MIXING*, vol. 1. John Wiley & Sons, Inc.: New Jersey, 2004.

[22] A. Marefati and M. Rayner, "Starch granule stabilized Pickering emulsions: an 8-year stability study," *J. Sci. Food Agric.*, vol. 100, no. 6, pp. 2807–2811, 2020, doi: 10.1002/jsfa.10289.

[23] B. P. Binks, "Particles as surfactants—similarities and differences," *Curr. Opin. Colloid Interface Sci.*, vol. 7, no. 1–2, pp. 21–41, Mar. 2002, doi: 10.1016/S1359-0294(02)00008-0.

[24] J. Frelichowska, M.-A. Bolzinger, J. Pelletier, J.-P. Valour, and Y. Chevalier, "Topical delivery of lipophilic drugs from o/w Pickering emulsions," *Int. J. Pharm.*, vol. 371, no. 1–2, pp. 56–63, Apr. 2009, doi: 10.1016/j.ijpharm.2008.12.017.

[25] K. Zhang, W. Wu, K. Guo, J. Chen, and P. Zhang, "Synthesis of temperature-responsive poly(N-isopropyl acrylamide)/ poly(methyl methacrvlate)/silica hybrid capsules from inverse pickering emulsion polymerization and their application in controlled drug release," *Langmuir*, vol. 26, no. 11, pp. 7971–7980, 2010, doi: 10.1021/la904841m.

[26] L. Chen, F. Ao, X. Ge, and W. Shen, "Food-Grade Pickering Emulsions: Preparation, Stabilization and Applications," *Molecules*, vol. 25, no. 14, p. 3202, Jul. 2020, doi: 10.3390/molecules25143202.

[27] Y.-S. Wei, Z.-C. Niu, F.-Q. Wang, K. Feng, M.-H. Zong, and H. Wu, "A novel Pickering emulsion system as the carrier of tocopheryl acetate for its application in cosmetics.," *Mater. Sci. Eng. C. Mater. Biol. Appl.*, vol. 109, p. 110503, Apr. 2020, doi: 10.1016/j.msec.2019.110503.

[28] D. Gonzalez Ortiz, C. Pochat-Bohatier, J. Cambedouzou, M. Bechelany, and P. Miele, "Current Trends in Pickering Emulsions: Particle Morphology and Applications," *Engineering*, vol. 6, no. 4, pp. 468–482, Apr. 2020, doi: 10.1016/j.eng.2019.08.017.

[29] B. P. Binks and S. O. Lumsdon, "Influence of Particle Wettability on the Type and Stability of Surfactant-Free Emulsions," *Langmuir*, vol. 16, no. 23, pp. 8622–8631, Nov. 2000, doi: 10.1021/la000189s.

[30] R. Pal, “A simple model for the viscosity of pickering emulsions,” *Fluids*, vol. 3, no. 1, 2018, doi: 10.3390/fluids3010002.

[31] S. Levine and B. D. Bowen, “Capillary interaction of spherical particles adsorbed on the surface of an oil/water droplet stabilized by the particles. Part I,” *Colloids and Surfaces*, vol. 59, pp. 377–386, Nov. 1991, doi: 10.1016/0166-6622(91)80260-U.

[32] È. Tsabet and L. Fradette, “Effect of the properties of oil, particles, and water on the production of Pickering emulsions,” *Chem. Eng. Res. Des.*, vol. 97, pp. 9–17, May 2015, doi: 10.1016/j.cherd.2015.02.016.

[33] B. P. Binks and J. H. Clint, “Solid wettability from surface energy components: Relevance to pickering emulsions,” *Langmuir*, vol. 18, no. 4, pp. 1270–1273, 2002, doi: 10.1021/la011420k.

[34] V. N. Paunov, O. J. Cayre, P. F. Noble, S. D. Stoyanov, K. P. Velikov, and M. Golding, “Emulsions stabilised by food colloid particles: Role of particle adsorption and wettability at the liquid interface,” *J. Colloid Interface Sci.*, vol. 312, no. 2, pp. 381–389, 2007, doi: 10.1016/j.jcis.2007.03.031.

[35] R. Aveyard, B. P. Binks, and J. H. Clint, “Emulsions stabilised solely by colloidal particles,” *Adv. Colloid Interface Sci.*, vol. 100–102, no. SUPPL., pp. 503–546, 2003, doi: 10.1016/S0001-8686(02)00069-6.

[36] B. P. Binks and S. O. Lumsdon, “Pickering emulsions stabilized by monodisperse latex particles: Effects of particle size,” *Langmuir*, vol. 17, no. 15, pp. 4540–4547, 2001, doi: 10.1021/la0103822.

[37] H. Tan, G. Sun, W. Lin, C. Mu, and T. Ngai, “Gelatin particle-stabilized high internal phase emulsions as nutraceutical containers,” *ACS Appl. Mater. Interfaces*, vol. 6, no. 16, pp. 13977–13984, 2014, doi: 10.1021/am503341j.

[38] T. Yang, J. Zheng, B. S. Zheng, F. Liu, S. Wang, and C. H. Tang, “High internal phase emulsions stabilized by starch nanocrystals,” *Food Hydrocoll.*, vol. 82, pp. 230–238, 2018, doi: 10.1016/j.foodhyd.2018.04.006.

[39] I. Capron and B. Cathala, “Surfactant-free high internal phase emulsions stabilized by cellulose nanocrystals,” *Biomacromolecules*, vol. 14, no. 2, pp. 291–296, 2013, doi:

10.1021/bm301871k.

[40] Y. T. Xu, T. X. Liu, and C. H. Tang, “Novel pickering high internal phase emulsion gels stabilized solely by soy β-conglycinin,” *Food Hydrocoll.*, vol. 88, no. September 2018, pp. 21–30, 2019, doi: 10.1016/j.foodhyd.2018.09.031.

[41] M. A. Creighton, Y. Ohata, J. Miyawaki, A. Bose, and R. H. Hurt, “Two-Dimensional Materials as Emulsion Stabilizers: Interfacial Thermodynamics and Molecular Barrier Properties,” *Langmuir*, vol. 30, no. 13, pp. 3687–3696, Apr. 2014, doi: 10.1021/la500216n.

[42] Abdullah, J. Weiss, T. Ahmad, C. Zhang, and H. Zhang, “A review of recent progress on high internal-phase Pickering emulsions in food science,” *Trends Food Sci. Technol.*, vol. 106, pp. 91–103, Dec. 2020, doi: 10.1016/j.tifs.2020.10.016.

[43] B. P. Binks and C. P. Whitby, “Nanoparticle silica-stabilised oil-in-water emulsions: improving emulsion stability,” *Colloids Surfaces A Physicochem. Eng. Asp.*, vol. 253, no. 1–3, pp. 105–115, Feb. 2005, doi: 10.1016/j.colsurfa.2004.10.116.

[44] T. S. Horozov, B. P. Binks, and T. Gottschalk-Gaudig, “Effect of electrolyte in silicone oil-in-water emulsions stabilised by fumed silica particles,” *Phys. Chem. Chem. Phys.*, vol. 9, no. 48, p. 6398—6404, Dec. 2007, doi: 10.1039/b709807n.

[45] Y. Chevalier and M.-A. Bolzinger, “Emulsions stabilized with solid nanoparticles: Pickering emulsions,” *Physicochem. Eng. Asp.*, vol. 439, pp. 23–34, 2013, doi: 10.1016/j.colsurfa.2013.02.054.

[46] B. Wan and L. Fradette, “Phase inversion of a solid-stabilized emulsion: Effect of particle concentration,” *Can. J. Chem. Eng.*, vol. 95, no. 10, pp. 1925–1933, Oct. 2017, doi: 10.1002/cjce.22892.

[47] J. Frelichowska, M.-A. Bolzinger, and Y. Chevalier, “Effects of solid particle content on properties of o/w Pickering emulsions,” *J. Colloid Interface Sci.*, vol. 351, no. 2, pp. 348–356, Nov. 2010, doi: 10.1016/j.jcis.2010.08.019.

[48] È. Tsabet and L. Fradette, “Semiempirical Approach for Predicting the Mean Size of Solid-Stabilized Emulsions,” *Ind. Eng. Chem. Res.*, vol. 54, no. 46, pp. 11661–11677, Nov. 2015, doi: 10.1021/acs.iecr.5b02910.

[49] B. Wan, E. Tsabet, and L. Fradette, “Impact of Particles on Breakage and Coalescence Processes during the Preparation of Solid-Stabilized Emulsions,” *Ind. Eng. Chem. Res.*, vol. 58, no. 14, pp. 5631–5639, Apr. 2019, doi: 10.1021/acs.iecr.8b05900.

[50] M. V. Kempin, M. Kraume, and A. Drews, “W/O Pickering emulsion preparation using a batch rotor-stator mixer – Influence on rheology, drop size distribution and filtration behavior,” *J. Colloid Interface Sci.*, vol. 573, pp. 135–149, Aug. 2020, doi: 10.1016/j.jcis.2020.03.103.

[51] K. Köhler, A. S. Santana, B. Braisch, R. Preis, and H. P. Schuchmann, “High pressure emulsification with nano-particles as stabilizing agents,” *Chem. Eng. Sci.*, vol. 65, no. 10, pp. 2957–2964, May 2010, doi: 10.1016/j.ces.2010.01.020.

[52] A. Gupta, H. B. Eral, T. A. Hatton, and P. S. Doyle, “Controlling and predicting droplet size of nanoemulsions: scaling relations with experimental validation,” *Soft Matter*, vol. 12, no. 5, pp. 1452–1458, 2016, doi: 10.1039/C5SM02051D.

[53] R. G. Holdich, I. Y. Ipek, M. Lazrigh, and G. Shama, “Production and evaluation of floating photocatalytic composite particles formed using pickering emulsions and membrane emulsification,” *Ind. Eng. Chem. Res.*, vol. 51, no. 38, pp. 12509–12516, 2012, doi: 10.1021/ie3001748.

[54] X. Yao, Z. Liu, M. Ma, Y. Chao, Y. Gao, and T. Kong, “Control of Particle Adsorption for Stability of Pickering Emulsions in Microfluidics,” *Small*, vol. 14, no. 37, p. 1802902, Sep. 2018, doi: 10.1002/smll.201802902.

[55] È. Tsabet and L. Fradette, “Effect of Processing Parameters on the Production of Pickering Emulsions,” *Ind. Eng. Chem. Res.*, vol. 54, no. 7, pp. 2227–2236, Feb. 2015, doi: 10.1021/ie504338d.

[56] A. Al-haiek, “Titre: Scaling the Production of Solid-Stabilized Emulsions,” 2018.

[57] D. Donmez and I. Ayranci, “Effect of dispersed phase feed time on the droplet size of Pickering emulsions produced in a stirred tank,” *AIChE J.*, vol. 66, no. 6, Jun. 2020, doi: 10.1002/aic.16942.

[58] S. Röhl, L. Hohl, M. Kempin, F. Enders, N. Jurtz, and M. Kraume, “Influence of Different Silica Nanoparticles on Drop Size Distributions in Agitated Liquid-Liquid Systems,”

Chemie Ing. Tech., vol. 91, no. 11, pp. 1640–1655, Nov. 2019, doi: 10.1002/cite.201900049.

[59] A. Utomo, N. J. Alderman, G. A. Padron, and N. G. Özcan-Taşkın, "A comparative study on emulsification in the presence of a nanoclay (Pickering emulsion) or a surfactant using high intensity mixing," *Chem. Eng. Res. Des.*, vol. 197, pp. 617–627, 2023, doi: 10.1016/j.cherd.2023.07.041.

[60] H. T. Chen and S. Middleman, "Drop size distribution in agitated liquid-liquid systems," *AIChE J.*, vol. 13, no. 5, pp. 989–995, 1967, doi: 10.1002/aic.690130529.

[61] R. V. Calabrese, C. Y. Wang, and N. P. Bryner, "Drop breakup in turbulent stirred-tank contactors. Part III: Correlations for mean size and drop size distribution," *AIChE J.*, vol. 32, no. 4, pp. 677–681, 1986, doi: 10.1002/aic.690320418.

[62] B. Wolf, S. Lam, M. Kirkland, and W. J. Frith, "Shear thickening of an emulsion stabilized with hydrophilic silica particles," *J. Rheol. (N. Y. N. Y).*, vol. 51, no. 3, pp. 465–478, 2007, doi: 10.1122/1.2714642.

[63] R. Pal, "Viscosity-concentration relationships for nanodispersions based on glass transition point," *Can. J. Chem. Eng.*, vol. 95, no. 8, pp. 1605–1614, Aug. 2017, doi: 10.1002/cjce.22810.

[64] R. Pal, "Viscosity–Concentration Equation for Emulsions of Nearly Spherical Droplets," *J. Colloid Interface Sci.*, vol. 231, no. 1, pp. 168–175, Nov. 2000, doi: 10.1006/jcis.2000.7133.

[65] A. M. Bago Rodriguez and B. P. Binks, "High internal phase Pickering emulsions," *Curr. Opin. Colloid Interface Sci.*, vol. 57, p. 101556, Feb. 2022, doi: 10.1016/j.cocis.2021.101556.

[66] V. O. Ikem, A. Menner, T. S. Horozov, and A. Bismarck, "Highly Permeable Macroporous Polymers Synthesized from Pickering Medium and High Internal Phase Emulsion Templates," *Adv. Mater.*, vol. 22, no. 32, pp. 3588–3592, Aug. 2010, doi: 10.1002/adma.201000729.

[67] A. T. Tyowua, D. Harbottle, and B. P. Binks, "3D printing of Pickering emulsions, Pickering foams and capillary suspensions – A review of stabilization, rheology and applications," *Adv. Colloid Interface Sci.*, vol. 332, no. August, 2024, doi: 10.1016/j.cis.2024.103274.

[68] M. S. Silverstein, “PolyHIPEs: Recent advances in emulsion-templated porous polymers,” *Prog. Polym. Sci.*, vol. 39, no. 1, pp. 199–234, Jan. 2014, doi: 10.1016/j.progpolymsci.2013.07.003.

[69] N. R. Cameron, “High internal phase emulsion templating as a route to well-defined porous polymers,” *Polymer (Guildf).*, vol. 46, no. 5, pp. 1439–1449, 2005, doi: 10.1016/j.polymer.2004.11.097.

[70] Q. Zhao, F. Zaaboul, Y. Liu, and J. Li, “Recent advances on protein-based Pickering high internal phase emulsions (Pickering HIPEs): Fabrication, characterization, and applications,” *Compr. Rev. Food Sci. Food Saf.*, vol. 19, no. 4, pp. 1934–1968, 2020, doi: 10.1111/1541-4337.12570.

[71] U. K. Abdulrasaq and I. Ayranci, “The effect of hydrodynamic parameters on the production of Pickering emulsions in a baffled stirred tank,” *AIChE J.*, vol. 65, no. 10, pp. 1–12, 2019, doi: 10.1002/aic.16691.

[72] S. Arditty, C. P. Whitby, B. P. Binks, V. Schmitt, and F. Leal-Calderon, “Some general features of limited coalescence in solid-stabilized emulsions,” *Eur. Phys. J. E*, vol. 11, no. 3, pp. 273–281, 2003, doi: 10.1140/epje/i2003-10018-6.

[73] Y. Guntzburger, L. Fradette, M. Farhat, M. Héniche, P. A. Tanguy, and K. Takenaka, “Effect of the geometry on the performance of the Maxblend ™ impeller with viscous Newtonian fluids,” *Asia-Pacific J. Chem. Eng.*, vol. 4, no. 5, pp. 528–536, Sep. 2009, doi: 10.1002/apj.275.

[74] J. P. Gingras, L. Fradette, P. Tanguy, and E. Jorda, “Concentrated bitumen-in-water emulsification in coaxial mixers,” *Ind. Eng. Chem. Res.*, 2007, doi: https://doi.org/10.1021/ie061169+.

[75] B. Delacroix, L. Fradette, F. Bertrand, and B. Blais, “Which impeller should be chosen for efficient solid–liquid mixing in the laminar and transitional regime?,” *AIChE J.*, vol. 67, no. 11, Nov. 2021, doi: 10.1002/aic.17360.

[76] A. Kazemzadeh, F. Ein-Mozaffari, A. Lohi, and L. Pakzad, “Investigation of hydrodynamic performances of coaxial mixers in agitation of yield-pseudoplasitc fluids: Single and double central impellers in combination with the anchor,” *Chem. Eng. J.*, vol. 294, pp. 417–430,

2016, doi: 10.1016/j.cej.2016.03.010.

[77] N. A. M. F. (Editor) Suzanne M. Kresta (Editor), Arthur W. Etchells III (Editor), David S. Dickey (Editor), Victor A. Atiemo-Obeng (Editor), *Advances in Industrial Mixing: A Companion to the Handbook of Industrial Mixing*. WILEY, 2015.

[78] H. P. GRACE†, "DISPERSION PHENOMENA IN HIGH VISCOSITY IMMISCIBLE FLUID SYSTEMS AND APPLICATION OF STATIC MIXERS AS DISPERSION DEVICES IN SUCH SYSTEMS," *Chem. Eng. Commun.*, vol. 14, no. 3–6, pp. 225–277, Mar. 1982, doi: 10.1080/00986448208911047.

[79] L. Fradette, H. Z. Li, L. Choplin, and P. Tanguy, "Gas/liquid dispersions with a SMX static mixer in the laminar regime," *Chem. Eng. Sci.*, vol. 61, no. 11, pp. 3506–3518, 2006, doi: 10.1016/j.ces.2005.12.022.

[80] R. A. De Bruijn, "Tipstreaming of drops in simple shear flows," *Chem. Eng. Sci.*, vol. 48, no. 2, pp. 277–284, 1993, doi: https://doi.org/10.1016/0009-2509(93)80015-I.

[81] R. G. Larson, *The structure and rheology of complex fluids*, vol. 150. Newyork: oxford university press, 1999.

[82] F. J. Muzzio, M. Tjahjadi, and J. M. Ottino, "Self-similar drop-size distributions produced by breakup in chaotic flows," *Phys. Rev. Lett.*, vol. 67, no. 1, pp. 54–57, 1991, doi: 10.1103/PhysRevLett.67.54.

[83] V. Stobiac, L. Fradette, P. A. Tanguy, and F. Bertrand, "Pumping characterisation of the maxblend impeller for Newtonian and strongly non-Newtonian fluids," *Can. J. Chem. Eng.*, vol. 92, no. 4, pp. 729–741, 2014, doi: 10.1002/cjce.21906.

[84] T. Sharma, G. S. Kumar, and J. S. Sangwai, "Viscoelastic Properties of Oil-in-Water (o/w) Pickering Emulsion Stabilized by Surfactant–Polymer and Nanoparticle–Surfactant–Polymer Systems," *Ind. Eng. Chem. Res.*, vol. 54, no. 5, pp. 1576–1584, Feb. 2015, doi: 10.1021/ie504501a.

[85] X. Cheng, J. H. McCoy, J. N. Israelachvili, and I. Cohen, "Imaging the microscopic structure of shear thinning and thickening colloidal suspensions," *Science (80-.).*, vol. 333, no. 6047, pp. 1276–1279, 2011, doi: 10.1126/science.1207032.

[86] C. H. Lee, V. Moturi, and Y. Lee, “Thixotropic property in pharmaceutical formulations,” *J. Control. Release*, vol. 136, no. 2, pp. 88–98, 2009, doi: 10.1016/j.jconrel.2009.02.013.

[87] A. Y. Malkin, I. Masalova, P. Slatter, and K. Wilson, “Effect of droplet size on the rheological properties of highly-concentrated w/o emulsions,” *Rheol. Acta*, vol. 43, no. 6, pp. 584–591, Dec. 2004, doi: 10.1007/s00397-003-0347-2.

[88] B. Wu *et al.*, “Attractive Pickering Emulsion Gels,” *Adv. Mater.*, vol. 33, no. 33, p. 2102362, Aug. 2021, doi: 10.1002/adma.202102362.

[89] R. Pal, “Rheology of high internal phase ratio emulsions,” *Food Hydrocoll.*, vol. 20, no. 7, pp. 997–1005, Oct. 2006, doi: 10.1016/j.foodhyd.2005.12.001.

[90] M. Capdevila, A. Maestro, M. Porras, and J. M. Gutiérrez, “Preparation of Span 80/oil/water highly concentrated emulsions: Influence of composition and formation variables and scale-up,” *J. Colloid Interface Sci.*, vol. 345, no. 1, pp. 27–33, May 2010, doi: 10.1016/j.jcis.2010.01.045.

[91] J. P. Gingras, L. Fradette, P. Tanguy, and J. Bousquet, “Inline bitumen emulsification using static mixers,” *Ind. Eng. Chem. Res.*, vol. 46, no. 8, pp. 2618–2627, 2007, doi: 10.1021/ie0611913.

[92] A. May-Masnou, M. Porras, A. Maestro, C. González, and J. María Gutiérrez, “Scale invariants in the preparation of reverse high internal phase ratio emulsions,” *Chem. Eng. Sci.*, vol. 101, pp. 721–730, 2013, doi: 10.1016/j.ces.2013.07.033.

[93] A. May-Masnou, J. Ribó-Besolí, M. Porras, A. Maestro, C. González, and J. M. Gutiérrez, “Scale-up model obtained from the rheological analysis of highly concentrated emulsions prepared at three scales,” *Chem. Eng. Sci.*, vol. 111, pp. 410–420, 2014, doi: 10.1016/j.ces.2014.03.004.

[94] A. H. P. Skelland and R. Seksaria, “Minimum Impeller Speeds for Liquid-Liquid Dispersion in Baffled Vessels,” *Ind. Eng. Chem. Process Des. Dev.*, vol. 17, no. 1, pp. 56–61, 1978, doi: 10.1021/i260065a010.

[95] C. Bujoreanu, F. Nedeff, M. Benchea, and M. Agop, “Experimental and theoretical considerations on sound absorption performance of waste materials including the effect of backing plates,” *Appl. Acoust.*, vol. 119, pp. 88–93, Apr. 2017, doi:

10.1016/j.apacoust.2016.12.010.

[96] X. H. Yang, S. W. Ren, W. B. Wang, X. Liu, F. X. Xin, and T. J. Lu, “A simplistic unit cell model for sound absorption of cellular foams with fully/semi-open cells,” *Compos. Sci. Technol.*, vol. 118, pp. 276–283, Oct. 2015, doi: 10.1016/j.compscitech.2015.09.009.

[97] M. J. Nine, M. Ayub, A. C. Zander, D. N. H. Tran, B. S. Cazzolato, and D. Losic, “Graphene Oxide-Based Lamella Network for Enhanced Sound Absorption,” *Adv. Funct. Mater.*, vol. 27, no. 46, pp. 1–10, 2017, doi: 10.1002/adfm.201703820.

[98] A. Hasani Baferani, A. A. Katbab, and A. R. Ohadi, “The role of sonication time upon acoustic wave absorption efficiency, microstructure, and viscoelastic behavior of flexible polyurethane/CNT nanocomposite foam,” *Eur. Polym. J.*, vol. 90, pp. 383–391, May 2017, doi: 10.1016/j.eurpolymj.2017.03.042.

[99] Y. Huang, D. Zhou, Y. Xie, J. Yang, and J. Kong, “Tunable sound absorption of silicone rubber materials via mesoporous silica,” *RSC Adv.*, vol. 4, no. 29, pp. 15171–15179, 2014, doi: 10.1039/C4RA00970C.

[100] S. Ghaffari Mosanenzadeh, H. E. Naguib, C. B. Park, and N. Atalla, “Design and development of novel bio-based functionally graded foams for enhanced acoustic capabilities,” *J. Mater. Sci.*, vol. 50, no. 3, pp. 1248–1256, 2015, doi: 10.1007/s10853-014-8681-6.

[101] S. Butler, E. R. Fotsing, and A. Ross, “Acoustic thermoset open-cell foams produced by particulate leaching process,” *J. Mater. Sci.*, vol. 54, no. 19, pp. 12553–12572, Oct. 2019, doi: 10.1007/s10853-019-03790-4.

[102] E. R. Fotsing, A. Dubourg, A. Ross, and J. Mardjono, “Acoustic properties of periodic micro-structures obtained by additive manufacturing,” *Appl. Acoust.*, vol. 148, pp. 322–331, May 2019, doi: 10.1016/j.apacoust.2018.12.030.

[103] D. Oliva and V. Hongisto, “Sound absorption of porous materials - Accuracy of prediction methods,” *Appl. Acoust.*, vol. 74, no. 12, pp. 1473–1479, 2013, doi: 10.1016/j.apacoust.2013.06.004.

[104] S. R. Pride, F. D. Morgan, and A. F. Gangi, “Drag forces of porous-medium acoustics,” *Phys. Rev. B*, vol. 47, no. 9, pp. 4964–4978, 1993, doi: 10.1103/PhysRevB.47.4964.

[105] K. Verdiere, R. Panneton, N. Atalla, and S. Elkoun, “Inverse Poroelastic Characterization of Open-Cell Porous Materials Using an Impedance Tube,” in *SAE Technical Papers*, Jun. 2017, vol. 2017-June, no. June, doi: 10.4271/2017-01-1878.

[106] L. Jaouen, “Acoustical Porous Material Recipes.” https://apmr.matelys.com/Parameters/Characterization/Acoustics/OpenPorosity.html.

[107] D. Lafarge, P. Lemarinier, J. F. Allard, and V. Tarnow, “Dynamic compressibility of air in porous structures at audible frequencies,” *J. Acoust. Soc. Am.*, vol. 102, no. 4, pp. 1995–2006, Oct. 1997, doi: 10.1121/1.419690.

[108] D. L. Johnson, J. Koplik, and L. M. Schwartz, “New Pore-Size Parameter Characterizing Transport in Porous Media,” *Phys. Rev. Lett.*, vol. 57, no. 20, pp. 2564–2567, Nov. 1986, doi: 10.1103/PhysRevLett.57.2564.

[109] R. Panneton and X. Olny, “Acoustical determination of the parameters governing viscous dissipation in porous media,” *J. Acoust. Soc. Am.*, vol. 119, no. 4, pp. 2027–2040, 2006, doi: 10.1121/1.2169923.

[110] “Theoretical background for tortuosity,” *mecanum*, 2024. https://mecanum.com/measuring-instruments/tortuosity-meter/.

[111] J. Gostick *et al.*, “OpenPNM: A Pore Network Modeling Package,” *Comput. Sci. Eng.*, vol. 18, no. 4, pp. 60–74, Jul. 2016, doi: 10.1109/MCSE.2016.49.

[112] F. Košek, J. Dudák, V. Tymlová, J. Žemlička, D. Řimnáčová, and J. Jehlička, “Evaluation of pore-fracture microstructure of gypsum rock fragments using micro-CT,” *Micron*, vol. 181, no. February, 2024, doi: 10.1016/j.micron.2024.103633.

[113] S. Duan *et al.*, “Three-dimensional reconstruction and computational analysis of a structural battery composite electrolyte,” *Commun. Mater.*, vol. 4, no. 1, pp. 1–9, 2023, doi: 10.1038/s43246-023-00377-0.

[114] F. Sabri, K. Berthomier, C.-S. Wang, L. Fradette, J. R. Tavares, and N. Virgilio, “Tuning particle–particle interactions to control Pickering emulsions constituents separation,” *Green Chem.*, vol. 21, no. 5, pp. 1065–1074, 2019, doi: 10.1039/C8GC03007C.

[115] Y. Hu, S. Zou, W. Chen, Z. Tong, and C. Wang, “Mineralization and drug release of

hydroxyapatite/poly(l -lactic acid) nanocomposite scaffolds prepared by Pickering emulsion templating," *Colloids Surf. B*, vol. 122, pp. 559–565, Oct. 2014, doi: 10.1016/j.colsurfb.2014.07.032.

[116] J. Wu, W. Xue, C. Wang, H. Gu, J. Zhou, and W. Lin, "Bioactive Porous Protein Scaffolds Enabled by High Internal Phase Emulsion Templates," *Ind. Eng. Chem. Res.*, vol. 62, no. 44, pp. 18463–18472, Nov. 2023, doi: 10.1021/acs.iecr.3c02475.

[117] A. M. B. Rodriguez and B. P. Binks, "Catalysis in Pickering emulsions," *Soft Matter*, vol. 16, no. 45, pp. 10221–10243, 2020, doi: 10.1039/D0SM01636E.

[118] Y. Zhu, R. Zhang, S. Zhang, Y. Chu, and J. Chen, "Macroporous Polymers with Aligned Microporous Walls from Pickering High Internal Phase Emulsions," *Langmuir*, vol. 32, no. 24, pp. 6083–6088, 2016, doi: 10.1021/acs.langmuir.6b00794.

[119] G. P. Hao *et al.*, "Structurally designed synthesis of mechanically stable poly(benzoxazine-co- resol)-based porous carbon monoliths and their application as high-performance CO2 capture sorbents," *J. Am. Chem. Soc.*, vol. 133, no. 29, pp. 11378–11388, 2011, doi: 10.1021/ja203857g.

[120] M. Saghaei, A. Ross, E.-R. Fotsing, and L. Fradette, "Creating Optimized Acoustic Structure Via Concentrated Emulsions," *Can. Acoust.*, vol. 51, no. 3 SE-Proceedings of the Acoustics Week in Canada, pp. 148–149, Oct. 2023, [Online]. Available: https://jcaa.caa-aca.ca/index.php/jcaa/article/view/4120.

[121] F. Yi, F. Xu, Y. Gao, H. Li, and D. Chen, "Macrocellular polymer foams from water in oil high internal phase emulsion stabilized solely by polymer Janus nanoparticles: preparation and their application as support for Pd catalyst," *RSC Adv.*, vol. 5, no. 50, pp. 40227–40235, 2015, doi: 10.1039/C5RA01859E.

[122] X. Zhao, Y. Cui, J. Wang, and J. Wang, "Preparation of Fluorescent Molecularly Imprinted Polymers via Pickering Emulsion Interfaces and the Application for Visual Sensing Analysis of Listeria Monocytogenes," *Polymers (Basel).*, vol. 11, no. 6, p. 984, Jun. 2019, doi: 10.3390/polym11060984.

[123] J. Wu and G.-H. Ma, "Recent Studies of Pickering Emulsions: Particles Make the Difference," *Small*, vol. 12, no. 34, pp. 4633–4648, Sep. 2016, doi:

https://doi.org/10.1002/smll.201600877.

[124] Q. Y. Xu, M. Nakajima, and B. P. Binks, “Preparation of particle-stabilized oil-in-water emulsions with the microchannel emulsification method,” *Colloids Surfaces A Physicochem. Eng. Asp.*, vol. 262, no. 1–3, pp. 94–100, Jul. 2005, doi: 10.1016/j.colsurfa.2005.04.019.

[125] J. M. Zalc, E. S. Szalai, F. J. Muzzio, and S. Jaffer, “Characterization of flow and mixing in an SMX static mixer,” *AIChE J.*, vol. 48, no. 3, pp. 427–436, 2002, doi: 10.1002/aic.690480303.

[126] A. Kritikos, R. Singh, G. Tsilomelekis, and F. J. Muzzio, “A Novel CFD Model of SMX Static Mixer Used in Advanced Continuous Manufacturing of Active Pharmaceutical Ingredients (API),” *J. Pharm. Innov.*, vol. 19, no. 2, 2024, doi: 10.1007/s12247-024-09813-1.

[127] M. M. Alvarez, J. M. Zalc, T. Shinbrot, P. E. Arratia, and F. J. Muzzio, “Mechanisms of mixing and creation of structure in laminar stirred tanks,” *AIChE J.*, vol. 48, no. 10, pp. 2135–2148, 2002, doi: 10.1002/aic.690481005.

[128] G. Delaplace, J. C. Leuliet, and V. Relandeau, “Circulation and mixing times for helical ribbon impellers. Review and Experiments,” *Exp. Fluids*, vol. 28, no. 2, pp. 170–182, 2000, doi: 10.1007/s003480050022.

[129] P. J. Carreau, R. P. Chhabra, and J. Cheng, “Effect of rheological properties on power consumption with helical ribbon agitators,” *AIChE J.*, vol. 39, no. 9, pp. 1421–1430, Sep. 1993, doi: 10.1002/aic.690390902.

[130] E. Brito-De La Fuente, L. Choplin, and P. A. Tanguy, “Mixing with helical ribbon impellers: Effect of highly shear thinning behaviour and impeller geometry,” *Chem. Eng. Res. Des.*, vol. 75, no. 1, pp. 45–52, 1997, doi: 10.1205/026387697523381.

[131] G. C. Bushell, Y. D. Yan, D. Woodfield, J. Raper, and R. Amal, “On techniques for the measurement of the mass fractal dimension of aggregates,” *Adv. Colloid Interface Sci.*, vol. 95, no. 1, pp. 1–50, Jan. 2002, doi: 10.1016/S0001-8686(00)00078-6.

[132] S. Lazzari, L. Nicoud, B. Jaquet, M. Lattuada, and M. Morbidelli, “Fractal-like structures in colloid science,” *Adv. Colloid Interface Sci.*, vol. 235, pp. 1–13, Sep. 2016, doi:

10.1016/j.cis.2016.05.002.

[133] W. Krasny-Ergen, “Untersuchungen über die Viskosität von Suspensionen und Lösungen. 2. Zur Theorie der Elektroviskosität,” *Kolloid-Zeitschrift*, vol. 74, no. 2, pp. 172–178, Jun. 1936, doi: 10.1007/BF01429631.

[134] Yeow, “Improved Dielectric Model for Polyvinyl Alcohol-Water Hydrogel at Microwave Frequencies,” *Am. J. Appl. Sci.*, vol. 7, no. 2, pp. 270–276, Feb. 2010, doi: 10.3844/ajassp.2010.270.276.

[135] R. Pal, “New Generalized Viscosity Model for Non-Colloidal Suspensions and Emulsions,” *Fluids*, vol. 5, no. 3, p. 150, Sep. 2020, doi: 10.3390/fluids5030150.

[136] F. Zhou *et al.*, “Influences of surfactant (PVA) concentration and pH on the preparation of copper nanoparticles by electron beam irradiation,” *Radiat. Phys. Chem.*, vol. 77, no. 2, pp. 169–173, Feb. 2008, doi: 10.1016/j.radphyschem.2007.05.007.

[137] C. P. Johnson, X. Li, and B. E. Logan, “Settling Velocities of Fractal Aggregates,” *Environ. Sci. Technol.*, vol. 30, no. 6, pp. 1911–1918, May 1996, doi: 10.1021/es950604g.

[138] L. Fradette, P. Tanguy, H.-Z. Li, and L. Choplin, “Liquid/Liquid Viscous Dispersions with a SMX Static Mixer,” *Chem. Eng. Res. Des.*, vol. 85, no. 3, pp. 395–405, Jan. 2007, doi: 10.1205/cherd06206.

[139] B. J. Bentley and L. G. Leal, “An experimental investigation of drop deformation and breakup in steady, two-dimensional linear flows,” *J. Fluid Mech.*, vol. 167, no. 1, p. 241, Jun. 1986, doi: 10.1017/S0022112086002811.

[140] I. Gurevitch and M. S. Silverstein, “Polymerized pickering HIPEs: Effects of synthesis parameters on porous structure,” *J. Polym. Sci. Part A Polym. Chem.*, vol. 48, no. 7, pp. 1516–1525, Apr. 2010, doi: 10.1002/pola.23911.

[141] J. X. Liu, H. J. Zhu, P. Wang, and J. M. Pan, “Recent studies of Pickering emulsion system in petroleum treatment: The role of particles,” *Pet. Sci.*, vol. 18, no. 5, pp. 1551–1563, 2021, doi: 10.1016/j.petsci.2021.10.001.

[142] S. Arditty, V. Schmitt, J. Giermanska-Kahn, and F. Leal-Calderon, “Materials based on solid-stabilized emulsions,” *J. Colloid Interface Sci.*, vol. 275, no. 2, pp. 659–664, Jul. 2004,

doi: 10.1016/j.jcis.2004.03.001.

[143] H. Jiang, Y. Sheng, and T. Ngai, “Pickering emulsions: Versatility of colloidal particles and recent applications,” *Curr. Opin. Colloid Interface Sci.*, vol. 49, pp. 1–15, Oct. 2020, doi: 10.1016/j.cocis.2020.04.010.

[144] R. Pal, “Recent Developments in the Viscosity Modeling of Concentrated Monodisperse Emulsions,” *Foods*, vol. 12, no. 18, 2023, doi: 10.3390/foods12183483.

[145] I. Masalova, M. Taylor, E. Kharatiyan, and A. Y. Malkin, “Rheopexy in highly concentrated emulsions,” *J. Rheol. (N. Y. N. Y).*, vol. 49, no. 4, pp. 839–849, 2005, doi: 10.1122/1.1940641.

[146] M. Saghaei, E. R. Fotsing, A. Ross, and L. Fradette, “Production of Monodisperse Large Drop Emulsions by Means of High Internal Phase Pickering Emulsions─Processing and Formulation,” *Ind. Eng. Chem. Res.*, vol. 63, no. 42, pp. 17917–17929, Oct. 2024, doi: 10.1021/acs.iecr.4c01855.

[147] M. Bousmina, A. Ait-Kadi, and J. B. Faisant, “Determination of shear rate and viscosity from batch mixer data,” *J. Rheol. (N. Y. N. Y).*, vol. 43, no. 2, pp. 415–433, 1999, doi: 10.1122/1.551044.

[148] I. Ayranci and S. M. Kresta, “Critical analysis of Zwietering correlation for solids suspension in stirred tanks,” *Chem. Eng. Res. Des.*, vol. 92, no. 3, pp. 413–422, 2014, doi: 10.1016/j.cherd.2013.09.005.

[149] J. L. Salager, J. Bertrand, and M. Bricen, “Oil-in-Water Emulsions in the Transition,” *Carbon N. Y.*, vol. 79, no. November, pp. 419–426, 2001.

[150] L. Fritschi, A. L. Brown, R. Kim, D. Schwela, and S. Kephalopoulos, *Burden of disease from environmental noise: Quantification of healthy life years lost in Europe*, First Edit. Copenhagen (Denmark): WHO Regional Office for Europe, 2011.

[151] T. Zhang, R. A. Sanguramath, S. Israel, and M. S. Silverstein, “Emulsion Templating: Porous Polymers and Beyond,” *Macromolecules*, vol. 52, no. 15, pp. 5445–5479, Aug. 2019, doi: 10.1021/acs.macromol.8b02576.

[152] J. L. Robinson, R. S. Moglia, M. C. Stuebben, M. A. P. McEnery, and E. Cosgriff-

Hernandez, “Achieving Interconnected Pore Architecture in Injectable PolyHIPEs for Bone Tissue Engineering,” *Tissue Eng. Part A*, vol. 20, no. 5–6, pp. 1103–1112, Mar. 2014, doi: 10.1089/ten.tea.2013.0319.

[153] M. Ottens, G. Leene, A. A. C. M. Beenackers, N. Cameron, and D. C. Sherrington, “PolyHipe: A New Polymeric Support for Heterogeneous Catalytic Reactions: Kinetics of Hydration of Cyclohexene in Two- and Three-Phase Systems over a Strongly Acidic Sulfonated PolyHipe,” *Ind. Eng. Chem. Res.*, vol. 39, no. 2, pp. 259–266, Feb. 2000, doi: 10.1021/ie990452o.

[154] S. Kovačič, H. Kren, P. Krajnc, S. Koller, and C. Slugovc, “The use of an emulsion templated microcellular poly(dicyclopentadiene-co-norbornene) membrane as a separator in lithium-ion batteries.,” *Macromol. Rapid Commun.*, vol. 34, no. 7, pp. 581–7, Apr. 2013, doi: 10.1002/marc.201200754.

[155] R. Cai, Y. You, P. Wu, Q. Liu, Y. Zhu, and S. Zhang, “Preparation of Open-Cell Rigid Polyimide Foam via Nonaqueous High Internal Phase Emulsion-Templating Technique,” *ACS Appl. Polym. Mater.*, vol. 5, no. 10, pp. 7795–7804, 2023, doi: 10.1021/acsapm.3c00994.

[156] G. Mingliang and C. Luoxiang, “Nanohybrid drug carrier prepared by pickering emulsion template method with magadiite as emulsifier and preparation method therefor,” US20200222404A1, 2017.

[157] L. Leclercq *et al.*, “Pickering Emulsion Stabilized by Catalytic Polyoxometalate Nanoparticles: A New Effective Medium for Oxidation Reactions,” *Chem. - A Eur. J.*, vol. 18, no. 45, pp. 14352–14358, Nov. 2012, doi: 10.1002/chem.201201799.

[158] J. E. Norton and I. T. Norton, “Designer colloids—towards healthy everyday foods?,” *Soft Matter*, vol. 6, no. 16, p. 3735, 2010, doi: 10.1039/c001018a.

[159] W. Wu, S. Gao, W. Tu, J. Chen, and P. Zhang, “Intensified photocatalytic degradation of nitrobenzene by Pickering emulsion of ZnO nanoparticles,” *Particuology*, vol. 8, no. 5, pp. 453–457, Oct. 2010, doi: 10.1016/j.partic.2010.05.006.

[160] J. R. Houston Bragg, “Solid-stabilized emulsion, its use for oil recovery and process for its preparation,” DE19882406B4, 1998.

[161] W. Zhai, Z.-M. Wu, X. Wang, P. Song, Y. He, and R.-M. Wang, “Preparation of epoxy-acrylate copolymer@nano-TiO2 Pickering emulsion and its antibacterial activity,” *Prog. Org. Coatings*, vol. 87, pp. 122–128, Oct. 2015, doi: 10.1016/j.porgcoat.2015.05.019.

[162] D. J. Voorn, W. Ming, and A. M. van Herk, “Polymer−Clay Nanocomposite Latex Particles by Inverse Pickering Emulsion Polymerization Stabilized with Hydrophobic Montmorillonite Platelets,” *Macromolecules*, vol. 39, no. 6, pp. 2137–2143, Mar. 2006, doi: 10.1021/ma052539t.

[163] M. Bokhari, R. J. Carnachan, S. A. Przyborski, and N. R. Cameron, “Emulsion-templated porous polymers as scaffolds for three dimensional cell culture: effect of synthesis parameters on scaffold formation and homogeneity,” *J. Mater. Chem.*, vol. 17, no. 38, p. 4088, 2007, doi: 10.1039/b707499a.

[164] J. Fu, H. R. Thomas, and C. Li, “Tortuosity of porous media: Image analysis and physical simulation,” *Earth-Science Rev.*, vol. 212, no. October 2020, 2021, doi: 10.1016/j.earscirev.2020.103439.

[165] L. Holzer, P. Marmet, M. Fingerle, A. Wiegmann, M. Neumann, and V. Schmidt, *Tortuosity and Microstructure Effects in Porous Media*, vol. 333. Cham: Springer Nature Switzerland AG, 2023.

[166] J. F. Allard and N. Atalla, *Propagation of Sound in Porous Media: Modelling Sound Absorbing Materials*. 2009.

[167] M. A. Mudassir, H. Z. Aslam, T. M. Ansari, H. Zhang, and I. Hussain, “Fundamentals and Design-Led Synthesis of Emulsion-Templated Porous Materials for Environmental Applications,” *Adv. Sci.*, vol. 8, no. 22, p. 2102540, Nov. 2021, doi: 10.1002/advs.202102540.

[168] N. Raval, R. Maheshwari, D. Kalyane, S. R. Youngren-Ortiz, M. B. Chougule, and R. K. Tekade, *Importance of physicochemical characterization of nanoparticles in pharmaceutical product development*. Elsevier Inc., 2018.

[169] T. N. Zwietering, “Suspending of solid particles in liquid by agitators,” *Chem. Eng. Sci.*, vol. 8, no. 3–4, pp. 244–253, Jun. 1958, doi: 10.1016/0009-2509(58)85031-9.

[170] O. Bertrand, B. Blais, F. Bertrand, and L. Fradette, “Complementary methods for the

determination of the just-suspended speed and suspension state in a viscous solid-liquid mixing system," *Chem. Eng. Res. Des.*, vol. 136, pp. 32–40, 2018, doi: 10.1016/j.cherd.2018.04.035.

[171] I. Ayranci and S. M. Kresta, "Corrigendum to 'Critical analysis of Zwietering correlation for solids suspension in stirred tanks' [Chem. Eng. Res. Des. 92 (2014) 413–422, (S0263876213003675), (10.1016/j.cherd.2013.09.005)]," *Chem. Eng. Res. Des.*, vol. 209, no. August, p. 1, 2024, doi: 10.1016/j.cherd.2024.06.046.

APPENDIX A SUPPORTING INFORMATION FOR PAPER1

A.1 Polydispersity index and uniformity

The polydispersity equation represents the square ratio of standard deviation to the median size of the particle[168].

$$PDI = (\frac{\sigma}{d_{50}})^2 \quad \text{(S-1)}$$

The highest uniform particle size distribution has a PDI of 0.1. In our case, since the PDI is higher, it is concluded that a polydisperse emulsion is obtained. Furthermore, the uniformity number, obtained through the following equation (S-2), is higher than 0.1. This is another indication that we have a polydisperse distribution. However, this number does not exceed 0.5 in our emulsions, concluding that the emulsion has a unimodal size distribution graph.

$$uniformity = \frac{\sum vi|D_{50} - D_i|}{D_{50} \sum v_i} \quad \text{(S-2)}$$

A.2 Particle Video Microscopy images of samples

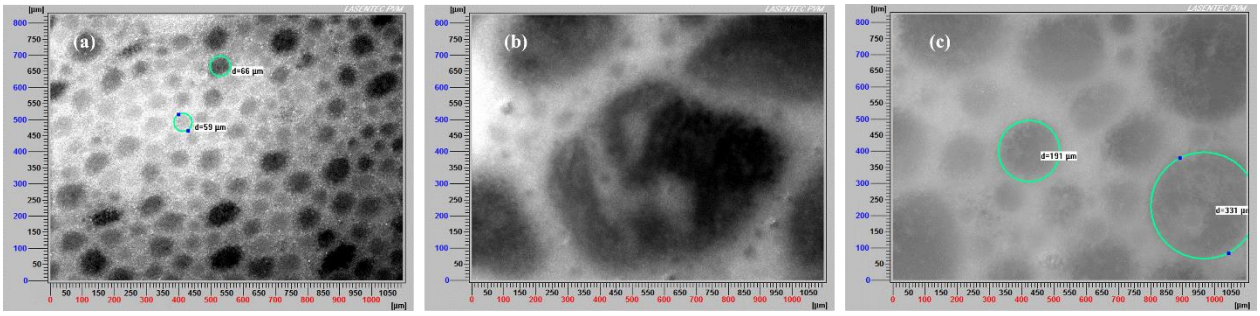

Figure A.1. PVM images of prepared emulsions at a) C6 condition, with PVA3 and PI 28 vol. b) C1 Condition, with PVA 2, PI 20 vol.% c) C3) C3 condition, with PVA 2, and PI 25 vol.%

A.3 Interfacial tension

Table A.1.Interfacial tension of PVA solutions with silicon oil

Solution	Interfacial tension (mN/m) with silicon oil 100cst
PVA 2 wt.%	27.73±0.05
PVA 3 wt.%	25.36±0.02
PVA 4 wt.%	24.64±0.01

A.4 Process conditions of samples in all groups defined for plotting *Ca* vs. *p*

Table A.2Three categories for plotting *Ca* vs. p

G1				G2				G3			
rpm	**Nr**	**oil**	**PVA**	**rpm**	**Nr**	**oil**	**PVA**	**rpm**	**Nr**	**oil**	**PVA**
100	800	75	2	100	800	80	3	100	1600	80	4
150	800	75	2	100	1600	80	3	150	1600	75	4
150	800	80	2	100	2400	75	3	150	2400	80	4
150	1600	75	2	150	800	80	3	100	2400	80	3
150	1600	80	2	150	1600	75	3	150	2400	80	3
150	2400	75	2	150	2400	75	3	100	800	80	4
100	800	75	3	100	2400	75	4	150	800	80	4
150	800	75	3	150	800	75	4	150	1600	80	3
100	1600	75	3	150	2400	80	2	150	1600	80	4
100	1600	80	2	100	2400	80	2	150	2400	75	4
100	1600	75	2	100	2400	75	2	100	2400	80	4
100	800	75	4	100	800	80	2	100	1600	75	4

A-5 SEM images of Polyimide particles in pre-determined Groups

SEM images reveal that the PVA chains formed clusters of particles; the PVA chain remains intact due to the freeze-drying method and attaches individual particles. Despite this clustering, individual particles can be detected, and their size evaluated. These SEM images confirm our results obtained from Mastersizer analysis, which indicated that the particles are not fully spherical, and that each particle is composed of an aggregation of nm-size particles.

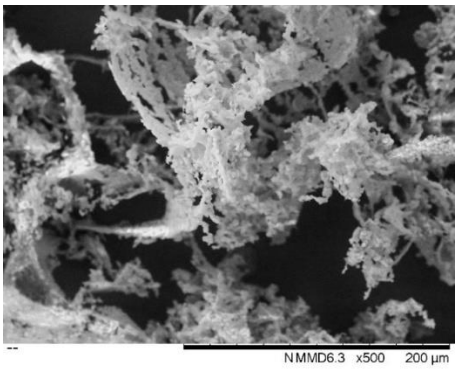

Figure A.2. SEM image of freeze-dried PVA-PI particles prepared with PVA 3wt.%, 80 vol% oil, at C1 condition.

A-6 Statistical analysis of particles

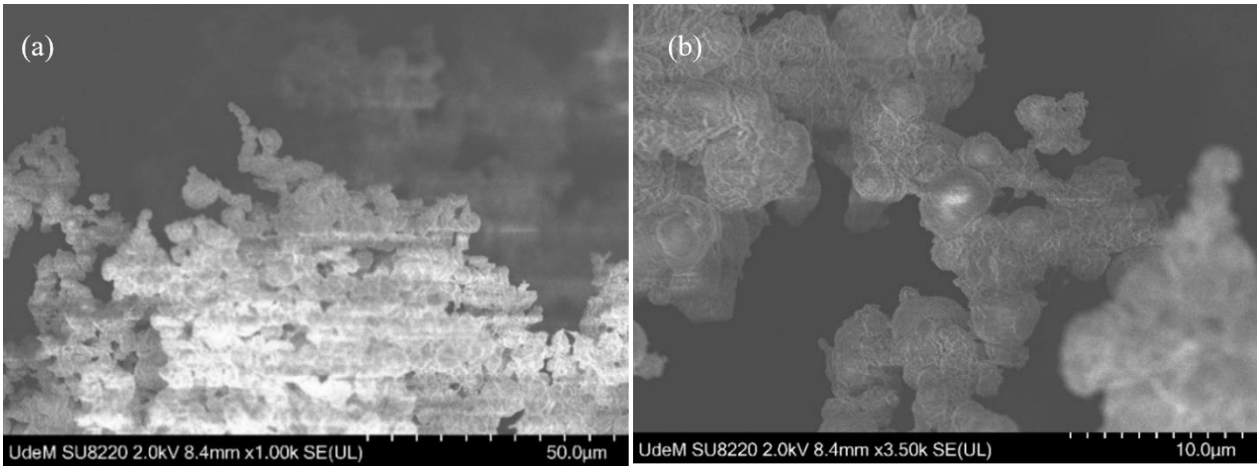

Figure A.3.SEM image of freeze-dried PVA-PI particles prepared with PVA 2wt.%, 75 vol% oil, at G1 condition. a)1k magnifications; b) 3k magnification

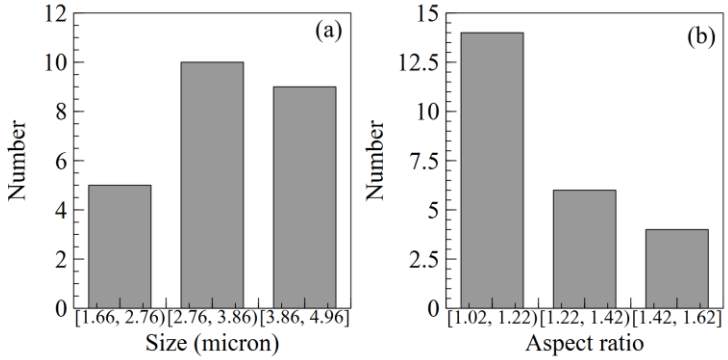

Figure A.4.Statistical analysis of PI particle at G1 condition; a) particle size b) aspect ratio

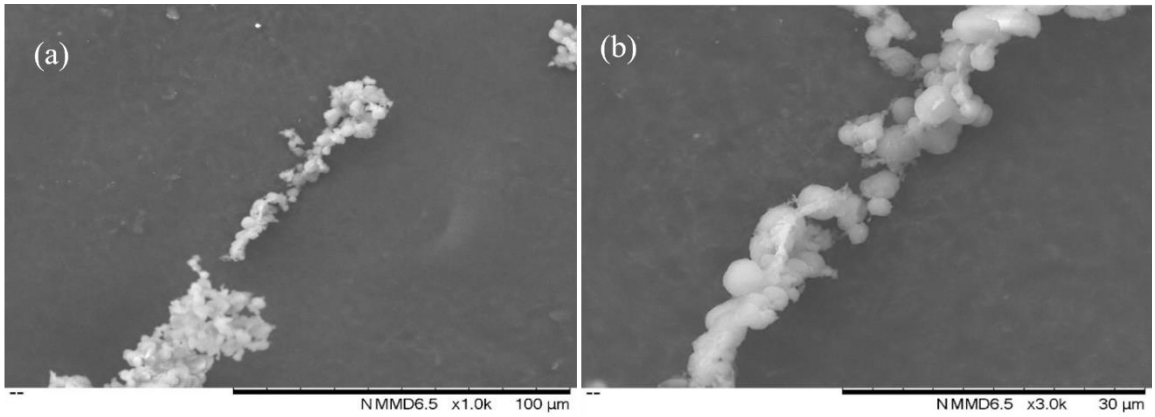

Figure A.5SEM image of freeze-dried PVA-PI particles prepared with PVA 3wt.%, 80 vol% oil, at G2 condition

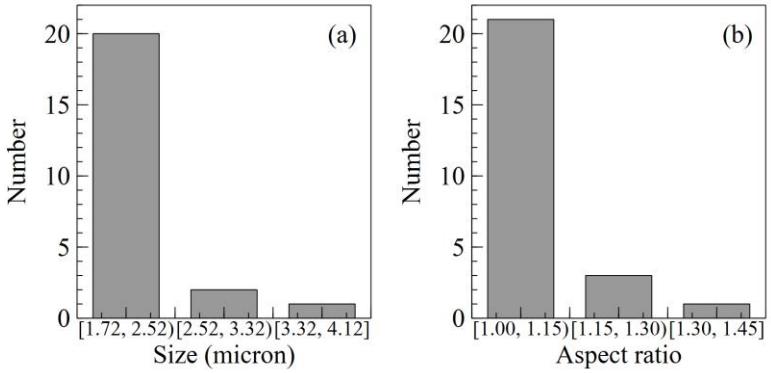

Figure A.6.Statistical analysis of PI particle at G2 condition; a) particle size b) aspect ratio

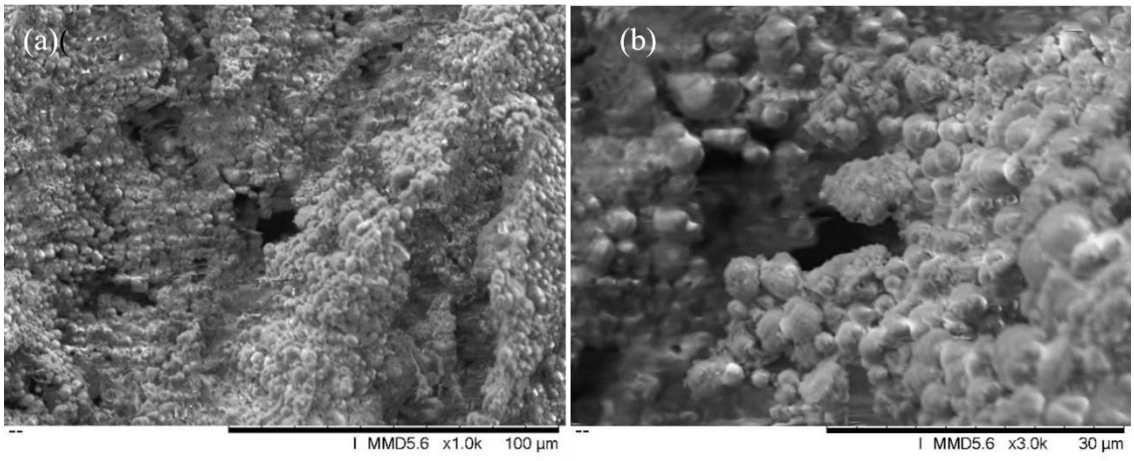

Figure A.7. SEM image of freeze-dried PVA-PI particles prepared with PVA 4wt.%, 80 vol%, at G3 condition

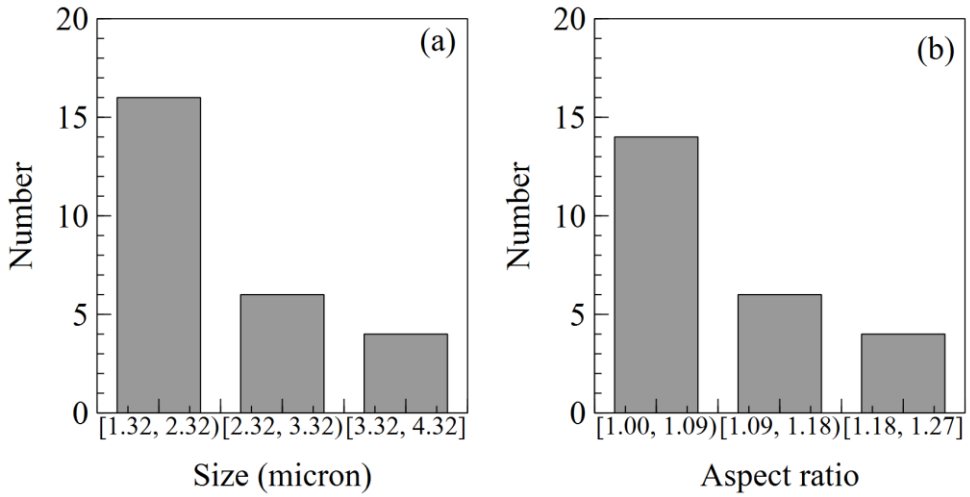

Figure A.8. Statistical analysis of PI particle at G3 conditions; a) particle size b) aspect ratio

APPENDIX B SUPPORTING INFORMATION FOR PAPER2

B.1 Determining the reference rotational speed (Nref)

To achieve a constant available particle for stabilizing droplets in HIPPE, the impeller rotational speed must exceed the just-suspended rotational speed (N_{js}) across all scales and process conditions. The Zwietering [169] equation is well-known for estimating particle suspension, but it has certain limitations. For instance, the off-bottom clearance, which is critical for double helical ribbon (DHR) impellers, is not accounted for in the Zwietering equations.[148] Additionally, the equation is typically limited to a solid concentration below 2 wt.% in low-viscosity media.[148] However, the particle concentration in our formulation exceeds this threshold. Although the Zwietering's constant (S) has been determined for several impellers, there is a lack of data for the DHR impellers. Only Bertrand et al. [170] have estimated a S value of 2 for the DHR impeller.

Ayranci et al. [148],[171] reported that specific power input is more relevant than just-suspended speed for scaling up the particle suspension process. They proposed the following model for estimating the required just-suspended specific power (P_{js}) for each scale.

$$\frac{P_{js}}{\rho_{sl}V} = A\left(\frac{g(\rho_s - \rho_l)}{\rho_l}\right)^{1.5} d_p^{\frac{1}{2}} X^{3m} \qquad (B.1)$$

where ρ_{sl} is density of suspension of particles, V is the total volume, g is gravity, ρ_s and ρ_l are particle and liquid density, *dp* is the particle diameter. *X* represents the weight ratio percentage of particle to liquid, while *m* is a function of *X*. Ayranci et al. also demonstrated that the average value of 0.23 can be applied across all *X* ranges. *A* is a function of tank and impeller geometries, as well as the properties of particles [148]:

$$A = \frac{4}{\pi} * (S * \frac{D}{T})^3 * \left(\frac{d_p^{\frac{1}{10}} N_p v^{0.3}}{D^{\frac{11}{20}}} \right) * \left(\frac{g\Delta\rho}{\rho_l} \right)^{-0.15} \qquad \text{(B.2)}$$

where $\Delta\rho$ is the difference of particle and liquid density, υ is the kinetic viscosity, and N_p is the power number.

In our laminar mixing process, N_p equals the ratio of power constant (K_p) to Reynolds number (*Re)*. The K_p value is a function of impeller geometry and is equal to 324 for our impeller. *Re* was calculated for each rotational speed based on continuous phase viscosity and the impeller diameter. Then, N_p was determined for all scales and process conditions, and P_{js} was subsequently calculated for each condition. The experimental value of *P,* which was employed during emulsification, was also measured in the preliminary tests and compared with P_{js}.

For the smallest scale, the value of P/P_{js} was determined for a series of rotational speeds. We found that at *N=100 RPM,* P/P_{js} was slightly less than 1, and this speed was selected as the first reference rotational speed (N_{ref}). Two additional N_{ref} values were chosen with increments of 50 RPM, corresponding to the P/P_{js} values of 2, and 4 at N_{ref} =150 RPM and N_{ref} =200 RPM, respectively.

B.2 Power per volume ratio to the small scale

The ratio of *P/V* in medium and large scale to the *P/V* of the smallest scale are illustrated in Figure . These graphs confirm our previous observation that the power per volume across all scales overlaps each other at α=0, with the ratio being close to 1 in Figure a-b-c. As the α value increases, the ratio value deceases sharply; for instance, the ratio drops to 0.03 for large scale at α=1 and N_{ref}=200.

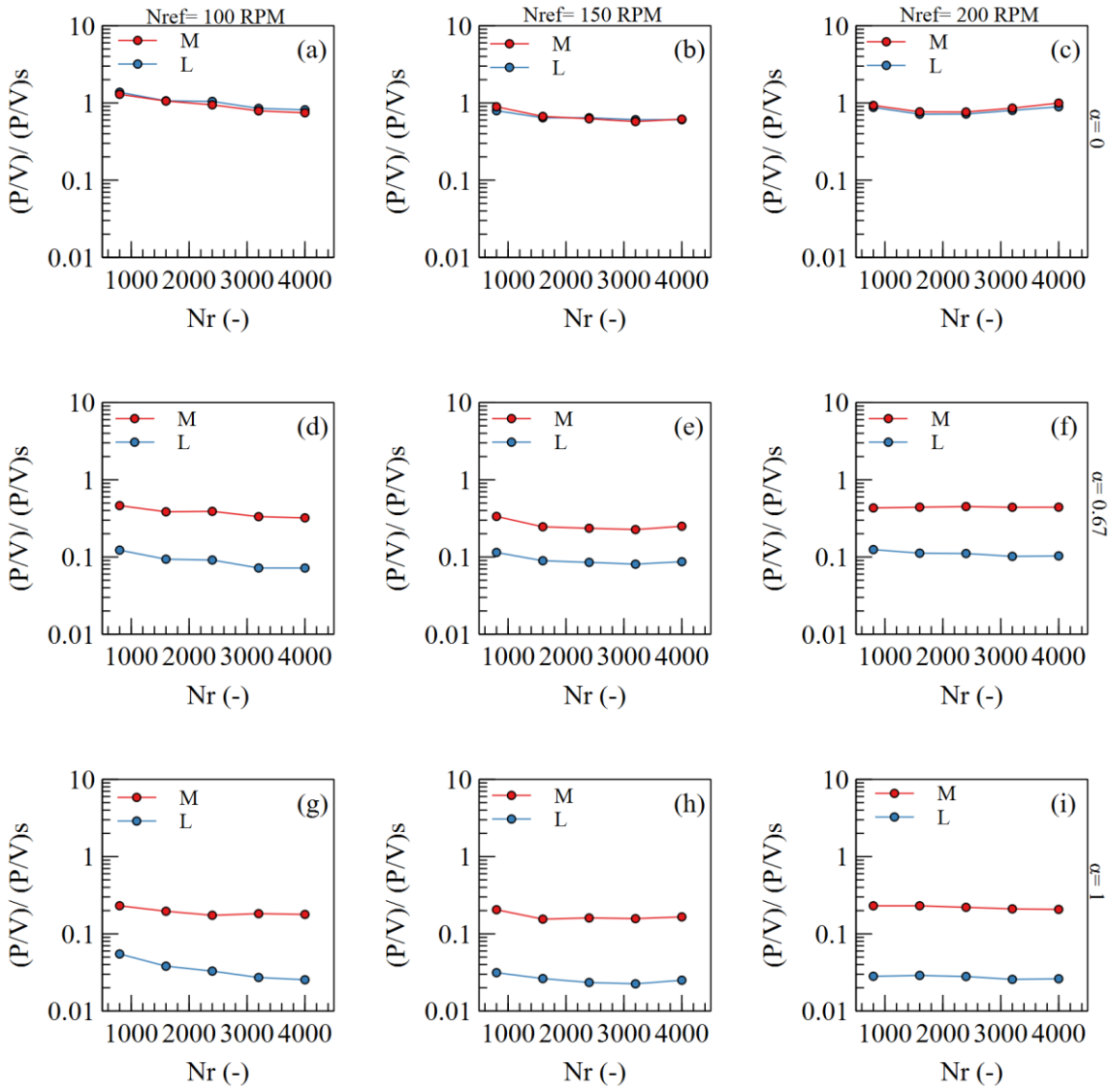

Figure B.1. The evolution of power ratio over the revolution numbers (Nr) for three scale-up exponents and three system sizes (S, M, L). (a), (b), (c) α=0 (constant speed). (d), (e), (f) α=0.67 (N2/N1 $=(D1/D2)^{0.67}$ (g), (h), (i) α=1 (N2/N1 =D1/D2).

B.3 Correlation of consistency index, Metzner and Otto constant , and power-law index with droplet size

The power-law index, Metzner and otto constant and consistency index of all samples at different scale-up exponents, reference rotational speeds, and scales were determine using the following equation and plotting the Γ/N versus N.

$$\frac{\Gamma}{N} = \frac{D^3 K_p k K_s^{n-1}}{2\pi} * N^{n-1} \qquad (B.3)$$

The correlations between these rheological values and droplet size are illustrated in Figure B.2.. The results reveal that, regardless of process conditions and scales, the rheological properties are strongly dependent on droplet size.

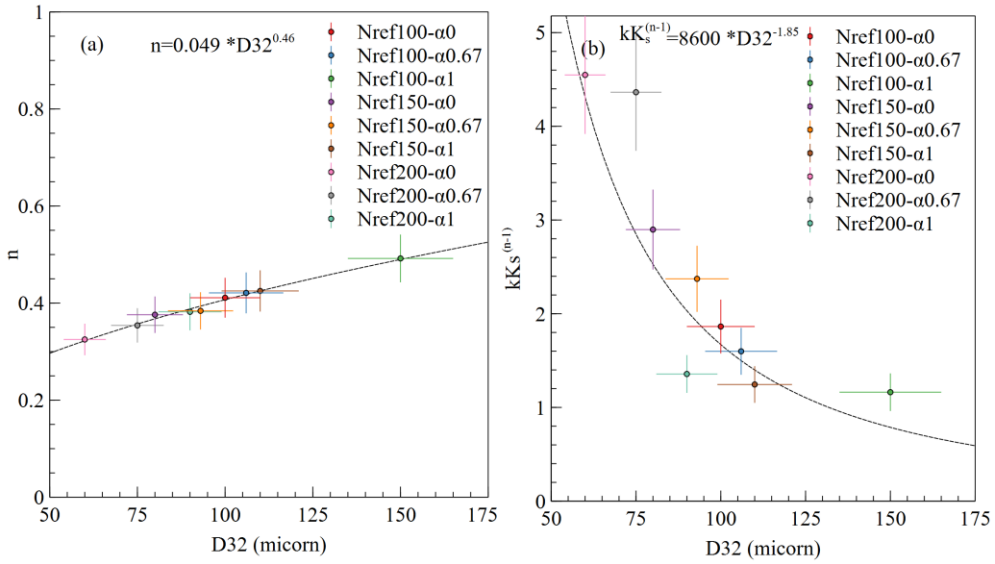

Figure B.2.Correlation between (a) power law index (n) and D_{32}, and (b) correlation between consistency index (k), Metzner and Otto constant (K_s), n and D_{32}.

B.4 Power-law behavior with rheometer

To validate the power-law and consistency indexes obtained through torque monitoring, the data were also measured using a rheometer. The MCR501 SN902199 was employed with the Rheoplus

rheometer. The test was conducted during the stability phase, meaning the maximum shear rate for each sample did not exceed the shear rate used during its emulsification, in order to prevent further droplet breakage. For instance, the maximum shear for sample M1-0, which was produced at 100 rpm, was set to 50 (1/s). Figure B3 shows the results of M1-0 to M3-0, corresponding to emulsions prepared at 100, 150, and 200 rpm at scale medium. The results confirm that the power-law index obtained with the rheometer- 0.38,0.32, and 0.27 for samples with 100,150, 200 rpm, respectively- agree well with the values obtained through torque monitoring, as shown in Figure B.2.

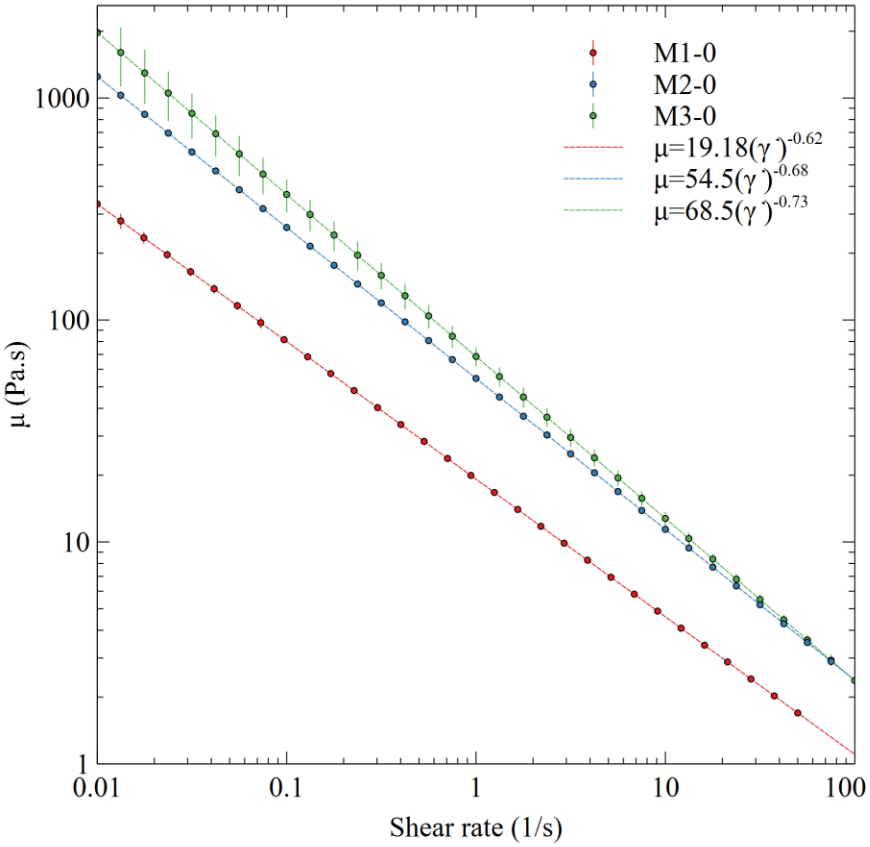

B.5 Comparison between measured and estimated power per volume

The estimated power per volume, based on the calculated viscosity of the emulsion, was compared with the actual power per volume for all scales, at all values of α and rotational speed. The results

reveal that the estimated values closely match the real value of power per volume when at α equal 0 for all rotational speed and at α equal 0.67 and 1 for N_{ref} 150 and 200 RPM. This indicates that, at low rotational speed especially for large scales and α=1 a significant portion of total power consumption is used for particle suspension.

The ratio of power to the just suspended power in the large scale at α=1 and ref=100 RPM was calculated to be less than 1, further confirming the hypothesis that, at very low rotational speed, particularly in large-scale systems, most of the power is consumed for particle dispersion.

It is worth mentioning that at the highest rotational speed, there remains a 4-6% deviation between estimated and real power per volume, which can be attributed to the omission of elongational flow effect in estimation of power per volume.

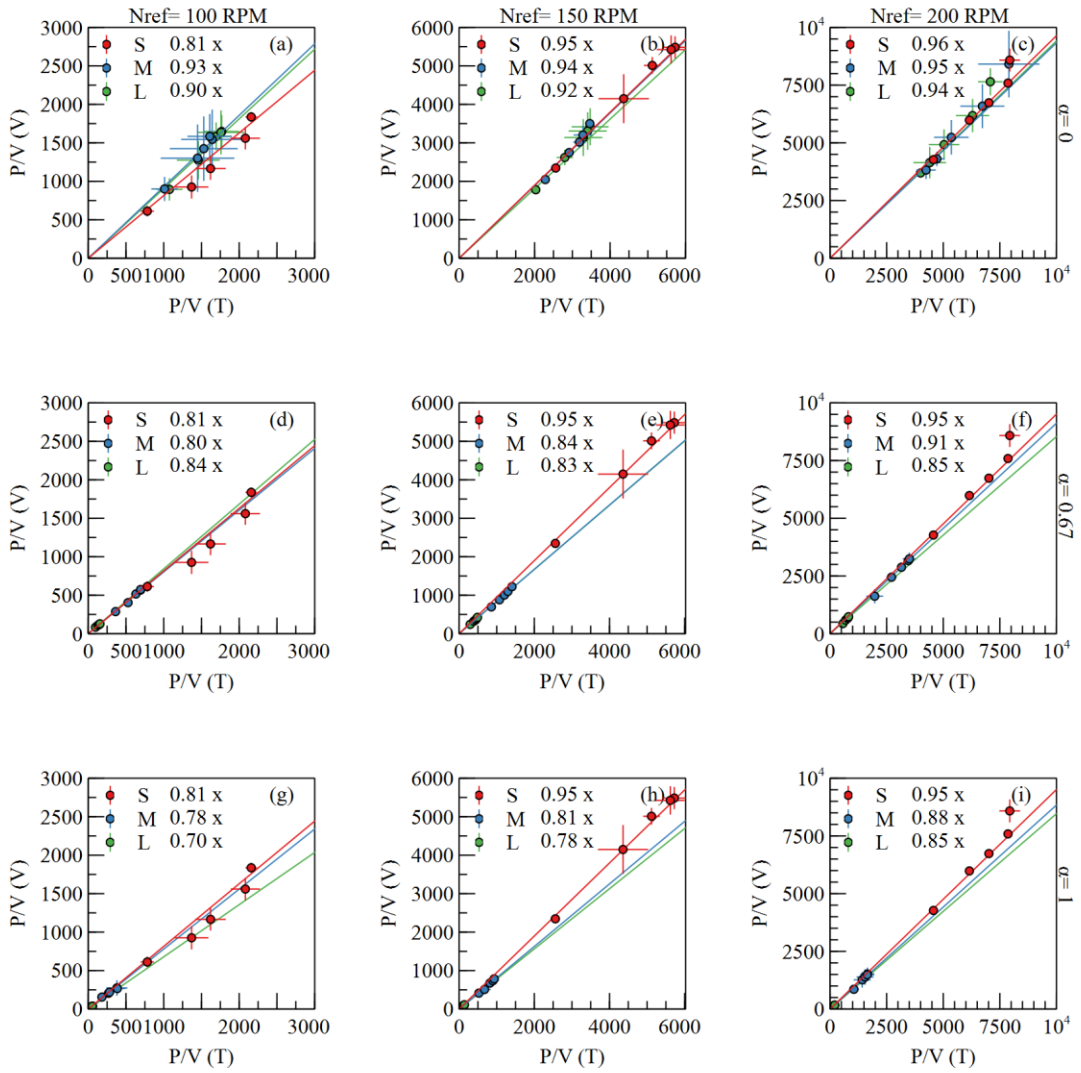

Figure B.3. comparison of measured P/V (P/V(T)) with the estimated P/V (P/V(V)); (a), (b), and (c) scale up exponent 0 and Nref =100, 150, and 200 rpm, respectively. (d), (e), (f) scale up exponent 0.67 and Nref= 100, 150, 200 rpm, respectively. (g), (h), and (i) scale up the exponent of 1 and Nref= 100, 150, and 200 rpm, respectively.

B.6 Effect of just-suspended power on final D32

The Ayranci equations (Equations1-2) were employed to determine the effect of just suspended power on D_{32}. By substituting all parameters based on our formulation and impeller geometry, the just-suspended power was calculated in each rotational speed. These values were then compared

with the experimental value of P, which was employed during emulsification and measured by torquemeter.

Figure B illustrates the effect of the ratio of input power (*P*) to just suspended power (*Pjs*) on the final droplet size. When the ratio is less than 1, the input power is insufficient to fully suspend particles. Conversely, when the ratio exceeds 1, all particles are fully suspended and contribute to droplet coverage. The figure also shows that the final droplet size is not solely a function of P/Pjs but also it is a function of scales. For instance, at constant P/Pjs between 2 and 4, the droplet sizes in large, medium, and small scales are about 200, 100, and 50 microns, respectively. Thus, other parameters such as breakage capacity should be investigated.

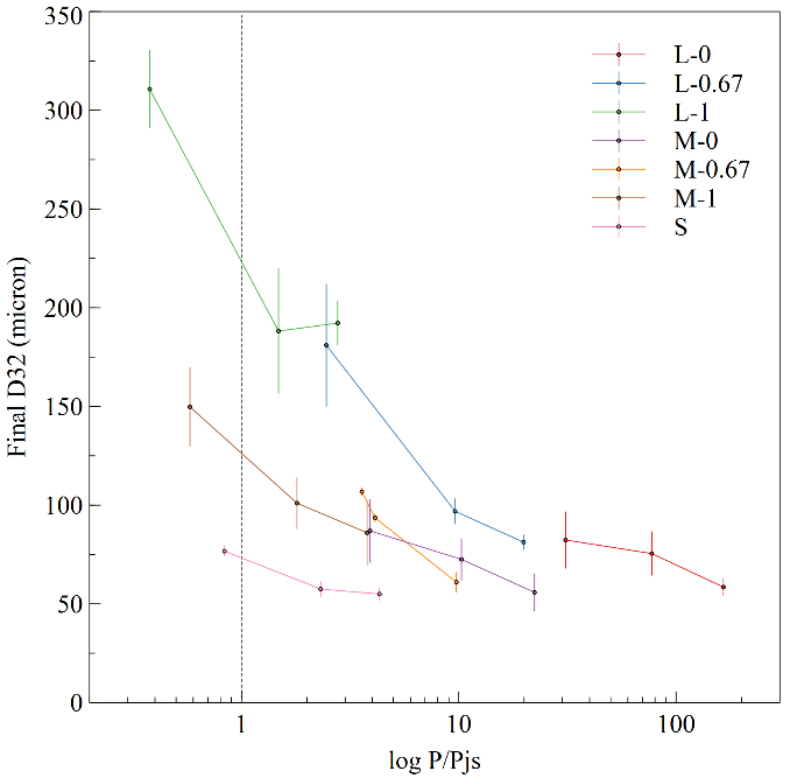

Figure B.4. Final D32 vs. P/Pjs

B.7 The statistical analysis of the correlation between D32-e/v and D32- P/V

It is reported that D_{32} evolves with *e/V* before the equilibrium droplet state and after that point, it correlates with *P/V*.

A logarithmic correlation is considered :

$$\log(D_{32}) = a + b.\log\left(\frac{e}{V}\right) \qquad (B.4)$$

$$\log(D_{32}) = c + d.\log\left(\frac{P}{V}\right) \qquad (B.5)$$

The statistical regression data are summarized in Table B.1., where the P-values of all regression parameters are much smaller than 0.5, indicating the strong validity of these correlations.

Table B.1.Regression summary of D32 number of runs 50

	Regression parameters		Statistics		
			p-value	-95%CL	+95%CL
e/V	a	3.84	$4.38*10^{-32}$	3.57	4.01
	b	-0.30	$4.2*10^{-19}$	-0.34	-0.26
	F-value	$4.2*10^{-19}$			
	R^2	0.81			
P/V	c	3.24	$8.05*10^{-35}$	3.05	3.44
	d	-0.38	$5.23*10^{-18}$	-0.44	-0.32
	F-value	$5.23*10^{-18}$			
	R^2	0.79			